Durham E-Theses

An evaluation of NS-001 and TIMS data for lithological mapping and mineral exploration in weathered vegetated terrain

Hook, Simon John

An evaluation of NS-001 and TIMS data for

lithological mapping and mineral exploration

in weathered vegetated terrain

A thesis presented for the degree of

Doctor of Philosophy

by

Simon John Hook

University of Durham

Department of Geological Sciences

May 1989

1 2 JAN 1990

DECLARATION

The work contained in this thesis has not been submitted elsewhere for any other degree or qualification and that unless otherwise referenced it is the author's own work.

IF

If you can keep your head when all about you
Are losing theirs and blaming it on you,
If you can trust yourself when all men doubt you.
But make allowance for their doubting too;
If you can wait and not be tired by waiting,
Or being lied about, don't deal in lies,
Or being hated, don't give way to hating,
And yet don't look too good, nor talk too wise.

If you can dream-and not make dreams your master
If you can think-and not make thoughts your aim
If you can meet with Triumph and Disaster
And treat those two imposters just the same;
If you can bear to hear the truth you've spoken
Twisted by knaves to make a trap for fools,
Or watch the things you gave your life to, broken,
And stoop and build'em up with worn-out tools:

If you can make one heap of all your winnings
And risk it in one turn of pitch-and-toss,
And lose, and start again at your beginnings
And never breathe a word about your loss;
If you can force your heart nerve and sinew
To serve your turn long after they are gone,
And so hold on when there is nothing in you
Except that Will which says to them, 'hold on!'

If you can talk with crowds and keep your virtue,
Or walk with Kings - nor lose the common touch,
If neither foes nor loving friends can hurt you,
If all men count with you, but none too much,
If you can fill the unforgiving minutes
With sixty seconds' worth of distance run,
Yours is the Earth and everything that's in it,
And-which is more-you'll be a Man, my son!

RUDYARD KIPLING

ABSTRACT

This thesis evaluates the combined use of multispectral remotely sensed data from the 0.45-2.35μm and 8μm-12μm wavelength regions for lithological mapping and mineral exploration in weathered, vegetated terrain.

The area studied is located in N. E. Queensland, Australia, and consists of a mixture of igneous, metamorphic and sedimentary rocks. The extrusive and intrusive igneous rocks of acid to intermediate composition are currently the focus of active exploration for gold mineralisation.

The results from this study indicate data from the 0.45-2.35μm wavelength region are of more use for mineral exploration than data from the 8-12μm wavelength region in this terrain. Evaluation of data from the 0.45-2.35μm wavelength region resulted in the discovery of an area of epithermal alteration with potential for gold mineralisation at Blackfellow Mountain.

Data from both wavelength regions proved useful for litholgical mapping but certain lithological units could only be discriminated with the data from the 8-12μm wavelength region.

In order to obtain these results the data were reduced to physically meaningful parameters (reflectance, temperature and emittance). This necessitated the removal of radiometric and geometric distortions. The techniques used to remove these distortions are outlined, including two new methods for the removal of atmospheric effects from data from the 8-12μm wavelength region.

After correction, the data from the 0.45-2.35μm wavelength region were analysed by a variety of techniques to extract the relevant reflectance information. These included compositing, channel ratios, log residuals, directed principal components and least squares fit residuals (LRES). The log residual and LRES techniques proved most effective for lithological mapping and mineral exploration respectively.

The corrected data from the 8-12μm wavelength region were also analysed by several techniques for extracting emittance and temperature information. These techniques were the decorrelation stretch, model emittance calculation and thermal log residuals. The latter technique, developed during this study, proved most effective for lithological mapping.

TABLE OF CONTENTS

CHAPTER 3. RADIOMETRIC AND GEOMETRIC CORRECTION
OF AIRBORNE MULTISPECTRAL DATA FROM THE
0.45μm-2.35μm WAVELENGTH REGIONS

CHAPTER 4. ANALYSIS AND INTERPRETATION OF DATA FROM THE 0.4μm-2.5μm WAVELENGTH REGION FOR LITHOLOGICAL MAPPING AND MINERAL EXPLORATION IN WEATHERED VEGETATED TERRAIN

CHAPTER 5. ANALYSIS AND INTERPRETATION OF DATA FROM THE 8μm-12μm WAVELENGTH REGION FOR LITHOLOGICAL MAPPING AND MINERAL EXPLORATION IN WEATHERED VEGETATED TERRAIN

CHAPTER 6. ANALYSIS AND INTERPETATION OF SAMPLES
COLLECTED FROM BLACKFELLOW MOUNTAIN BY X RAY
DIFFRACTION AND LABORATORY SPECTROMETRY

CHAPTER 7. SUMMARY, CONCLUSIONS AND FURTHER RECOM-
MENDATIONS

LIST OF TABLES

LIST OF FIGURES

LIST OF PLATES

CHAPTER 1

INTRODUCTION

1.1 Background

Numerous studies have demonstrated the utility of multispectral remotely sensed data from the 0.45μm-2.5μm (VNIR/SWIR) wavelength region for lithological mapping and mineral exploration (*eg.* Rowan 1974; 1976; Goetz 1981; Abrams 1983, 1985; Loughlin and Taylor 1985; Kruse 1986). The data for these studies has been acquired by scanners mounted on aircraft and satellites.

Similar but fewer studies have shown the potential of remotely sensed data from the 8μm-12μm (MIR) wavelength region for lithological mapping (*eg.* Kahle *et al.,* 1980; Goetz 1981; Kahle 1983,1987,1989; Gillespie *et al.,* 1984; Blodget *et al.,* 1985; Lahren *et al.,* 1986,88; Watson *et al.,* 1988). Fewer studies have been conducted in the MIR since the only thermal multispectral scanners with suitable channel locations and spatial resolutions for lithological mapping are aircraft mounted. However, a space-borne instrument is recommended for inclusion on Landsat 7* which will probably result in far greater use of data from this wavelength region.

The majority of studies using these data have been undertaken in arid sparsely vegetated terrain with little surface weathering. Few studies have attempted to utilise such data in deeply weathered vegetated terrain (*eg.* Fraser *et al.,* 1986; Hook and Munday 1988a and b; Drury and Hunt 1988).

The use of multispectral remote sensing for lithologic discrimination in

---

* Landsat refers to a series of satellites launched sequentially from 1972. Five Landsats have now been launched. Landsats 1-3 only acquire digital multispectral data in four channels between 0.5μm and 1.1μm. An additional sensor was included on Landsats 4 and 5 which acquired 6 channels of digital data between 0.45μm and 2.35μm and 1 channel of digital data between 10.42μm and 11.66μm.

deeply weathered terrains is particularly problematic because an understanding of the type and association of the weathered products is neccessary to infer the lithology at depth. The presence of vegetation creates further problems because the rock reflectance can be obscured and mixed with that of vegetation. Therefore, the application of multispectral remote sensing in the VNIR, SWIR and MIR to semi-arid vegetated weathered regions requires an understanding of both the weathering process and the effect of rock, mineral and vegetation mixing at the sub-pixel level.

More recently investigators have attempted to use the complimentary information from the VNIR, SWIR and MIR to improve their ability to discriminate between lithologic units (*eg.* Kahle and Goetz 1983; Vincent *et al.,* 1984; Rickman and Grant 1985; Evans 1988; Drury and Hunt 1989). However, until now this approach has not been applied to deeply weathered, vegetated terrain.

A unique opportunity to examine the complimentary use of the VNIR, SWIR and MIR remotely sensed data in weathered vegetated terrain resulted from the US/Australia Joint Scanner Project. This project was undertaken in 1985 when NASA brought its Hercules C-130 aircraft to Australia. On board were three sensors, the NS-001 multispectral scanner, the Thermal Infrared Multispectral Scanner (TIMS) and the Airborne Imaging Spectrometer (AIS). These sensors enabled the simultaneous acquisition of multispectral remote sensing data from the VNIR, SWIR and MIR. The aircraft was flown over a series of test sites throughout Australia. The NS-001 and TIMS data used in this study were obtained from one of these test sites located in weathered vegetated terrain close to Charters Towers, N. E. Queensland. The NS-001 sensor measures the energy reflected from the ground surface in seven channels located in the VNIR and SWIR. The TIMS measures radiance in six channels located in the MIR.

1.2   Aims and Objectives of the Study

The primary objective of this study is an evaluation of the combined use of airborne multispectral data from the 0.45μm-2.35μm and 8μm-12μm wavelength regions for lithological mapping and mineral exploration in weathered vege-

tated terrain.

This objective is best achieved if the data are reduced to physical terms, that is reflectance, emittance and temperature. This permits comparison of the airborne data with field and laboratory data sets and with other remotely sensed data expressed in physical terms obtained elsewhere.

In order to interpret the data in this manner several other secondary objectives need to be addressed. First, the data need to be corrected for various inherrent radiometric and geometric distortions. Radiometric distortions alter the the absolute value of the radiation measured by the sensor, whereas geometric distortions alter the spatial relationships between objects. Secondly, the corrected data need to be analysed by a variety of image processing techniques to extract the relevant geological reflectance, emittance or temperature information. These should include standard techniques such as band ratios and advanced techniques such as the log residual technique developed by Green and Craig (1985). Thirdly, the processed data from each wavelength region need to be evaluated as an aid for lithological mapping and mineral exploration. This evaluation will be achieved through comparison with existing geological maps, fieldwork and laboratory analysis of field samples. Laboratory studies will include thin section identification, X-ray diffraction and spectral analysis. Fourthly, the relative merits of each technique should be assessed and where possible, existing techniques improved or new techniques developed for lithological mapping and mineral exploration with these data in this terrain. This approach to data analysis and interpretation is summarised in Figure 1.1.

Once these secondary objectives were fulfilled it was possible to address the primary objective. This would include an evaluation of the mineralisation potential of any targets detected through the analysis of the remotely sensed data.

1.3   Specific Aims and Objectives

1. Radiometric Correction

   a   Calibration of the NS-001 and TIMS data to remove sensor-related

distortions.

    b   Removal of X-track shading from NS-001 data.

    c   Development of techniques for atmospheric correction of TIMS data using scene derived parameters.

2. Geometric Correction

    a   Correction for varying lateral scales at right angles to the direction of flight (tangential scale distortion) in NS-001 and TIMS data.

    b   Correction for oversampling in the direction of flight in NS-001 data.

3. Analysis and Interpretation of NS-001 Data

    a   Analysis of corrected NS-001 data using standard and advanced image processing techniques. These include compositing, channel ratios, log residuals, least squares fit residuals (LRES) and directed principal components (DPC).

    b   Interpretation of processed NS-001 data and comparison with existing maps, fieldwork and laboratory analyses of field samples.

    c   Assessment of the relative merits of each image processing technique and if possible, improvement of these techniques and the development of new techniques.

4. Analysis and Interpretation of TIMS Data

    a   Analysis of corrected TIMS data using standard and advanced image processing techniques, such as include the decorrelation stretch and model emittance calculation.

    b   Interpretation of processed TIMS data and comparison with existing maps, fieldwork and laboratory analyses of field samples.

    c   Assessment of the relative merits of each technique and if possible, improvement of these techniques and the development of new techniques.

    d   An evaluation of the complimentary use of data from both wavelength regions for lithological mapping and mineral exploration in weathered vegetated terrain.

5. Evaluation of the mineralisation potential of any areas detected through the analysis and interpretation of the remotely sensed data.

1.4 Structure of the Thesis

The thesis is divided into 7 chapters. Chapter 1 provides the background for the overall objective of the thesis and details the specific aims and objectives which need to be achieved to fulfill that objective. Also given are the details of the remote sensing data sets utilised for the study.

Chapter 2 describes the characteristics of the study area. This includes its location, physiography, climate, geology, vegetation and weathering history.

Chapter 3 has been divided into two main sections dealing with radiometric and geometric corrections respectively. The radiometric corrections are separated into two categories dealing with the removal of sensor-related effects (calibration) and scene-related effects including atmospheric correction and the the removal of view angle effects (X-track shading).

The steps involved in calibration of both the NS-001 and TIMS data are given together with an example of the effect of not calibrating such data using an algorithm designed to select the best channels for discrimination. The atmospheric and view angle effects are described according to the wavelength region they occur in and algorithms are presented for their removal using scene derived parameters.

The geometric distortions relate to the effect of varying lateral scales (tangential scale distortion) and oversampling in the flight direction. Such distortions are common in data acquired from aircraft mounted scanners and so these corrections are widely applicable.

Chapter 4 presents the results from the analysis and interpetation of the data from the 0.4μm-2.5μm wavelength region for lithological mapping and mineral exploration. Initially the physical basis for remote sensing in this region is described. This is followed by the results from the analysis and interpretation of the airborne multispectral data from the 0.45μm-2.35μm wavelength region at the first of two test sites termed Camp Oven and Plateau respectively. These test sites typify the variety of rock types, weathering history and vegetation cover in the scene. They are also characteristic of much of NE Queensland which should ensure that the results from this study are widely applicable to other areas.

The data from the Camp Oven test site were analysed using the compositing, channel ratio, log residual, least squares residual and directed principal

components techniques. The background and method of each technique is discussed before the results and interpretations are presented. High resolution laboratory spectra are then described and interpretated from field samples collected at the test site. The results are then presented from the analysis and interpretation of airborne multispectral data from the Plateau test site using those techniques found to be most effective with the data from the Camp Oven test site. Finally, the conclusions are presented together with a brief summary.

Chapter 5 presents the results from the analysis and interpetation of the data from the 8μm-12μm wavelength region for lithological mapping and mineral exploration. Initially the physical basis for remote sensing in this region is described followed by the results from the analysis and interpretation of the airborne multispectral data from the 8μm-12μm wavelength region at Camp Oven test site. These data were analysed using the decorrelation stretch, model emittance calculation and thermal log residuals. The methodology behind each technique is described before the results are presented. The results from the 0.4μm-2.5μm and 8μm-12μm wavelength regions are then compared and contrasted over the Camp Oven test site. The results from the analysis and interpretation of the data from the Platea test site using those techniques found to be most effective with the data from the Camp Oven test site are then presented. This is followed by the results from a comparison of the data from the 0.4μm-2.5μm and 8μm-12μm wavelength regions over the Plateau test site.

The results from the application of the thermal log residual technique to data from Cuprite, Nevada, W. USA are then given. The thermal log residual technique was developed as part of this study and the results from the Cuprite data demonstrate its wider applicability. Finally, the conculsions are presented together with a brief summary.

Chapter six decribes the results from the laboratory analysis of samples collected from Blackfellow Mountain. This area was identified as altered with the remotely sensed data from the 0.45μm-2.35μm wavelength region. Laboratory analysis included X-ray diffraction and laboratory spectrometry. The relative merits of each technique are also assessed. These data together with field observations are used to propose a model for the alteration development

6

and a evaluation of the mineralisation potential.

Chapter 7 consists of a summary of the preceeding chapters and highlights areas requiring further research.

1.5 Data Sets Utilised and Flight Parameters

The NS-001 and TIMS data were acquired as part of the US/Australia Joint Scanner Project undertaken in October 1985. The data were acquired at an altitude of 6130m above mean sea level and had a nominal spatial resolution of 15m^2. Atmospheric conditions during the flight were excellent. However, there had been several days of heavy rain prior to the flight.

The NS-001 airborne multispectral scanner acquires data in 8 discrete channels. Of these, 4 are located in the VNIR, 3 in the SWIR and 1 in the MIR. Table 1.1 gives the widths and locations of each channel together with a comparison of these with those from other systems mounted on both aircraft and satellites. The data are stored on 1600 bpi computer compatible tapes (CCT)s. The logical user format of these tapes is given in Appendix I.

The TIMS is a six channel airborne system acquiring data in the MIR. The widths and location of these channels are also given in Table 1.1 and logical format of the data also stored on 1600 bpi CCT's is given in Appendix I.

Two flightlines of both the NS-001 and TIMS data were collected over the study area. These were obtained along NE-SW flightpaths. The location of the flightpaths are given in Chapter 2. The most northerly flightpath is referred to as flightline 1 and the most southerly flightline 2.

Table 1.1 Comparison of the Band Edges of ATM, LANDSAT 4 TM, NS-001, LANDSAT MSS, TIMS and AIS data.

Region	ATM Band	ATM Band Edges	LANDSAT 4 TM Band	LANDSAT 4 TM Band Edges	NS-001 Band	NS-001 Band Edges	LANDSAT MSS Band	LANDSAT MSS Band Edges	TIMS Band	TIMS Band Edges	AIS
VISIBLE	1	0.42-0.45									
	2	0.45-0.52	1	0.45-0.52	1	0.45-0.52					
	3	0.52-0.60	2	0.52-0.60	2	0.52-0.60	4	0.5-0.6			
	4	0.605-0.625									
	5	0.63-0.69	3	0.63-0.69	3	0.63-0.69	5	0.6-0.7			
NEAR INFRARED	6	0.695-0.75									128 CONTINUOUS BAND BETWEEN 1.3 & 2.4
	7	0.76-0.90	4	0.76-0.90	4	0.76-0.90	6	0.7-0.8			
	8	0.91-1.05			5	1.0-1.30					
SHORTWAVE INFRARED	9	1.55-1.75	5	1.55-1.75	6	1.55-1.75	7	0.8-1.1			
	10	2.08-2.35	7	2.08-2.35	7	2.08-2.35					
MID INFRARED	11	8.5-13	6	10.42-11.66	8	10.4-12.5			1	8.2-8.6	
									2	8.6-9.0	
									3	9.0-9.4	
									4	9.6-10.2	
									5	10.3-11.1	
									6	11.3-11.7	

Wavelength scale (microns): 0.4, 0.7, 1.3, 2.4, 8.0, 13.0

Band Edges in Microns
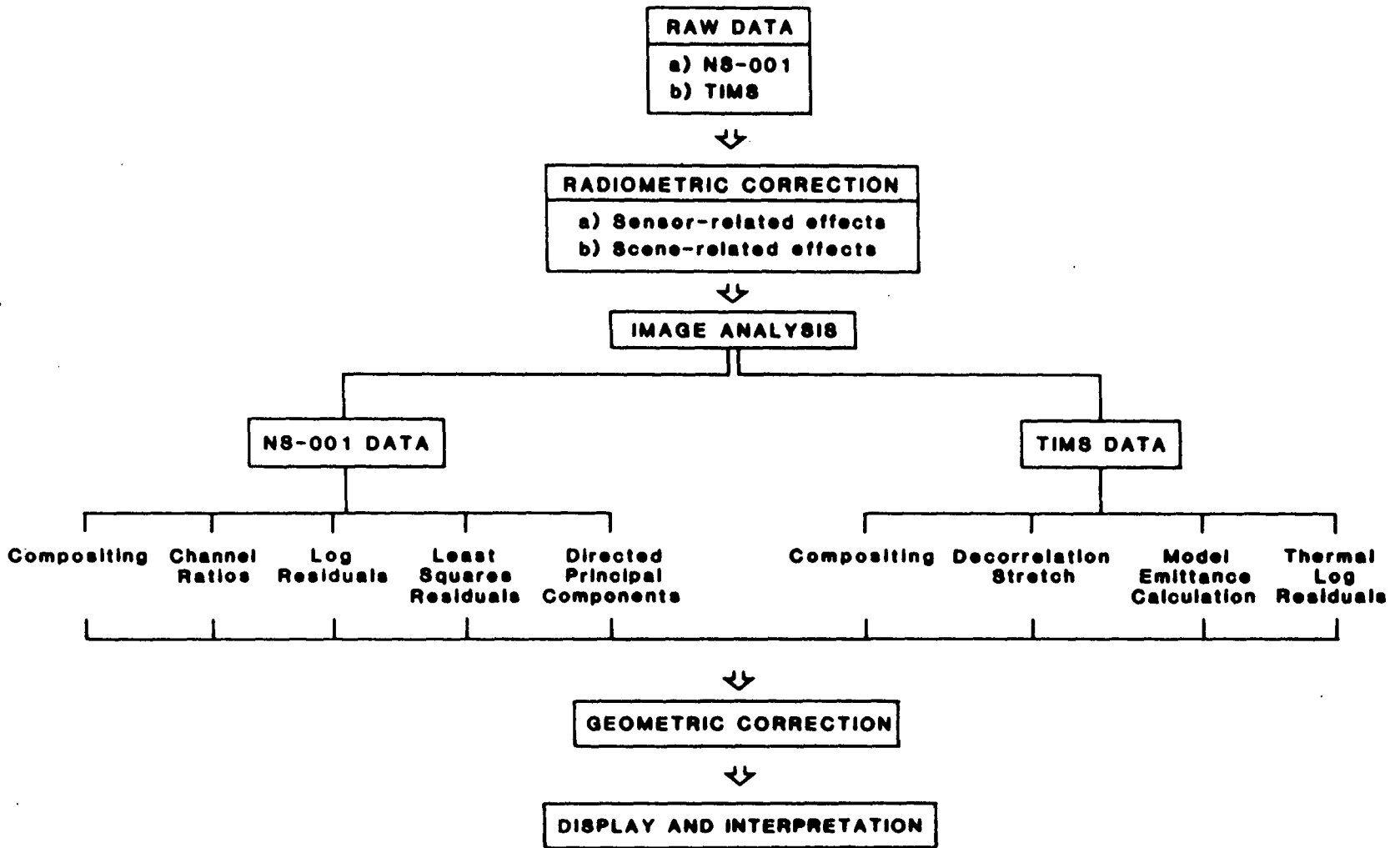
Figure 1.1 Summary Diagram of Research Approach

9

CHAPTER 2

CHARACTERISITCS OF THE STUDY AREA

2.1 Location and Access

The study area is located approximately 62.5 km southeast of Charters Towers, N. E. Queensland, Australia (Figure 2.1). The nearest major settlement is Townsville which lies 150km to the east on the Queensland coast (Figure 2.1). Access is provided by the Broughton Road which is a secondary dirt road, which runs through the study area. Several tracks off the main road provide 4 wheel drive access to the remaining area.

2.2 Climate

The climate of the area is tropical, with warm dry winters and hot wet summers. Two thirds of the annual rainfall falls from December to March, with July to October being the driest period. During the wet summers the area is largely inaccessable with most of the exploration work taking place in the winter. The Burdekin river on the northern edge of the study area is the main river in the Charters Towers area. The Burdekin river flows for most of the year breaking down into a series of water holes during extremely dry spells. The remaining rivers in the study area only flow after periods of heavy rain.

2.3 Physiography

The area can be separated into lowlands (180 to 300m) and uplands (greater than 300m), the maximum elevation being 476m. Seventy Mile Range, Camp Oven Mountain, Blackfellow Mountain and Three Sisters represent most of the upland area (Figure 2.2). Also shown is the areal extent of the coverage acquired by C-130. Two flightlines of remotely sensed data were acquired. These are henceforth referred to as flightline 1 and flightline 2 (Figure 2.2).

The following description of the geological setting is largely based on the work of Wyatt *et al.*, (1971) unless otherwise stated. Only those units which outcrop in the area covered by the remotely sensed data are described.

2.4 Structure

The study area straddles two major structural elements within NE Queensland. These are the Lolworth-Ravenswood block and the Drummond Basin (Figure 2.3)

The Lolworth-Ravenswood block has been divided into three components. These are the Cape River Canopy, the Ravenswood Granodiorite Complex and Lolworth Igneous Complex. Parts of the first two components occur in the study area and are now described

The Ravenswood Granodiorite Complex is considered late synorogenic, its intrusion stabilized the Lolworth-Ravenswood block in the late Silurian. The block separated the marine Burdekin Basin (north of the study area) from the continental Drummond Basin to the south. The complex is considered to intrude the Cape River Beds at shallow depth with the latter forming a canopy.

The Cape River canopy consists of folded, intruded and locally metamorphosed remnants of a thick sequence of early Palaeozoic sediments and volcanics. The Cape River Beds, which include the Mount Windsor Volcanics crop out in the study area. They have an E-W trend and dip to the south. The beds are folded, sheared, faulted and jointed with shearing decreasing away from the contact.

The Drummond Basin is a N-S structure 400km in length. The study area includes the northern tip of the basin.

2.5 Stratigraphy

The geology is dealt with in chronological order starting with the oldest. The distribution of the various geological units is given in Figure 2.2.

2.5.1 Cambro -Ordovician:

The Cape River Beds, (which include the Mount Windsor Volcanics) outcrop around Dreghorn and make up the Cambro - Ordovician in the study

area. They form a discontinuous belt of thermally and dynamically metamorphosed volcanics and sediments termed the Mount Windsor Subprovince.

Mount Windsor Subprovince

The Mount Windsor Subprovince forms an E-W strip approximately 180km long and up to 30km wide stretching from the Leichhardt Range east of Burdekin River to Pentland in the west. The subprovince consists of volcano-sedimentary rocks. The southern margin of the Mount Windsor subprovince is intruded by the Ravenswood Granodiorite. Wyatt, (1970), dates the subprovince as 530-510 my (Late Cambrian) on the basis of Rb-Sr whole rock analyses.

The lithologies which characterise the subprovince consist of a conformable sequence of acid and intermediate volcanics with both volcanic and non-volcanic sedimentary sequences. The entire sequence is up to 15km thick and termed the Seventy Mile Range Group. The sequence generally dips south away from the Lolworth-Ravenswood Batholith.

Four formations are recognized in the Seventy Mile Range Group. The characteristics of these formations are given in Table 2.1.

Within the study area Gregory (1985) considers the sequence around Dreghorn to belong to the Trooper Creek Formation because of the dominant occurrence of andesite-basalt-dacite. South, around Warrawee, the rhyolite lithology indicates the rocks belong to the Mount Windsor Volcanic Unit. Further south around Plateau these are overlain by andesite and shale of the Trooper Creek Formation.

The Seventy Mile Range Group has been intruded by an early phase of the Ravenswood Granodiorite (481 my., Middle Ordovician). A metamorphic aureole has formed around the Lolworth-Ravenswood Batholith. The aureole is well developed in the Dreghorn area consisting of biotite, cordierite, andalusite assemblages. The Lolworth-Ravenswood Batholith has steep contacts, with rocks of the Mount Windsor Subprovince dipping steeply at the contact with dips decreasing to 20 to 30 degrees away from the contact.

Volcanogenic mineralisation occurs in either the Trooper Creek Formation or Mount Windsor Volcanics along the entire length of the Mount Windsor Subprovince.

2.5.2 Middle Ordovician to Lower Devonian

Ravenswood Granodiorite Complex

The Ravenswood Granodiorite Complex is a large batholith of Ordovician age (395 my), occupying several thousand square kilometres. Its intrusion brought to a close a period of geosynclinal sedimentation, welding the early Palaeozoic strata to the Precambrian Craton.

The subsequent sedimentary cycle was of a shelf or intracratonic type. The Ravenswood Complex together with the Lolworth Igneous Complex are termed the Ravenswood-Lolworth Block. Some characteristics of the batholith are given in Table 2.2.

The Ravenswood Granodiorite Complex has been divided into several phases; the earlier phases are characterised by rocks of granodioritic composition, whilst the later phases were of granitic (acidic) composition.

The main granodioritic phase and late acid phase outcrop in the area covered by the imagery.

Main Granodiorite Phase

This consists of granodiorite and minor tonalite. The granodiorite is medium grained and may contain hornblende and/or biotite. Within the main phase there are numerous granitoid bodies ranging from gabbro to diorite to adamellite and granite (Henderson and Stephen, 1980). The main phase is high in Al_2O_3 and K_2O (Henderson and Stephenson, 1980). Shearing is widespread and dykes are common. A series of ENE ridges composed of chlorite, quartz and muscovite occur between the Cardigan Homestead and Camp Oven. The main granodiorite phase is the host of most of the gold mineralisation found within the Charters Towers/Ravenswood area.

Late Acid Phase

Porphyritic pink biotite granite outcrops to the SE of Camp Oven Mountain. The granite has been brecciated, fractured and mylonised. the granite breccias are monomict, composed of angular clasts up to 300cm in length in a granulated matrix.

Age

The batholith has intruded Lower Palaeozoic Strata. Rb-Sr total whole rock analyses give two distinct isochrons with ages of 454 ± 30my (late Ordovician)

and 394 ± (Mid Devonian) according to Henderson and Stephenson (1980). Samples from the main granodiorite phase lie on both isochrons. This is explained as the younger isochron being the result of widespread resetting or the lack of recognition of the later granodiorite- tonalite phases in the main phase (see Henderson and Stephenson, 1980).

2.5.3 Upper Devonian to Lower Carboniferous:

Drummond Basin Succession:

The imagery covers the northern end of the Drummond Basin. The Scartwater formation is the only unit of the Drummond Basin Succession present in the study area. The formation consists of characterisitic feldspathic quartz sandstones and green mudstones.

2.5.4 Upper Carboniferous

NE Queensland was continental in the Late Palaeozoic. It was occupied by volcanic fields which mostly overlay deformed, variably metamorphosed older Palaeozoic and Proterozoic rocks with a marked regional unconformity (Henderson and Stephenson, 1980).

Acid to Intermediate Volcanics

These outcrop at and around Camp Oven Mountain. This area has been selected as a test site and is described in detail in section 4.3.1

Intrusive Rhyolite Porphyry

Several isolated intrusive rhyolite bodies occur within the Charters Towers Sheet area. Most of these are found between Camp Oven Mountain and Malakof Mountain to the SW of the study area. Four such bodies outcrop in the study area consisting of flow banded rhyolite presumed to be Upper Carboniferous in age. They produce high ground and support a thin cover of broad leaved iron bark trees.

Two areas of rhyolite outcrop in the west of the study area and are termed the Western Rhyolites.

The third area of rhyolite outcrops at Three Sisters four miles SSW of Camp Oven. It consists of several quartz porphyry dykes and irregular intrusions which cut the Ravenswood Granodiorite Complex.

The fourth area consists of numerous irregular dykes of light grey acid

volcanic(?) breccia which outcrop in the late brecciated mylonised granitic phase of the Ravenswood Granodiorite Complex on the SE border of the Camp Oven Complex.

2.5.5 Tertiary

During the Tertiary, much of the south of the study area was subject to the widesperead development of laterite and ferricrete. The laterites were typically developed on Tertiary sediments, however, older units were also affected. The Tertiary sediments consist of coarse white to buff coloured argillaceous sandstone, feldspathic sandstone and argillaceous sandstone with lenses of pebble or conglomerate. These sediments which are flat-lying formed a widespread sheet which has been dissected into scattered mesas and plateaus. The edges of these mesas and plateaus, where weathering profiles are exposed, are termed breakaways.

2.5.6 Quaternary

Superficial Sand :

Sands and grits form outwash deposits outcropping as low rises and covering much of the catchment area of the Rollston River. They result from erosion of the tertiary sediments and laterites. These sands and grits are considered older than the modern day alluvium bordering the present day streams.

2.5.7 Mineralisation

Known Gold and Silver mineralisation occurs in and around the Ravenswood Granodiorite Complex. This mineralisation is usually associated with shearing in either the complex or the surrounding rocks. A low grade porphyry copper prospect occurs at the Three Sisters and an epithermal gold prospect at Plateau.

2.6 Vegetation

Most of the area is characterised by open savannah woodland with eucalyptus and acacias dominating the tree and shrub species. Beneath the woodland there is an understorey of a variety of grasses and leaf litter. *Heteropogon contortus* (spear grass) is the dominant grass (Wyatt *et al.,* 1971). Most of the upland areas of Upper Carboniferous acid volcanics are characterised by broad leaved ironbark trees (Plate 2.1).

Plates 2.2-2.3 illustrate the typical vegetation cover in the study area. Generally cover was far greater in the south around Plateau than in the north around Camp Oven. Normally the understorey of grasses are tinder dry in October when the remote sensing data were collected. However, prior to the flight there was a period of heavy rain. As a result many previously dry areas began turning green (Plate 2.3).

The vegetation cover encountered in this area is typical of much of Northern Queensland and other areas within Australia.

2.7 Weathering

Much of Australia has been tectonically stable since the Permian and subject to subaeriel weathering (Butt, 1983). This has resulted in the development of a mantle of deep weathering over much of the landscape, lateritic in nature, which has subsequently been partly eroded. In order to map the geology at depth an understanding of how this weathering profile develops and the secondary minerals it produces is required.

The profile is thought to develop progressively with each subsequent horizon forming from the one beneath it (McFarlane, 1976). The profile typically progresses from fresh rock - saprolite - mottled zone - ferruginous zone - sand (Figure 2.4). The saprolite is the first product that develops and consists of the original rock texture, stable primary minerals and neo - formed secondary minerals with the loss of mobile elements. White kaolinitic saprolites which typically develop over igneous rocks are termed pallid zones. The top of the saprolite is marked by the loss of primary textures and passes into a mottled zone. In this zone iron oxides have accumulated together with secondary structures such as coatings and concretions (Plate 2.4). Further reworking, settling and compaction leads to the development of a ferruginous zone, often massive, which passes into the uppermost sandy horizon accumulated largely as a residum.

This simple profile has been complicated in many areas by the development of multiple phases of lateritic weathering with intervening periods of partial stripping. These effects may not be obvious but profiles have been found which contain multiple ferruginous zones considered to indicate a mul-

tiphase origin.

Lateritic weathering terminated in the Miocene with increasing aridity spreading from the centre of the continent. Since that time water tables have lowered leading to dehydration and subsequent hardening of the ferruginous layers. The increasing aridity has significantly slowed erosional processes. However, backward stream erosion has continued leading to the development of flat plateau surfaces surrrounded by an escarpment and debris slope, and a piedmont slope down to the valley floor (Figure 2.5). This stripping process has exposed varying parts of this profile, including relatively fresh rocks in places.

If this mantle has been transported the weathering profile will be a function of the parent lithology and the level to which the weathering profile has been dissected. Figure 2.6 is a schematic representation of the minerals that develop within the profile through weathering of a variety lithologies. Clearly the most common surface products are quartz and iron oxides with kaolinite being exposed if the profile has been eroded. All these minerals are detectable through remote sensing at various wavelengths (Table 2.3).

Within the study area a deep weathering mantle is common over most of the low-lying regions. Areas underlain by the Ravenswood Granodiorite are typified by an iron-stained sandy residum with scattered outcrops of the granodiorite. The Cape River Beds and Mount Windsor Volcanics also have an iron-stained sandy residum. However, where exposed, the profile appears deeper than over the Ravenswood Granodiorite and their appears to be far more internal colour variation probably relating to compositional variations in the underlying rocks.

In the south the weathering mantle is far thicker than in the north and there are large areas of Tertiary laterite. The laterites have developed extensively over areas of buff coloured kaolinitic sandtones, siltstones and conglomerates also of Tertiary age.

The Cape River Beds and Mount Windsor Volcanics are also extensively weathered, however, there is less lateritic development which probably reflects a difference in susceptability to lateritization between these rocks and the Tertiary sediments.

In both the north and the south the Upper Carboniferous volcanics show

little surface weathering. Good exposure is found throughout the Camp Oven Complex, Three Sisters and the Western Rhyolites (Figure 2.2). The Upper Carboniferous rhyolites and granites at Plateau in the south also show little surface weathering although exposure is reduced due to an increase in vegetation cover.

2.8 Summary

The area covered by the remotely sensed data consists of a mixture of igneous, metamorphic and sedimentary rocks with a complex weathering history and variable vegetation cover. This combination of geology, weathering and vegetation typifies much of N. E. Queensland. Whilst this study area is reasonably accessible, large parts of N. E. Queensland are not. As a result the geology of large parts of the region has only been mapped at the 1:250,000 scale and its mineral potential has not been fully explored.

In semi-arid areas with a sparse vegetation cover and little surface weathering remote sensing studies have demonstrated the utility of such data for lithological mapping and mineral exploration. The availability of these data over weathered, vegetated terrain offers an opportunity to evaluate their usefulness for similar geologic studies. It is anticipated the presence of deep weathering will degrade the utility of the results from this study compared with other studies of less weathered terrain. This is because the weathering products obscure variations in the primary mineralogy and also produce mineralogies similar to those which result from hydrothermal alteration. Consequently, it may be difficult to detect the latter.

Vegetation creates futher difficulties, since it obscures any signal from the underlying substrate and further reduces the usefulness of the remotely sensed data for lithological mapping and mineral exploration.

These problems necessiate the use of new and improved image processing techniques to extract the relevant geological information. It is also desireable that results be presented in terms of physically meaningful parameters (reflectance and emittance). This enables the remotely sensed data to be compared with laboratory reflectance and emittance data. The results from this study can then be compared with those obtained from similar studies

undertaken elsewhere in which the data have been interpreted in terms of reflectance and emittance. This data reduction can only be undertaken if the data are corrected for various inherrent distortions. The next chapter describes the proceedures for the correction of these distortions. The results are then presented from the analysis and interpetation of the corrected data from the two wavelength regions.

Top 1500+	Rollston Range Formation: laminated siltstone, siliceous siltstone, and shale with intercalations of volcanoclastic sandstone.
1500-300m	Trooper Creek Formation: interbedded andesite and dacite crystal tuff, vitric tuff and agglomerate with intercalations of volcanoclastic sandstone and siltstone.
1600-3500m	Mt. Windsor Volcanics: massive rhyolite and rhyodacite with minor agglomerate, ignimbrite, and vitric tuff.
Base 8000m+	Puddler Creek Formation: interbedded andesitic tuff volcanoclastic greywacke and micaceous siltstone.

Table 2.1   The Four Formations recognised in the Seventy Mile Range Group

Setting	Contact effects and aureole type	Age	Structure
Intrudes Precambrian Basement and Lower Palaeozoic Strata	Sharp or faulted contacts with metamorphism in the hornblede hornfels facies	454-394my	foliated in part

Table 2.2   Characteristics of the Ravenswood-Lolworth Block (after Henderson and Stephenson, 1980).

Wavelength Region (μm)	Minerals Detected
Visible - Near Infrared (0.4 -1.0)	Iron Oxides Hematite, Goethite, Limonite
Short Wave Infrared (1.6 -2.5)	Phyllosilicates and Carbonates
Mid Infrared (8 -14)	Silicates and Carbonates

Table 2.3   Minerals which can be Detected by Remote Sensing (after Gabell and Green, 1982)
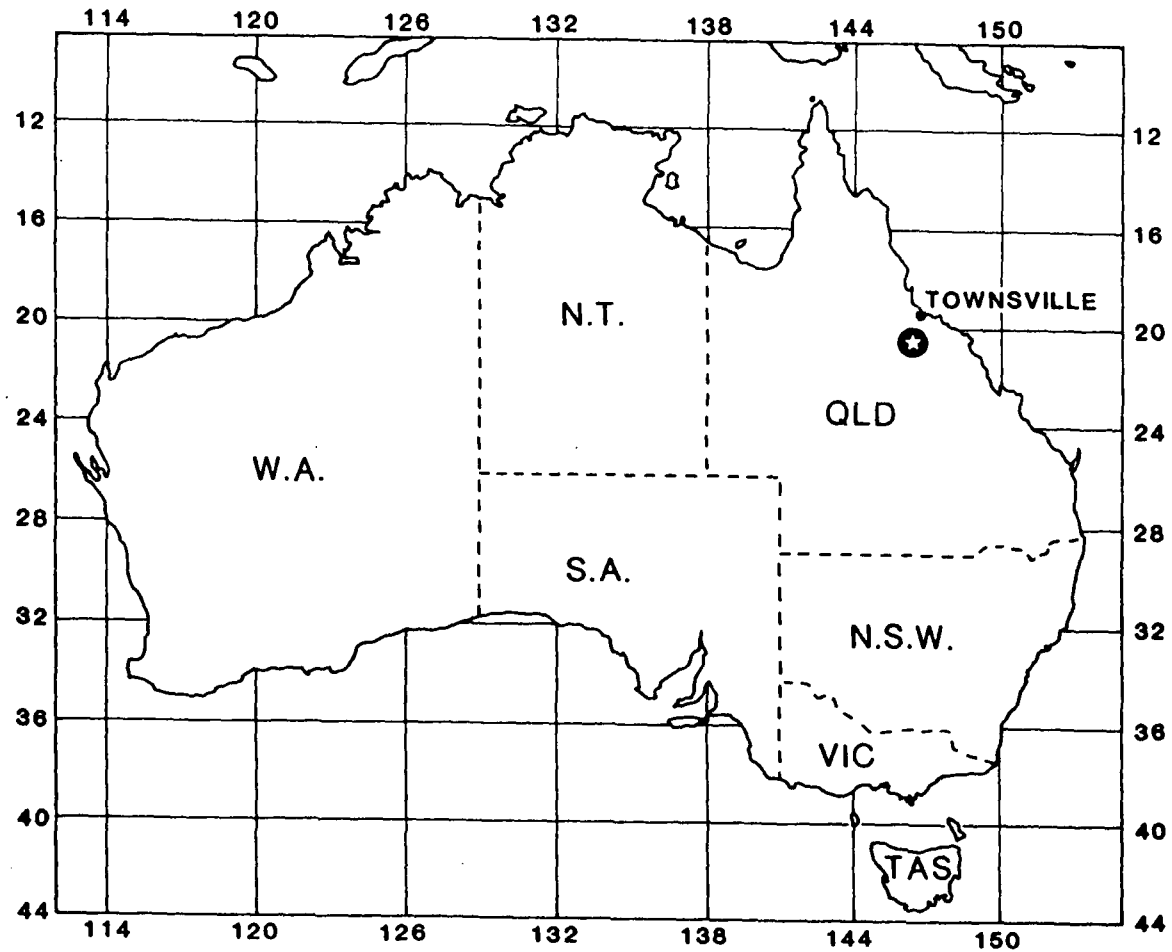
Figure 2.1   Location of the Study Area (test site 713 US/Australia
Joint Scanner Project).

Legend:

- Quaternary
- Tertiary
- Upper Carboniferous to Lower Permian
- Upper Carboniferous
- Upper Carboniferous

Raymond Fm. — Lower Carboniferous

Scartwater Fm. — Upper Devonian ? to
St. Annes Fm. — Lower Carboniferous

RAVENSWOOD GRANODIORITE COMPLEX — Upper Silurian or Middle Ordovician and Lower Devonian

Cape River Beds Mount Windor — Cambrian to Ordovician

—— Fault   ---- Geological contact
═══ Road   ==== Vehicle track
• Abandoned mine

Map labels: Dreghorn, WESTERN RHYOLITES, Camp Over Mountain, Blackfellow Mountain, K 2, SEVENTY MILE RANGE, PLATEAU, The Three Sisters, Mount Cooper, FLIGHTLINE 1, FLIGHTLINE 2, Burdekin R.

Figure 2.2   Regional Geology of the Study Area and Area covered by the Flightlines (after Wyatt *et al.*, 1971).

Figure 2.3 Structural Elements of NE Queensland (from Henderson and Stephenson 1980). Box indicates location of study area

■ Location of study area
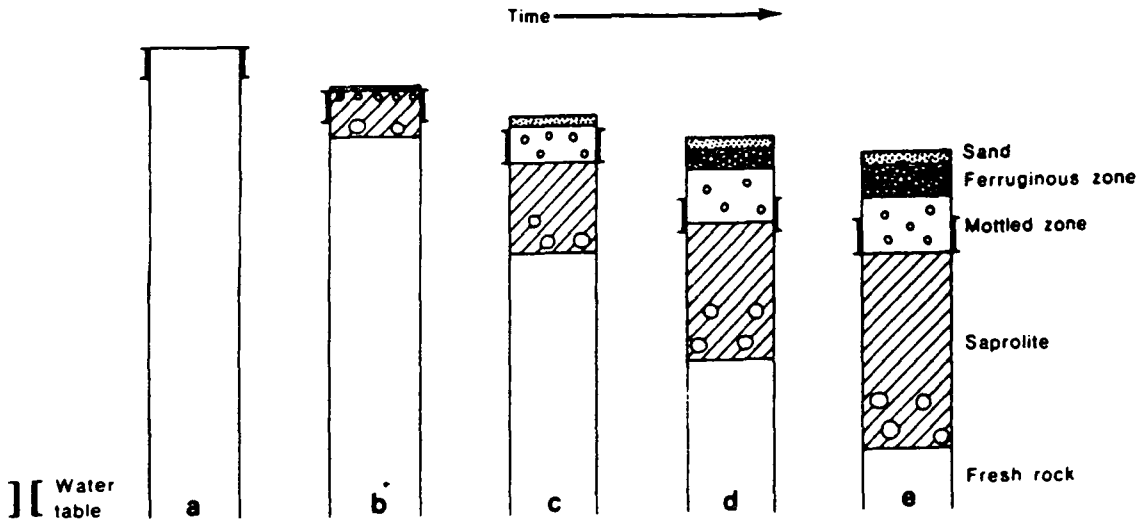
Figure 2.4   Profile Formation through Lateritic Deep Weathering (after Butt, 1983).
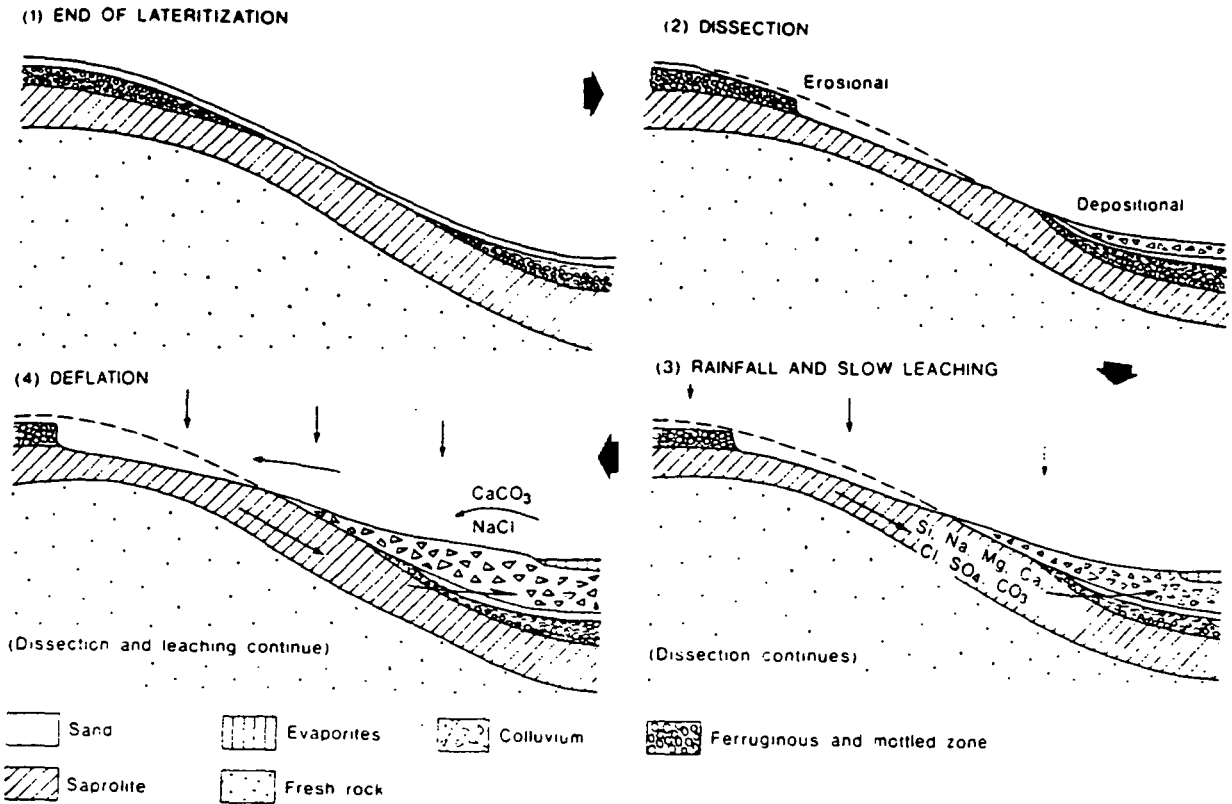
Figure 2.5   Landscape modification occurring with the onset of aridity. Erosion occurs as a result of slope instability (2) with deposition of colluvial and alluvial detritus in lower slopes and valleys giving a further reduction in relief. Leaching and weathering occur at a greatly reduced rate (3) but soluble products tend to accumulate in the lower parts of the landscape; alkalis are also added in the rainfall. Deflation from playas can recycle evaporite deposits within the landscape (4) (from Butt, 1981).

Figure 2.6   Generalised Representation of the Resultant Minerals after Lateritic Weathering of a Variety of Rocks and Minerals (after Gabell and Green, 1983).
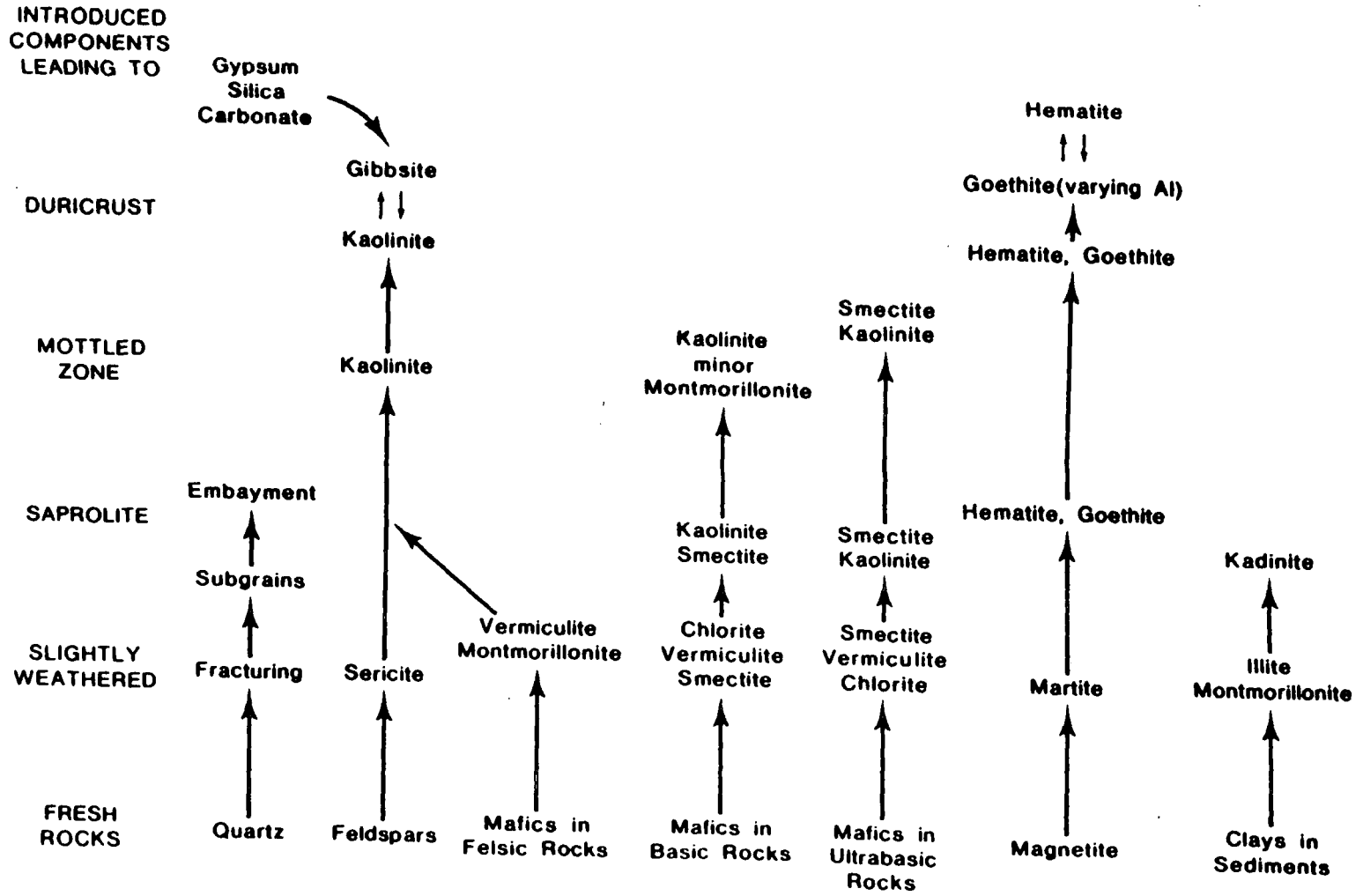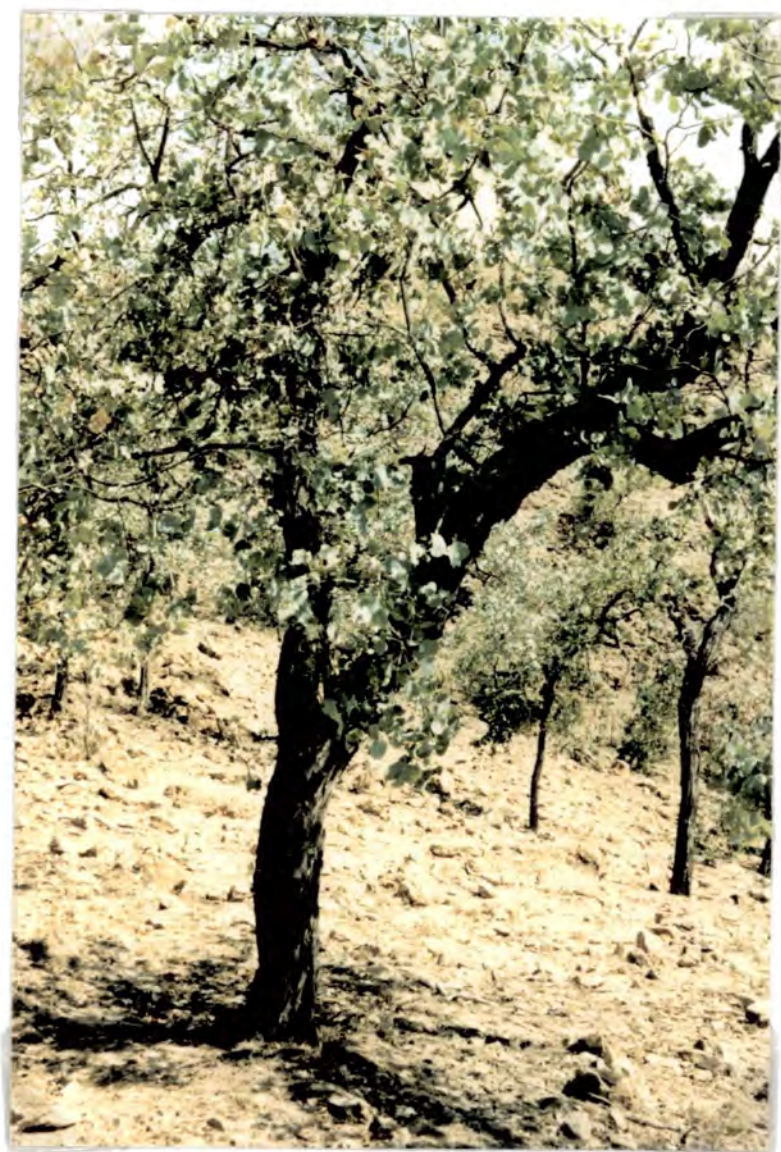
Plate 2.1   Ironbark Tree on Upper Carboniferous Volcanics

Plate 2.2   Illustration of Vegetation Cover in the South of the Study
Area

Plate 2.3   Illustration of Vegetation in the North of the Study Area

Plate 2.4   Mottled Zone in Laterite in South of the Study Area

Plate 2.5   Sandy Residuum after Deep Weathering over the Granodiorite
in the North of the Study Area

Plate 2.6   Stream Section through Weathered Mantle

CHAPTER 3

RADIOMETRIC AND GEOMETRIC CORRECTION OF

AIRBORNE MULTISPECTRAL DATA FROM THE

0.45μm-2.35μm AND 8μm-12μm

WAVELENGTH REGIONS

3.1 Introduction

In order to fully evaluate the remotely sensed data for lithological mapping and mineral exploration it is desireable to be able to relate the data to the physical attributes of the ground surface. This is best achieved by reducing the data to physically meaningful parameters such as reflectance and emittance. This also permits comparison of the results with laboratory studies and other studies conducted elsewhere in which the data were interpreted in terms of reflectance and emittance.

This chapter deals with the removal of various inherrent distortions which restrict the interpretation of the remotely sensed data in terms of physical meaningful parameters. These distortions have been separated into two categories: radiometric and geometric. Radiometric distortions alter the absolute value of the radiation recorded by the sensor, whereas geometric distortions falsely portray the spatial relationships that exist between objects.

The radiometric distortions present have been separated into two categories: sensor-related and scene-related. Sensor-related distortions are corrected by the accurate conversion of the sensors output (in digital counts) to the radiance level at the entrance to the sensor.

Scene-related distortions are more complex and relate to atmospheric effects and georadiometric factors, primarily topography, illumination and view angle (Teillet, 1986).

The complete correction of scene-related effects depends on the availability of certain auxiliary information. This includes information of the types and abundance of atmospheric gases and aerosols to remove atmospheric effects together with digital terrain data to remove georadiometric factors. Unfortunately, such information was not available to this study. Therefore, techniques were developed to correct for these scene-related effects using scene-derived parameters.

Numerous studies have been conducted on the causes and effects of these scene-related distortions. This study concentrates on techniques for removing the most obvious of these distortions relating to changing view angle in the 0.45μm-2.35μm data and atmospheric effects in the 8μm-12μm data. The reader is referred to Barnsley, (1984); Chanine, (1983); Dave and Bernstein, (1982); Duggin, (1985); Holben and Justice (1981); Holben and Fraser, (1984); Irons *et al.*, (1988); Kimes, (1983); Teillet, (1986); Teillet, (1985); Sjoberg and Horn (1983) for examples of the causes and effects of these various scene-related distortions.

Geometric distortions present in the data relate to varying lateral scales orthogonal to the direction of flight (tangential scale distortion) and oversampling in the direction of the flight (Lillesand and Kiefer, 1979). Their presence prevents the registration of the raw data to existing map bases. Correction of these geometric distortions was undertaken after data analysis and prior to data interpretation. Data analysis refers to the use of image processing algorithms to enhance or extract relevant information for example, principal components analysis. These algorithms are often dependant on the overall scene statistics which are altered through geometric correction. Therefore, image processing algorithms should be undertaken before any geometric correction. (see Figure 1.1 for a summary of this approach).

3.2 Correction of Sensor-Related Radiometric Distortions

3.2.1 Calibration

Calibration refers to the determination of the quantitative relation of an instrument response to the input values it is intended to measure (Norwood and Lansing, 1983). Most remote sensing instruments are designed such that the output data numbers are linearly related to the input radiation (Slater, 1980). Therefore, calibration is undertaken by converting the raw DN values obtained by the sensor into spectral radiance using the linear model:

$$Radiance_\lambda = (DN_\lambda - Offset_\lambda) \times Gain_\lambda \qquad 3.1$$

λ = Wavelength

DN = Digital Number

The resultant spectral radiance is the total energy radiated by a unit of area per solid angle of measurement. The Gain and Offset values are instrument dependent and linearly convert the DN values to radiance.

New gain and offset values may be derived for each new scanline as in the case of the NS-001 or TIMS data (Gabell *et al.,* 1985; Palluconi and Meeks, 1985). If new calibration values are derived for each scanline, calibration accounts for any scan to scan differences in system operation during the flight. If the data are not calibrated, the accurate quantitative comparison of different scanlines and data sets (scenes) is not possible. Alternatively, the calibration values may be set in the laboratory for example Airborne Thematic Mapper data (ATM). If the gain and offset values are set, gainsettings are necessary which are adjusted prior to each flight in order to utilize the full dynamic range of the recording system. If the gain and offset values are fixed, calibration is only necessary for comparsion between data sets. Calibration of the NS-001 and TIMS sensors are described in more detail in the subsequent sections.

3.2.2   NS-001 Data Calibration

Calibrated radiance values are obtained by subtracting the offset value from the each of the raw DN values and multipling by the gain value (Gabell *et al.*, 1985). The offset value and gain value are referred to in certain references as the blackbody radiance count tare value and calibration value respectively (Gabell *et al.*, 1985). The gain value is determined in the laboratory using a source with a known radiance. This radiance value is then related to the digital numbers recorded by way of an in-flight reference lamp.

The gain and offset values are contained in the header information which preceeds the digital video counts (raw DN values) on each scanline on the magnetic tape (see Appendix I, Figure 1.1, Format of NS-001 Tape).

Figures 3.1 and 3.2 are plots of every gain and offset value down NS-001 flightline 1. The vertical scale has been reduced to illustrate the effect of corrupted gain and offset values in the header information of each scanline which result in 'spikes' in these values (Figures 3.1 and 3.2). Scanlines which have corrupted header information have been discarded otherwise the resultant calibrated data would be corrupted and may bias later statistics.

Small scale variation also exists in the gain and offset values for a given flightline (Figs 3.1 and 3.2). The result of not calibrating such data is best illustrated by examining the effect of two different gains on nearby scanlines for Band One (Table 3.1). These radiance values are then quantized to an eight bit (0-255:byte) range using the formula:

$$\left(\frac{L - L_{min}}{L_{max} - L_{min}} \right) \times 255 \qquad\qquad 3.2$$

L =radiance

L_{min} =minimum radiance value

L_{max} =maximum radiance value

The resultant byte values are given in Table 3.2. This example clearly demonstrates two adjacent scanlines with similar DN values could represent very different calibrated values. If calibration is not undertaken it is not possible to assume the same DN value on two different scanlines reprsents the same amount of radiance reaching the sensor. This could result in an erroneous interpetation of the data if they were analysed in either a qualitative or quan-

titive manner.

3.2.3 TIMS Data Calibration

The following description of the proceedure for calibration of TIMS data is based on Palluconi and Meeks (1985). Calibration of TIMS data to spectral radiance requires the derivation of calibration values for each scanline. These calibration values (gain and offsets) are determined using the blackbody temperature and blackbody reference source values. Prior to recording the radiation from the surface for each scanline, the TIMS looks at two inbuilt blackbodies set at the minimum and maximum temperatures thought to be encountered on the ground surface. These are referred to as the blackbody 1 and 2 reference source values and are recorded in the header information for the appropriate scanline together with the actual temperature of the blackbodies. These values are used to derive the calibration values to convert the digital numbers to apparent temperature. The physical location of these values on the TIMS data tapes are given in Figure 1.2. Appendix I.

Examination of the mean and standard deviation of the blackbody temperature and reference source values for the data sets from each flightline reveals that the temperatures have remained constant while the reference source values have varied considerably (Tables 3.3 and 3.4). This point is further illustrated by examining how the blackbody 1 and blackbody 2 reference source values vary down a given flightline (Figures 3.3 and 3.4). Clearly if these variations are not removed through calibration it is not possible to assume similar DN values represent similar radiance values.

The proceedure for the calibration of TIMS data is outlined below:

Definitions:

T_1 = Low reference source temperature (K^o)

T_2 = High reference source temperature (K^o)

D_1 = Low reference source data number

D_2 = High reference source data number

R_1 = Low reference source spectral radiance

$(Wm^{-2}sr^{-1}\mu m^{-1})$

R_2 = High reference source spectral radiance

$(Wm^{-2}sr^{-1}\mu m^{-1})$

Tx, Dx, Rx = scene values of brightness temperature, data number and spectral radiance respectively for any sample x on the same scanline as the reference source values.

$S(\lambda)_i$ = relative response of channel i (Figure 1.3, Appendix I).

$P(\lambda T)$ = Planck's Radiation Formula

TIMS is designed such that the output data numbers are linearly related to the input photon radiance, e.g.,

$$R_x = a + b(D_x) \qquad\qquad 3.3$$

The two internal reference sources can be used to determine the constants a and b relating spectral radiance to data number D_x for any given scanline by :-

$$R_1 = \frac{\int_\lambda P(\lambda , T_1) \times S(\lambda)_i \, d\lambda}{\int_\lambda S(\lambda)_i \, d\lambda} \qquad\qquad 3.4$$

$$R_2 = \frac{\int_\lambda P(\lambda , T_2) \times S(\lambda)_i \, d\lambda}{\int_\lambda S(\lambda)_i \, d\lambda} \qquad\qquad 3.5$$

where:

$$P(\lambda T) = A\lambda^{-5}(\exp[C^2/\lambda T] - 1)^{-1} \qquad\qquad 3.6$$

A = First Radiation Constant $= 2c^2 h$

c = speed of light

h = Planck's constant

C_2 = Second Radiation Constant $\frac{hc}{k}$

k = Stefan-Boltzman constant

for each of the six spectral channels i. Given R_1 and R_2 equation 3.3 can be solved for a and b using :-

$$a = \frac{R_2 D_1 - R_1 D_2}{D_1 - D_2} \qquad\qquad 3.7$$

$$b = \frac{R_1 - R_2}{D_1 - D_2} \qquad\qquad 3.8$$

Equation 3.3 can then be applied channel by channel and scan by scan to solve R_x from D_x. R_x is then in physical units ($Wm^{-2}sr^{-1}\mu m^{-1}$) and to first order is independent of the TIMS system state at the time of measurement.

3.3 Radiometric Sensitivity

Once the data have been calibrated the numerical difference between channels is far greater. This is made clear by comparing the mean and standard deviation of each channel before and after calibration (Table 3.5). Many image analysis sytems require the calibrated data quantized to eight bits (0-255 scale) for processing. If the user intends maintaining the same physical relationship between channels in the byte data as in the calibrated floating-point data rescaling must be undertaken using the overall maximum, minimum and range of all channels (see equation 3.2). This often results in an image which appears density sliced. This effect can be cancelled by rescaling each channel individually. This is similar to displaying the data in its raw byte form thereby negating the point of calibration.

It should be stressed that calibration should always be undertaken if unique calibration values have been used for each scanline eg. NS-001 and TIMS. In this situation the variation between byte values on adjacent scanlines may be attributable to changing calibration values. This effect is removed by calibrating the data then reducing each channel to a byte scale using equation 3.2.

If calibration is undertaken to compare data sets collected at different times from the same or different areas, the calibrated floating-point values should be used throughout the data processing. For example, if each data set is classified or channel ratios are calculated, the calibrated floating-point data should be used for the classification or the ratio calculation. The classified or ratioed data from each data set can then be compared numerically. Certain image analysis techniques such as the extraction of temperature and emittance information from thermal data (Kahle *et al.*, 1980), also require calibrated data.

In this study the NS-001 and TIMS data sets were calibrated with separate coefficients for each scanline. The calibrated floating-point data were used for subsequent data analysis and only quantized to eight bits for display. The floating-point value of any given data point was displayed graphically from the processed data prior to eight-bit quantization. It should be noted if the data are only to be used for qualitative interpretation no radiometric correction is necessary.

Scaling of the processed data from each channel was undertaken using the mean ± 3 standard deviations to obtain the minimum and range used for rescaling. Initially, the data were rescaled using its mean ± 1, 2, 3 and 4 standard deviations. The mean ± 3 standard deviations gave a good visual data range and excluded any extreme calibrated values. All images presented in this thesis were produced from image data that had been rescaled using the mean ± 3 standard deviations.

3.4 The Effect of Calibration on the Sheffield Algorithm for the Selection of Best Channels

In sections 3.2 and 3.3 the methodology involved in calibrating NS-001 and TIMS data was described. This section presents an example of how not calibrating data may lead to an erroneous interpretation with certain image processing techniques.

Drury and Hunt (1989) compared the results from the visual selection of the best channels for geological analysis with those selected using a statistical technique described by Sheffield (1985). Their results indicated that the channels chosen by visual analysis were different to those selected by the Sheffield algorithm. Drury and Hunt (1989) concluded this was due to the algorithm not selecting channels which best enhanced the geological information. Instead, the algorithm selected the channels which showed maximum scene variation. Whilst this statement is correct it is important to realise the channels chosen by the algorithm would have been different if the data had been calibrated. They may even haven been the same as those visually chosen by Drury and Hunt (1989). This is due to the algorithm using the variance-covariance between channels to select the best channels for display which is changed by calibration. This means their results are sensor-dependant since if a new set of raw data were acquired by another instrument with similar channel widths from the same area, but different calibration values, a different set of channels would be selected. This would not have been the case if the data used had been calibrated. Clearly, if they had used calibrated data their results would have been more widely applicable and their conclusions

may well have been different. The remainder of this section illustrates this point by comparing the results obtained using this algorithm on data from this test site in a raw and calibrated form.

Table 3.6 lists the five, best three channel combinations for both flight-lines using NS-001 data. The ranking of these combinations is observed to change after calibration. This is because calibration changes the variance of the data. Therefore, if data were collected over a site at approximately the same time with different gain and offset settings, different best channel combinations would be selected from the raw data. However, the best channel combinations would be the same if the data were calibrated assuming ground and atmospheric conditions remained unchanged. If this technique is applied to airborne data, calibration is necessary if workers need to compare the best channels selected from temporally or spatially different images.

3.5 Correction of Scene-Related Radiometric Distortions

Scene-related effects can be separated into two groups, atmospheric effects and georadiometric factors, primarily topography, illumination and view angle (Teillet, 1986). Complete removal of scene-related effects is not possible without certain auxillary information such as atmospheric composition and terrain elevation, some of which needs to be obtained at the time and place of sensing (Lillesand and Kiefer, 1979). Such information was not available for this study so techniques were devised to correct the most severe scene-related distortions using scene-based parameters. These enabled the removal of view angle effects from the airborne multispectral data from the 0.45μm-2.35μm wavelength region. Two further techniques were also examined for the removal of atmospheric effects from the airborne multispectral data from the 8μm-12μm wavelength region. The cause and correction technique for the view angle effects is now described after which the cause and correction technique for the atmospheric effects is described.

3.6   Correction of View Angle Effects in VNIR and SWIR Data

View angle effects are manifest in airborne multispectral data as systematic differences in brightness approximately orthogonal to the direction of flight and here termed X-track shading (Plate 3.1).

The causes of X-track shading in areas with varying proportions of soil and vegetation are discussed in Kimes (1983) and Irons *et al.*, (1988) and references contained therein. The effect is more pronounced in areas with a sparse vegetation canopy for several reasons outlined in Kimes (1983). This study area had such a canopy. The causes of X-track shading in areas with a sparse vegetation canopy are now summarised from Kimes (1983).

Areas with a sparse vegetation canopy have a high soil exposure. Particulate soils have strong vertical components and are largely opaque. The front surface of these components (towards the sun) reflects the incoming radiation back toward the sun both specularly and diffusely whilst the back surface is shaded. These components also shade other components with their shadows. This is illustrated in Figure 3.5. In the antisolar direction (backscatter towards the sun) only those surfaces which are in direct sunlight are viewed by the sensor and thus the reflectance is at a maximum in that direction. The peak in reflectance occurs on this side of the image and reflectance decreases in any direction away from it since the contribution of the shadows increases. As the sensor direction moves away from the antisolar direction two mechanisms cause the reflectance to decrease. First, the relative proportions of shadowed surfaces in the sensors field of view increase. Secondly, the proportion of particle facets with normals that deviate from the solar direction increase causing decreased solar irradiance on these facets.

If the flight direction was N-S and the sun directly overhead, maximum reflectance should occur along the nadir line with reflection decreasing equally to the left and right of this line. If the sun is not directly overhead and/or the flight direction is not N-S this maximum will shift to one or the other side of nadir. This is illustrated in the column means from the flightline where the maximum reflectance occurs around the 400th column (nadir column=350) due to the NE-SW direction of the flightline. The flight time was approximately 1pm and the sun in the west. Examination of Figure 3.6 reveals the X-track shading is wavelength dependant and decreases in magnitude from the

visible into the infrared. Kimes (1983), attribute this wavelength dependant decrease from the visible into the infrared to two causes. First, the reflectance of soil is much lower than vegetation in the infrared, the reverse of which is true in the visible. Therefore, the strong backscatter peak of soil should have less effect on directional reflectance in the infrared band. Second, the strong multiple scattering (diffuse reflectance) in the infrared tends to decrease variations in reflectance. Occassionally, X-track shading may not be apparent in a visual inspection of the data but is usually revealed by examining the column means from left to right in the image (Plate 3.2, Figure 3.7). There is also considerable geometric distortion between Plate 3.1 and 3.2, correction of geometric distortions are dealt with at the end of this chapter.

X-track shading can be removed by normalising the data to a single view angle by means of an empirical profile correction of either an additative or multiplicative nature (Irons and Labovitz, 1982; Royer *et al.*, 1985).

Four methods are now presented for the removal of X-track shading in visible/near infrared data. These are channel ratios, nadir normalisation, scene normalisation and polynomial fitting. The latter three methods are empirical profile corrections and may be applied in either a multiplicative or additive manner as will be discussed later.

3.6.1   Method 1 - Band Ratioing

Spectral ratioing is the simplest method for the removal of view angle effects. This involves the division of two channels at different wavelength regions.

The method assumes the view angle effect is the same in both channels. Therefore:

$$\frac{Band\ A \times e_1}{Band\ B \times e_2} = \frac{Band\ A}{Band\ B} \qquad 3.9$$

where e_1 and e_2 are equal and represent the view angle effect (Rowan *et al.*, 1974).

The assumption that e_1 and e_2 are equal is reasonable for narrow adjacent channels however for larger channelwidths which are not adjacent significant effects will remain. This is illustrated by looking at the residual curve from the division of the column mean curve from one channel with the column mean curve from another channel at a different wavelength (Figure 3.8).

Several further difficulties can arise when a correction for scan angle effects is made using this method. Firstly, the original data needs to be kept available to determine whether a change in the ratio results from a change in the denominator channel, the numerator channel or both. Secondly, once ratioed, the data cannot be used to retrieve spectral reflection information since the data are no longer in reflectance terms which may be required with other image processing techniques.

3.6.2   Method 2 : Nadir Normalisation

The nadir normalisation method makes two basic assumptions. These are:

1. The column means would be equal if X-track shading is absent.

2. The effect of X-track shading is minimal at nadir when the scan angle is zero.

Therefore, if the mean of each column is normalised to the nadir column mean the effect of X-track shading should be removed. This is undertaken in a two stage process. Firstly a set of shading coefficients are obtained, one per column, for the image. This involves dividing each column mean into the nadir column mean thus:

$$S_{i\lambda} = \frac{\sum\limits_{j=1}^{nrows} X_{nadirj\lambda}}{\sum\limits_{j=1}^{nrows} \dfrac{X_{ij\lambda}}{CSAMPS}} \qquad 3.10$$

S = shading coefficient

λ = wavelength

i = column

$nrows$ = number of rows (lines) in the image

$nadir$ = centre column

X = pixel value

j = row

Examination of the shading coefficients for the NS-001 flightline 1 reveals several spikes (Figure 3.9). Spikes in the shading coefficents result when a column is dominated by a certain cover type *eg.* a road. Since these spikes reflect true differences in cover type they should not be removed from the

data. Therefore the shading coeffcents are smoothed by a weighted average so when applied to the data they will not remove the spike but will remove the view angle effect.

The shading coefficients are applied to the data either multiplicatively or additively. The significance of application of the shading coefficients to the data is discussed after the methods for derivation of the shading coefficients have been described.

3.6.3   Method 3 :Scene Normalisation

This method also makes two basic assumptions. These are:

1. The column means should be equal

2. The image contains an equal number of overly bright and overly dark pixels, thus the scene mean remains unbiased.

Therefore, each column mean is normalised to the scene mean. This involves deriving a series of shading coefficients using the scene mean thus:

$$S_{i\lambda} = \frac{\frac{1}{nrows \times ncols} \sum\limits_{j=1}^{nrows} \sum\limits_{i=1}^{ncols} X_{ij}\lambda}{\frac{1}{nrows} \sum\limits_{j=1}^{nrows} X_{ij}\lambda} \qquad 3.11$$

$ncols$ = number of columns in the image

3.6.4   Method 4: Polynomial Fitting

The final method for calculating the shading coefficients involves generating a curve from the observed variation in the column mean values P_i. The observed variations are then described by a polynomial fit of the form:

$$P_i = a + bi + ci^2 \qquad 3.12$$

P_i = observed variation in the column mean values

i = view angle

This method has been described by Irons and Labovitz (1982), and Royer et al., (1985).

44

3.6.5 Application of the Shading Coefficients to the Data

The shading coefficients calculated by methods 2 and 3 are applied to the data in a multiplicative manner:

$$C'_{ij} = S_i \times X_{ij} \qquad\qquad 3.13$$

C'_{ij} = shade corrected value using multiplicative approach

i = column

j = row

S_i = shading coefficient

X_{ij} = pixel value

Plate 3.3 shows the data from NS-001 channel 1 after the removal of X-track shading using the nadir normalisation method applied multiplicatively. However, The shading coefficients could be determined as additive terms by taking the difference between the nadir column mean or scene mean and the mean for a given column. The difference for a particular column would then be added to all the values in that column.

The shading coefficients calculated using the polynomial method can also be determined multiplicatively or additively. Using the additive approach the corrected value C_{ij} is calculated from the equation:

$$C_{ij} = X_{ij} + (Pn - P_i) \qquad\qquad 3.14$$

X_{ij} = pixel value

P_i =mean column value

Pn =minimum value of P_i, this usually occurs at nadir

Alternatively, using the multiplicative approach the corrected value is calculated from the equation:

$$C'_{ij} = \frac{X_{ij}}{P_i} \times Pn \qquad\qquad 3.15$$

Trivially by inspection the values for C_{ij} and C'_{ij} will not be the same, however, the means of the columns using either approach should be equal:

$$\bar{C}_i = \bar{C}'_i \qquad\qquad 3.16$$

$\bar{C}_i$ = mean of a column using the additive approach

$\bar{C}'_i$ = mean of a column using the multiplicative approach

Irons and Labovitz (1982), argue for an additive correction because the addition of a factor within an image column does not change the within column variance whilst a multiplicative adjustment would. However, Royer *et al.*, (1985), prefer a multiplicative adjustment. Clearly the technique used depends on whether a change in the column variance will bias the results from the application of other image processing techniques at a later date such as the Sheffield method for the selection of best bands. In this study the data were corrected by multiplicative nadir normalisation since a change in column variance would not bias the results from the processing of the data with any of the subsequent algorithms.

3.7 Correction of Atmospheric Effects in MIR Data

The causes and effects of the atmosphere on MIR data are reviewed in Deschamps *et al.*, (1983) and Chahine (1983). In general, these effects are considered with regard to additive and transmittance terms. The additive term is often referred to as the path radiance. It accounts for the additional energy received by the sensor, from a given pixel, from atmospheric scattering and radiation scattered from the background surface of a pixel (Deschamps *et al.*, 1983). These contributions are illustrated schematically in Figure 3.10. The transmittance term accounts for the energy attenuated in a direct path from the surface to the sensor (Deschcamps *et al.*, 1983; Figure 3.10).

Kahle *et al.*, (1980) utilised an atmospheric model to correct for the effects of the transmittance and additive atmospheric effects in TIMS data. They wrote the total spectral radiance at the sensor for wavelength λ as:

$$L_l = [\epsilon_\lambda L_{bb\lambda}(T) + (1 - \epsilon L_{sky\lambda})]\tau_{A\lambda} + L_{V\lambda} \qquad 3.17$$

where:

ϵ = surface emittance

$L_{bb\lambda}(T)$ = spectral radiance of a blackbody at surface temperature T

$L_{sky\lambda}$ = spectral radiance incident upon the surface, from the atmosphere

$\tau_{A\lambda}$ = spectral atmospheric transmissivity

$L_{V\lambda}$ = spectral radiance from atmospheric emission and scattering that reaches the sensor

In this model $\tau_{A\lambda}$ represents the transmittance term and $L_{V\lambda}$ represents the additive term. The average values of $L_{sky\lambda}$, $\tau_{A\lambda}$ and $L_{V\lambda}$ are then obtained using the atmospheric model LOWTRAN 4 (Selby *et al.*, 1978). Radiosonde data for the day of the overflight were used to define atmospheric conditions used with the model. The model produces transmissivity $\tau_{A\lambda}$, atmospheric directional upward radiance $L_{V\lambda}$ and directional downward radiance. The latter is integrated over the sky hemisphere to obtain the $L_{V\lambda}$ term and values given in Table 3.7 from Kahle *et al.*, (1980). These values provide an indication of the magnitude of atmospheric effects expected with these data.

Once the atmospheric parameters are determined equation 3.17 can be used to correct the data. It should be noted that Kahle *et al.*, (1980) used the model in an average sense only correcting for an atmospheric column of length equal to the difference between the height on the ground and the height of the aircraft above the ground. This corresponds to the length of the atmospheric column at nadir (when the scanner is pointing directly down to the ground). As the scan angle increases away from nadir the length of the atmospheric column increases and atmospheric effects will remain proportional to the difference in length between the atmospheric column at nadir and at each new scan angle. The significance of not correcting for these differences has yet to be determined.

The two methods described subsequently attempt to remove the atmospheric effect and account for any scan angle differences that may occur in the data.

3.7.1 Atmospheric Correction using the Callison Method

Callison *et al.*, (1985), developed a technique for removing atmospheric effects in AVHRR and ATM thermal data in order to map variations in sea surface temperatures. They defined the irradiance at the sensor E^* in terms of radiant emittance ϵMs^*, the optical depth $\alpha_\lambda z$ and view angle θ as :

$$E^* = exp(\frac{-\alpha_\lambda z}{cos\theta})\epsilon Ms^* \qquad\qquad 3.18$$

Callison *et al.*, (1985), then looks for an area where $\alpha_\lambda z$ and ϵMs^* are constant over a few scanlines. Equation 3.18. can then be written after taking the natural logs as:

$$lnE^* = \frac{-\alpha_\lambda z}{\cos\theta} + ln(\epsilon Ms^*) \qquad\qquad 3.19$$

This equation implies that a plot of the lnE^* versus sec θ will give a straight line of slope $-\alpha_\lambda z$ and an intercept $ln\epsilon M^*$, the intercept being the natural log of the radiant emittance after the removal of atmospheric effects.

The radiant emittance could then be related to absolute variations in the sea surface temperature by way of Planck's equation. This requires that the emmitance ϵ remains constant. This is not the case with land data so it was assumed that ϵ should be constant for each column mean. This implies a plot of lnE^* versus sec θ, where LnE^* is equal to the log of the column means, should give a straight line of slope $-\alpha_\lambda z$ and intercept $ln\epsilon M^*$ (Figure 3.11).

Clearly the slopes of the natural log of the column means versus $sec\theta$ are different either side of nadir (Figure 3.11). Therefore, the slopes and intercept values have been calculated for the left hand side (lhs) and right hand side (rhs) of nadir (Table 3.8).

The intercept values on the lhs of nadir are lower than those on the rhs. This implies the ground was hotter on the rhs than on the lhs. This can be explained by examining the sun sensor geometry (Figure 3.5). The slopes facing the sun will be hotter than those facing away from the sun. These slopes will be imaged when the sensor scans the rhs of the image.

This difference in the apparent temperature either side of nadir will be minimised if the sun were overhead and the flight direction N-S. In such a situation both sides of nadir should be heated approximately equally.

48

The difference between the radiance value for the nadir column and the intercept value is equal to the effect of an atmospheric column equal in length to the height difference between the ground and the aircraft (Table 3.8)

Examination of the percentage difference between the intercept (ground radiance values) either side of nadir and the radiance values for the nadir column reveals the greatest atmospheric effect on the lhs of nadir occurs in channels 1, 4 and 6 (Table 3.9). These correspond to the positions of the H_2O, O_3 and CO_2 absorptions respectively (Figure 3.12) On the rhs of nadir the atmospheric attenuation is greatest in channel 1 then decreases through channels 2 to 6 (Table 3.9). This situation would seem unlikely since it suggests that the greatest atmospheric effect does not occur at the positions of known atmospheric absorptions. One possible cause for this deviation could be the initial model was inaccurate (see equation 3.17). Examination of this model reveals the model does not attempt to separate the multiplicative ($\tau_{A\lambda}$) and additive ($L_{V\lambda}$) terms of the atmosphere. The multiplicative effect reduces the radiance reaching the sensor by scattering and absorption whilst the additive effect increases the radiance reaching the sensor by emission of radiation from the atmospheric gases and particles.

In order to determine the magnitude of these multiplicative and additive terms and how they varied either side of nadir an alternative correction method was developed and evaluated by A. A. Green of CSIRO, Sydney Australia and the author, whilst the author was visiting CSIRO as part of his studies. The method was developed by A. A. Green using the assumption for land data suggested by the author with the Callison Method. This method was then implemented, tested and evaluated by the author.

3.7.2 Atmopsheric Correction using the Green and Hook Method

Equation 3.18 can be more accurately written for a given pixel at a known wavelength as:

$$A_{ij} = K1\, e^{K2sec\theta_i} G_{ij} + K3sec\theta_i \qquad 3.20$$

A_{ij} = irradiance recieved by the sensor

i = column

j = row

$K1$ = instrument gain

$K2$ = optical depth

θ = scan angle

$e^{K2sec\theta_i}$ = transmissivity

G_{ij} = radiant emittance from the ground

$K3$ = spectral radiance from atmospheric emission and scattering which reaches the sensor

The G_{ij} term in equation 3.20 includes the effect of sky radiance (see equation 3.17). However, the effect of sky radiance is very small. Equation 3.20 can be rewritten after taking the standard deviation for a given column as:

$$\sigma(A_i) = K1 e^{K2sec\theta_i}\, \sigma(G_i) \qquad 3.21$$

If we assume the standard deviation for all columns in the image are equal:

$$\sigma(G_i) = \sigma(G) \qquad 3.22$$

then after taking natural logs equation 3.20 becomes:

$$ln[\sigma(A_i)] = lnK1 + K2sec\theta_i ln[\sigma(G_i)] \qquad 3.23$$

If the data have been calibrated K1 can be set to 1, and ignored. This implies a plot of $ln[\sigma(A_i)]$ against $sec\theta$ will give a slope of $K2$ and an intercept of $ln\sigma(G_i)$.

The mean of each column is equal to:

$$A_{i\bullet} = e^{K2sec\theta_i} G_{i\bullet} + K3sec\theta_i \qquad 3.24$$

$A_{i\bullet}$ =column mean

• = mean of j's

since we know $K2$ we can calculate $e^{K2sec\theta_i}$:

$$Y_{i\bullet} = \frac{A_{i\bullet}}{e^{K2sec\theta_i}} = G_{i\bullet} + \frac{K3sec\theta_i}{e^{K2sec\theta_i}}$$ 3.25

This implies a plot of $Y_{i\bullet}$ against $e^{\frac{sec\theta}{K2sec\theta_i}}$ will give a slope of K3 and intercept $G_{i\bullet}$. If we assume:

$$G_{i\bullet} = G$$

Then by normalising each column to $G_{i\bullet}$ we have removed both the multiplicative and additive effects of the atmosphere. This model is dependant on the multiplicative term behaving in an exponential manner and the additive term behaving in a linear manner with increasing scan angle. The LOWTRAN model was employed to determine whether the additive term increased in a linear manner with scan angle. Results confirmed this was indeed the case. However, further work is required using data for which atmospheric measurements were made at the time and place of data acquisition and over a variety of different atmospheres to determine how widely applicable the technique is.

Examination of a plot of $ln[\sigma(A_i)]$ versus $sec\theta$ reveals that $K2$ (the slope) increases, albeit small on the lhs side of nadir, with increasing values of sec theta (Figure 3.13). In contrast, examination of a similar plot for the rhs of nadir reveals $K2$ decreases with increasing values of $sec\theta$ (Figure 3.14).

This results in positive values of $K2$ for the lhs of nadir and negative values for the rhs of nadir (Table 3.10). Having obtained $K2$ we can calculate $e^{K2sec\theta}$ for the lhs and rhs of nadir. The column means divided by $e^{K2sec\theta}$ are then plotted against $\frac{sec\theta}{e^{K2sec\theta}}$ to obtain the $K3$ (the slope) and $G_{i\bullet}$ (the intercept)(Figures 3.15 to 3.18). The values of $K3$ and $G_{i\bullet}$ for the lhs and rhs of nadir are given in Table 3.10

Having obtained $K2$, $K3$ and $G_{i\bullet}$ it is possible to calculate what the radiance would be for any given value of $sec\theta$ The percentage difference between the ground radiance and the radiance received by the sensor at nadir and the maximum scan angle are given in Table 3.11. Also given are the percentage effects of the K2 and K3 terms on these differences.

There is a marked difference in the atmospheric effect between the lhs and rhs of nadir. On the lhs of nadir the greatest atmsopheric effect occurs

51

in channel 4. This corresponds to the position of the ozone absorption in the atmosphere. Strong atmospheric effects also occur in channels 1, 5 and 6. The effect in channel 1 corresponds to the position of H_2O absorption in the atmosphere and the effects in channels 5 and 6 to CO_2 in the atmosphere. On the rhs of nadir the greatest reduction in radiance also occurs in channels 1, 4, 5 and 6 although maximum attenuation occurs in channel 6.

Both the Callison Method and this method indicate the radiance from the ground is far greater on the rhs-than the lhs-of nadir. This is attributed to the sun sensor geometry resulting in slopes facing the sun being hotter than those facing away from the sun. The hot slopes are imaged when the sensor scans the rhs of nadir and the cold slopes are imaged when the sensor images the lhs of nadir. The Green and Hook method agrees with known atmospheric models which suggest the greatest atmospheric effects should occur in channels 1, 4 and 6. These models relate these effects to the atmospheric gases H_2O, O_3 and CO_2 respectively. This is not the case with the Callison method on the rhs of nadir.

Table 3.11 gives a breakdown of the effect of multiplicative $K2$ and additive $K3$ terms as percentages of the reduction in the energy received by the sensor. On the lhs of nadir $K2$ increases the energy received by the sensor whilst $K3$ decreases it. Since $K3$ has a greater effect than $K2$ there is an reduction in the energy received by the sensor. On the rhs of nadir $K2$ decreases the energy received by the sensor and $K3$ increases it. Since $K3$ has a greater effect than $K2$ again the energy received by the sensor is reduced.

Table 3.11 also shows a similar breakdown of percentage effects of the $K2$ and $K3$ at the maximum scan angle. On the lhs of nadir $K3$ has increased more than $K2$ resulting in a further reduction in energy received by the sensor. On the rhs of nadir $K2$ has increased more than $K3$ again causing a reduction in the energy received by the sensor.

The calculated energy received by the sensor using $K2$, $K3$ and G_i values obtained by this method agrees well with the actual values recorded by the sensor for the mean columns values at each scan angle. This suggests the method should provide a means of correcting thermal data without having to rely on theoretical models which require atmsopheric information which is often not obtained at the time or location of the flight.

Clearly, further work is needed to fully evaluate both these methods for atmospherically correcting MIR data. At present, both methods indicate the slopes images on the rhs side of nadir with this sun-sensor-geometry are hotter than those imaged on the lhs. However, the methods do not agree in terms of the magnitude of these effects. Future work should be carried out on a data set obtained when the sun was overhead and the flight direction N-S. Furthermore, radiosonde data should be obtained within the vicinity of the flight at the time of the flight to enable the comparison with a theoretical models such as LOWTRAN 4.

3.8 Correction of Geometric Distortions

Comparsion of the black and white 1:25,000 regional air photo over Camp Oven with the raw NS-001 image of Band 1 over the same area reveals the image is distorted both laterally and longitudinally (Plates 3.3 and 3.4), assuming the air photo has only limited distortion. Comparison of the same air photo with the raw TIMS image for Band 1 over the same area reveals the TIMS data are laterally but not longitudinally distorted (Plate 3.2).

The lateral and longitudinal distortions are referred to as tangential scale- and aspect-distortions respectively. These inhibit the accurate location of sample from the image to an area on the ground. The proceedures by which each distortion was removed are now described.

3.8.1 Correction of Tangential Scale Distortion

Tangential scale distortion results from a varying lateral scale at right angles to the direction of flight. It is manifest in the imagery as a 'flattening'of objects toward the edges of the image (Figure 3.19; Lillesand and Kiefer 1979). Such distortions restrict useful interpretation near the edges of unrectified imagery since accurate ground location is often difficult.

Figure 3.20 shows the elements involved in computing true ground positions from measurements made on distorted imagery. On the unrectified imagery the y coordinates relate directly to angular dimensions, not the lineal dimensions. This causes the imaged plane to appear as a curved surface beneath the aircraft.

In order to determine the ground position Y_p corresponding to the image

point p, we first compute θ_p from the relationship:

$$\frac{Y_p}{Y_{max}} = \frac{\theta_p}{\theta_{max}}$$ 3.26

rearranging:

$$\theta_p = \frac{Y_p \times \theta_{max}}{Y_{max}}$$

where:

Y_p = the distance measured on the imagery from the nadir line to point p

Y_{max} = the distance from the nadir line to the edge of the image.

$\theta_{max} = \frac{1}{2}$ the total field of view of the scanner.

θ_p = scan angle corresponding to point Y_p.

Once θ_p has been computed, it may be trigonometrically related to the ground distance Y_p by:

$$Y_p = H tan\theta_p$$ 3.27

where:

H = the flying height of the aircraft.

The magnitude of the lateral distortion can be observed by plotting the distance on the ground for a given column against the column number (Figure 3.21). Clearly, the magnitude of the effect increases in a non linear fashion with increasing scan angle. Therefore, the larger the scanner angle used to obtain the data the greater the resultant distortion at the edges of that data. Thus, there is more distortion at the edges of the NS-001 data which has a full scan angle of 90° compared with data from the TIMS which has a full scan angle of 76.56^o. data. In satellite data the scan angle is only a few degrees and therefore the effect of tangential scale distortion is negligable.

Having calculated the ground position from nadir to a given scan angle, the data can be geometrically corrected by the insertion of columns of dummy pixels. These transform the angular relationship to a linear relationship. Since the amount of distortion increases towards the edge of the image, the number of columns of dummy pixels required to correct the data increases. Therefore, near the edges of the image one original column may require four columns of dummy pixels (two either side) in order to maintain a constant lateral scale. The number of columns to be inserted was determined by comparing

the distance between two adjacent pixels at nadir with the distance between two adjacent pixels from nadir to the left and right side of the image. If the distance between two adjacent pixels was twice the distance between the nadir pixel pair then one column was inserted, if three times two columns were inserted and so on. Since so many columns were being inserted, these could not all have the same values as the actual column otherwise the image would appear striped. Variation in these columns of dummy pixels was obtained using a weighted average from the eight surrounding pixels (including those from any dummy columns).

An advantage of this method of correction for the effects of tangential scale distortion over methods involving resampling is the values in the original columns remain the same. Therefore, one can confidently relate the values in these columns to the ground beneath. An alternative to this technique would be to resample the image such that all pixels covered the same area as pixels at the edge of the image. However, this would result in a loss of information in the centre of the image unlike this method which does not involve resampling to a larger scale.

Plate 3.5 shows an NS-001 image from channel one over Camp Oven after correction for radiometric-and tangential scale-distortions. Correction has resulted in the insertion of an extra 254 columns, 127 either side of nadir. It should be noted further correction is required to remove the effects of longitudinal distortion.

Plate 3.6 shows a TIMS image from channel one over Camp Oven after correction for radiometric-and tangential scale-distortions. Correction results in the insertion of an extra 114 columns of dummy pixels, 57 either side of nadir.

3.8.2 Correction of Aspect Distortion

Comparison of the black and white air photo over Camp Oven with the radiometrically-and tangential scale-corrected NS-001 channel one data over the same area reveals the NS-001 data is distorted longitudinally. This longitudinal distortion results from oversampling down the flightline. This was not the case with the TIMS imagery. Since both scanners were switched on and off at the same time and have similar resolutions, the number of lines in the NS-001 image should equal the number of lines in the TIMS image.

Therefore, the NS-001 data were resampled so the number of lines in both images were equal. This results in approximately every second line of NS-001 data being dropped. Plate 3.7 shows the NS-001 data from the channel centered on 0.48μm after calibration, removal of X-track shading, tangential scale correction and aspect correction.

3.9 Conclusions

1. Calibration should always be undertaken when the data has been obtained by sensors which derive new calibration values for each scanline. If calibration is not undertaken it it not possible to assume that the same DN value on adjacent scanlines represents the same amount of radiation from the earths surface.

2. Prior to calibration, the calibration values should be checked for any corrupted values or 'spikes'. Scanlines which contain these values can either be discarded or if the data on the scanline are not corrupted, the calibration value can be replaced by an average value derived from the two adjacent scanlines. If these scanlines are not adjusted the resultant calibrated data may bias the scene statistics and the data produced by any techniques which use these statistics.

3. Care should be taken when interpreting the results from the use of uncalibrated data with image processing algorithms which are affected by the calibration process. For example, the algorithm described by Sheffield, (1985) for the selection of best channels for display.

4. The affect of X-track shading on airborne multispectral data from the 0.45μm-2.35μm wavelength region can be easily removed using an empirical profile correction. This can be undertaken in a multiplicative or additive manner. The manner used should depend on whether any subsequent image processing would be biased by a given approach.

5. Preliminary results suggest it should be possible to correct for atmospheric effects with multispectral data from the 8μm-12μm wavelength region used models based on scene-derived parameters. Further work is required to fully evaluate these models.

6. The remotely sensed data used in this study contained geometric distortions due to varying lateral scales at right angles to the direction of flight and oversampling down the flightline. It was possible to remove the lateral distortions by the insertion of columns of dummy pixels. The longitudinal distortions were removed by dropping every other line.

3.10 Summary

In order to fully evaluate remotely sensed data for lithological mapping and mineral exploration it is desireable to reduce the data to physically meaningful parameters such as reflectance and emittance. This permits the comparison of the remotely sensed data with laboratory studies of the reflectance and emittance of rocks, minerals soils and vegetation. This reduction is inhibited by the presence of various inherrent distortions termed radiometric and geometric. Radiometric distortions alter the absolute value of a pixel whilst geometric distortions alter the spatial relationship between objects. The presence of these distortions also restricts the comparison of results between studies since these can be scene dependant.

The radiometric distortions were divided into sensor-and scene-related distortions. The sensor related distortions were removed by calibrating the data. Methods were described for the calibration of NS-001 and TIMS data. The importance of calibration was illustrated by comparing the channels selected by a best channel selection algorithm described by Sheffield, (1985) on raw and calibrated data from the same area. The results showed that the channels selected from raw data differed from those selected using calibrated data. This indicates that if raw data are used the results will be sensor-dependant. If raw data are used it is not possible to accurately compare the results obtained using this algorithm on data obtained by different sensors with similar channel widths. The scene-related distortions result from atmospheric effects and georadiometric factors primarily topography, view angle and illumination (Teillet, 1986). Of these the most obvious scene-related distortions in the airborne multispectral data from the 0.45μm-2.35μm region were due to changing view angle resulting in X-track shading. This was removed using an empirical profile correction. In the data from the 8μm-12μm region the

most obvious scene-related distortions resulted from atmospheric effects. The correction of these effects normally requires the availability of data on the composition of the atmosphere at the time and place of sensing. Such data were not available and two methods were developed to enable corrections using scene-derived parameters. Both methods indicated the temperature on the rhs of the image was greater than that on the lhs of the image. This temperature difference was explained in terms of sun-sensor-geometry which resulted in the sensor imaging sun facing slopes (hot) slopes when it imaged the rhs of the scene and shadowed (cold) slopes when it imaged the lhs of the scene. Preliminary results suggest it should be possible to correct for the atmospheric effects using these models, however, further work is needed.

The geometric distortions present in the data were attributed to two causes. First, varying lateral scales at right angles to the direction of flight. Secondly, oversampling down the flightline. The lateral distortions were removed by the insertion of columns of dummy pixels whilst the longitudinal distortions were removed by dropping every other line.

Once the data were corrected for these distortions they were analyed by a series of techniques aimed at reducing them to physically meaningful parameters. These data were evaluated in terms of lithological mapping and mineral exploration potential by making comparisons with geological maps, field maps and laboratory measurements of field samples over the same wavelength regions. The next chapter descibes the results from the analysis and interpretation of the data from the 0.4μm-2.4μm wavelength region and is followed by a similar chapter dealing with the data from the 8μm-12μm wavelength region. This latter chapter also examines the combined use of data from these wavelength regions for geological studies in this terrain.

SCANLINE 1				
PIXEL	GAIN	RAW DN	OFFSET	CALIBRATED RADIANCE VALUE
(a)	76	255	10	18620
(b)	76	11	10	76
SCANLINE 2				
PIXEL	GAIN	RAW DN	OFFSET	CALIBRATED RADIANCE VALUE
(c)	70	255	10	17150
(d)	70	11	10	70

Table 3.1   Raw DN and Calibrated Radiance Values from two Scanlines of NS-001 Data.

SCANLINE 1		
PIXEL		CALIBRATED BYTE VALUE
(a)	=	255
(b)	=	1
SCANLINE 2		
PIXEL		CALIBRATED BYTE VALUE
(c)	=	235
(d)	=	0

Table 3.2   Calibrated Byte Values for Scanlines in Table 3.1

TIMS Flightline 1.				
Blackbody 1				
Temperature			Reference Source Value	
Channel	Mean	Variance	Mean	Variance
1	18.95	0.20	64.59	2.28
2	18.95	0.20	78.22	2.99
3	18.95	0.20	74.35	2.74
4	18.95	0.20	76.18	2.81
5	18.95	0.20	74.69	2.78
6	18.95	0.20	71.74	2.70
Blackbody 2				
Temperature			Reference Source Value	
Channel	Mean	Variance	Mean	Variance
1	48.92	1.13	170.53	13.57
2	48.92	1.13	171.40	13.62
3	48.92	1.13	161.25	12.22
4	48.92	1.13	159.57	11.74
5	48.92	1.13	157.58	11.45
6	48.92	1.13	160.43	12.10

Table 3.3   Blackbody 1 and 2 Temperature and Reference Source Values
Channels 1-6 TIMS Flightline 1.

TIMS Flightline 2.				
Blackbody 1				
Temperature			Reference Source Value	
Channel	Mean	Variance	Mean	Variance
1	19.00	0.0	64.57	0.25
2	19.00	0.0	78.22	0.10
3	19.00	0.0	74.40	0.24
4	19.00	0.0	75.99	0.05
5	19.00	0.0	74.74	0.19
6	19.00	0.0	71.75	0.26
Blackbody 2				
Temperature			Reference Source Value	
Channel	Mean	Variance	Mean	Variance
1	48.93	0.07	170.88	0.29
2	48.93	0.07	171.53	0.26
3	48.93	0.07	161.35	0.25
4	48.93	0.07	159.89	0.26
5	48.93	0.07	157.87	0.22
6	48.93	0.07	160.63	0.34

Table 3.4   Blackbody 1 and 2 Temperature and Reference Source Values Channels 1-6 TIMS Flightline 2.

Raw Digital Numbers (DN)			Calibrated data	
0-255 Range			$mWcm^{-2}sr^{-1}\mu m^{-1}$	
Channel	Mean	Standard	Mean	Standard
		Deviation		Deviation
1	95.63	16.42	6043.25	1072.32
2	74.04	16.00	6334.91	1429.16
3	78.67	20.41	6792.77	1927.16
4	83.35	14.90	7625.87	1445.17
5	107.59	18.97	7922.95	1490.49
6	109.49	23.65	2372.62	554.47
7	83.00	23.57	485.99	157.13

Table 3.5   Channel Mean and Standard Deviations before and after Calibration NS-001 data, Flightline 1.

NS-001 Data					ATM Data	
Flightline 1			Flightline 2			
Rank	Raw	Calibrated	Raw	Calibrated	Raw	Calibrated
1	367	345	367	345	4510	345
2	567	235	567	235	2410	456
3	167	234	167	234	2510	346
4	356	135	267	135	3410	356
5	357	245	356	134	3510	457

Table 3.6   Best Three Channel Combinations of Raw and Calibrated NS-001 and ATM Data using the Sheffield Method.

| Channel | Wavelength Interval | $\tau A\lambda$ | $L_{sky\lambda}$ | $L_{V\lambda}$ |
	(μm)		$(Wm^{-2}sr^{-1}\mu m^{-2})$	$(Wm^{-2}sr^{-1}\mu m^{-2})$
1	8.3-8.8	0.848	4.198	0.962
2	8.8-9.3	0.885	3.286	0.650
3	9.3-9.8	0.801	5.116	1.180
4	10.1-11.0	0.910	3.248	0.603
5	11.0-12.0	0.912	2.696	0.498
6	12.0-13.0	0.816	4.945	1.143

Table 3.7   Atmospheric Parameters from LOWTRAN 4 after Kahle *et al.* (1980).

	Left Hand Side of Nadir			Right Hand Side of Nadir		
Channel	Slope $-\alpha\lambda z)$	Intercept $(Ln\epsilon M s^*)$	Intercept at $sec\theta = 1$	Slope $-\alpha\lambda z)$	Intercept $(Ln\epsilon M s^*)$	Intercept at $sec\theta = 1$
1	-0.1032	2.491	2.387	-0.2506	2.637	2.386
2	-0.0627	2.520	2.458	-0.2223	2.678	2.456
3	-0.0565	2.523	2.467	-0.2055	2.671	2.465
4	-0.0850	2.554	2.468	-0.1795	2.645	2.466
5	-0.0734	2.529	2.456	-0.1571	2.609	2.452
6	-0.0734	2.463	2.389	-0.1510	2.537	2.386

Table 3.8   Slope $(-\alpha\lambda z)$ and Intercept $(Ln\epsilon M S^*)$ Values obtained using Callison Method

Channel	Left Hand Side	Right Hand Side
	% Decrease in Radiance	% Decrease in Radiance
1	9.61	22.19
2	5.87	19.92
3	5.21	18.62
4	8.02	16.41
5	6.70	14.57
6	6.99	14.00

Table 3.9   Percent Decrease in Radiance due to the Atmospheric Effect using the Callison Method

	Left Hand Side of Nadir				Right Hand Side of Nadir			
Channel	$K2$	Correlation Coefficient (r)	$K3$	$G_i \bullet$	$K2$	Correlation Coefficient (r)	$K3$	$G_i \bullet$
1	0.1555	0.3472	-3.370	12.202	-1.417	0.7967	4.748	25.424
2	0.2104	0.4917	-4.144	12.822	-1.121	0.7465	4.517	21.973
3	0.1725	0.4304	-3.327	12.720	-0.914	0.6822	4.020	19.368
4	0.4340	0.7118	-11.751	15.271	-1.608	0.8582	5.861	29.728
5	0.4208	0.6893	-10.768	14.728	-1.803	0.8668	6.194	33.203
6	0.4152	0.6669	-9.815	13.686	-2.011	0.8467	6.078	36.197

Table 3.10   Multiplicative ($K2$)and Additive ($K3$) Atmospheric Terms obtained using Green and Hook Method. Correlation coefficients are given for the fit of line to the data used to obtain the $K2$ term. Correlation coefficents for the $K3$ term were always greater than 9.0.

At $Sec\theta = 1$					
Left Hand Side of Nadir			Right Hand Side of Nadir		
Channel	Total % Difference	% Effect of $K2$ Term	% Effect of $K3$ Term	Total % Difference	% Effect of $K2$ Term	% Effect of $K3$ Term
1	10.788	16.825	27.614	57.090	75.767	18.677
2	8.905	23.413	32.318	46.836	67.394	20.558
3	7.327	18.829	26.156	39.168	59.922	20.754
4	22.609	54.342	76.951	60.258	79.973	19.716
5	20.794	52.317	73.111	64.867	83.521	18.654
6	20.0974	51.464	71.720	69.820	86.612	16.792
At $Sec\theta = 1.27$					
Left Hand Side of Nadir			Right Hand Side of Nadir		
Channel	Total % Difference	% Effect of $K2$ Term	% Effect of $K3$ Term	Total % Difference	% Effect of $K2$ Term	% Effect of $K3$ Term
1	13.269	21.909	35.706	59.771	83.564	23.792
2	10.437	30.733	41.170	49.823	76.013	26.189
3	8.7411	24.579	33.320	42.363	68.800	26.438
4	24.203	73.824	98.027	61.992	87.108	25.116
5	22.212	70.924	93.136	66.180	89.944	23.763
6	21.658	69.705	91.363	70.890	92.281	21.197

Table 3.11 Overall Percentage Decrease and Percent Effect of Multiplicative and Additive Terms on Left Hand Side and Right Hand Side of Nadir for $sec\theta = 1$ and $Sec\theta = 1.2738972$.
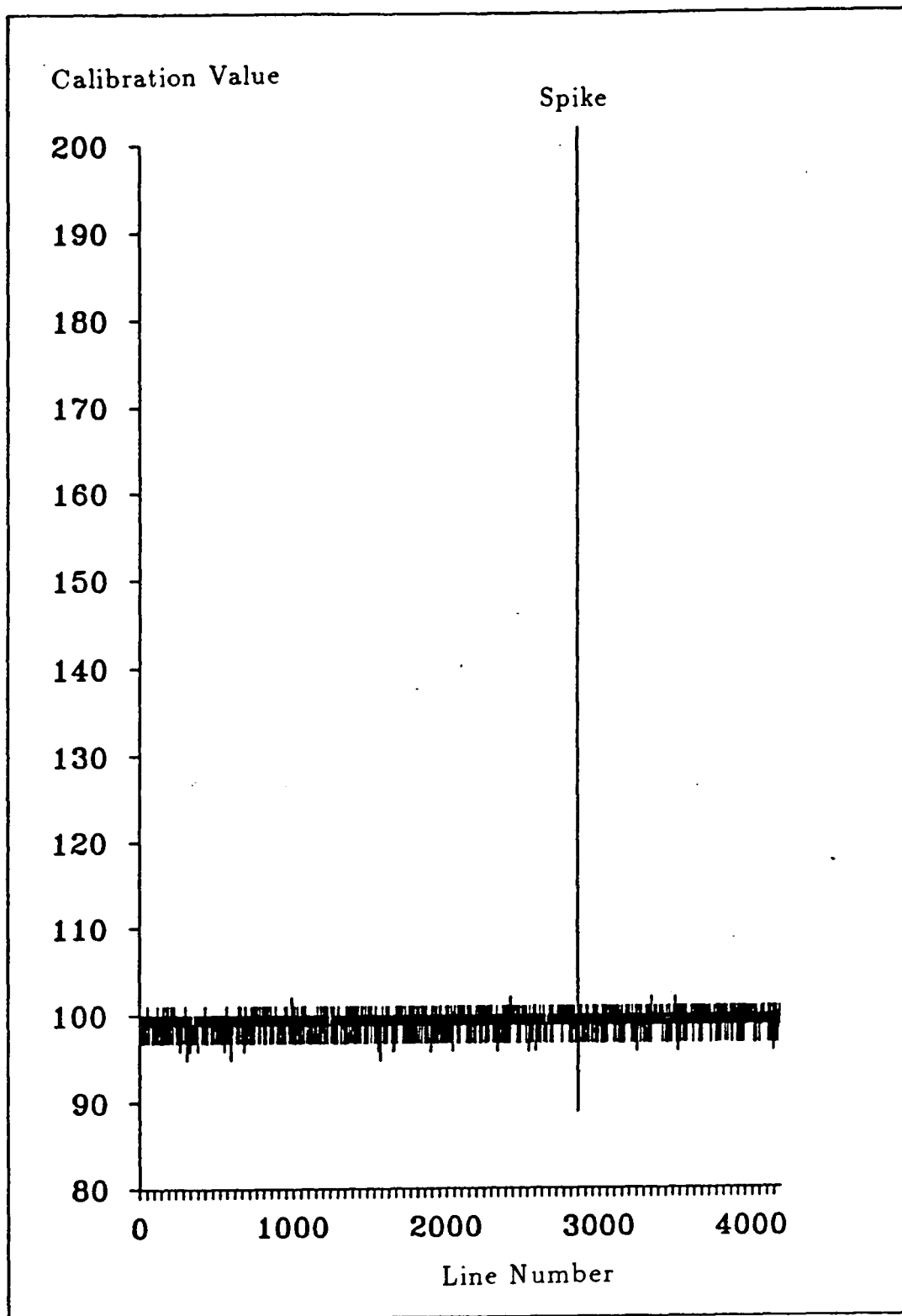
Figure 3.1   Variation in Calibration Values of Channel Two down NS-001
   Flightline 1.
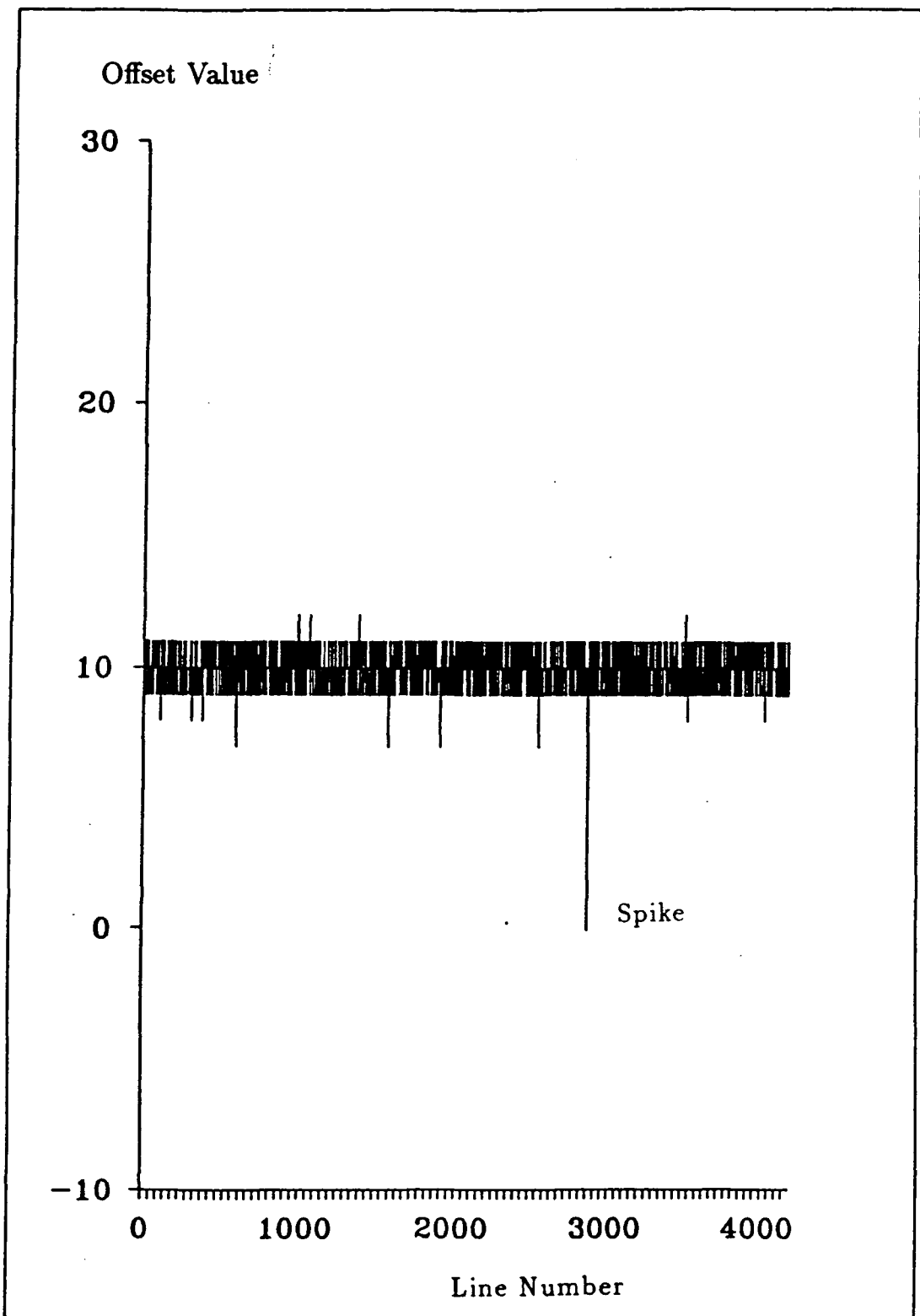
Figure 3.2 Variation in Offset Values of Channel Two down NS-001
Flightline 1.
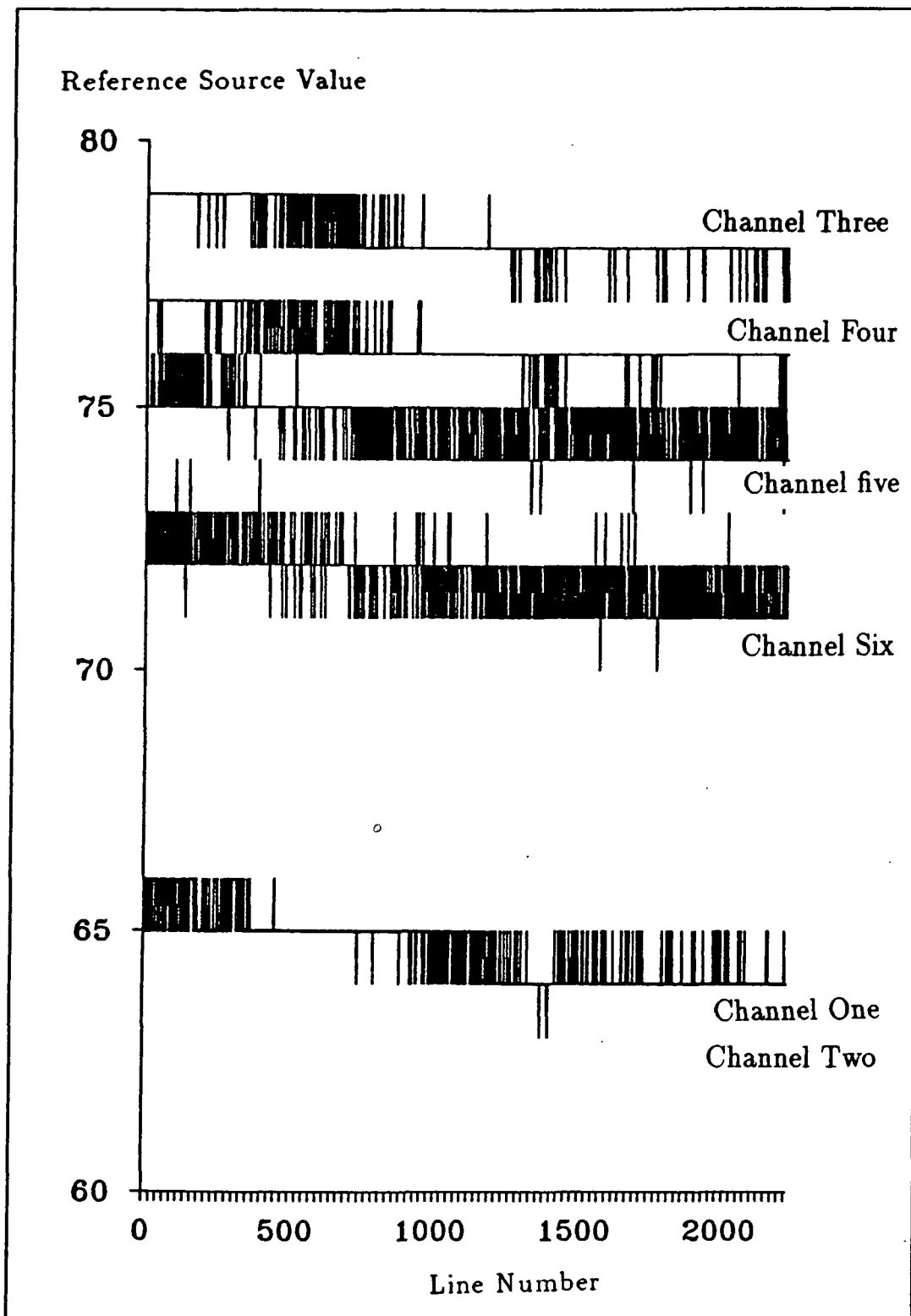
Figure 3.3   Variation in Low Temperature Reference Source Values down
TIMS Flightline 1.
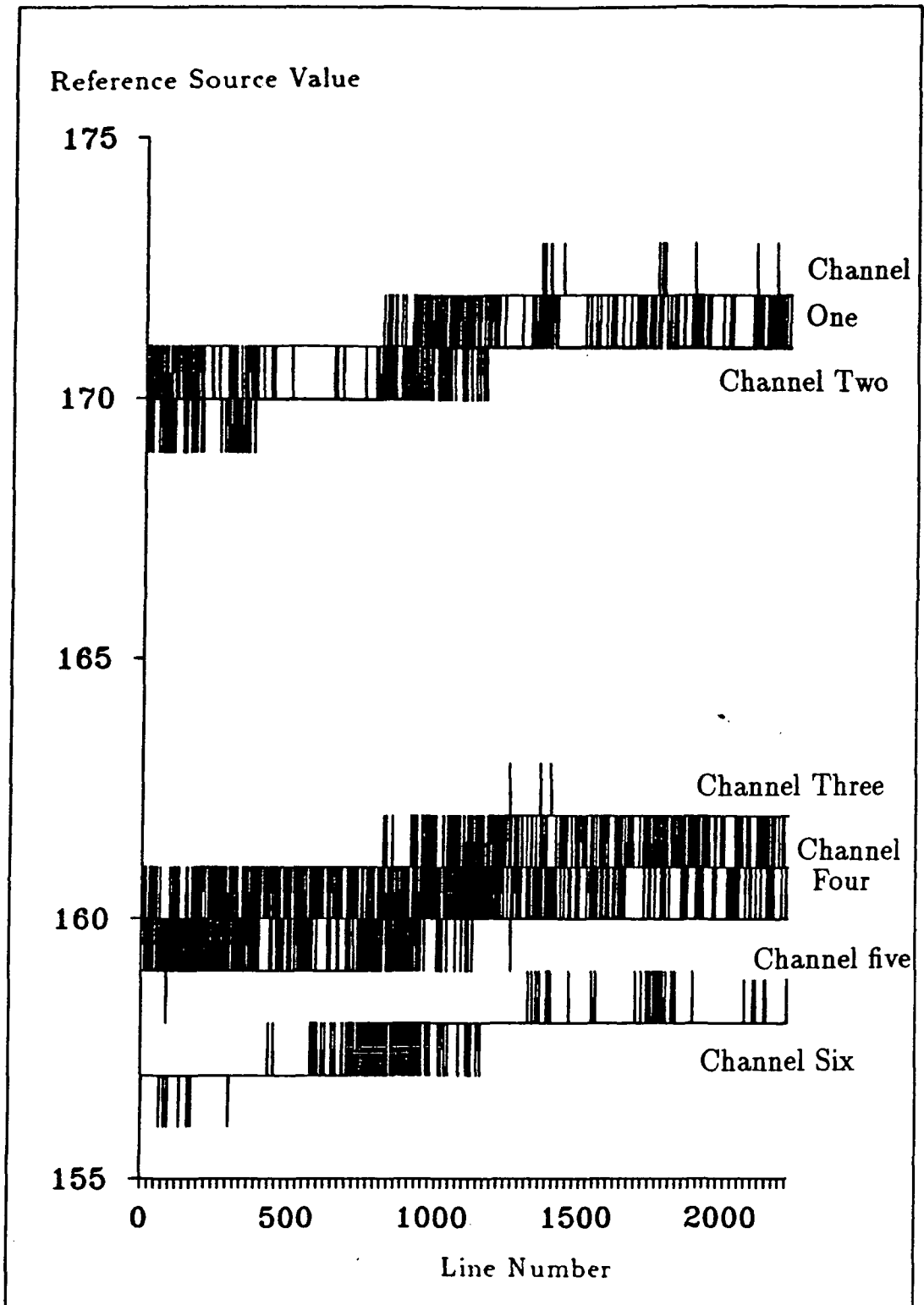
Figure 3.4   Variation in High Temperature Reference Source Values down TIMS Flightline 1.
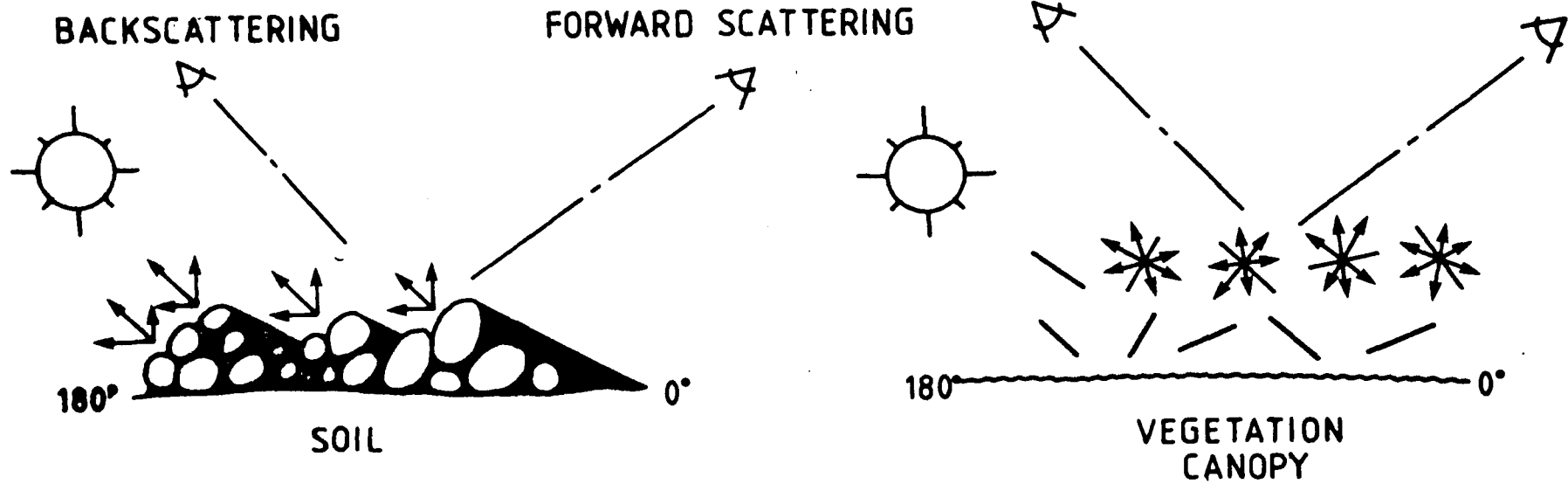
Figure 3.5 Forward scattering and backscattering of soil and vegetation. soil has strong backscatter and weak forward scatter due to vertical components. By contrast, complete vegetation canopies have similar amounts of scatter in all directions due to the transmittance and reflectance of leaves being roughly equal in all directions. (from Kimes, 1983)
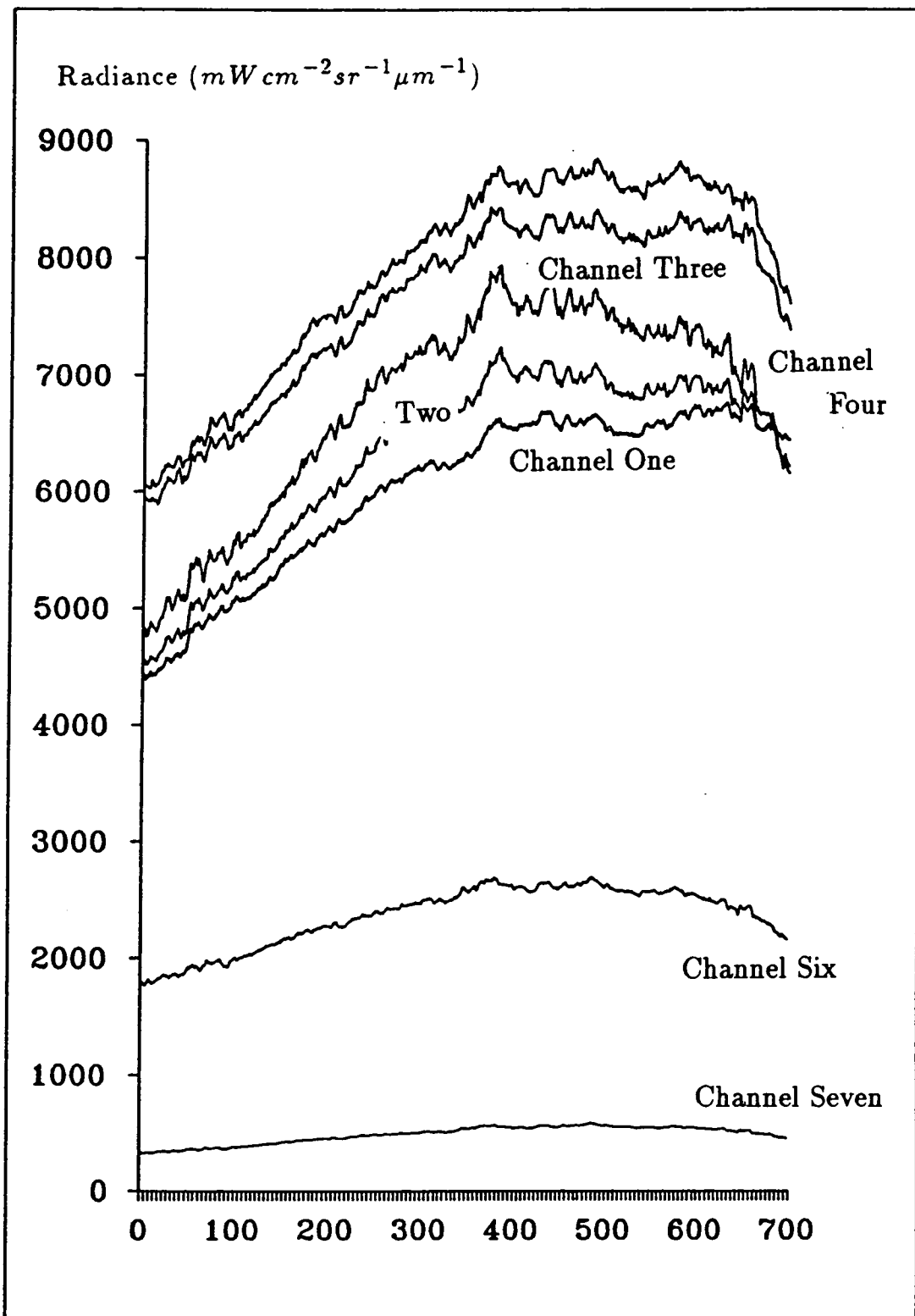
Figure 3.6   Variation in Column Means from Left to Right across NS-001
Image, Flightline 1.
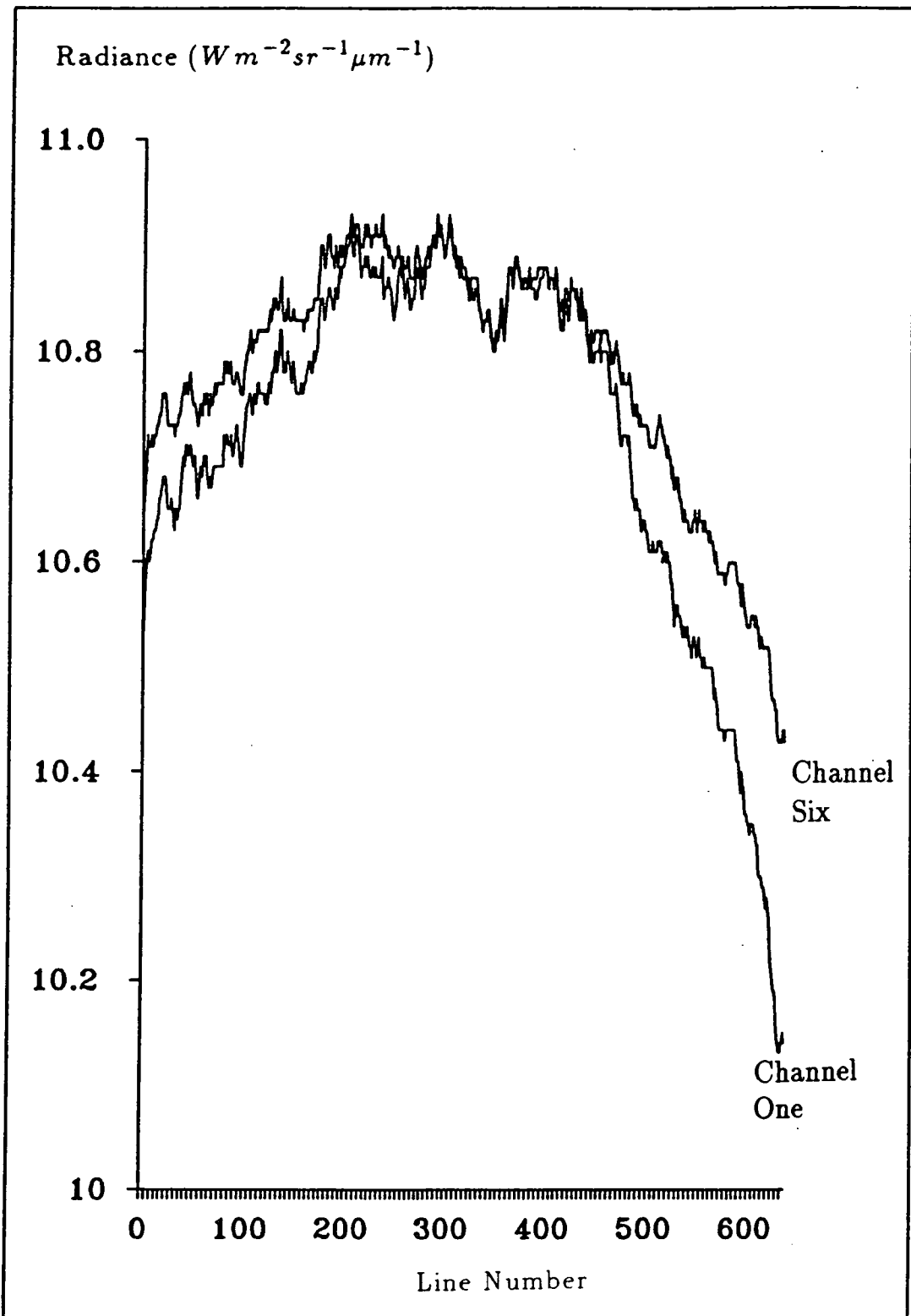
Figure 3.7   Variation in Column Means from left to right across TIMS
image, flightline 1.

Figure 3.8   Residual Curve from Dividing NS-001 Column Means of
Channel Six by Channel Seven, Flightline 1.
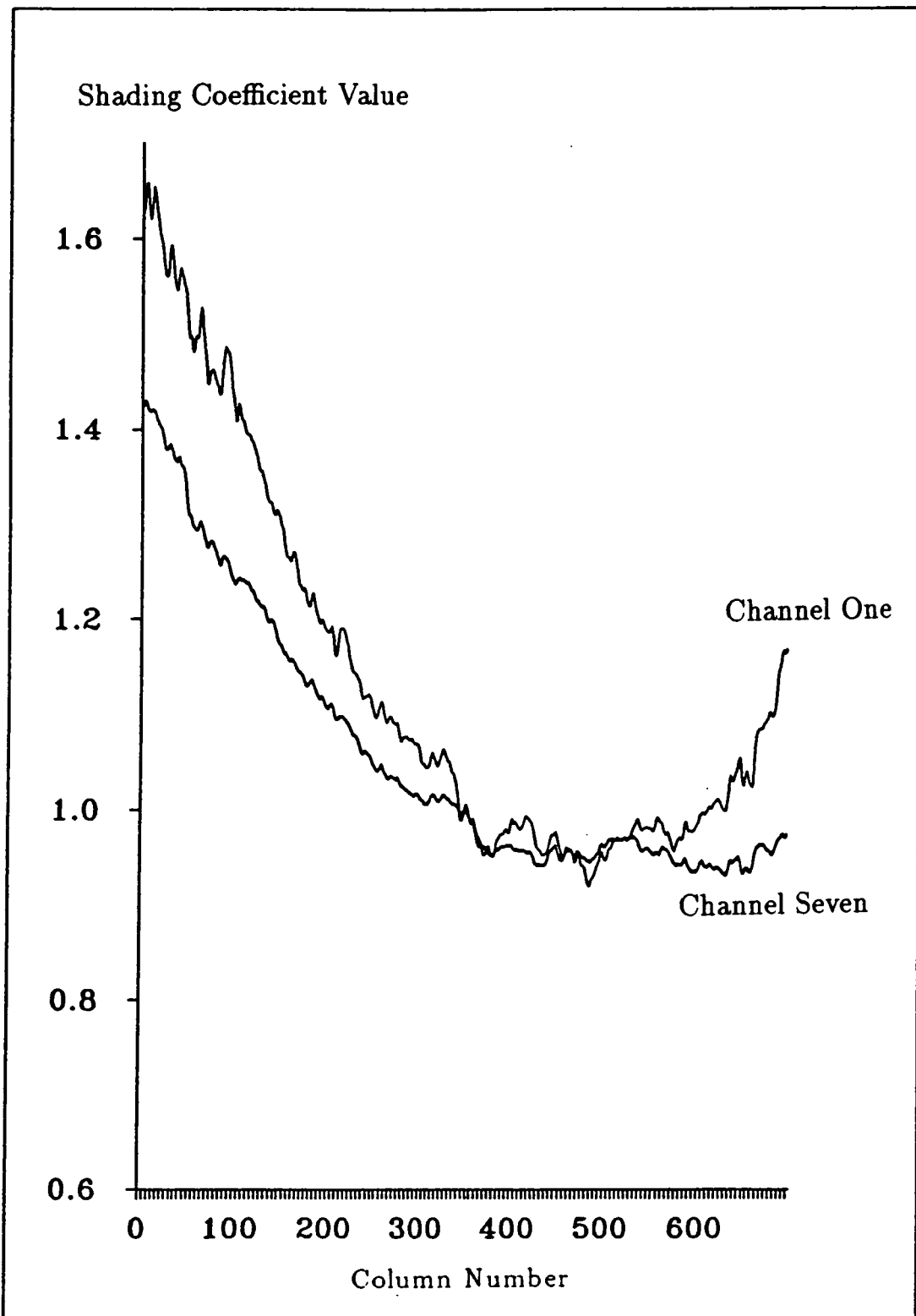
Figure 3.9   Shading Coefficients from Left to Right across NS-001 Image,
Flightline 1.
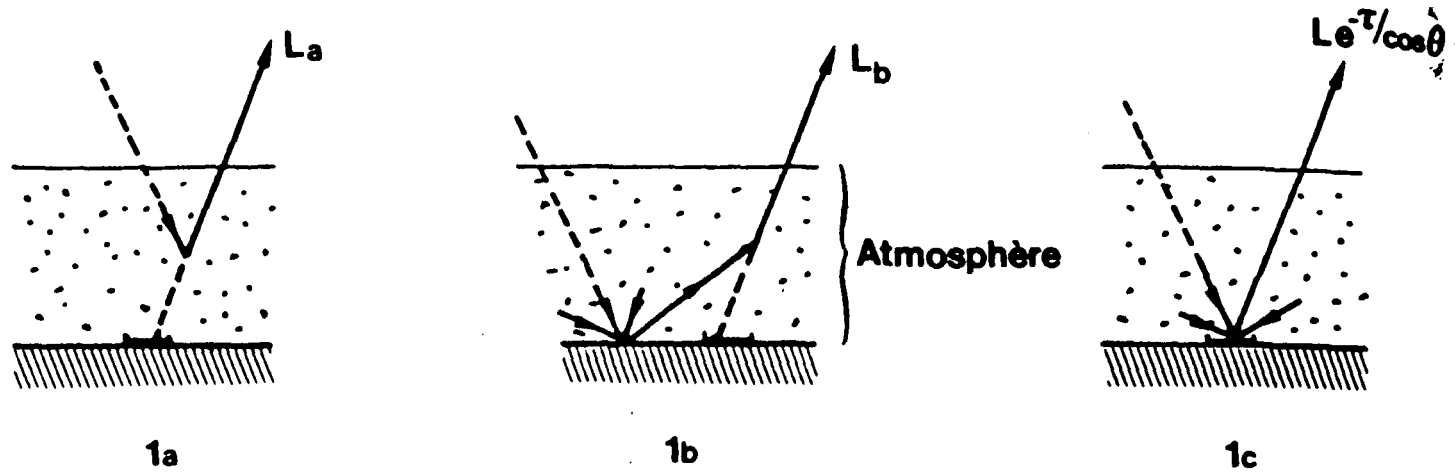
Figure 3.10   Schematic of the definition of : (a) the atmospheric radiance;
(b) the background radiance; and (c) the useful radiance from the
pixel target. $L_a + L_b$ = path radiance; L = radiance reflected by the
surface at ground level; τ' = optical thickness of the atmosphere; θ =
zenith viewing angle. (from Deschamps *et al.*, 1983)
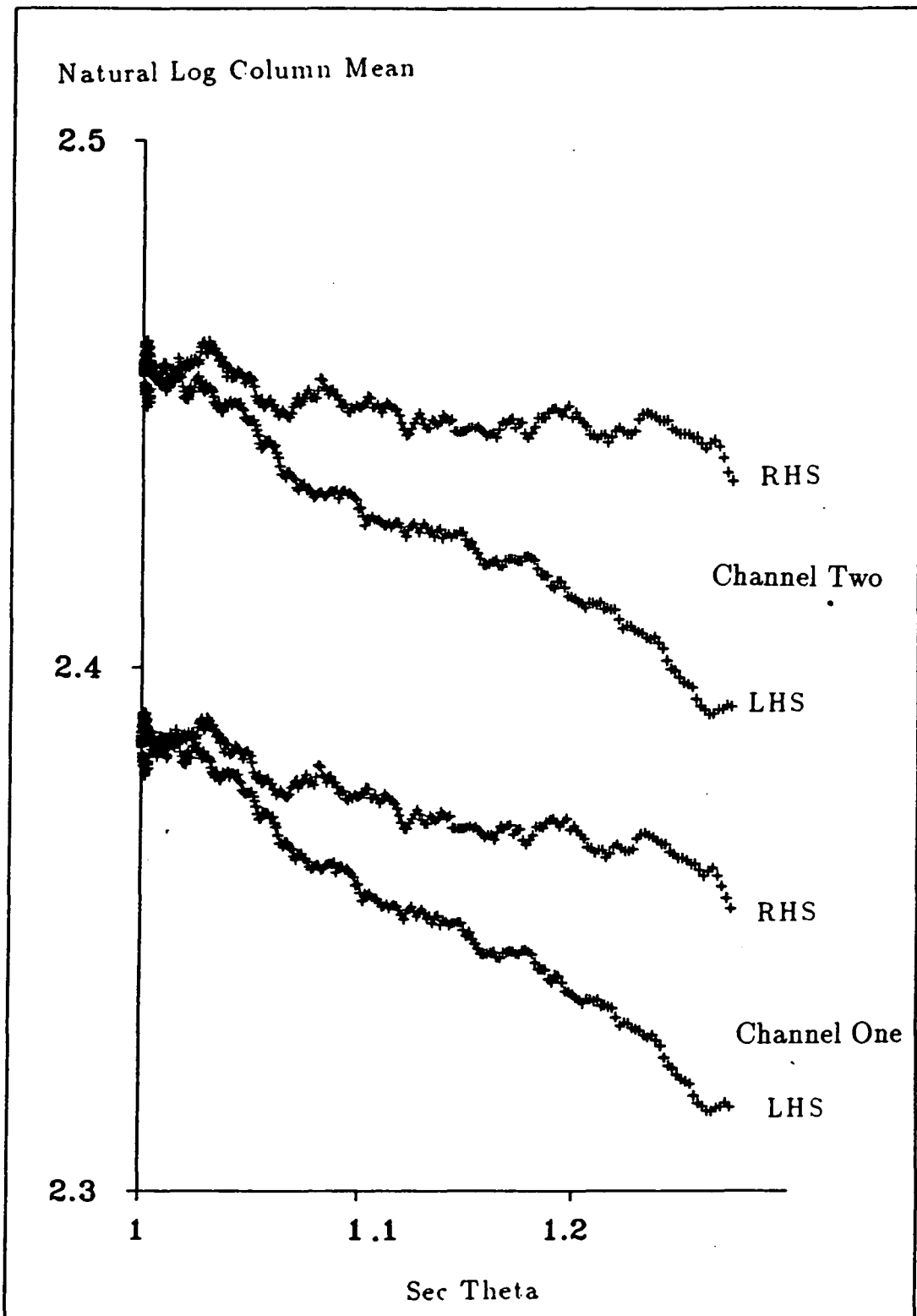
Figure 3.11   Plot of Natural Log of Column Means Versus Sec Theta
TIMS Line 1, LHS = left hand side of nadir, RHS = right hand side
of nadir.
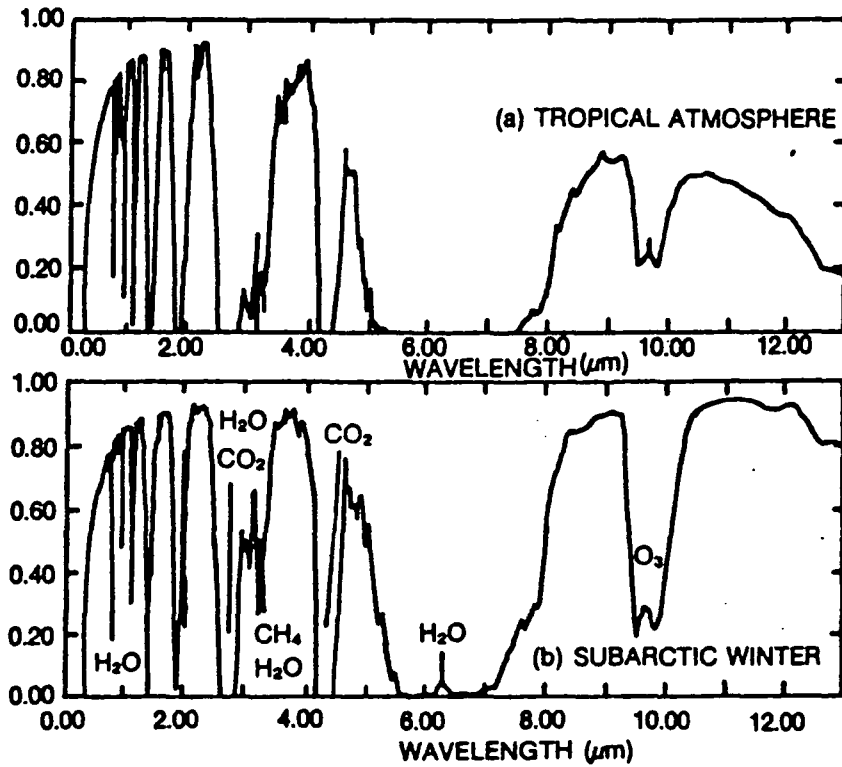
Figure 3.12   Position and Causes of Atmospheric Absorptions in the
Wavelength Region between 0.0 and 13.0μm (from Putman, 1985)

77
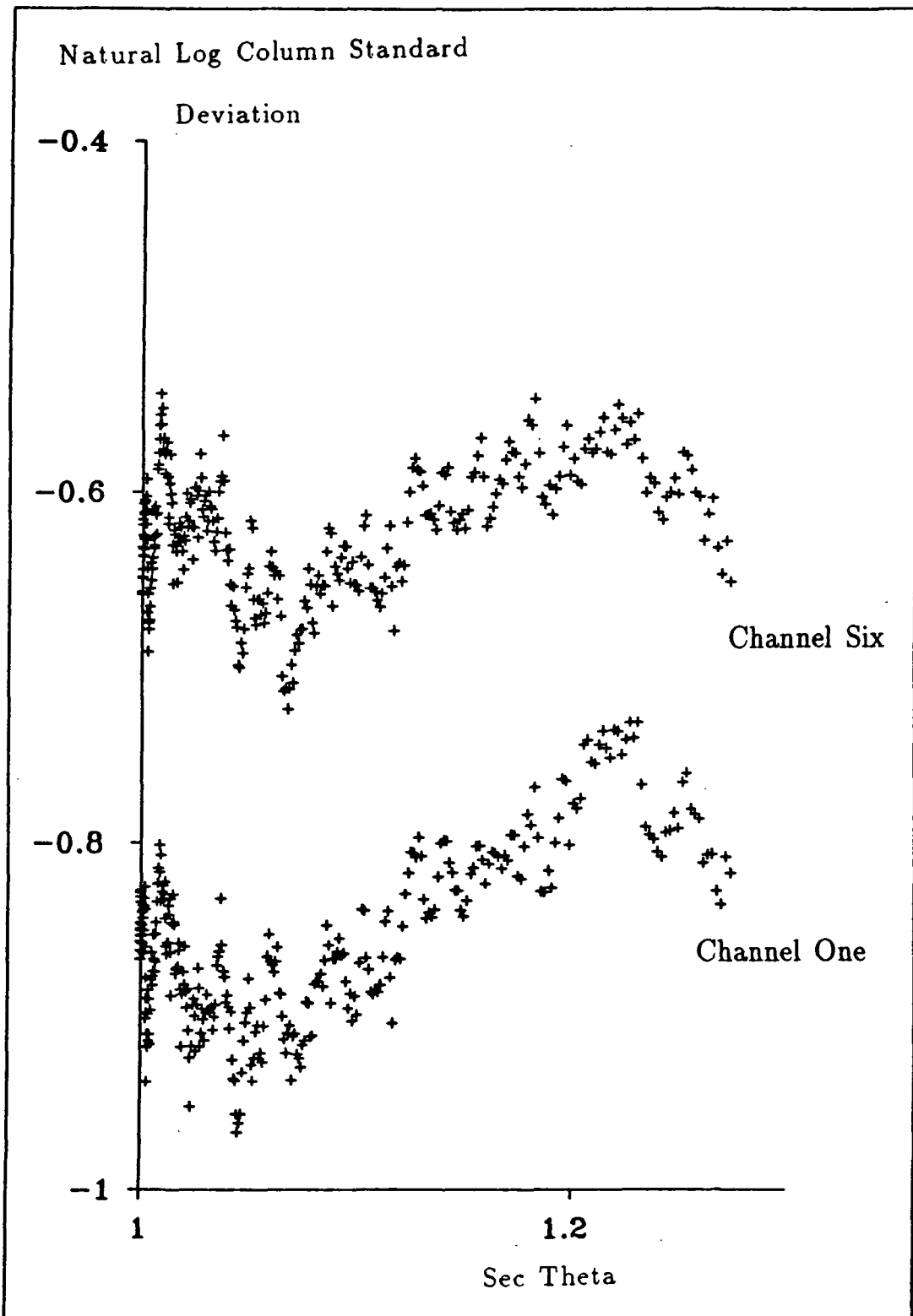
Figure 3.13   Plot of Natural Log of Column Standard Deviation Versus
Sec Theta Left Hand Side of Nadir TIMS Channels One and Six,
Flightline 1.
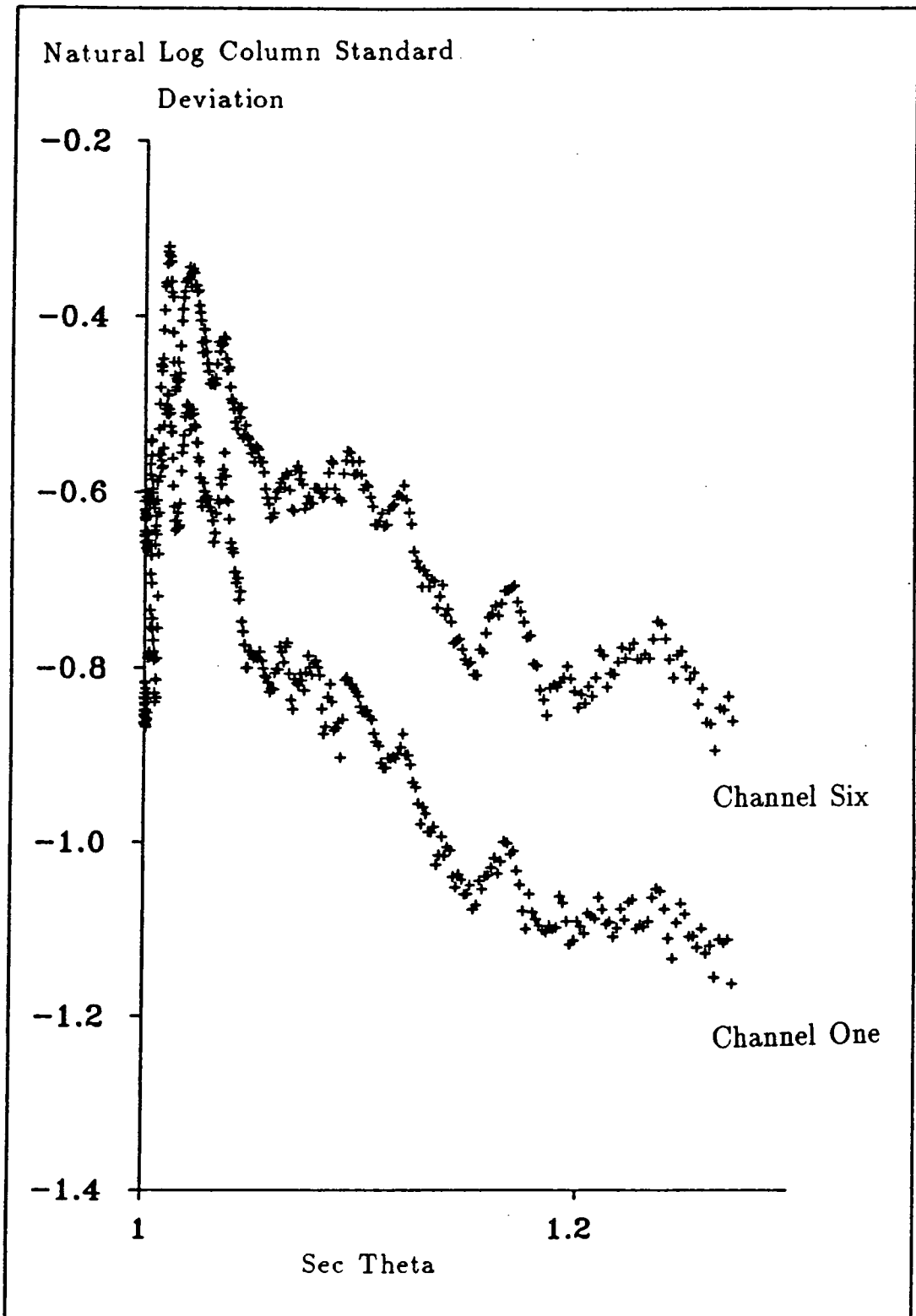
Figure 3.14   Plot of Natural Log of Column Standard Deviation Versus
Sec Theta Right Hand Side of Nadir TIMS Channels One and Six,
Flightline 1.
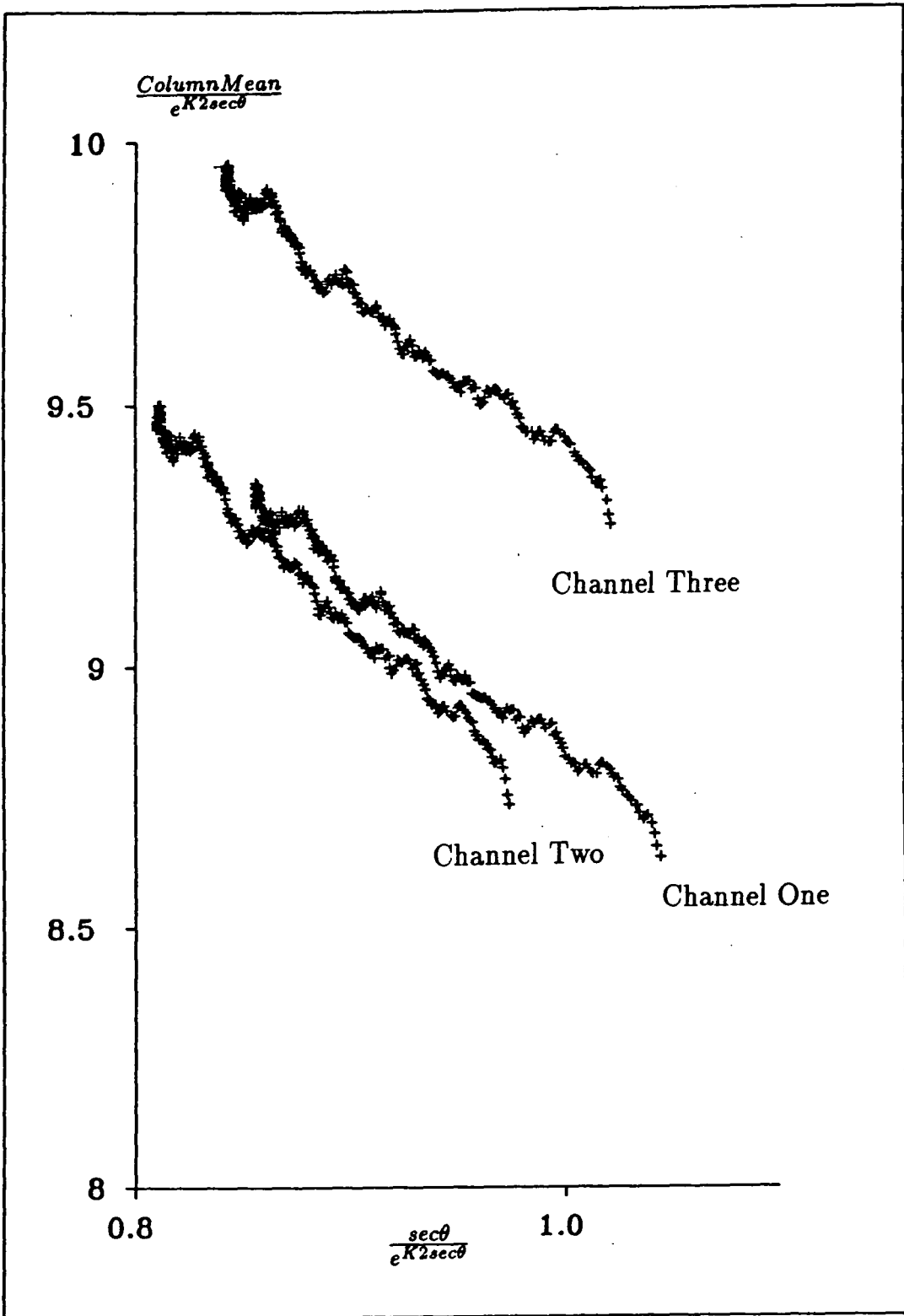
Figure 3.15   Plot of $\frac{ColumnMean}{e^{K2sec\theta}}$ Versus $\frac{sec\theta}{e^{K2sec\theta}}$ Channels One, Two and Three Left Hand Side of Nadir TIMS data, Flightline 1.
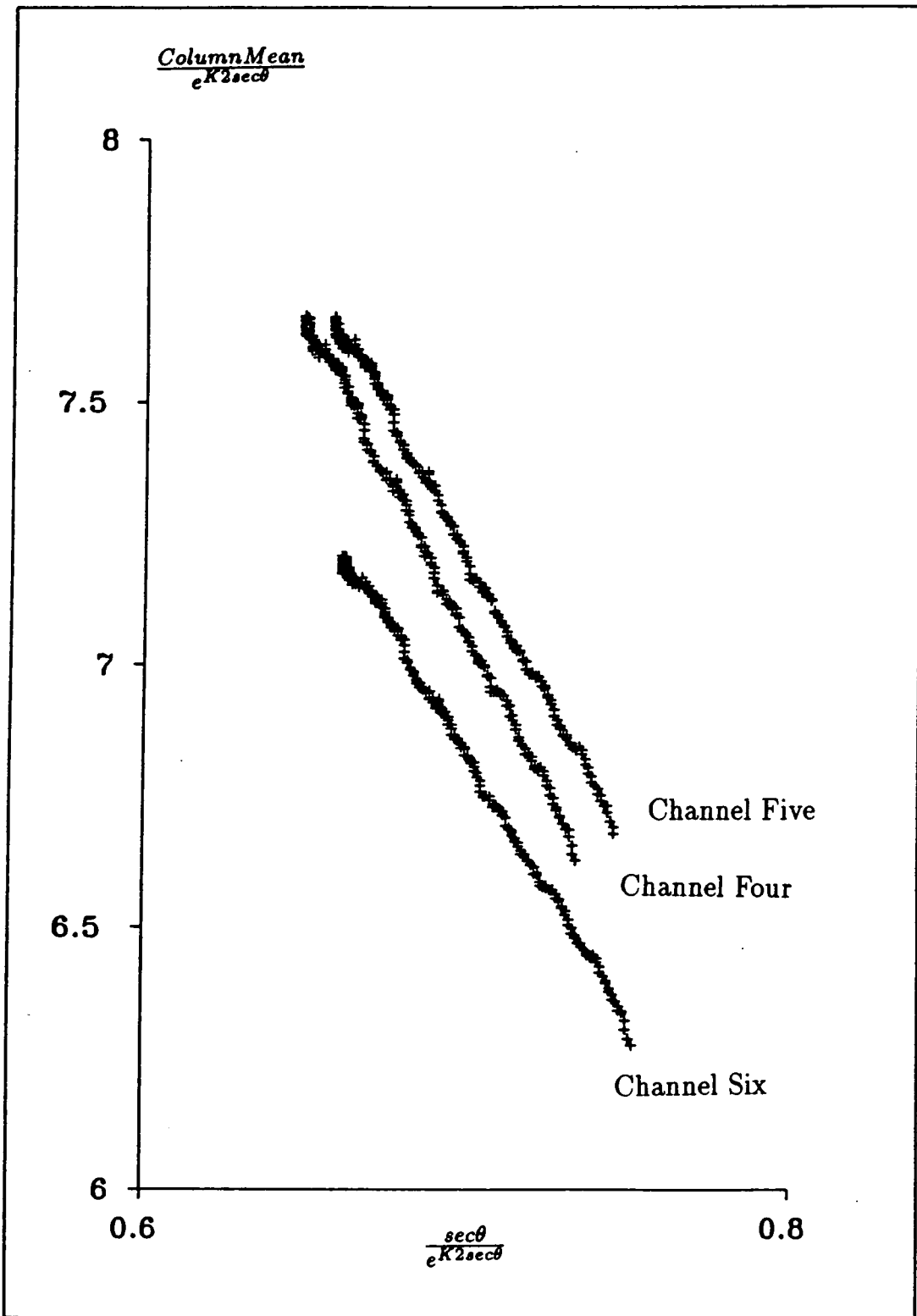
Figure 3.16 Plot of $\frac{ColumnMean}{e^{K2sec\theta}}$ Versus $\frac{sec\theta}{e^{K2sec\theta}}$ Channels Four, Five and Six Left Hand Side of Nadir TIMS data, Flightline 1.
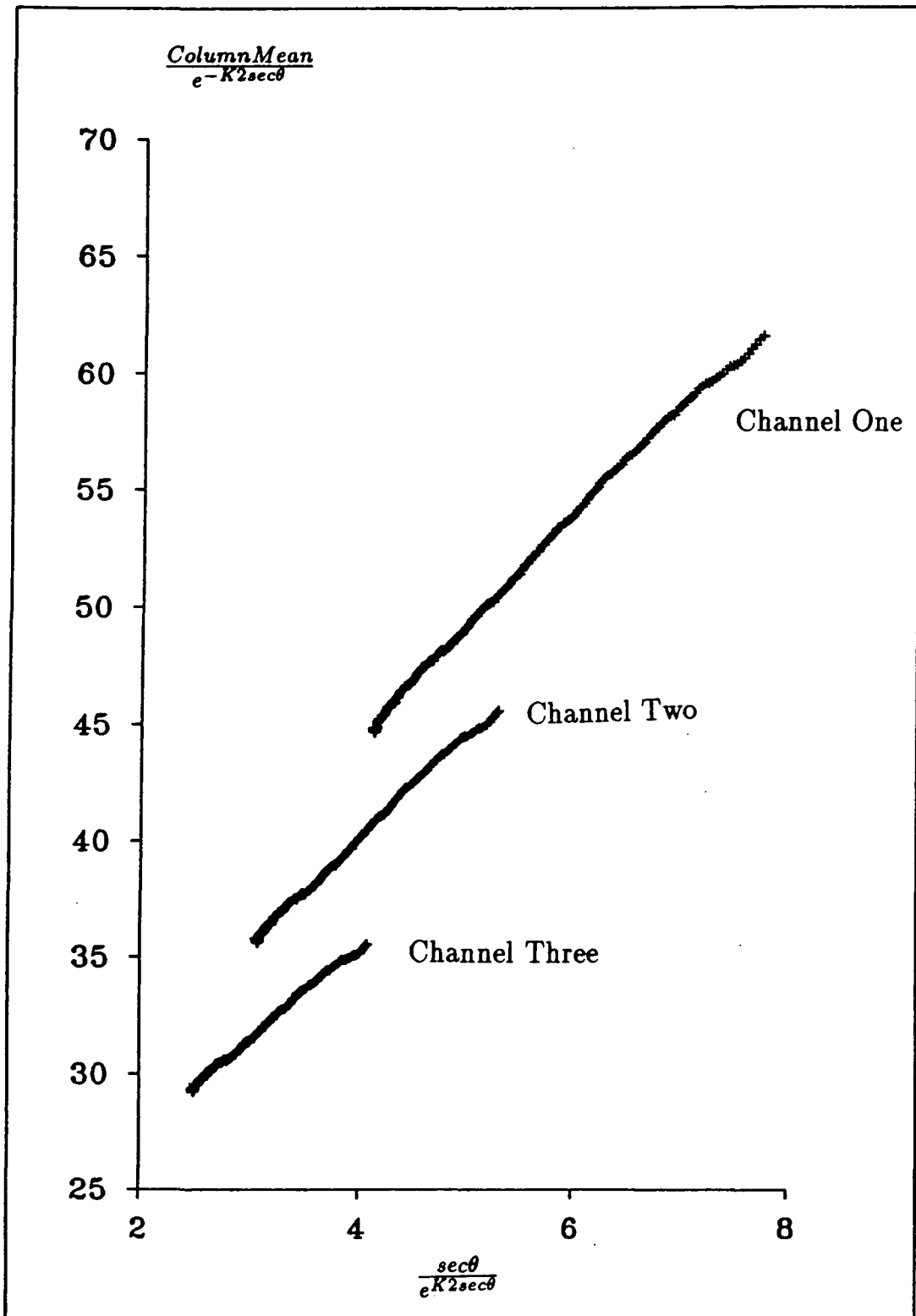
Figure 3.17 Plot of $\frac{ColumnMean}{e^{-K2sec\theta}}$ Versus $\frac{sec\theta}{e^{K2sec\theta}}$ Channels One Two and Three Right Hand Side of Nadir TIMS data, Flightline 1.
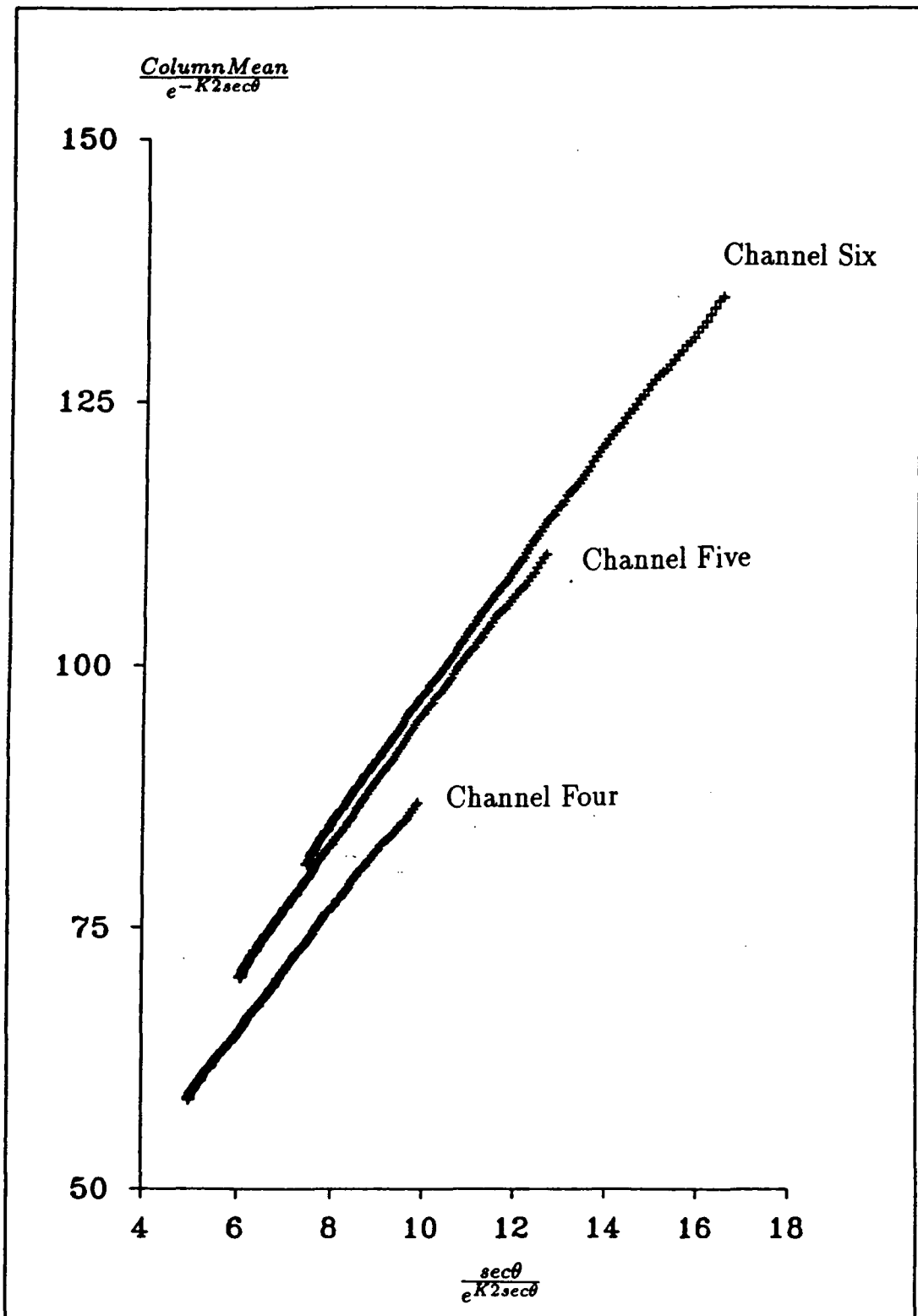
Figure 3.18   Plot of $\frac{Column\,Mean}{e^{-K2sec\theta}}$ Versus $\frac{sec\theta}{e^{K2sec\theta}}$ Channels Four Five and Six Right Hand Side of Nadir TIMS data, Flightline 1.

Constant lateral scale

Varying lateral scale

Flight direction

Constant longitudinal scale

Constant longitudinal scale

(a) Vertical aerial photograph

(b) Line scanner image
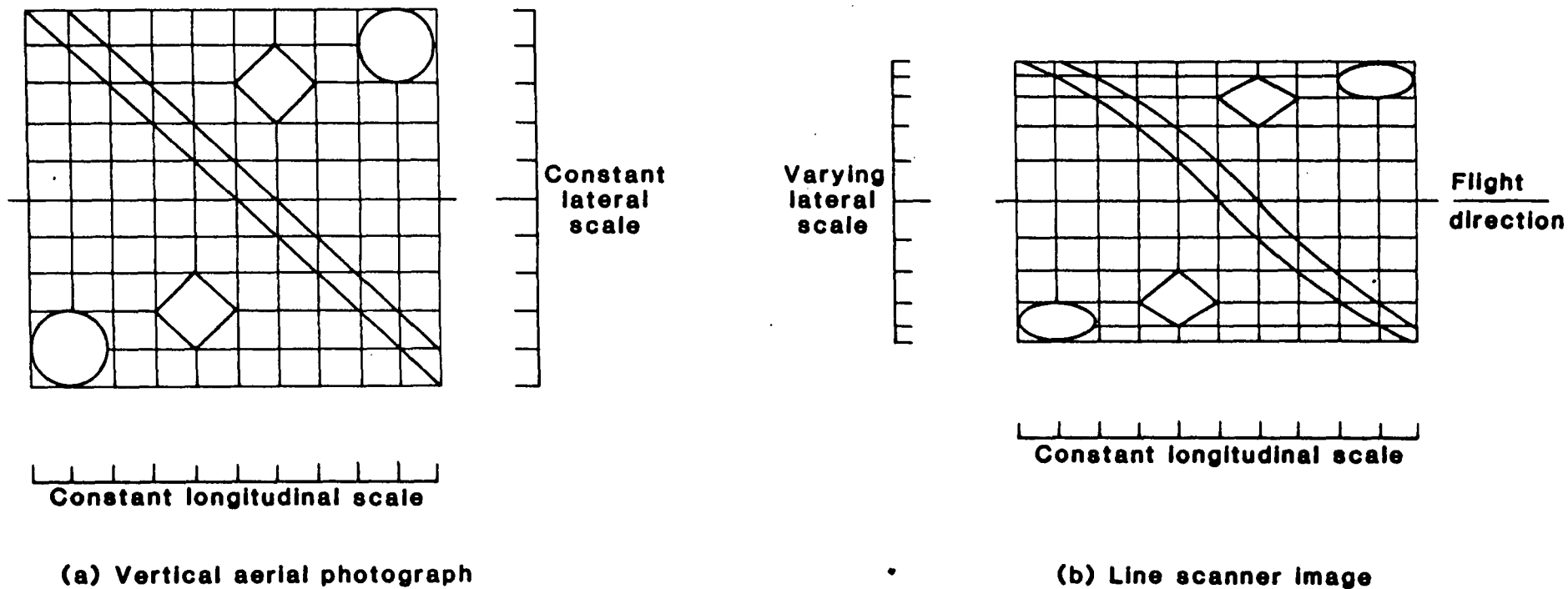
Figure 3.19   Illustration of the Effect of Tangential Scale Distortion.
(from Lillesand and Kiefer, 1979)
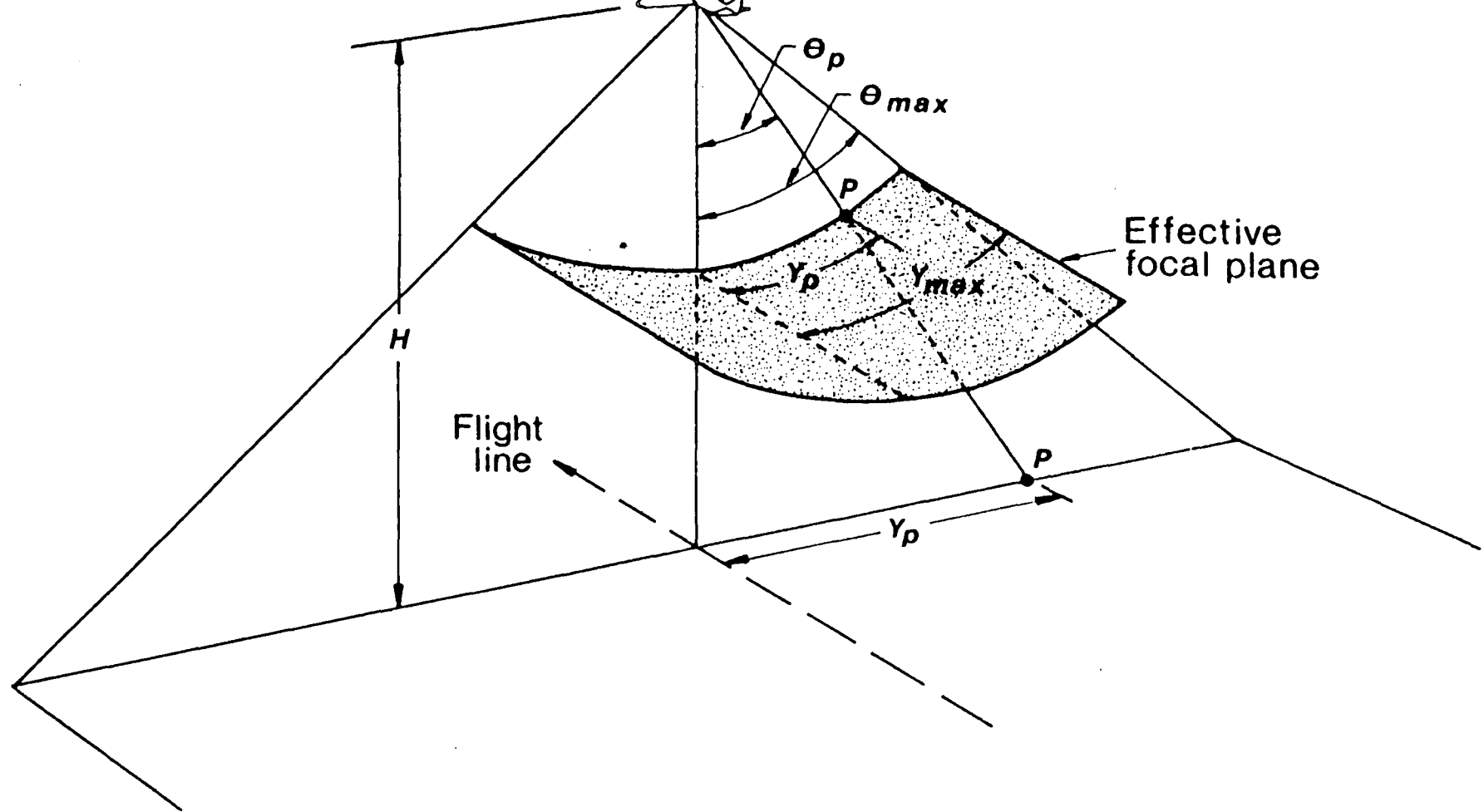
Figure 3.20   Elements Involved in Computing True Ground Positions from Measurements Made on Distorted Imagery. (from Lillesand and Kiefer, 1979)
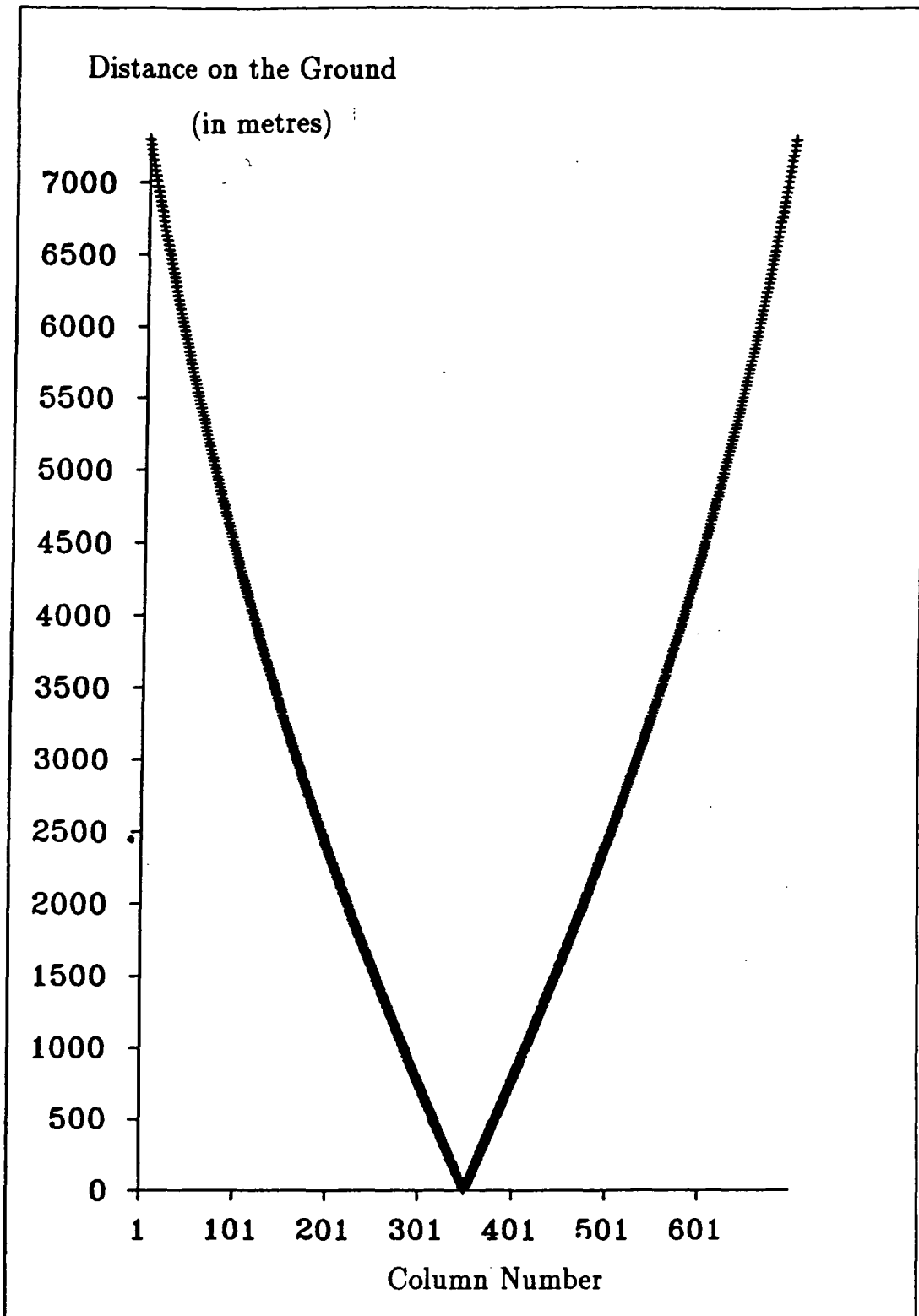
Figure 3.21   Plot of Distance on the Ground Versus Column Number for
    TIMS data.
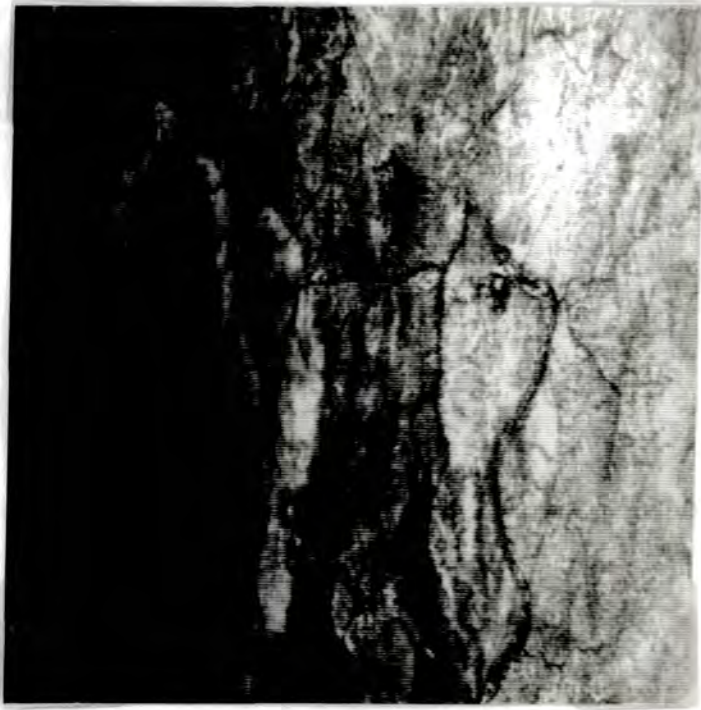
Plate 3.1 X-track Shading in 0.48μm Channel NS-001 Data, Camp Oven Test Site.

Plate 3.2 Colour Composite of the 10.7μm, 9.2μm and 8.4μm Raw TIMS Channels Displayed as Red, Green and Blue respectively, Camp Oven Test Site.

Plate 3.3   0.48μm Channel NS-001 data After Calibration and Removal
of X-track Shading, Camp Oven Test Site.

Plate 3.4   Regional Air Photo, Scale 1:25000, Camp Oven Test Site.

Plate 3.5 0.48μm Channel NS-001 Data After Calibration, Removal of X-track Shading and Correction for Tangential Scale Distortion, Camp Oven Test Site.
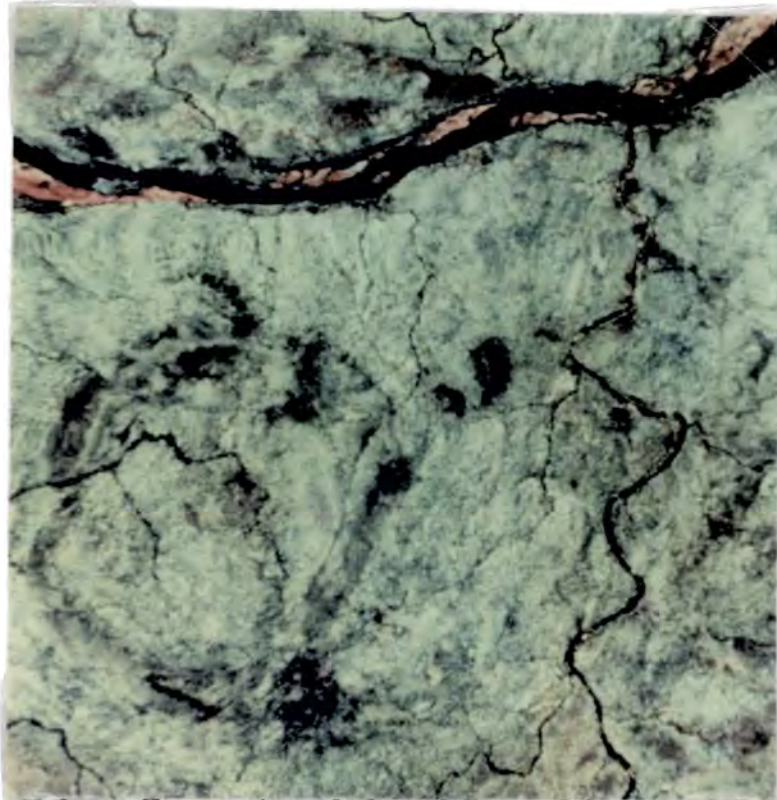
Plate 3.6   Colour Composite of the 10.7μm, 9.2μm and 8.4μm TIMS Channels Displayed as Red, Green and Blue respectively, After Calibration, Removal of X-track Shading and Correction for Tangential Scale Distortion.
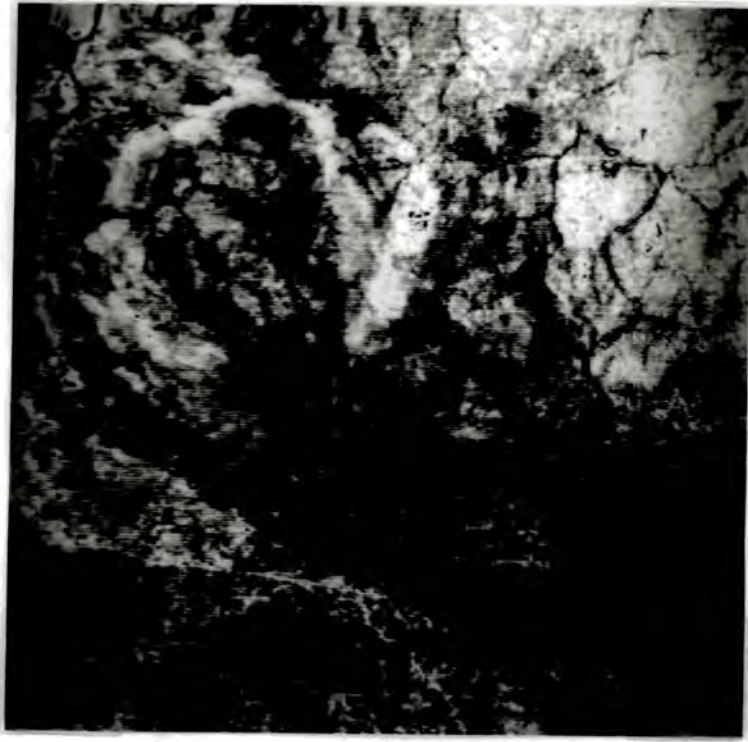
Plate 3.7   0.48µm Channel NS-001 Data After Calibration, Removal of X-track Shading, and Correction for Tangential Scale and Aspect Distortions, Camp Oven Test Site.

CHAPTER 4

ANALYSIS AND INTERPRETATION OF DATA FROM THE

$0.4\mu m$ - $2.5\mu m$ WAVELENGTH REGION FOR

LITHOLOGICAL MAPPING AND MINERAL EXPLORATION

IN WEATHERED VEGETATED TERRAIN

4.1 Introduction

The principle objective of the analysis and interpretation of the data from the 0.4μm-2.5μm region was to evaluate its usefulness for lithological mapping and mineral exploration in deeply weathered vegetated terrain. The results from this study could then be compared with those from a similar study over the same area, using data from the 8μm-12μm wavelength region. This comparison should determine which wavelength region is most effective for geological studies in weathered, vegetated terrain.

The data from the 0.45μm-2.5μm region were obtained by the NS-001 sensor and Geophysical Environment Research Mark IV InfraRed Intelligent Spectrometer (GER MK IV IRIS). The NS-001 sensor acquires eight discrete channels of data. Four of these are located in the Visible/Near InfraRed (VNIR) between 0.45μm and 1.0μm. Three channels are located in the ShortWave InfraRed (SWIR) between 1.0μm and 2.5μm. A further channel is located in the Mid InfraRed (MIR) between 8μm and 12μm. The exact wavelength range of each of these channels is given in Table 1.1. The NS-001 data were radiometrically and geometrically corrected according to the methods described in Chapter Three. The GER MK IV IRIS obtains a complete spectrum between 0.4μm-2.5μm from samples in the field or laboratory. The specifications of this instrument are given in Milton and Rollins, (1987).

The geologic information present in the NS-001 data was enhanced us-

ing a variety of image processing techniques, including compositing, channel ratios, log residuals, least squares fitting residuals (LRES) and directed principal components (DPC). These techniques enable the data to be interpeted in terms of reflectance. This permits comparison of the remotely sensed data with reflectance spectra obtained by the IRIS. The log residuals and LRES techniques were developed at CSIRO, Sydney, Australia and were not available in the U.K. Therefore, it was necessary to write and implement software to calculate these at Durham University in order to evaluate the various techniques. This differs from previous approaches in the U.K. in which the processing techniques used were selected on the basis of whether they were installed at a given site rather than whether a different technique had been developed which if installed could significantly improve data interpretation. The computer programme to calculate log residuals has been passed on to the British Geological Survey at Keyworth, Nottingham and should now be available to other U. K. users. To the best of the authors knowledge the software to calculate LRES is only available at Durham University and CSIRO in Australia. Software to calculate the remaining image processing techniques is avialable as standard on many image processing systems and is made available to the British Geological Survey by NERC.

Colour compositing and channel ratios have been successfully used for lithological mapping and mineral exploration in semi-arid, sparsely vegetated terrain with limited weathering (eg Abrams et al., 1983; Taylor and Loughlin 1985). The remaining techniques have been successfully used for similar geological studies in weathered vegetated terrain (Fraser et al., 1986; Fraser and Green 1987; Hook and Munday 1988a). The relative merits of these techniques are assessed in order to determine which is/are most effective at enhancing the geological information in NS-001 data in this terrain.

In order to fully evaluate the information obtained using these techniques, two test sites, each 512 x 512 pixels in size were selected from the NS-001 data. The two test sites chosen were centered on Camp Oven Mountain in the NE of flighline 1 and Plateau in the SW of flightline 2 (Figure 2.2). The lithologies, cover types and weathering history of these test sites is typical of much of NE Queensland. Therefore, the results from the study of these test sites should be widely applicable to other areas.

Initially, the physical basis for remote sensing of rocks, soils and vegetation in the 0.4μm-2.5μm region is reviewed. This provides an outline of the potential information available in this wavelength region for lithological mapping and mineral exploration.

This review is followed by the results from the analysis and interpetation of the NS-001 data covering the Camp Oven test site using the five techniques (compositing, channel ratios, log residuals, LRES and DPC). The geology of this site is described prior to the presentation of these results. Where appropriate, the methodology behind each technique is also given. The interpretations of the NS-001 data were assessed through comparison with existing maps and field checking. Field checking/mapping was undertaken for six weeks from October to mid November in 1985 and three months from August to October in 1987. Laboratory spectra from samples collected during field checking are then presented and interpreted. These data were checked by thin section analysis and X-Ray Diffraction. They provide an indication of the additional information which should be available from new sensors which have a greater number of channels in this wavelength region such as the Airborne Imaging Spectrometer (AIS), Goetz and Srivastava, (1985); and GER II Airborne Scanner, Huntington, (1988).

This is followed by the results from the analysis and interpretation of the NS-001 data at the Plateau test site for lithological mapping and mineral exploration. The NS-001 data from Plateau were analysed using the techniques which were found to be most effective in the study at the Camp Oven test site.

Finally, the conclusions from the study at both sites are presented together with a brief summary.

4.2 Physical Basis for Remote Sensing in the 0.4μm-2.5μm Wavelength Region

4.2.1 Rocks, Minerals and Soils

Rocks are assemblages of minerals so the spectrum of a rock is a composite of the constituent mineral spectra. Similarly, the spectra of soils consist of a composite of mineral spectra. However, these also contain organic material and water which contribute to the resultant spectrum. The largest collection of rock mineral and soil spectra in the 3.5μm-2.5μm region is available from a series of papers presented by Hunt and his co-workers at the Air Force Cambridge Research Laboratories between 1963 and 1975 (Hunt and Salisbury 1970; 1971a,b,c; Hunt *et al.*, 1971a,b; 1972; 1973a,b; 1974a,b; Hunt 1977; Hunt and Ashley 1979).

The features in mineral spectra in the region from 0.4μm-1.0μm are determined by the presence or absence of transition metals (Goetz *et al.*, 1983). These produce either charge transfer bands or electronic transitions. (Hunt, 1980). Charge transfer bands result from the exchange of electrons between neighbouring metal ions and create absorptions in the region below 0.4μm (Goetz *et al.*, 1983). The wings of these absorptions extend into the visible part of the spectrum and produce a falloff in reflectance toward shorter wavelengths in rocks, soils and minerals (Figure 4.1).

Electronic transitions result from changes in the energy level in the d-shell electrons within the crystal field of the mineral, producing absorptions similar to those in the iron bearing rock or soil spectrum in Figure 4.1 (Hunt, 1977).

In naturally occurring geologic materials iron is the most common transition metal. Figure 4.2 illustrates the spectra of a variety of iron-bearing minerals. Electronic transitions involving the ferric ion typically produce three absorption bands. The first occurs between 0.75μm and 0.95μm; the second occurs between 0.55μm and 0.65μm(usually as a shoulder) and a third occurs near 0.45μm (Hunt and Ashley 1979). The last feature is rarely observed due to the effect of the charge transfer bands which cause the rapid falloff in reflectance to shorter wavelengths. Variations in the position of the 0.75μm-0.95μm absorption has been successfully used to dicriminate between haematite and goethite (Fraser *et al.*, 1985).

Spectral features in the region between 1.0μm and 2.5μm are principlely the result of molecular vibrational processes (Goetz *et al.*, 1983). These produce absorption features which are diagnostic of the composition of minerals. The fundamental vibrational modes of silicon and oxygen occur near 10μm (Hunt, 1980). In the SWIR features are due to overtones and combinations involving these very high fundamental frequencies (Hunt, 1980). The most common of these involves the strong fundamental OH vibration which occurs at 2.74μm and influences the behaviour of hydroxyl bearing minerals (Goetz *et al.*, 1983). The first overtone vibration produces a feature at 1.4μm. This feature is common in the spectra of terrestial materials. The fundamental OH stretching mode may combine with the X-OH bending modes where X is Al or Mg to produce features near 2.2μm and 2.35μm respectively (Hunt, 1980). These combinations are particularly diagnostic of hydrous minerals (Figure 4.3). In addition similar features involving carbon and oxygen produce five other features at 1.9μm, 2.0μm, 2.16μm, 2.35μm and 2.55μm (Hunt, 1980).

Overtone and combinations involving the liquid water molecule occur around 1.4μm and 1.9μm (Hunt 1980). The presence of both these bands is completely diagnostic of molecular water in the sample (Hunt 1980).

Absorptions in the 1.4μm and 1.9μm region coincide with those due to atmospheric water inhibiting the use of this region with remotely sensed data for mineralogical identification.

The maximum reflectance of most rocks occurs around 1.6μm, midway between the ultraviolet-visible charge transfer bands and strong OH vibration at 2.74μm (Goetz and Rowan 1981). In particular, rocks altered by hydrothermal fluids and rich in iron oxide and hydrous minerals have a pronounced peak in reflectance at 1.6μm. This may account for more than 70% of the overall reflectance in the 0.4μm-2.5μm region (Rowan *et al.*, 1977).

The grain size of a rock or soil also affects the depth of any absorption features. In general, for opaque materials, the smaller the particle size the smaller are any absorption features (Hunt, 1980).

4.2.2 Vegetation

The spectral properties of vegetation in the VNIR and SWIR are best illustrated by examining the spectral reflectance curve of a leaf (Figure 4.4). Its spectral properties in the VNIR-SWIR region are a function of leaf pigments (primarily the chlorophylls), the cell morphology, internal refractive index discontinuities and water content (Raines and Canney 1980). Pigments of the chlorophyll group control the spectral properties between 0.4 and $0.7\mu m$, the cell morphology and internal refractive index discontinuities are the primary controls from $0.7\mu m$ to $1.3\mu m$ and water content is the principle control in the 1.3 to $2.5\mu m$ region.

The absorptions at $0.45\mu m$ and $0.68\mu m$ relate to the presence of chlorophyll a and b, but are widened by the presence of other pigments. The weak reflectance between $0.52\mu m$ and $0.60\mu m$ accounts for the green appearance of plants to the human eye. The high reflectance region from $0.7\mu m$ to $1.3\mu m$ is due to the refractive index discontinuities within the leaf. The principle discontinuity is the internal air-cell interfaces of the leaf.(Gates *et al.*, 1965). The sharp rise in reflectance between the $0.68\mu m$ feature and the near infrared plateau is usually referred to as the red edge (Horler *et al.*, 1983). In the region from $1.3\mu m$ to $2.5\mu m$ the spectral reflectance curve of a healthy leaf is the same as an equivalent thickness of pure water (Raines and Canney 1980). If the vegetation is dead and dry absorptions occur at $2.09\mu m$, $2.36\mu m$ and $2.9\mu m$ relating to the presence of ligno-cellulose (Elvidge, 1988).

4.3 Analysis and Interpretation of Data from the $0.4\mu m$-$2.5\mu m$ Wavelength Region over the Camp Oven Test Site for Lithological Mapping and Mineral Exploration

The Camp Oven test site is 512 x 512 pixels in size and located in the NE of the study area (Figure 2.2). The site was selected on the basis that it was typical of the geology, vegetation and weathering history encountered in much of NE Queensland.

The data from the $0.4\mu m$-$2.5\mu m$ wavelength region were acquired by the NS-001 sensor and the GER MK IV IRIS. Data from this wavelength region can be used to identify different iron oxide and Al-OH ± Mg-OH ± CO bear-

ing minerals (see section 4.2). The NS-001 sensor acquires seven discrete channels of data between 0.45μm and 2.35μm. The large wavelength range of each channel means these data can only be used to determine the presence of, rather than identify the diagnostic absorption features of iron oxides and/or Al-OH $\pm$ Mg-OH $\pm$ CO bearing minerals. The FeO and Al-OH $\pm$ Mg-OH $\pm$ CO bearing minerals are rarely the primary rock forming minerals but are produced through alteration. An altered rock is one which has undergone changes in its chemical and mineralogical structure since formation. The amount and type of alteration minerals is dependant, in part, on the primary mineralogy of the rock and in certain cases can be used to infer the original composition of that rock. Alteration may occur through weathering or by hydrothermal alteration. The latter is due to the interaction of aqueous solutions heated by magma, hydrothermal fluids or solutions. These same hydrothermal solutions are often rich in precious metals which, if deposited, can result in the formation of an ore deposit. Hydrothermal alteration typically produces greater abundances of these minerals together with certain Al-OH $\pm$ Mg-OH $\pm$ CO bearing minerals which cannot be produced by weathering. Therefore, whilst small differences in the quantity of these minerals, often due to weathering, can be used for lithological discrimination, intensely altered areas are excellent targets for mineral exploration.

Initially the geology of the Camp Oven test site is described. This is followed by the methodology and results from the analysis and interpetation of the NS001 data using a variety of image processing techniques.

Finally, high resolution laboratory spectra obtained from the 0.4μm-2.5μm wavelength range are presented and interpreted from samples collected from this test site. These were aquired by the GER MK IV IRIS. They permit identification of any iron oxide and/or Al-OH $\pm$ Mg-OH $\pm$ CO bearing minerals present. These results provide an indication of the possible discrimination and identification using airborne instruments with a similar high spectral resolution.

4.3.1 Geology of the Camp Oven Test Site

The following geological description of the Camp Oven Test Site is based on the work of Lorraway (1976) and field mapping by the author in 1985 and 1987.

The Ravenswood Granodiorite Complex forms the basement at this test site and is of Mid-Ordovician to Lower Devonian age (Figure 4.5). Two phases of the complex are present: the main granodioritic phase and later granitic phase (Figure 4.5). The granodioritic phase consists of a medium grained hornblende biotite granodiorite. The granitic phase consists of pink and red biotite granite and microgranite termed quartz feldspar in Figure 4.5.

The basement is overlain in places by a red micaceous mudstone and grey shale of Lower Carboniferous age (Figure 4.5). The mudstone is dominant with the largest outcrop, approximately 1km wide, being centered on the eastern part of the central depression of the Camp Oven Complex (Figure 4.5). The mudstone is often highy brecciated as a result of the subsequent intrusion of the Upper Carboniferous Camp Oven Complex.

The Camp Oven Complex consists of intrusive rhyolites and extrusive volcanic rocks, pyroclastics and breccias (Figure 4.5). Three areas of intrusive rhyolitic rock have been mapped. These are Blackfellow Mountain, K2 and a ridge to the west of K2 (Figure 4.6).

The extrusive rocks comprise lavas, pyroclastic ignimbrites and volcanic breccias. The lavas consist of andesite, dacite and possibly rhyolite. The andesite lavas have been separated into two main types. The first type are only found in the south and termed the andesite lavas of the south (Lorraway, 1976). They are dark green in colour medium grained, porphyritic and contain numerous inclusions. The second type are found in the south and other areas. They are grey in colour and often contain phenocrysts of plagioclase, clinopyroxene and hornblende. They are often found interbedded with the volcanic breccias and dacite lavas. The dacite lavas have also been separated into two types. First, pink dacite which may be of rhyolitic composition. The pink dacites are porphyritic and have phenocrysts of plagiclase and alkali feldspar and quartz set in a fine feldspar-quartz matrix. Secondly, grey dacite, coarser than the pink dacite with numerous large phenocrysts of plagioclase and some quartz.

The pyroclastic rocks consist of ignimbrites and volcanic breccias. The ignimbrites appear to be the most voluminous rocks in the area. They consist of fragmented phenocrysts of plagiocalse and alkali feldspar, biotite, quartz and flattened pumice in a fine grained matrix. The rock is hard and resistant to weathering forming the prominent elliptical ridge system. The ignimbrites are predominantly rhyolitic in composition, however, there is great variation in both composition and texture.

The volcanic breccias are also voluminous. They too show great variation in fragment size, shape, texture and composition and matrix colour and composition.

4.3.2 Radiometrically Corrected Data

Plate 4.1 is a colour infrared composite of the Camp Oven test site with the channels centered upon 0.83μm, 0.66μm and 0.56μm displayed as red green and blue respectively. Henceforth, the channels are referred to according to their centre wavelength (for example, the 0.83μm channel). In general, the red areas relate to vegetation, the green areas to iron oxide and the yellow areas to mixtures of vegetation and iron oxides. The differences in reflectance of iron oxide bearing rock or soil and vegetation in the wavelength regions covered by these channels is illustrated in Figure 4.1. The cause for these differences is given in Section 4.2.

The aim now is to examine the relative changes in radiance from a variety of rock types within the test site to establish if these differences, related to the amount of iron oxide and Al-OH $\pm$ Mg-OH $\pm$ CO bearing minerals are sufficient for lithological discrimination.

Sixteen subsites were chosen from the Camp Oven test site covering a variety of rock types, soils and vegetation. These subsites were selected to represent the typical cover types encountered at this test site and throughout NE Queensland. The location of these subsites within the Camp Oven test site are given in Figure 4.6. All subsites were ten pixels in size except for subsite Q which was five pixels in size. The subsites were selected during fieldwork on the basis that they were homogenous and contained little vegetation.

The variation in radiance at each of these subsites was examined by plotting pixel spectra. These pixel spectra were produced by taking the average of a group of pixels at each subsite, in each channel, and plotting these val-

ues against the wavelength of each channel. These pixel spectra enable the data from all seven channels to be interpreted simultaneously. Plate 4.1 had been produced by rescaling each band individually to utilize the full 0-255 dynamic range of the image processing system. The system used was an I^2S with a Model 75 processor and system 500 software. Rescaling in this manner inhibits the examination of the relative changes in radiance between each of the channels. Therefore, the pixel spectra were produced from the data prior to rescaling for display.

Figures 4.7 and 4.8 show the pixel spectra derived from subsites A and B respectively. Both subsites had been mapped as granite (Lorraway 1976). However, field mapping by the author identified the latter as an area of siliceous breccias. The two spectra appear identical yet both areas are easily separated in the colour infrared composite (Plate 4.1). This discrepency results from the pixel radiance spectra being dominated by the solar irradiance curve and absorption features which subdue subtle variations in reflectance due to different mineralogies. These features are not apparent in the image data since each channel has been rescaled independantly.

Several techniques have been used to remove the effects of the solar irradiance curve and atmospheric absorptions. These include channel ratios, calibration using field spectral measurements, flat field correction, logarithmic (log) residuals, least upper bound residuals (Green and Craig 1985) and Principal Components Analysis (PCA). The channel ratioing technique has been described in section 3.6.1 and results from this technique are presented after this discussion.

Calibration using field spectral measurements requires that such measurements are taken over a variety of cover types along each flightline at approximately the same time as data aquisition (Roberts *et al.*, 1985). Such measurements were not obtained for this study so this approach could not be utilized. The remaining techniques are all laboratory based and do not require field measurements.

Flat field correction assumes a cover type is spectrally flat in the wavelength region of interest. Therefore, any variations in the spectrum obtained by the remotely sensed data result from the effects of the solar irradiance curve and atmospheric absorptions. The rest of the pixels in the scene are divided

into the 'flat field' to remove these effects. This approach obviously assumes these effects operate on the data in a multiplicative manner. Quartzite is spectrally flat in this wavelength region and commonly used for flat field correction. Unfortunately, no areas of quartzite outcropped in the area covered by the Camp Oven test site or any other cover type which was spectrally flat. If an alternative cover type had been used which was not spectrally flat, artifacts would have been introduced into the data relating to that cover type.

The least upper bound residual and log residual techniques normalise the data using a modelled relationship between topography, wavelength and radiance to calculate reflectance (Green and Craig, 1985). The least upper bound residual uses a maximum spectrum in the modelled relationship. The log residual replaces the maximum spectrum with an average spectrum. Roberts *et al.*, (1985) found the log residual technique to be the most effective of the flat field, least upper bound residual and log residual techniques for removing these effects on the basis the technique introduced the least artifacts and noise into the data.

PCA has also been used to remove atmospheric effects. This approach assumes that the atmospheric effects are highly correlated between channels and are therefore contained in the first principal component. The remaining principal components contain the information relating to differences in reflectance. However, after transformation the data are extremely difficult to interpret in terms of reflectance limiting the usefulness of this approach for mapping variation in the amount of iron oxides or Al-OH $\pm$ Mg-OH $\pm$ CO bearing minerals as a means of lithological discrimination.

Therefore, log residuals and band ratios were calculated from the data in order to suppress the effects of the solar irradiance curve and atmospheric absorptions to enable mapping of variations in iron oxide and/or Al-OH $\pm$ Mg-OH $\pm$ CO bearing minerals for lithological mapping and mineral exploration. The log residual results are presented after interpretation of the channel ratio data.

4.3.3 Channel Ratio Data

The wavelength range between $0.45\mu m$ and $2.35\mu m$ has been shown to contain information relating to the presence of FeO, Al-OH, CO and Mg-OH bearing minerals (see section 4.2).

Radiance data acquired in this wavelength region by the NS-001 sensor are dominated by the solar irradiance curve and atmospheric absorptions which mask subtle differences due to variations in mineralogy (see section 4.3.1). Channel ratios remove these effects thereby enhancing these subtle mineralogical variations (see section 3.6.1).

Numerous studies have successfully demonstrated the use of channel ratioing as a means of enhancing variations due to these alteration minerals for both lithological mapping and mineral exploration (eg Rowan *et al.*, 1974; Goetz, 1981; Abrams, 1983,1984; Taylor and Loughlin, 1988). However, the majority of these studies have been undertaken in semi-arid terrains with a sparse vegetation cover and limited surface weathering. Far fewer studies have successfully demonstrated the use of channel ratioing for similar purposes in deeply weathered vegetated terrain (Segal, 1983).

The aim of this part of the study is to assess channel ratioing as a means for enhancing subtle differences in FeO and Al-OH $\pm$ Mg-OH $\pm$ CO bearing minerals for lithological mapping and mineral exploration in this deeply weathered vegetated terrain. These results will be compared with those obtained using other image processing techniques for similar purposes to determine which technique or combination of techniques are most useful for geologic studies in this terrain

The ratios typically chosen with NS-001 data to enhance areas of iron oxides and Al-OH $\pm$ Mg-OH $\pm$ CO bearing minerals are the $0.66\mu m/0.56\mu m$, $1.65\mu m/2.2\mu m$ and $0.83\mu m/1.65\mu m$. Areas rich in iron oxides have high values in the $0.66\mu m/0.56\mu m$ ratio. This results from iron oxide minerals having a reflectance maxima around $0.66\mu m$, in the red part of the spectrum, and strongly absorbing around $0.56\mu m$ in the green part of the spectrum (Hunt *et al.*, 1971). Areas rich in Al-OH $\pm$ Mg-OH $\pm$ CO bearing minerals have high values in the $1.65\mu m/2.2\mu m$ ratio. This is due to these minerals having a reflectance maxima around $1.65\mu m$ and strongly absorbing around $2.2\mu m$ (Hunt and Ashley 1979). The $1.65\mu m/2.2\mu m$ ratio is typically displayed in red, the $0.66\mu m/0.56\mu m$ ratio in green and the $0.83\mu m/1.65\mu m$ ratio in blue (Abrams 1977). This combination results in areas rich in Al-OH $\pm$ Mg-OH $\pm$ CO bearing minerals appearing red, areas rich in iron oxides appearing green, and areas rich in both these appearing yellow.

Plate 4.2 has been produced using this colour-ratio combination. The area mapped as granodiorite appears green with occasional red patches south of Camp Oven Mountain (Figure 4.6; Plate 4.2). This is due to a deep iron oxide rich red sandy soil which typically develops over the granodiorite. The iron oxide is produced through weathering of the mafic minerals in the granodiorite. Thin section analysis of samples from the granodiorite revealed hornblende and biotite were typically altering to iron oxides. The red patches south of Camp Oven Mountain suggest these areas are particularly abundant in Al-OH ± Mg-OH ± CO bearing minerals. The granodiorite has been subject to hydrothermal alteration which would produce these minerals. These include chlorite, epidote and calcite (Wyatt *et al.*, 1971). However, field mapping showed that these areas did not contain anomalous levels of these minerals compared with the surrounding terrain, rather, they had a dense grass cover. which is not apparent in the ratio image. Vegetation also has high values in the $1.65 \mu m/2.2 \mu m$ ratio. This is due to the reflectance in the numerator ratio being far greater than in the denominator ratio (Figure 4.1). Vegetation was particularly dense in the area north of the fenceline labelled A (Plate 4.2). The fencing had stopped the area being heavily grazed by cattle. Clearly, using this ratio to map areas of Al-OH ± Mg-OH ± CO bearing minerals in vegetated terrain can cause considerable confusion.

The late granitic phase of the Ravenswood Granodiorite east of Pinnacle Creek appears blue (Figure 4.6, Plate 4.2). This infers the area was not particularly rich in either iron oxide or Al-OH ± Mg-OH ± CO bearing minerals. This was confirmed by field mapping. The granites did have a red appearance due to their high orthoclase content. The reduced mafic mineral content of the granites compared with the granodiorite accounts for the absence of a iron oxide rich sandy soil over this unit.

The sediments in the centre of Camp Oven Mountain also appear green (Figure 4.6, Plate 4.2). This suggests they are rich in iron oxide minerals. Field mapping confirmed the presence of an iron oxide rich sandy soil developing on ferruginous micaceous sandstones. These sediments are rich in mica and therefore a high $1.65sm/2.2 \mu m$ ratio was expected. This was not the case and can be explained if the surrounding area was also rich in mica which would result in both areas having similar ratio values. The presence of mica

throughout the area resulting from weathering was noted during fieldwork.

The majority of the Upper Carboniferous volcanics of the Camp Oven Complex appear blue (Figure 4.6, Plate 4.2). This infers they are not particularly rich in either iron oxide or Al-OH ± Mg-OH ± CO bearing minerals. This was again corroborated by field mapping which established these were relatively 'fresh' compared with the surrounding terrain. It was not possible to discriminate most of the units that make up these Upper Carboniferous volcanics (Figure 4.6). This resulted from the lack of any variations in iron oxides or Al-OH ± Mg-OH ± CO bearing minerals in these units. Three areas could be discriminated within the Upper Carboniferous volcanics which all appear red suggesting they contain Al-OH ± Mg-OH ± CO bearing minerals. These correspond to Blackfellow Mountain, K2 and the ridge west of K2, all of which have been mapped by Lorraway (1976) as rhyolitic intrusives (Figure 4.6, Plate 4.2). Fieldwork identified both K2 and Blackfellow Mountain as being altered, the ridge to the west of K2 was not altered. The ridge was in fact greywacke which was not particularly rich in Al-OH ± Mg-OH ± CO bearing minerals but had a dense vegetation cover and therefore high $1.65\mu m/2.2\mu m$ ratio value (see earlier discussion). The alteration at K2 was of a silicic nature. It did contain sericite, an Al-OH bearing mineral. However, high resolution laboratory spectra collected from other unaltered subsites had similar amounts of sericite produced through weathering (see section 4.3.7). The area did have a dense vegetation cover which helps to explain the high values in the ratio imagery (see earlier discussion). Field mapping identified the third area at Blackfellow Mountain as the result of advanced argillic alteration. It was extremely rich in Al-OH ± Mg-OH ± CO bearing minerals sufficient to explain its high $1.65\mu m/2.2\mu m$ ratio values. However, its high ratio value could be due to the dense vegetation cover on the top of the mountain. There was an apron of scree which surrounded Blackfellow Mountain which was largely devoid of vegetation. This apron appears yellow infering it is particularly rich in iron oxides and Al-OH ± Mg-OH ± CO bearing minerals (Plate 4.2). The discovery of this area of advanced argillic alteration is particularly important for mineral exploration for the reasons stated at the beginning of this section. The results from the analysis of samples collected from this area by laboratory spectrometry and X-Ray Diffraction analysis and

their significance for mineralisation are discussed in detail in Chapter Six

In summary, these results suggest the ratio data are useful for mapping areas of iron oxide but areas of Al-OH $\pm$ Mg-OH $\pm$ CO bearing minerals are easily confused with vegetated areas. One possible solution to this problem is the use of vegetation masks to separate Al-OH $\pm$ Mg-OH $\pm$ CO bearing minerals from vegetation. A vegetation mask is produced using a ratio in which the vegetated areas are easily distinguished from the rest of the scene. The ratio used for this purpose is the infrared/red ratio (0.83μm/0.66μm). Vegetated areas will have high values in this ratio due to the strong rise in reflectance starting around 0.68μm due to refractive index discontinuites within the leaf (Raines and Canney 1980; Figure 4.1). An arbitary threshold is determined in the ratio above which areas are considered vegetated. The vegetated pixels are set to zero and the non vegetated pixels are set to one (Plate 4.3). This binary image is multiplied by the 1.65μm/2.2μm ratio to produce an image in which the vegetated areas are set to zero and the non-vegetated areas keep their original 1.65μm/2.2μm ratio value.

Plate 4.3 is the vegetation mask for the Camp Oven test site. The tops of Blackfellow Mountain, K2 and the ridge west of K2 are clearly apparent as dark (zero) values in this image inferring they are vegetated (Plate 4.3). The river channels also appear dark due to the dense vegetation along their banks (Plate 4.3). The area north of the fenceline (labelled A) in the colour ratio composite, which has a red appearance attributed to vegetation does not appear dark in the vegetation mask as would be expected (Plates 4.2 and 4.3). This is due to the arbitary threshold in the vegetation mask being set too high to include areas which are mixtures of other materials such as soil and vegetation. This illustrates a major problem with the masking technique. That is, areas which are mixtures of vegetation and other materials are not separated into those areas which are mixtures of vegetation and Al-OH $\pm$ Mg-OH $\pm$ CO bearing minerals. Using this technqiue both areas would be classed as vegetated or non-vegetated depending where the arbitary threshold was set. What it needed is to be able to separate mixtures of vegetation and other materials from mixtures of vegetation and Al-OH $\pm$ Mg-OH $\pm$ CO bearing minerals in order to produce a map of the latter.

An alternative technique for removing the effects of the solar irradiance

curve and atmospheric absorptions is log residuals (Green and Craig 1985). This technique is considered the most effective of the other laboratory based methods for the reasons discussed previously. The technique has the additional advantage over the ratio method that the resultant data can be interpreted in terms of pseudo reflectance. This means the change in shape of the log residual pixel curves can be related to changes in the shape of laboratory reflectance curves. This represents a considerable improvement over the ratioing technique where a change in a ratio can result from a change in the numerator channel, the denominator channel or both. This should result in less confusion between areas of vegetation and Al-OH ± Mg-OH ± CO bearing minerals which should have different shaped pixel spectra.

4.3.4   Log Residual Data

Laboratory studies have demonstrated that the wavelength region between $0.45\mu m$ and $2.35\mu m$ contains information relating to the presence of iron oxides and Al-OH ± Mg-OH ± CO bearing minerals (see section 4.2). Remotely sensed data from this wavelength region acquired by the NS-001 are dominated by the solar irradiance curve and atmospheric effects which mask any changes relating to mineralogy (see section 4.3.2). These effects can be reduced by channel ratioing. However, the resultant data can be difficult to interpret (see section 4.3.3).

The log residual technique provides an alternative method for removing these effects and also brightness differences associated with topography using a modelled relationship (Green and Craig 1985). In addition, the resultant data can be interpreted in terms of pseudo-reflectance. There are other laboratory based techniques designed to remove these effects including flat field correction and least upper bound residuals. Of these the log residual technique proved by effective and introduced the least number of artifacts and noise into the data compared with the other techniques (Roberts et al., 1986). However, the log residual technique has proved most effective on the basis of the number of artifacts and noise introduced into the data (Roberts et al., 1986). It should be noted that the most effective way of removing these effects involves the use of field measurements obtained at time and place of sensing (Roberts et al., 1985). Such data were not available to this study so log residuals was considered the most effective alternative method.

The aim of this aspect of the study is to evaluate the log residual data as a means for enhancing subtle variations in iron oxides and/or Al-OH $\pm$ Mg-OH $\pm$ CO bearing minerals as an aid for lithological mapping and mineral exploration. These results can then be compared with those obtained using other techniques to determine the most effective techniques for such geologic studies in weathered vegetated terrain. Prior to the evaluation of the log residual data the method is described and compared with a similar scene averaging method described by Conel (1986).

The log residual technique was developed by Green and Craig (1985) in order to remove the effects of solar illumination and brightness differences due to topography using scene parameters.

The technique uses a simple model to relate the radiance measurement $X_{i\lambda}$ to the reflectance $R_{i\lambda}$ in sample i, wavelength λ, by means of a multiplicative formula:

$$X_{i\lambda} = T_i R_{i\lambda} I_\lambda \qquad 4.1$$

The topographic factor (T_i) is constant for all wavelengths and accounts for brightness variations between pixels. The illumination factor (I_λ) is constant for a given wavelength and accounts for the effect of the solar illumination curve. The aim now is to remove both of these terms and get at the reflectance $R_{i\lambda}$

If $X_{i\bullet}$ is equal to the mean of $X_{i\lambda}$ over all wavelengths (λ). Using a similar notation for the other symbols in equation 4.1 we obtain:

$$X_{i\bullet} = T_i R_{i\bullet} I_\bullet \qquad 4.2$$

division of equation 4.2 into equation 4.1 results in:

$$\frac{X_{i\lambda}}{X_{i\bullet}} = \frac{R_{i\lambda}}{R_{i\bullet}} \frac{I_\lambda}{I_\bullet} \qquad 4.3$$

Thus, we have now removed the effect of topography and the resultant spectra are topographically (or albedo) equalized. In order to remove the illumination factor I_λ we first take the mean over all samples for a given wavelength of equation 4.3:

$$\frac{X_{\bullet\lambda}}{X_{\bullet\bullet}} = \frac{R_{\bullet\lambda}}{R_{\bullet\bullet}} \frac{I_\lambda}{I_\bullet} \qquad 4.4$$

Then by division

$$\frac{X_{i\lambda}}{X_{i\bullet}} \bigg/ \frac{X_{\bullet\lambda}}{X_{\bullet\bullet}} = \frac{R_{i\lambda}}{R_{i\bullet}} \bigg/ \frac{R_{\bullet\lambda}}{R_{\bullet\bullet}} \qquad\qquad 4.5$$

Thus from the original radiance spectra $X_{i\lambda}$ a new set of spectra have been calculated without the effect of topography or the solar illumination curve. The means are computed from the arithmetic means of the logarithms and are therefore geometric means. The logarithmic residuals calculation can written as:

$$log(R_{i\lambda}) = log(X_{i\lambda}) - log(T_i) - log(I_\lambda) \qquad\qquad 4.6$$

where:

$log(X_{i\lambda})$ = The log of the digital number value for sample (i) at wavelength (λ).

$log(T_i)$ = The average of the logs of sample (i) for all wavelengths (one value per channel).

$log(I_\lambda)$ = The average of the logs of all samples for a given wavelength (λ) (one value per channel).

Roberts *et al.*, (1985), add a fourth value, the average of the logs of all samples at all wavelengths (one value per image). This is used to standardize each processed flight. This increases the log residual values so they centre around zero. The log residuals calculated in this study included this fourth value in order to standardize each flightline.

Conel *et al.*, (1987) use a similar method to compensate for the atmospheric effect, which they refer to as the residual or scene average method. The radiance observed by the aircraft mounted sensor is written as:

$$L(x, y, \tau - \tau') = P(x, y, \tau - \tau') + T(x, y, \tau - \tau')R(x, y) \qquad\qquad 4.7$$

where:

(x, y) = coordinates of a particular point within the image.

$(\tau - \tau')$ = total optical depth of the atmosphere minus the optical depth of the observation measured from the top downward.

P = path radiance, and represents the sunlight that is directly or diffusely transmitted by the upper part of the atmosphere (above the depth of observation) and that is reflected upward by the lower part of the atmosphere (below the depth of the observation).

T = Directly and diffusely transmitted upwelling surface radiation.

R = Surface reflectance that is assumed Lambertian.

It is further assumed that the data are in radiance units (calibrated) and the path radiance term is negligable so:

$$L(x, y, \tau - \tau') = T(x, y, \tau - \tau')R(x, y) \qquad 4.8$$

For a homogenous atmosphere, constant elevation of terrain above sea level, constant observation elevation and aircraft attitude it is justified to assume $T(x, y, \tau - \tau') = \langle T(\tau - \tau') \rangle$, a constant independant of position. A simple method for estimating $\langle T(\tau - \tau') \rangle$ is to calculate the averages of the radiance $L(x, y)$ over the image resulting in:

$$\langle L \rangle = \langle T \rangle \langle R \rangle \qquad 4.9$$

where: $\langle L \rangle = (1/area) \int \int L(x, y) dx dy$ etc.

Applying this equation to equation 4.8 particularised for a constant transmittance $\langle T \rangle$ yields:

$$L(x, y) = \frac{\langle L \rangle}{\langle R \rangle} R(x, y) \qquad 4.10$$

where:

$\frac{R(x,y)}{\langle R \rangle}$ = scaled reflectance based on image derived quantities.

This is similar to the illumination correction in logarithmic residuals except this method does not use logarithms and geometric means.

The application of this approach requires that $\langle R \rangle$ is not dependant on wavelength. However, if the terrain is homogenous $\langle R \rangle$ is dependant on wavelength. Under these conditions $R(x, y)/\langle R \rangle$ approaches unity. In the the case of log residuals if the illumination factor (I_λ) is equal to the value of a pixel the difference between the two logarithms will equal zero. Any variations present will reflect variations in the atmospheric transmittance for a given pixel and not the surface reflectance. Furthermore, if there is a dominant component within a scene this component will be effectively removed from the scene since it will equal $\langle L \rangle$ or I_λ depending on the method. Conel *et al.*, (1987), stress that the logarithmic residual or as they have used the scene average technique 'proved powerless' in a homogenous terrain. This point is also made by Green and Craig (1985).

Plates 4.4-4.10 are the log residual images for the channels centered on 0.48μm, 0.66μm, 0.83μm, 1.13μm, 1.65μm and 2.2μm respectively, over the Camp Oven test site. Each channel is henceforth referred to according to its centre wavelength (eg. the 0.48μm channel). Table 1.1 gives the wavelength range of each channel. Each of the log residual images has a 'flat' appearance, as expected since the effects of topography are removed as part of the log residual calculation (Plates 4.4-4.10, equation 4.3).

Plate 4.11 is an image produced from the mean of the logs of the radiance of each pixel at all wavelengths (one value per pixel). This corresponds to the topographic factor (Ti) in equation 4.6, and accounts for topographic/ albedo variations. Examination of this image shows that most of the variation contained therein does correspond to topography (Plate 4.11). Plate 4.12 is a colour composite image produced using the 0.83μm, 0.66μm and 0.56μm log residual channels displayed as red, green and blue respectively. In general, green areas correspond to areas of iron oxide, red areas to vegetation and blue areas to bare rock/soil with little iron oxide or vegetation. If desired the topographic image can be added back into each channel (Plate 4.13). This produces an image similar to the radiance colour infrared composite produced using these channels except the reflectance information has now been preferentially enhanced (Plates 4.1 and 4.13).

These images are useful for visual interpetation. However, the principle advantage of using the log residual technique is the ability to examine the relative differences between channels in pixel spectra and relate these to reflectance spectra obtained from laboratory studies.

Plates 4.4-4.13 were produced by rescaling each channel independantly to utilize the full 0-255 range of the image display system. This inhibits examination of changes in the log residual spectrum and therefore the log residual spectra presented subsequently were produced from the data prior to rescaling for display.

Figure 4.9 illustrates the log residual spectra from subsites A-D. The location of these subsites are given in Figure 4.6. Clearly, these spectra do not resemble the laboratory spectra (Figure 4.1). However, they can be interpreted in terms of reflectance, and the methodology enabling this is now discussed.

If we take a solar irradiance curve (Figure 4.10a) and assume a target with 100% reflectance at all wavelengths (Figure 4.10b). Then the radiance curve (Figure 4.10c) will be the same as the solar irradiance curve. The resultant log residual spectrum will be a horizontal line intersecting the Y axis at zero (Figure 4.10d).

If the surface is not a perfect reflector, say the reflectance between 2.0 and 2.4μm is zero (Figure 4.11x). Then the radiance curve will be identical to the solar irradiance curve except that their will be no radiance in the 2.0-2.4μm region (Figure 4.11y). The log residual spectrum will be a horizontal line intersecting the Y axis at zero for the wavelength range 0.4-2.0μm. Between 2.0μmand 2.4μm the spectrum will drop below zero by an amount equal to the difference between the solar irradiance curve and the radiance curve (Figure 4.11z).

The illumination factors for each wavelength interval in equation 4.6 can be equated to the solar irradiance curve. These are calculated from the means of the logs of the radiance of all pixels in a given channel. The resultant log residual spectra will have values greater than zero, in a given channel, when the pixel radiance is greater than this channel mean. Values less than zero result when a pixel's radiance value, in a given channel, is less than this channel mean.

The illumination curve produced from the illumination factors calculated from equation 4.6 is also shown in Figure 4.9 with the log residual spectra from subsites A-D. The absolute value of this curve cannot be related to the log residual spectra since other values have been extracted as part of the log residual calculation (equation 4.6). However, the shape of this curve is different to the shape of the solar irradiance curve (Figure 4.10a). The maxima in the illumination curve occurs at longer wavelengths, around 1.1μm. This suggests the illumination curve is biased by a dominant component in the scene. The most likely candiate for this is vegetation, which commonly has its reflectance peak in this region (Figure 4.4).

If we re-examine the log residual spectrum from subsite A, there is a distinct maxima in the 0.66μm channel and minima in the 0.48μm and 1.15μm channels. (Figure 4.9). The maxima in the log residual spectrum in the 0.66μm channel suggests iron oxide is present, since this has a re-

flectance peak in the wavelength region covered by this channel relative to other materials including vegetation (Figure 4.1). The presence of iron also accounts for the negative minima in the $0.48\mu m$ channel where iron bearing minerals strongly absorb radiation due to the charge transfer bands (Hunt, 1980; Figure 4.1). The negative minima in the $1.13\mu m$ channel would result from the illumination curve being biased by vegetation which has a higher reflectance than rock or soil in the wavlength region covered by this channel (Figure 4.1). The negative value in the $1.65\mu m$ channel is more difficult to explain since green vegetation has a lower reflectance than rock/soil around this wavlength region (Figure 4.1). However, dry vegetation has a higher reflectance than rock or soil in this region (Fraser *et al.*, 1986). The vegetation in this scene was predominantly dry, the data being acquired at the end of the dry season. This may account for the low negative value in this channel.

The area covered by subsite A was mapped as granite (Wyatt *et al.*, 1971; Figure 4.6). Laboratory spectra measured from samples collected at this test site contained the spectral features characteristic of amorphous iron oxide and sericite (see section 4.3.7). The presence of iron oxide was inferred from the log residual spectrum but no Al-OH bearing minerals such as sericite were thought to be present. If sericite was present, the value of the illumination curve should have been greater than the area covered by the subsite in the $2.2\mu m$ channel due to absorption associated with Al-OH molecule. However, if the illumination curve was biased by small amounts of vegetation, as suggested, then the illumination curve would also have low values in this channel where vegetation has a low reflectance (Figure 4.1). Taking this bias into account, the log residual value around zero in the $2.2\mu m$ channel infers the presence of small amounts of Al-OH $\pm$ Mg-OH $\pm$ CO bearing minerals. .

The log residual spectrum for subsite B closely resembles that obtained from subsite A and is interpreted similarly (Figures 4.6 and 4.9). The main difference between the spectra is that the value in the $0.56\mu m$ channel is greater. This would suggest the area has a yellow appearance. This was confirmed by fieldwork, the area being identified as a siliceous breccia. Laboratory spectra from samples collected from this subsite contained spectral features which inferred the presence of iron oxides and sericite (see section 4.3.7). This concurs with the interpretation of the log residual spectrum from

this subsite.

The log residual spectrum from subsite C is similar to those from subsites A and B except the curve shape is far more exaggerated (Figures 4.6 and 4.9). The maxima in the 0.65μm channel is greater as is the value in the 0.56μm channel. The minima in the 1.13μm channel is also lower. The higher values in the 0.56μm and 0.65μm channels suggest the area is yellow in colour and brighter than the surrounding terrain. Fieldwork identified the area as an altered feldspar porphyry. The weathered material on the surface of the porphyry was bright compared with the surrounding terrain and had a yellow appearance. Laboratory spectra from field samples contained spectral features characteristic of iron oxide and sercite (see section 4.3.7). The absence of a negative value in the 2.2μm channel is considered to result from the illumination curve being biased by small amounts of vegetation as suggested for the log residual spectra from subsites A and B.

The log residual spectrum from subsite D has a different shape to the spectra from subsites A-C. The maxima now occurs in the 0.56μm channel. The values in both the 0.48μm and 0.66μm channels are slightly lower. The minima now occurs in the 1.65μm channel. The similar positive values in the 0.48μm , 0.56μm and 0.66μm channels suggest the area is light coloured and does not contain any iron bearing minerals. The area was mapped as undifferentiated rhyolitic rocks (Lorraway 1976). Fieldwork identified the area as having a light appearance and no obvious iron stain as with the previous subsites.

Figure 4.12 shows the log residual spectra from subsites E-H. The spectrum from subsite E closely resembles that from subsite D and is interpreted similarly (Figures 4.11 and 4.12). The area covered by the subsite was mapped as ignimbrites (Lorraway 1976, Figure 4.6). Field mapping showed these to be largely ash-flow tuffs of a rhyolitic composition. They were also particularly bright and did not have an iron oxide stain.

The log residual spectrum from subsite F closely resembled those from subsites A-C and is interpeted similarly. Lorraway (1976), mapped the area covered by this subsite as basalt. In fact, this was an area of ferruginous micaceous sandstones of presumed Lower Carboniferous age and of a similar origin to those in the centre of Camp Oven. The area did have an iron oxide

stain.

The log residual spectrum from subsite G is similar to that from subsite F except the maxima in the 0.65μm channel is greater. This suggests the area was more abundant in iron oxide minerals. The area was mapped as basalt (Lorraway 1976). Field mapping determined this area had an increased abundance of iron oxide minerals compared with area covered by subsite F.

The log residual spectrum from subsite H is clearly different to those from the previous subsites (Figures 4.6, 4.9 and 4.12). The maxima now occurs in the 0.48μm channel and the minima occurs in the 2.2μm channel. The value in the 1.65μm channel is close to zero unlike all the previous spectra in which the 1.65μm channel value was more negative. The area covered by this subsite is mapped basalt (Lorraway 1976, Figure 4.6). However, this area was covered by scree from the rocks to the north mapped as rhyolitic rocks (Lorraway 1976). The minima in the 2.2μm channel infers the presence of Al-OH $\pm$ Mg-OH $\pm$ CO bearing minerals or vegetation. However, the shape of the remainder of the of the log residual curve is not characteristic of vegetation (see subsequent discussion). In view of the absence of this feature in other areas which contained small amounts of Al-OH $\pm$ Mg-OH $\pm$ CO bearing minerals thought to be due to vegetation bias, these minerals should be particularly abundant at this subsite. The relatively high value in the 1.65μm channel value supports this view since altered rocks particularly abundant in Al-OH $\pm$ Mg-OH $\pm$ CO bearing minerals also have a higher reflectance than other rocks in the wavelength region covered by the 1.65μm channel (Hunt and Ashley 1979).

Field mapping identified that the area covered by this subsite had been subject to advanced argillic alteration. The presence of Al-OH $\pm$ Mg-OH $\pm$ CO bearing minerals was confirmed by laboratory spectral analysis and X-Ray Diffraction. The detection of this area is particularly important for mineral exploration for the reasons outlined at the start of this section. The results from both the X-Ray Diffraction analyses and laboratory spectral analysis are discussed in detail in Chapter Six.

Figure 4.13 illustrates the spectrum from subsite I. This subsite is contained within the same unit as subsite H. However, the spectrum is very different. It has two minima in the 0.66μm and 2.2μm channels and maxima

in the 0.48μm and 1.13μm channels. This spectrum is typical of vegetation which has a low reflectance in the red part of the spectrum, covered by the 0.66μm channel, due to the chlorophyll absorption (Raines and Canney 1980). The reflectance in the near infrared is high due to the cellular structure of the plant (Raines and Canney 1980), covered by the 0.83μm and 1.13μm channels. The reflectance in the 1.65μm channel remains high particularly in dry vegetation. The reflectance of both green and dry vegetation falls in the region covered by the 2.2μm channel (Figure 4.3). Field mapping confirmed the area covered by this subsite had been subject to advanced argillic alteration. The results from X-Ray Diffraction and laboratory spectral analysis of samples collected at this subsite are discussed in Chapter Six. The log residual spectrum does not relate to the alteration, rather the vegetation which covers it. The Al-OH $\pm$ Mg-OH $\pm$ CO bearing minerals may have contributed to the low value in the 2.2μm channel but this cannot be ascertained using this technique.

The log residual spectra from subsites J and K closely resemble this spectrum and are also thought to be typical of vegetation (Figure 4.13).

The log residual spectrum from subsite L has a mimima in the 0.48μm and 1.13μm channels and maxima in the 0.66μm and 2.2μm channels (Figure 4.13). The spectrum is similar to those from subsites A-C and considered to indicate the presence of iron oxide for the reasons outlined with those spectra. The area covered by the subsite was mapped as sandstones (Lorraway 1976). The sandstones were ferruginous and had an iron oxide stain as inferred from the log residual spectrum.

The log residual spectrum from subsite M has a similar shape to that from subsite L and is also interpreted to infer the presence of iron oxide. The area covered by this subsite was mapped as ignimbrite (Lorraway 1976). Field mapping confirmed these rocks had a strong iron oxide stain.

Figure 4.14 illustrates the log residual spectra from subsites M-P. The spectrum from subsite N has a maxima in the 0.48μm and 2.2μm channels and a minima in the 1.13μm channel (Figure 4.14). The maxima in the 0.48μm channel covering the blue part of the spectrum and high positive values in the 0.56μm and 0.66μm channels covering the green and red parts of the spectrum respectively infers the absence of any iron oxide and suggests the

area is blue/green in colour. Accounting for vegetation bias the value close to zero in the 2.2μm channel suggests small amounts of Al-OH $\pm$ Mg-OH $\pm$ CO bearing minerals are present. The area covered by the subsite was mapped as basalt/andesite (Lorraway 1976). Field mapping determined these rocks were blue/green in colour without notable iron oxide staining. Thin section analysis identified the feldspars were altering to sericite. However, this alteration was similar to that seen at other subsites with far higher 2.2μm channel values. A further sample collected from this subsite contained abundant epidote which also absorbs in this region (Hunt *et al.*, 1973b). This may account for the lower value in the 2.2μm channel compared with other samples with similar amounts of sericite.

The log residual spectrum from subsite O has maxima in the 0.66μm and 2.2μm channels and minima in the 0.48μm and 1.13μm channels (Figure 4.14). The difference between the 0.48μm channel minima and 0.66μm channel maxima is particularly large compared with spectra from other subsites. This infers the subsite contains large amounts of iron oxide minerals for the reasons discussed with similar spectra from subsites A-C. The area covered by the subsite was mapped as granodiorite (Wyatt *et al.*, 1971). The area had a particularly well developed iron oxide stain as suggested from the log residual spectrum. Thin section analysis identifed that this was the result of the breakdown of mafic minerals (biotite and hornblende).

Figure 4.14 also illustrates the spectrum from subsite P which covers an area of vegetation in a river channel. The spectrum closely resembles those from subsites I, J and K which were interpreted to result from vegetation.

4.3.5 Least Squares Fit Residual (LRES) Data

The wavelength region between 0.45μm and 2.35μm contains diagnostic information relating to the presence and abundance of iron oxides and Al-OH $\pm$ Mg-OH $\pm$ CO bearing minerals (see section 4.2). Remotely sensed data acquired from this region contain effects relating to the solar irradiance curve and atmospheric absorptions which mask these subtle mineralogical variations (see section 4.3.2). These effects can be reduced using either the band ratioing or log residual techniques (see sections 4.3.3 and 4.3.4) The band ratio and log residual data were used to map areas of iron oxides and in certain cases areas of Al-OH $\pm$ Mg-OH $\pm$ CO bearing minerals. However, areas of Al-OH

$\pm$ Mg-OH $\pm$ CO bearing minerals were confused with areas of vegetation. These minerals are normally distinguished on the basis they have a lower reflectance than other rocks and soils in the wavelength region covered by the $2.2\mu m$ channel. Unfortunately, vegetation also has a low reflectance in this channel resulting in numerous cases of possible confusion (see sections 4.3.3 and 4.3.4).

The LRES technique was developed in order to separate the response due to vegetation from that of Al-OH $\pm$ Mg-OH $\pm$ CO bearing minerals (Green 1985 pers. comm). This was achieved by finding the linear combination of all other channels which best predicts the response in the $2.2\mu m$ channel. If it is assumed that Al-OH $\pm$ Mg-OH $\pm$ CO bearing minerals only have a discernable effect in the $2.2\mu m$ channel and that linear mixing holds, then the prediction will account for all other materials except Al-OH $\pm$ Mg-OH $\pm$ CO bearing minerals (Fraser *et al.*, 1985). This prediction is done on a per pixel basis, and the predicted value subtracted from the actual value. The residual to this will be zero unless Al-OH $\pm$ Mg-OH $\pm$ CO bearing minerals are present in which case the residual will be negative and enhanced relative to the surrounding area.

The aim of this aspect of the study is to use this technique to produce a map of Al-OH $\pm$ Mg-OH $\pm$ CO bearing minerals. This map can then be used to examine variation due to these minerals as an aid to lithological mapping and mineral exploration. These results will be compared with an alternative technique for achieving the separation of Al-OH $\pm$ Mg-OH $\pm$ CO bearing minerals and vegetation responses. The methodology behind the LRES technique is now described based on notes provided by A. A. Green (1987).

The LRES technique uses a linear mixing model where if we consider a sample (X_i) made up various proportions of materials, represented schematically in Figure 4.15. The value for that sample will equal:

$$X_i = (0.25 \times 1) + (0.25 \times 2) + (0.5 \times 3) \qquad 4.11$$

or

$$X_{\lambda i} = b_\lambda + \sum_m P_{mi} L_{\lambda m} \qquad 4.12$$

where:

P_{mi} = proportion of material m in sample i.

$L_{\lambda m}$ = radiance from a pure pixel of m in channel λ.

b_λ = path radiance.

$X_{\lambda i}$ = observed radiance.

and

$$\sum_m P_{mi} = 1 \qquad\qquad 4.13$$

Using this model if we take three channels and two materials, all data will lie on a mixing line between L_1 and L_2 (Figure 4.16). However, in the natural environment the reflectance from a given sample is dependant on both the materials present and the exposure of those materials to the sensing device. That is a reduced radiance will be received from a pixel in shadow. This is illustrated schematically in Figure 4.17. Re-writing the simple linear model in terms of exposure we obtain:

$$X_{\lambda i} = b_\lambda + \sum_m l_{\lambda m}\epsilon_{mi} \qquad\qquad 4.14$$

where: ϵ_{mi} = the 'exposure' of material m in pixel i

For flat surfaces the exposure of a surface will be equal to the proportion of the material present. The exposure of all other surfaces will either be equal to or less than the proportion of material present. The lowest possible value for the exposure term will be zero when the material is not present or hidden and the resultant contribution of that material to the reflectance of the sample is zero. That is:

$$0 \le \epsilon_{mi} \le P_{mi} \qquad\qquad 4.15$$

$$\sum_m \epsilon_{mi} \ne 1 \qquad\qquad 4.16$$

Taking into account the effect of exposure the three channel two material scenario has been redrawn Figure 4.18.

All the data now lie on a mixing plane between L_1 and L_2 that is dependant on the exposure of the materials that constitute any given sample. Naturally, if the sum of the exposure is equal to one, the proportion terms from the simple linear mixing model must equal the exposure terms of the

exposure model. If the two materials in the exposure model are a non-clay soil and vegetation we find:

3 channels (including a 2.2μm channel)

2 materials

(1) non-clay soil

(2) vegetation

$$X_{Ai} = b_A + l_{AS}\epsilon_{Si} + l_{AV}\epsilon_{Vi} \qquad\qquad 4.17$$

$$X_{Bi} = b_B + l_{BS}\epsilon_{Si} + l_{BV}\epsilon_{Vi} \qquad\qquad 4.18$$

where:

X_{Ai} = radiance in channel A for sample i from non-clay soil and vegetation.

b_A =path radiance channel A

l_{AS} = radiance from a pure pixel of soil (S) in channel A.

ϵ_{Si} = exposure of soil in pixel i.

l_{AV} = radiance from a pure pixel of vegetation (V) in channel A.

ϵ_{Vi} = exposure of vegetation in pixel i.

X_{Bi} = radiance in channel B for sample i from non-clay soil and vegetation.

b_B =path radiance channel B

l_{BS} = radiance from a pure pixel of soil (S) in channel A.

l_{BV} = radiance from a pure pixel of vegetation (V) in channel B.

Using these two equations we can solve for ϵ_{Si} and ϵ_{Vi} in terms of X's b's and l's. These can then be substituted into the equivalent equation for the 2.2μm channel giving:

$$X_{2.2i} = \alpha + \beta X_{Ai} + \gamma X_{Bi} \qquad\qquad 4.19$$

where:

$X_{2.2i}$ =radiance in the 2.2μm channel for sample i consisting of a mixture of vegetation and a non clay soil.

where:

α = contribution of the path radiance term

βX_{Ai} = contribution of first material

γX_{Bi} = contribution of the second material

Using this equation we can estimate the value in the 2.2μm channel. If only two spectrally distinct materials are present and the value in one channel can be expressed as a linear combination of the other channels our estimate of the value in the 2.2μm channel should equal the actual value in the 2.2μm channel.

The Exposure Model can be written more generally as:

$$X_{\lambda i} = b_\lambda + \sum_m l_{\lambda m}\epsilon_{mi} \qquad 4.20$$

for $\lambda = 1........\Lambda$

where:

Λ = number of channels

Provided $m - 1$ is $\leq \Lambda - 1$ and the materials m are spectrally distinct the value in any one channel can be expressed as a linear combination of the other channels. Therefore, we can write the exposure model as:

$$X_{2.2i} = \alpha + \sum_\lambda^{(\Lambda-1)} \beta_\lambda X_{\lambda i} \qquad 4.21$$

The coefficients in equation 4.19 can be found through matrix inversion where:

$$\begin{bmatrix} n & \sum X_A & \sum X_B \\ \sum X_A & \sum X_A^2 & \sum X_A X_B \\ \sum X_B & \sum X_B X_A & \sum X_B^2 \end{bmatrix} \times \begin{bmatrix} \alpha_0 \\ \beta_1 \\ \gamma_2 \end{bmatrix} = \begin{bmatrix} \sum X_{2.2} \\ \sum X_A X_{2.2} \\ \sum X_B X_{2.2} \end{bmatrix} \qquad 4.22$$

X_A X_B $X_{2.2}$ are the values in channels A, B and the 2.2 μm . Having obtained good predicted values for the 2.2μm channel we need to determine what happens if a sample site used to obtain the coefficients did not contain Al-OH $\pm$ Mg-OH $\pm$ CO bearing minerals ('clay') but the image we apply these coefficients to does contain some clay. Taking the exposure model we now have: 3 channels (including the 2.2μm channel)

3 materials:

(1) Vegetation

(2) $f \times 100\%$ clay

(3) $(f - 1) \times 100\%$ non clay

where:

f = fraction of clay present

Assuming that the radiance of clay and non clay are the same except in the 2.2μm channel. We have:

ϵ_{Vi} = Vegetation exposure

ϵ_{Si} = Soil Exposure

$f_i \epsilon_{Si}$ = Clay Exposure

$(1 - f_i)\epsilon_{Si}$ = Non - clay Exposure

Then since there is no information about the amount of clay in the sample in channels A and B, the coefficients will estimate the value in the 2.2 μm channel for soil as if it did not contain any clay. So:

$$\hat{X}_{2.2i} = b_{2.2} + \epsilon_{Si} l_{2.2n} + \epsilon_{vi} l_{2.2v} \qquad 4.23$$

However in fact we have:

$$X_{2.2i} = b_{2.2} + f\epsilon_{si} l_{2.2c} + (1 - f)\epsilon_{si} l_{2.2n} + \epsilon_{vi} l_{2.2v} \qquad 4.24$$

Therefore :

$$X_{2.2i} - \hat{X}_{2.2i} = f\epsilon_{si}(l_{2.2c} - l_{2.2n}) \qquad 4.25$$

where: $(l_{2.2c} - l_{2.2n})$ = radiance difference between clay and non - clay in the 2.2 μm channel.

This is illustrated schematically in Figure 4.19. The upper plane is obtained from a linear regression of $X_{2.2}$ on X_A and X_B in a training area which does not contain clay. As clay is added to the sample it plots beneath the plane. Thus in the resultant predicted LRES images, the darker an area, the greater the amount of clay or Al-OH $\pm$ Mg-OH $\pm$ CO bearing minerals that area contains. The sample sites chosen can be of any size and ideally should not contain any clay. If they do contain clay only clay rich areas in the image which contain more than the amount of clay in the training area will show up in the LRES image.

Plates 4.14, 4.15 and 4.16 are the actual 2.2μm channel image, the predicted 2.2μm channel image and the LRES (actual minus predicted) 2.2μm channel image respectively. The area around Blackfellow Mountain is immediately apparent as an area of low values (labelled A , Plate 4.16). It

is possible to map the contact between these low values and the surrounding areas. (labelled B , Plate 4.16). This contact corresponds to the apron of scree which surrounds Blackfellow Mountain and the Pinnacles. Field mapping identified these as areas of advanced argillic alteration. Al-OH ± Mg-OH ± CO bearing minerals were identified in samples collected from Blackfellow Mountain by laboratory spectrometry and X-Ray Diffraction. The minerals identified were alunite, kaolinite, dickite, pyrophyllite and sericite. The results from laboratory analysis of samples collected at Blackfellow Mountain are described and discussed in Chapter Six.

The absence of any low values on the eastern lobe of Blackfellow Mountain is noted in the LRES image (labelled C, Plate 4.16). It is thought to result from the top of the Mountain being densely vegetated. As a result the radiation measured by the sensor is characteristic of vegetation which is 'perfectly' predicted and removed from the LRES image. Therefore, areas of mixed hydrous minerals and vegetation will only be apparent in the LRES image provided there is a sufficient hydrous mineral component in the radiation received by the sensor. The exact threshold above which only vegetation is seen and removed remains undetermined.

The majority of the rivers are not visible in the LRES image. These rivers are dominated by vegetation. This is 'perfectly' predicted and thereby removed from the LRES image. A portion of Pinnacle Creek is still visible as an area of low values in the LRES image. This is most likely due to Al-OH ± Mg-OH ± CO bearing minerals washed into the creek from Blackfellow Mountain and the surrounding area. (labelled D, Plate 4.16).

There are also some low values in the Ravenswood Granodiorite in the SW of the image (labelled E , Plate 4.16). These values result from the concentration of epidote carbonate and chlorite which are present in varying quantities throughout the granodiorite. These minerals represent a background propylitic type alteration of the granodiorite. The granodiorite has been mineralised in places and large amounts of gold have been extracted from it (Wyatt *et al.*, 1971). The gold is usually associated with shearing and typically emplaced in quartz veins. The association of these areas of more intense alteration with mineralisation has not been investigated. The area north of the fenceline in the SW of the granodiorite which appeared altered in the ratio data but was

found to cover an area of grasses without alteration is no longer apparent (Plates 4.2 and 4.16; section 4.3.2)

Two small water bodies also appear as dark areas in the LRES image (labelled F and G , Plate 4.16). These result because no water was present in the training area and so the coefficients calculated by the multiple linear regression do not predict the presence of water. This poor prediction results in the low values in the LRES image in the same manner as the areas of Al-OH ± Mg-OH ± CO bearing minerals.

The area around K2 was also mapped as an area of alteration by geologists from Terra Search (Figure 4.6). This area does not appear to contain Al-OH ± Mg-OH ± CO bearing minerals on the LRES image (labelled H , Plate 4.16). Field mapping at K2 revealed a different style of alteration to that seen at Blackfellow Mountain. K2 is strongly silicified with some sericite. Sericite is a Al-OH bearing mineral and if present in sufficient quantities should be detected on the LRES image assuming vegetation densities are similar to those at Blackfellow Mountain. Vegetation densities did appear similar. However, the amount of sericite on the weathered surfaces of samples collected from K2 was no greater than in samples collected from other areas (see section 4.3.7).

4.3.6 Directed Principle Component (DPC) Data

The wavelength region between 0.45μm and 2.35μm contains diagnostic information for the detection of iron oxides and Al-OH ± Mg-OH ± CO bearing minerals (section 4.2). Remotely sensed data acquired from this region are dominated by the effects of the solar irradiance curve and atmospheric absorptions which subdue any mineralogical variation (section 4.3.2)

These effects can be removed using either band ratios or log residuals (see sections 4.3.3 and 4.3.4). The band ratio and log residual data were successfully used to map the presence and abundance of iron oxides. However, areas of Al-OH ± Mg-OH ± CO bearing minerals which should be detectable in data from the 2.2μm channel where they absorb more strongly than other geologic materials were confused with vegetation which has a similar response.

Two techniques have been successfully used to separate areas of vegetation from Al-OH ± Mg-OH ± CO bearing minerals. . These are the LRES and DPC techniques (Fraser *et al.*, 1986). The LRES technique has been successfully used with NS-001 data from the Camp Oven test site to delineate

areas of Al-OH ± Mg-OH ± CO bearing minerals (see section 4.3.5) The aim now is to apply the DPC tecnique to the data and compare the results to those obtained using the LRES technique to establish which is most effective in mapping areas of Al-OH ± Mg-OH ± CO bearing minerals with these data. The DPC technique has the initial advantage over the LRES technique in that the software for its calculation is available as standard on many image processing systems unlike the LRES software which requires custom programming.

The DPC method is described by Fraser and Green (1987), and involves performing directed principal components analysis at two specific band ratio images. Band ratios are selected since the effects of the solar irradiance curve and atmospheric absoprtions have been removed and they can be theoretically interpreted in terms of reflectance spectra (Fraser and Green 1987).

The ratios are chosen on the basis that one is useful for geological discrimination but is confused by vegetation, whilst the other ratio is dominated largely by the effects of vegetation. The ratios used are the $1.65\mu m/2.2\mu m$ ratio in which Al-OH ± Mg-OH ± CO bearing minerals are confused by vegetation and the $0.83\mu m/0.66\mu m$ ratio which is dominated by vegetation effects.

The first principal component computed from these ratios contains the correlated information between the ratios relating to vegetation. The second principal component contains the uncorrelated information relating to variations in Al-OH ± Mg-OH ± CO bearing minerals (Figure 4.20).

Plate 4.17 is an image formed from the data contained in the first directed principal component. The vegetated areas appear dark. This indicates a high negative correlation between areas of vegetation. This suggests vegetated areas have high values in one ratio and low values in the other. This disagrees with the expected results since vegetation should have high values in both ratios giving a positive correlation and causing vegetated areas to appear bright in the first principal component.

Plate 4.18 is an image formed from the data contained in the second principal component. Blackfellow Mountain and its apron of altered scree is clearly visible as an area of high values. However, there are several other areas of high values. These include river channels, which did not contain any alter-

ation. Unlike the LRES technique which only enhances information relating to the presence of hydrous minerals this technique enhances any mineralogic information which is not correlated between channels.

4.3.7   Laboratory Spectra from 0.4µm-2.5µm Wavelength Region

The broad band NS-001 data were used to infer the presence of both iron oxide and hydrous minerals. Variations in the abundance of these minerals were used to discriminate a variety of lithologies from a set of subsites within the Camp Oven test site. Field samples were collected from each of these subsites and laboratory spectra obtained from them. The spectra were acquired from the external 'weathered ' surface of each sample unless otherwise stated. This is the same surface that would be observed by an airborne or spaceborne sensor.

The spectra were acquired using the GER MK IV IRIS. Full details of this instrument are given in Milton and Rollins (1987). The spectrometer was operated in the standard laboratory mode and a reflectance spectrum obtained between 0.4µm and 2.5µm. Reflectance was measured relative to a barium sulphate panel (Milton and Rollins, 1987).

The absorption features in these spectra were matched with those in published mineral spectra in order to identify the minerals present. An excellent collection of mineral spectra are available in a series of papers published by Hunt and Salisbury 1970; 1971a,b,c; Hunt *et al.*, 1971a,b; 1972; 1973a,b; 1974a,b; Hunt 1977; Hunt and Ashley 1979).

This information was used to determine which iron oxide or hydrous minerals caused the variations in the NS-001 data used for lithological discrimination. These spectra also provide an indication of the additional information which should be available in data acquired by an air-or space-borne sensor with an increased number of channels such as the AIS or GER II Airborne Scanner (Goetz and Srivastav, 1985; Huntington, 1988).

The spectra from samples collected at each of the subsites shown in Figure 4.6 are now presented and interpreted. Each interpretation is related to the results from hand specimen and thin section analysis of the sample

Figures 4.21 and 4.22 are the laboratory spectra from the external surfaces of samples collected at subsite A. Figure 4.21 has a decrease in reflectance from 1.7µm to 0.43µm and a strong rise in reflectance from 0.43µm to shorter

wavelengths. Absorptions are present at 1.42μm, 1.93μm, and 2.2μm and there is a positive inflection in the curve at 0.68μm. The decrease in reflectance to 0.43μm is characteristic of Fe-O (Hunt et al., 1971a). The rapid rise in reflectance from 0.43μm to shorter wavelengths is an instrument effect and is henceforth ignored. The twin absorptions at 1.42μm and 1.93μm indicate molecular water is present, typical of acid igneous rocks (Hunt et al., 1973b). The 2.2μm absorption is related to Al-OH combination (Hunt, 1980). The 2.2μm feature is seen in montmorillonite, illite and sericite. Montmorillonite/illite also have twin absorption at 1.42μm and 1.93μm indicating molecular water is present and seen in this spectrum which sericite does not. However, these could arise from other materials present in acid igneous rocks such a quartz and feldspar (Hunt et al., 1973a). Sercite normally has additional small features at 2.35μm and 2.44μm due to Al-OH and OH (Hunt et al., 1973b; Hunt and Ashley, 1979). However, these may not be apparent if the sample only contains small amounts of sericite. The positive inflection in the spectrum at 0.68μm is indicative of chlorophyll in lichen (Ager and Milton, 1987).

The sample was identified as a granite. The surface of the sample had a red stain with black patches. The red stain was identifed as iron oxide in the laboratory spectrum and the black patches as lichen. The sample contained abundant quartz and feldspar which may have contained molecular water identified from the spectrum. Thin section analysis revealed that feldspar in the sample was altering to sericite. In the laboratory spectrum it was only possible to identify the presence of sericite or montmorillonite/illite.

Figure 4.22 is the laboratory spectrum from the external surface of a second sample collected from subsite A. The spectrum has a decrease in reflectance from 1.7μm to 0.45μm, absorptions at 1.42μm, 1.93μm, 2.2μm, 2.35μm, 2.45μm and a positive inflection at 0.68μm. The decrease in reflectance to 0.45μm is characterisitc of Fe-O (Hunt et al., 1971a). The twin absorptions at 1.42μm and 1.93μm indicate molecular water is present, typical of acid igneous rocks (Hunt et al., 1973a). The absorptions at 2.2μm and 2.35μm result from Al-OH and the 2.45μm absorption is due to OH (Hunt et al., 1973b). The 2.2μm, 2.35μm and 2.45μm features are all characteristic of sericite (Hunt et al., 1973b). The positive inflection at 0.68μm is indicative

of lichen on the surface of the sample (Ager and Milton, 1987).

The sample was also identified as granite. The surface of the sample was stained red with black patches. The red was identified as Fe-O in the laboratory spectrum and the black patches as lichen. Molecular water identified in the laboratory spectrum could be present in quartz or feldspar identified in thin section. The feldspars were altering to sericite which was also identified in the laboratory spectrum.

Figure 4.23 is the laboratory spectrum from the external surface of a sample collected at subsite B. The spectrum has a strong decrease in reflectance to 0.42μm, absorptions at 1.42μm, 1.93μm and 2.2μm and a positive inflection at 0.68μm. The strong decrease in reflectance is typical of Fe-O (Hunt et al., 1971a). The twin absorptions at 1.42μm and 1.93μm indicate molecular water is present typical of acid igneous rocks (Hunt et al., 1973a). The 2.2μm absorption results from Al-OH (Hunt, 1980). The 2.2μm feature could result from sericite, montmorillonite or illite for the reasons discussed with the first sample from subsite A. The positive inflection at 0.68μm indicates the presence of lichen on the surface of the sample (Ager and Milton, 1987).

Figure 4.24 is the laboratory spectrum from the internal surface of the previous sample. The reflectance decreases from 0.77μm to 0.43μm. There is a sudden drop at 0.68μm. From 0.77μm the reflectance decreases slightly into the infrared then remains essentially flat to 2.5μm . The decrease in reflectance from 0.77μm to shorter wavelengths is typical of Fe-O (Hunt et al., 1971a). The sudden drop at 0.68μm is instrument related and is ignored.

The sample was identified as a siliceous welded tuff. The external surface of the sample had black patches identified as lichen in the spectrum from that surface. The remainder of the external surface was brown, identified as iron oxide in the spectrum from that surface. The molecular water absorption bands were only present in the spectrum from the external surface. This would suggest these relate to a weathering product. This is thought to be montmorillonite/illite which would account for the additional absorption at 2.2μm in the spectrum from the external surface of the sample (Hunt et al., 1973b). Thin section analysis revealed the sample also contained chlorite and biotite which were randomly distributed through the sample. These were not seen in the spectra from either surface suggesting they were not present in

sufficient quantitiy to enable spectral identification.

Figure 4.25 is the laboratory spectrum from the external surface of a sample collected at subsite C. There is a general decrease in reflectance in the spectrum from 1.7μm to 0.42μm. Major absorptions occur at 1.41μm, 1.92μm and 2.2μm; with minor absorptions at 2.35μm and 2.44μm. The general decrease in reflectance relates to the presence of Fe-O (Hunt *et al.*, 1971a). The 1.41μm and 1.92μm absorptions indicate molecular water is present, typical of acid igneous rocks (Hunt *et al.*, 1973a). The 2.2μm, 2.35μm and 2.44μm result from Al-OH and OH modes, and are characterisitc of sericite (Hunt *et al.*, 1973b; Hunt and Ashley, 1979).

The sample from subsite C was identified as an altered feldspar porphyry. The weathered surface of the sample was green/brown. This was suggested in the spectrum and the brown resulting from haematite. The surface of the sample had large rotted feldspar phenocryts (>5mm) on it. Thin section analysis revealed the feldspars were altering to sericite, which was identified in the laboratory spectrum.

Figure 4.26 is the laboratory spectrum from external surface of a sample collected at subsite D. The spectrum has a strong falloff in reflectance from 0.77μm to 0.42μm. Major absorptions occur at 1.44μm, 1.93μm and 2.22μm. There is also a minor absorption at 0.84μm . The falloff in reflectance indicates Fe-O is present (Hunt *et al.*, 1971a). The absorptions at 1.44μm and 1.93μm result from molecular water, typical of acid igneous rocks (Hunt *et al.*, 1973a). The feature at 2.2μm indicates an Al-OH bearing mineral is present (Hunt, 1980). This could be montmorillonite, illite or sericite for the reasons discussed in the spectrum from the first sample from subsite A. The absorption at 0.84μm results from ferric iron in haematite (Hunt *et al.*, 1971a).

The sample was identified as a dacite. The weathered surface of the sample was brown, interpreted from the laboratory spectrum to result from haematite. Thin section analysis revealed the feldspars were altering to sericite also tentatively identified in the spectrum. The molecular water in the spectrum may occur in the quartz or feldspar identifed in thin section.

Figures 4.27 and 4.28 are the laboratory spectra from the external surfaces of two samples collected from subsite E. Figure 4.27 has a strong decrease in reflectance from 1.7μm to 0.42μm. Major absorptions occur at

1.41μm, 1.91μm, 2.2μm and 2.34μm. There is also a weak absorption at 0.86μm and a reflectance maximum at 0.77μm. The decrease in reflectance from 1.7μm to 0.42μm indicates Fe-O is present (Hunt *et al.*, 1971a). The 1.41μm and 1.91μm absorptions indicate molecular water is present, typical of acid igneous rocks (Hunt *et al.*, 1973a). The 2.2μm and 2.34μm absorptions result from Al-OH and OH (Hunt *et al.*, 1973b). The 2.2μm absorption could result from sericite, montmorillonite or illite for the reasons discussed in the first sample from subsite A. The 2.34μm feature is typical of epidote (Hunt *et al.*, 1973b). The weak absorption at 0.85μm results from ferric iron present in haematite (Hunt *et al.*, 1971a).

The sample was identified as an epidote nodule. It had a brown surface, identified as haematite in the laboratory spectrum. Thin section analysis indicated the nodule was dominantly composed of epidote with lesser amounts of feldspar which was altering to sercite.

Figure 4.28 has a sharp decrease in reflectance from 0.77μm to 0.44μm. Major absorptions occur at 0.85μm and 2.2μm. A weak feature occurs at 1.41μm. The sharp decrease in reflectance is characteristic of Fe-O (Hunt *et al.*, 1971a). The 0.85μm absorption results from ferric iron in haematite (Hunt *et al.*, 1971a). The 2.2μm feature results from Al-OH and the 1.41μm feature is due to OH (Hunt *et al.*, 1973b; Hunt and Ashley 1979). The absence of well developed molecular water bands together with the Al-OH and OH features suggest sericite is present. This mineral has further absorptions at 2.35μm and 2.44μm but these are small and may not appear if there is an insufficient amount of the mineral present in the sample.

The sample was identifed as a basalt. Basalts are typically featureless in the 0.35μm to 2.5μm range with any features resulting from weathering or alteration (Hunt *et al.*, 1974). This is true of this sample which has a brown weathered surface due to haematite. Thin section anlaysis indicates the sericite, identified in the laboratory spectra results from feldspar alteration.

Figure 4.29 is the laboratory spectrum from the external surface of a sample collected at subsite F. The spectrum has a decrease in reflectance from 1.7μm to 0.46μm. A major absorption occurs at 1.93μm, and weak absorptions occur at 1.43μm, 2.19μm, 2.37μm and 2.48μm. There is also a positive inflection in the spectrum at 0.68μm. The decrease in reflectance

from 1.7μm to shorter wavelengths indicates Fe-O is present (Hunt *et al.*, 1971a). The remaining spectral features may all occur if lichen is present (Ager and Milton, 1987).

The sample was identified as a porphyritic andesite. The external surface was red in colour, resulting from iron oxide identified in the laboratory spectrum. The remainder of the surface was black, identified as lichen in the laboratory spectrum. Andesites are spectrally flat in this wavelength region with any spectral variations due to weathering or alteration products (Hunt *et al.*, 1974), or lichen.

Figure 4.30 is the laboratory spectrum from the external surface of a sample collected at subsite G. The spectrum has a low overall reflectance superimposed on which there are minor absorptions at 0.94μm and 2.23μm. The 0.94μm absorption may result from ferric iron seen in goethite (Hunt *et al.*, 1971a). The 2.23μm absorption may result from Al-OH bearing mineral (Hunt *et al.*, 1973b).

Figures 4.31 and 4.32 illustrate the laboratory spectra from the external and internal surfaces of samples collected from an area slightly south of subsite H. Both spectra have absorptions at 0.86μm, 1.43μm, 1.48μm, 1.76μm, 1.94μm, 2.16μm, 2.2μm and 2.33μm. There is also a decrease in reflectance from 0.75μm to 0.43μm. The well developed feature at 0.87μm is characterisitc of ferric iron as is the decrease in reflectance from 0.75μm to 0.43μm (Hunt *et al.*, 1971a). The remaining absorption features are all attributed to Al-OH or OH combinations and are diagnostic of alunite (Hunt *et al.*, 1971b). The feature at 1.76μm is particularly diagnostic of alunite (Hunt and Ashley, 1979). This mineral is characterisitc of areas of advanced argillic alteration (Hunt and Ashley, 1979). Its presence in the spectra from both the external and internal surfaces further indicates it is the result of alteration rather than weathering. This area of alteration had not previously been mapped and has obvious mineralisation potential. Several samples were collected from the area to determine the alteration minerals present and propose a model for their development. These data are presented in Chapter Six. The sample was bleached and contained red veins identified in the spectrum as haematite. It was not possible to identify alunite in thin section, its presence was confirmed by X-Ray Diffraction.

Figure 4.33 illustrates the laboratory spectrum from the external surface of a sample collected from subsite I. The sample has a rapid decrease in reflectance $1.6\mu m$ to $0.41\mu m$. Major absorptions occur at $0.91\mu m$, $1.41\mu m$, $1.42\mu m$, $1.50\mu m$, $1.77\mu m$, $1.95\mu m$, $2.19\mu m$, $2.21\mu m$, and $2.33\mu m$. The decrease in reflectance is typical of Fe-O (Hunt et al., 1971a). The absorption at $0.91\mu m$ results from ferric iron in either goethite or limonite (Hunt et al., 1971a). The remaining absorption features relate to OH or X-OH combinations; where X is Al or Mg (Hunt, 1980). They can only be explained by the presence of a mixture of minerals. The absorptions at $1.40\mu m$, $1.41\mu m$, $2.19\mu m$, $2.21\mu m$ and $2.34\mu m$ are within $0.02\mu m$ of those of kaolinite/dickite (Hunt and Ashley 1979). The absorptions at $1.50\mu m$ and $1.78\mu m$ are typical of alunite (Hunt et al., 1971b; Hunt and Ashley 1979). The absorptions are not in the exact location of those for the pure minerals. These subtle shifts are thought to relate to mixing of the minerals in the spectrum.

Figure 4.34 illustrates the laboratory spectrum from the internal surface of the previous sample. The absorptions are within $0.02\mu m$ of those from the external surface. However, the $1.41\mu m$ absorption is now deeper than the $1.42\mu m$ absorption and there is an additional weak absorption feature at $2.44\mu m$. Alunite does not have an absorption at $1.41\mu m$ and in kaolinite/dickite the longer wavelength $1.42\mu m$ absorption is always deeper than the shorter wavelength $1.41\mu m$ absorption (Hunt and Ashley 1979). This infers a further mineral in which the $1.41\mu m$ absorption only is present. Possible candidates for this would be sericite or pyrophyllite. Sericite would also account for the additional absorption at $2.44\mu m$. The other diagnostic absorption features of sericite or pyrophyllite would have been masked by those of alunite or kaolinite (Hunt and Ashley, 1979). The sample was identifed as altered and bleached. It was riddled with red veins, identified to be limonite in the spectrum. It was not possible to identify the hydrous minerals in thin section. X. Ray Diffraction identifed the minerals alunite, a kandite (kaolinite, dickite, halloysite or nacrite) and pyrophyllite. The mis-dentification of pyrophyllite is particularly important since this mineral only occurs through alteration not weathering (Lawrence et al., 1986). Whilst spectral analysis proved far more rapid than X-Ray Diffraction and requires less detailed interpretation, complicated mixtures of more than two minerals are more easily

separated by X-Ray Diffraction. This point is addressed further in Chapter Six.

Figures 4.35 and 4.36 illustrate the laboratory spectra from the external and internal surfaces of samples collected at subsite J. The spectrum from the external surface has a strong decrease in reflectance from 1.7μm to 0.43μm (Figure 4.34). Major absorptions occur at 1.43μm, 1.94μm and 2.2μm. The decrease in reflectance from 1.7μm is typical of Fe-O (Hunt et al., 1971a). The twin absorptions at 1.43μm and 1.94μm indicate molecular water is present, typical of acid igneous rocks (Hunt et al., 1973a). The 2.2μm feature results from an Al-OH bearing mineral (Hunt, 1980). This could result from either sericite, montmorilonite or illite for the reasons discussed with the first sample from subsite A.

The spectrum from the internal surface has absorptions at similar wavelengths to the spectrum from the external surface and it is interpreted similarly. There is an additional absorption at 0.86μm attributed to ferric iron in haematite (Hunt et al., 1971a).

The sample from subsite J was identifed as a silicified altered rock. It consisted predominantly of quartz, responsible for the molecular water bands and lesser amounts of sericite also seen in the spectrum. The sample also contained red veins identifed as haematite in the spectrum. Clearly, the amount of sericite present is not substantially greater than in the spectra from any of the other subsites. This suggests this style of silicic alteration, unlike the advanced argillic alteration, would be extremely difficult to distinguish using high resolution data from the 0.4-2.5μm region in this terrain.

Figure 4.37 illustrates the laboratory spectrum from the external surface of a sample collected from subsite K. The spectrum has a decrease in reflectance from 1.7μm to 0.43μm. There are well developed absorptions at 0.91μm, 1.41μm, 2.2μm, 2.35μm and 2.44μm. The general decrease in reflectance is characteristic of Fe-O (Hunt et al., 1971). The 0.91μm absorption results from ferric iron, and is typical of goethite (Hunt et al., 1971). The 2.2μm absorption is attributed to Al-OH and the remaining absorptions to OH in sericite (Hunt et al., 1973b).

The sample was identified as an iron stained micaceous sandstone. Both iron (goethite) and mica (sericite) were identified in the laboratory spectrum.

The absence of the molecular water bands typical of acid igneous rocks further points to the different origin of this sample.

Figure 4.38 illustrates the laboratory spectrum from the external surface of a sample collected from subsite L. There is a strong decrease in reflectance from 1.7μm to 0.34μm. Absorptions occur at 0.93μm, 1.42μm and 2.2μm. The decrease in reflectance results from Fe-O (Hunt and Ashley 1971a). The absorption at 0.91μm relates to ferric iron, and is typical of goethite (Hunt *et al.*, 1971a). The 2.2μm absorption results from the presence of Al-OH and the 1.41μm absorption from OH (Hunt, 1980). These absorptions suggest small amounts of sericite are present (Hunt *et al.*, 1973b).

The sample was identified as a quartz arenite. The surface was yellow brown, typical of geothite identifed in the laboratory spectrum. Thin section anlysis revealed abundant sericite also seen in the spectrum.

Figure 4.39 illustrates the laboratory spectrum from the external surface of of a sample collected at subsite M. The spectrum has a strong fall in reflectance from 1.7μm to 0.46μm. Absorptions occur at 1.43μm, 1.92μm and 2.2μm with a weak absorption at 2.35μm. The decrease in reflectance is typical of Fe-O (Hunt *et al.*, 1971a). The presence of the twin 1.43μm and 1.92μm absorptions indicates molecular water is present, typical of acid igneous rocks (Hunt *et al.*, 1973a). The 2.2μm and 2.35 absorptions are attributed to Al-OH and OH respectively (Hunt, 1980). These absorptions are characterisitic of small amounts of sericite (Hunt *et al.*, 1973b).

The sample was identified as a feldspar porphyry. The sample had a brown weathered surface typical of amorphous iron oxide, identified in the spectrum. Thin section analysis revealed the feldspars were altering to sericite also seen in the spectrum.

Figure 4.40 illustrates the laboratory spectrum from the external surface of a sample collected from subsite N. The spectrum has a low overall reflectance with absorptions at 1.41μm, 1.79μm, 2.2μm and 2.34μm. The low reflectance of the sample indicates it is dark coloured and probably rich in opaque minerals. The very weak 1.41μm and 1.79μm absorptions may indicate molecular water is present (Hunt, 1980). The 2.2μm and 2.34μm absorptions are attributed to Al-OH and OH respectively (Hunt *et al.*, 1973b). The absorptions are typical of small amounts of sericite (Hunt *et al.*, 1973b).

The sample was identifed as an altered basalt. Thin section analysis revealed it contained both sericite and calcite identifed in its spectrum. Basalts typically have a low overall reflectance in this region and any variations are due to weathering or alteration products (Hunt *et al.*, 1974), in this case sericite.

4.4   Analysis and Interpretation of Data from the $0.45\mu m$-$2.35\mu m$ Wavelength Region for Lithological Mapping And Mineral Exploration over the Plateau Test Site

The Plateau test site is 512 x 512 pixels in size and located in the SW of the study area (Figure 2.2). The site was selected on the basis that its geology, vegetation cover and weathering history is typical of much of NE Queensland. The site differs from the Camp Oven test site in that it is more deeply weathered and has a greater vegetation cover.

Data from the 0.45μm-2.35μm wavelength region can be used to identify iron oxides and Al-OH $\pm$ Mg-OH $\pm$ CO bearing minerals (see section 4.2). Seven channels of data from this region were acquired over the Plateau test site by the NS-001 sensor. The large wavelength range of these channels only allows discrimination of areas of iron oxides and/or Al-OH $\pm$ Mg-OH $\pm$ CO bearing minerals. .

These data were then processed using the log residual and LRES techniques in order to enhance variations in the abundance of iron oxide and/or Al-OH $\pm$ Mg-OH $\pm$ CO bearing minerals for lithological mapping and mineral exploration. These techniques proved to be the most effective means of enhancing this information of a variety of techniques which included compositing, channel ratios, log residuals, LRES and DPC at the Camp Oven test site (see section 4.3). The methodology behind the log residual and LRES techniques are given in sections 4.3.4 and 4.3.5).

The results from analysis of the NS-001 with these techniques over the Plateau test site for lithological mapping and mineral exploration should provide an indication of the wider applicability of these techniques in more deeply weathered and vegetated terrain.

Initially the geology of the Plateau test site is described followed by the

results from the analysis of the NS-001 data using the log residual then LRES techniques.

4.4.1 Geology of the Plateau Test Site

The following description of the geology of this area is derived from Beams (1986). The oldest rocks present are the Cape River Beds and Mount Windsor Volcanics (Figure 4.41). The Mount Windsor Volcanics are considered to be penecontemporaneous with the Cape River Beds. The Cape River Beds consist of siliceous shales and cherts. The Mount Windsor Volcanics consist of andesites which have been altered and epidotized in places.

These have been intruded by a granite body and rhyolite plug of Permo - Carboniferous age (Figure 4.41). The rhyolite plug is breccia-rimmed and cut by an associated vein system. This is termed the Plateau prospect. The granite body to the north is leucocratic and micaceous.

The remaining outcrop in the study area consists of sandstone (Figure 4.41). These sandstones have been tentatively interpreted as Triassic in age and form white kaolinitic bluffs.

In the Tertiary much of the area was subject to lateritization which affects all the units and resulted in the development of laterite in places (Figure 4.41).

4.4.2 Log Residual Data

Plate 4.19 is a composite image of the log residual channels centered upon 0.83μm, 0.65μm and 0.56μm displayed in red, green and blue respectively. Henceforth, the channels will be referred to according to their centre wavelength (for example the 0.83μm channel).

In general areas of vegetation appear red, areas of iron oxide green and areas without any vegetation or iron oxides appear blue. Whilst these data are useful for visual discrimination, the advantage of the log residual calculation is that the resultant data can be interpreted in terms of pseudo-reflectance (see section 4.3.4). This involves plotting pixel spectra from a variety of subsites. These pixel spectra are used to examine variations in the amount of iron oxides and/or Al-OH $\pm$ Mg-OH $\pm$ CO bearing minerals for lithological mapping and mineral exploration (see section 4.3.4). Eight subsites were chosen which represented the main cover types at Plateau. The location of the these subsites is given in Figure 4.41.

Figure 4.42 illustrates the log residual spectra from subsites A-D. The spectrum from subsite A has minima in the 0.56μm and 0.83μm channels and a maximum in the 2.2μm channel. These minima and maxima are not characteristic of iron oxides, vegetation or hydrous minerals (see section 4.3.4). If we assume that the area from which this spectrum was obtained is spectrally flat then the maximum and minima would be indicative of the mean atmospheric spectrum being biased by vegetation (see section 4.3.4). The value in the 1.65μm channel is slightly greater than expected from a spectrally flat surface with vegetation bias and infers the area was particularly bright in this channel typical of light coloured rocks. The subsite from which the spectrum was obtained covered the rhyolite plug at Plateau (Figure 4.41). The rhyolite had been stripped of vegetation and did not contain any iron oxide minerals. As a result of clearing it was brighter than the surrounding area. The plug had been cleared to gain access to a narrow breccia rim which contained gold mineralisation. The hydrothermal fluids which caused brecciation enriched the rhyolite in sericite, an Al-OH bearing mineral which should reduce the value in the 2.2μm channel (see section 4.3.4). This was not the case and probably results from the rhyolite not being sufficently enriched with this mineral, compared with the surroundings, for detection.

The log residual spectrum from subsite B has minima in the 0.48μm and 0.56μm channels with maxima in the 0.65μm and 2.2μm channels (Figures 4.41 and 4.42). The minimum in the 0.48μm channel and maximum in the 0.66μm channel infers the presence of iron oxide (see section 4.3.4). The minima in the 0.56μm channel implies the area lacks any green colour and, accounting for vegetation bias, the maxima in the 2.2μm channel infers the absence of any Al-OH $\pm$ Mg-OH $\pm$ CO bearing minerals (see section 4.3.4). The subsite from which the spectrum was obtained covers an area of laterite north of Plateau (Figure 4.41). The horizon of the laterite profile exposed at this subsite is the ferruginous sandy layer (Figure 2.4). This concurs with the interpetation of abundant iron oxide in the log residual spectrum.

The log residual spectrum from subsite C has minima in the 0.56μm, 0.83μm and 2.2μm channels and a maximum in the 1.65μm channel (Figures 4.41 and 4.42). The minima in the 0.56μm and 0.83μm channels are probably due to vegetation bias (see section 4.3.4). If the area was spectrally

flat then vegetation bias should also result in low values in the 1.13μm and 1.65μm channels and a high value in the 2.2μm channel, the reverse of which is true. This suggests the area is bright and rich in Al-OH $\pm$ Mg-OH $\pm$ CO bearing minerals (see section 4.3.4). The spectrum was obtained from an area of granite (Figure 4.41). The granite was leucocratic and rich in muscovite an Al-OH bearing mineral as inferred from the log residual spectrum.

The log residual spectrum from subsite D has maxima in the 0.48μm, 0.56μm and 1.65μm channels and minima in the 1.13μm and 2.2μm channels. The high value in the 0.48μm and 0.56μm channels infers the area is blue/green in colour. The minima in the 1.13μm and 2.2μm channels suggest the area is dark and rich in Al-OH $\pm$ Mg-OH $\pm$ CO bearing minerals (see section 4.3.4). The spectrum was obtained from an area of andesites (Figure 4.41). The andesites were dark green/blue in colour and rich in epidote an Al-OH bearing mineral as inferred from the log residual spectrum.

Figure 4.43 illustrates the log residual spectra from the subsites E-H. The log residual spectrum from subsite E has a maxima in the 0.65μm channel with similar high values in the other visible channels and minima in the 2.2μm channel (Figures 4.41 and 4.43). The high values in the visible channel suggest the area is white in colour and the minima in the 2.2μm channel that Al-OH $\pm$ Mg-OH $\pm$ CO bearing minerals are present (see section 4.3.4). The spectrum was obtained from an area of sandstones (Figure 4.41). These were white in appearance due to abundant kaolinite, an Al-OH bearing mineral. This concurs with the interpretation of the log residual spectrum.

The log residual spectrum from subsite F has a minima in the 0.65μm and 2.2μm channels with a maxima in the 0.83μm channel (Figures 4.41 and 4.43). The spectrum is typical of vegetation (see section 4.3.4). It represents the vegetation cover rather than the underlying substrate of siliceous shales and cherts.

The log residual spectrum from subsite G has maxima in the 0.66μm and 2.2μm channels and a minima in the 0.48μm channel (Figures 4.41 and 4.43). The spectrum is interpeted to indicate the presence of iron oxide and absence of any Al-OH $\pm$ Mg-OH $\pm$ CO bearing minerals for the reasons given in section 4.3.3. The spectrum was obtained over the andesites as was the spectrum from subsite D (Figure 4.40). However, the spectra are clearly

different (Figures 4.42 and 4.43). The spectrum from subsite D reflects the primary mineralogy whereas the spectrum from subsite G results from weathering products (iron oxide). The absence of a minima in the 2.2μm channel, due to epidote, reflects the variable development of this mineral within this unit.

The log residual spectrum from subsite H has its maximum values in the visible channels and a minima in the 2.2μm channel (Figures 4.41 and 4.43). The maximum values in the visible channel suggest the area is white in colour and the minimum value in the 2.2μm channel infers the presence of Al-OH $\pm$ Mg-OH $\pm$ CO bearing minerals (see section 4.3.4). The spectrum was obtained from an area of sandstones and is similar to an earlier spectrum also obtained from this unit further south at subsite E (Figures 4.41 and 4.43). The sandstones are rich in kaolinite an Al-OH bearing mineral and are white in colour as inferred from the log residual spectrum. Clearly, the mineralogy and weathering of the sandstones is more homogenous than that of the andesites.

4.4.3 LRES data

The methodology behind the LRES technique has been described in section 4.3.5. Areas of low values in the LRES images represent areas rich in Al-OH $\pm$ Mg-OH $\pm$ CO bearing minerals. . Plates 4.20-4.22 show the actual, predicted and LRES data for the 2.2μm channel. The fringes of the laterites and tops of the Tertiary sandstones have low values. The low values in the sandstones result from the presence of abundant kaolinite. The low values on the edges of the laterite also result from the presence of kaolinite. The kaolinite is present in the mottled zone of the laterite which is not normally exposed. However, around the perimeters of the laterite plateaus the edge breaks away and exposes this zone.

The rhyolite at Plateau does not have low values. However, the N-S grid lines across Plateau do have low values. The grid lines refer to tracts of land which have been stripped of vegetation along a grid centered on the rhyolite plug. This suggests there is a mantle of weathered material on the rhyolite which does not contain abundant Al-OH $\pm$ Mg-OH $\pm$ CO bearing minerals. However, where this mantle has been removed, along the grid lines, the underlying rhyolite is weakly altered.

Patches of low values occur in the andesites surrounding Plateau. The area covered by subsite D has particularly low values due to the presence of abundant epidote. In contrast, the area covered by subsite G, also in the andesites, does not have low values. This variation in the amount of epidote present, thought to relate to the intensity of the background propylitic alteration, is also observed in the Log Residual data.

Clearly, the LRES data does separate and enhance areas of Al-OH $\pm$ Mg-OH $\pm$ CO bearing minerals relative to vegetation. However, the Al-OH $\pm$ Mg-OH $\pm$ CO bearing minerals may result from weathering or hydrothermal alteration. For example, the low values in the andesites relate to areas of more intense background propylitc alteration. In contrast, the low values in the laterites result from weathering. Separating these areas is possible by examining their geomorphological characteristics in the image. The areas of laterite typically have a central area rich in iron oxides which can be identified using the 0.66μm log residual channel. The Al-OH $\pm$ Mg-OH $\pm$ CO bearing minerals are exposed around their fringes. Separating the kaolinitic Triassic sandstones from the areas of epidote alteration in the andesites is far more difficult, although, the Triassic sandstones have far higher values in the 1.65μm log residual channel. The use of imaging spectrometers should allow separation of these areas. This should be possible since the minerals present in the alteration could be identified. The areas rich in epidote from hydrothermal alteration could be easily separated from those rich in kaolinite from weathering. Blackfellow Mountain contains kaolinite, yet results from hydrothermal alteration. However, this could be separated on the presence of other minerals such as alunite, pyrophyllite and sericite.

4.5 Conclusions

1. Radiometrically corrected NS-001 data contain effects relating to the solar irradiance curve and atmospheric absorptions which subdue variations due to iron oxides and Al-OH $\pm$ Mg-OH $\pm$ CO bearing minerals.

2. These atmospheric effects can be removed using channel ratioing, log residuals, LRES and DPC techniques

3. The channel ratio and log residul data enabled variations in the abundance of iron oxide minerals to be mapped. These variations largely resulted from weathering and permitted discrimination of certain mapped units.

4. The log residual data were biased by vegetation which represented the most dominant component in the scene.

5. Using the log residual data it was possible to relate variations in pixel spectra to changes in reflectance. This permitted greater discrimination than with the channel ratio data.

6. Areas of Al-OH ± Mg-OH ± CO bearing minerals were confused with vegetation in both the channel ratio data and the log residual data limiting the use of variations in these minerals for lithological mapping and mineral exploration.

7. Confusion between areas of vegetation and Al-OH ± Mg-OH ± CO bearing minerals can be largely eliminated using the DPC and LRES techniques.

8. The LRES technique proved more effective than the DPC technique for separating the responses of vegetation and Al-OH ± Mg-OH ± CO bearing minerals.

9. Variations in the abundance of Al-OH ± Mg-OH ± CO bearing minerals resulted from weathering and hydrothermal alteration. These variations were particularly useful for lithological mapping and mineral exploration.

10. Areas of Al-OH ± Mg-OH ± CO bearing minerals resulting from hydrothermal alteration in certain cases could be separated from similar areas resulting from weathering using geomorphological characteristics. For example the areas of kaolinite produced by weathering typically occur at the fringes of laterites which form plateaux's.

11. The use of the LRES technique resulted in the discovery of an area of advanced argillic alteration at Blackfellow Mountain.

12. High resolution laboratory spectra from the $0.4\mu m$-$2.5\mu m$ wavelength region obtained from field samples enabled rapid identification of any iron oxide and Al-OH ± Mg-OH ± CO bearing minerals.

13. These interpretations indicated that amorphous iron oxide and sericite were the most common alteration minerals resulting from weathering and hydrothermal alteration.

14. These minerals were not present in sufficiently greater abundance over hydrothermally altered areas to indicate they were not the result of weathering.

15. Lab spectral analyses indicated that area of advanced argillic alteration contained additional minerals such as alunite which pointed to its hydrothermal origin.

16. Lab spectral analyses indicated areas of propylitic alteration also contained additional minerals such as epidote and chlorite which suggested they were the result of hydrothermal alteration.

17. Lab spectral analyses indicated that areas of silicic alteration only contained sericite. This was not present in sufficient quantity to indicate this was the result of hydrothermal alteration.

18. Thin section analysis permitted the identifcation of minerals present in insufficient quantities for laboratory spectral identification.

19. In some cases thin section analysis permitted identification of the mineral weathering to produce a hydrous or iron oxide mineral present in the laboratory spectra and XRD gave the best information on clay mineral species.

4.6 Summary

The 0.4μm-2.5μm wavelength region contains information enabling the identification of iron oxide and Al-OH $\pm$ Mg-OH $\pm$ CO bearing minerals. This information is masked in airbone data acquired by the NS-001 sensor by atmospheric effects. These atmospheric effects can be reduced using a variety of techniques including channel ratioing, log residuals, LRES and DPC. Of these, the log residual technique proved most effective for enhancing variations due to iron oxides and the LRES technique variations due to Al-OH $\pm$ Mg-OH $\pm$ CO bearing minerals in this weathered, vegetated terrain. Differences in the abundance of these minerals commonly resulted from weathering and allowed discrimination of the majority of mapped geological units. Several areas of Al-OH $\pm$ Mg-OH $\pm$ CO bearing minerals were also identified resulting from hydrothermal alteration including an area of advanced argillic alteration at Blackfellow Mountain. Areas of Al-OH $\pm$

Mg-OH $\pm$ CO bearing minerals produced by hyrothermal alteration could be separated from similar areas resulting from weathering. This was possible due to an increased abundance of Al-OH $\pm$ Mg-OH $\pm$ CO bearing minerals in hydrothermally altered areas or other geomorphic units typical of areas where these minerals were produced by weathering.

High resolution laboratory analysis of field samples indicated the iron oxide and Al-OH $\pm$ Mg-OH $\pm$ CO bearing minerals typically produced by weathering were amorphous iron oxide and sericite. These were present in varying abundance and permitted lithological discrimination with the airborne data. The hydrothermally altered areas did not contain a greater abundance of these minerals than the areas where they were produced through weathering. However, in areas of advanced argillic alteration and propylitic alteration additional Al-OH $\pm$ Mg-OH $\pm$ CO bearing minerals were present which inferred different origin of these minerals at these areas. An area of silicic alteration did not contain any additional Al-OH $\pm$ Mg-OH $\pm$ CO bearing minerals which would have enabled its separation from the surrounding weathered lithologies.
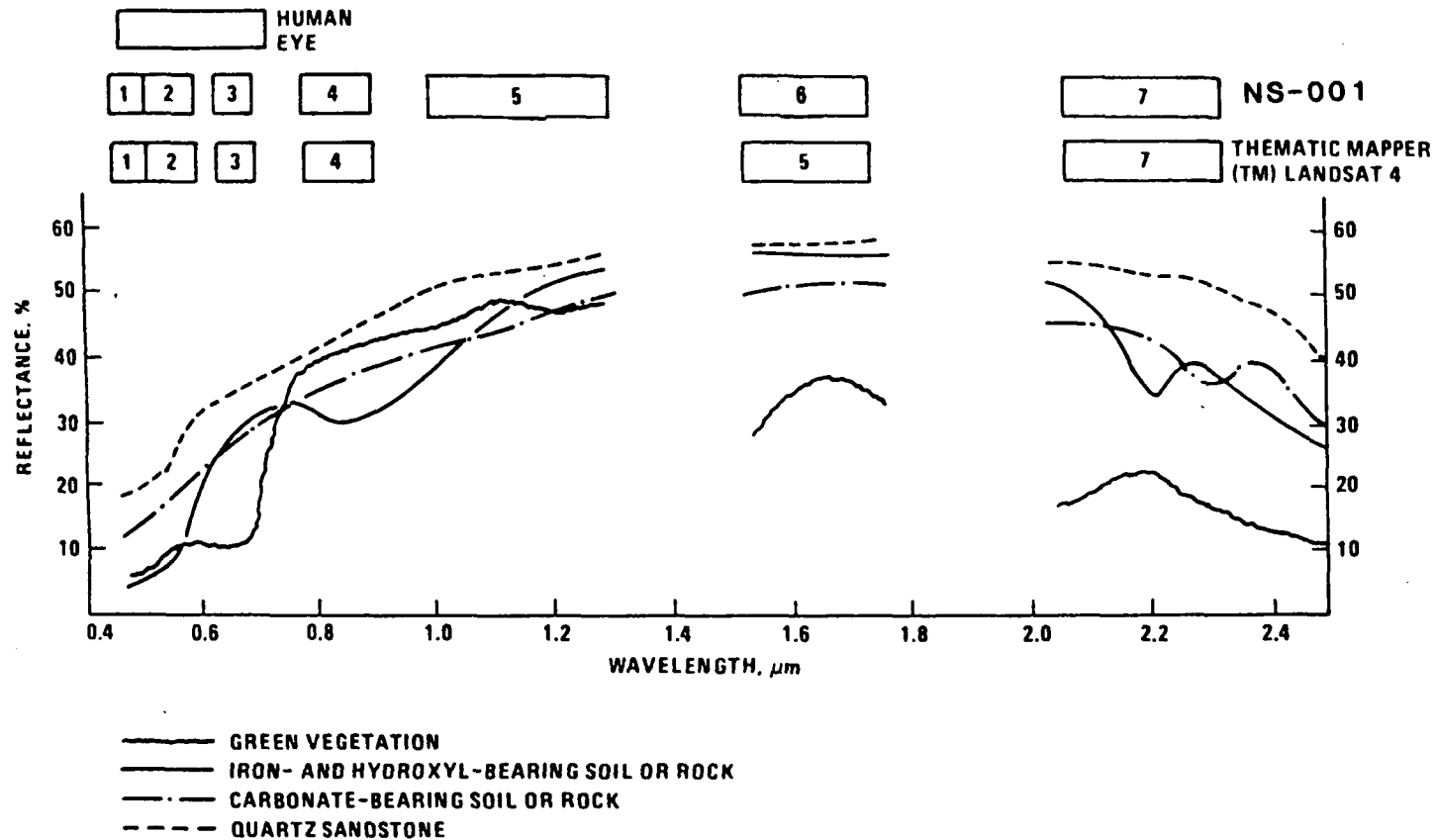
Figure 4.1   Spectra of a variety of rocks and minerals in the VNIR and SWIR (after Abrams *et al.*, 1984).
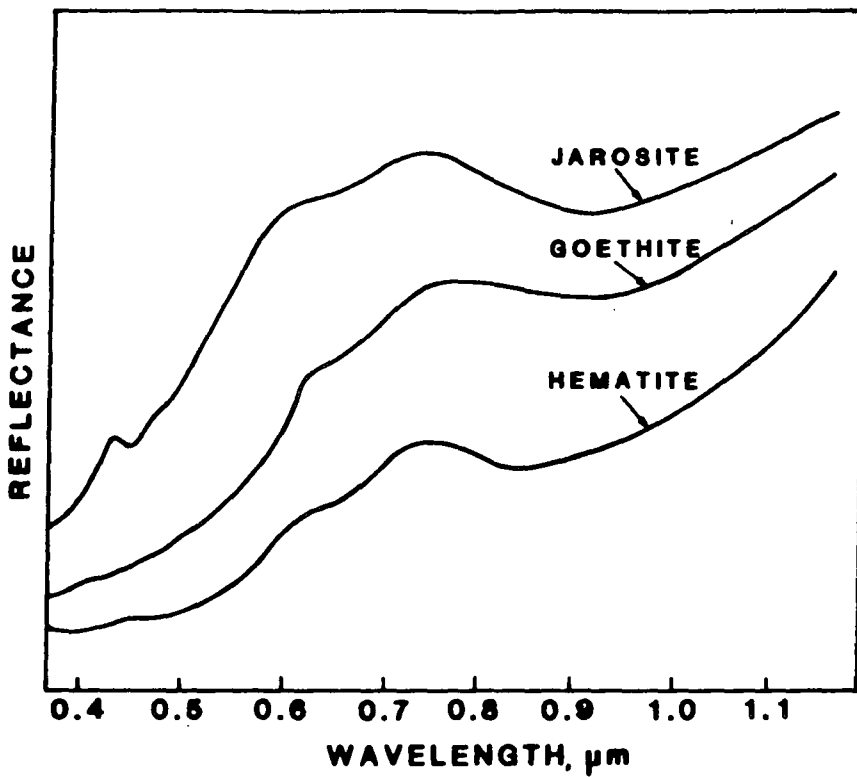
Figure 4.2 Spectra of a variety of Iron Oxides / Hydroxides in the VNIR and SWIR (after Ashley and Hunt 1979).
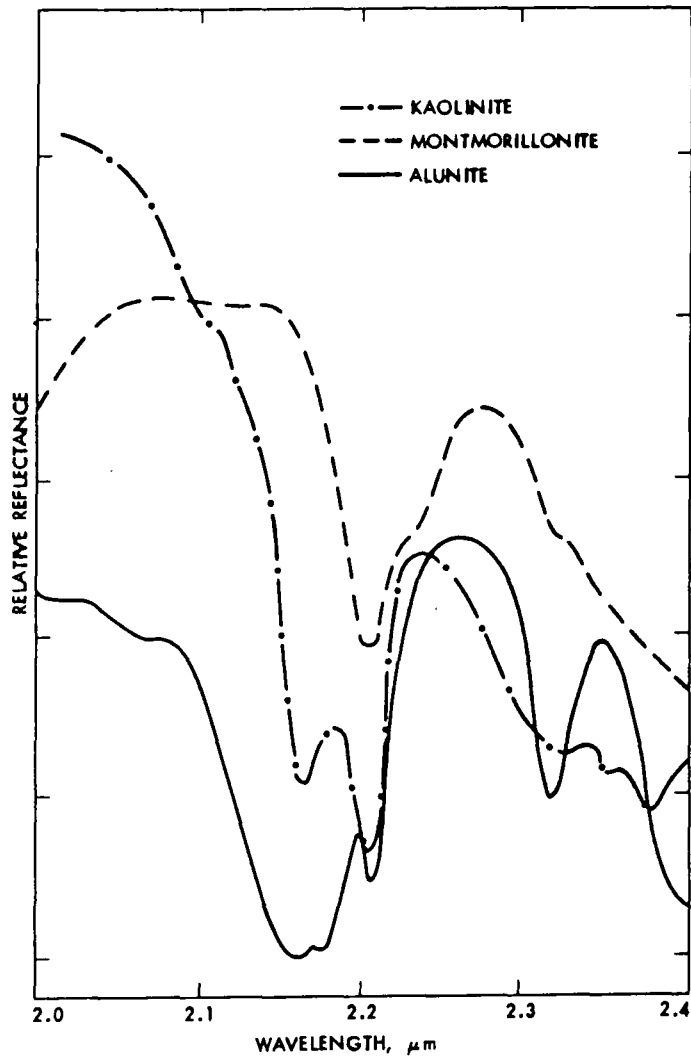
Figure 4.3   Spectra of a variety of hydroxyl bearing minerals in the
2.0 - 2.5μm region (after Abrams *et al.* al 1984).
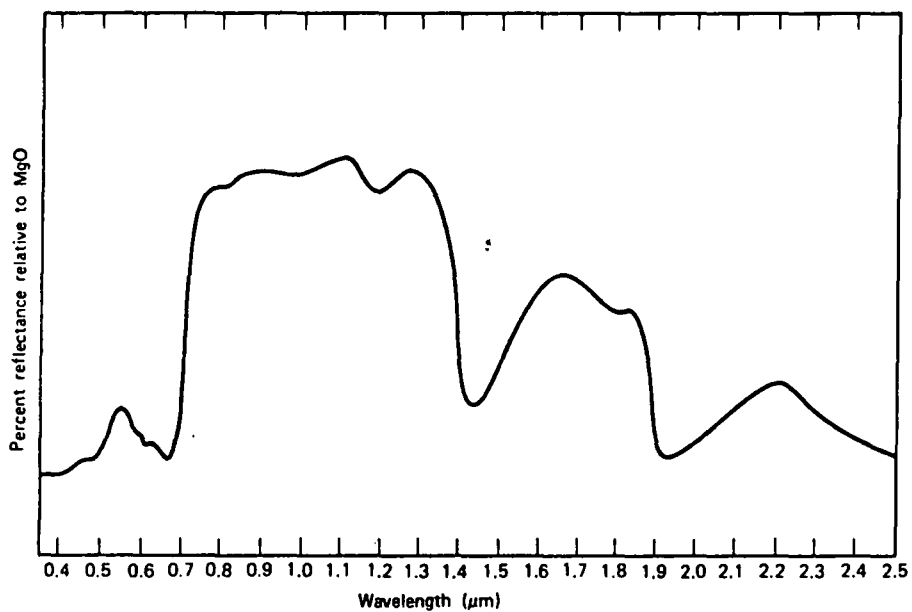
Figure 4.4   Spectrum of a leaf in the VNIR, SWIR region (after Raines
and Coney 1980).
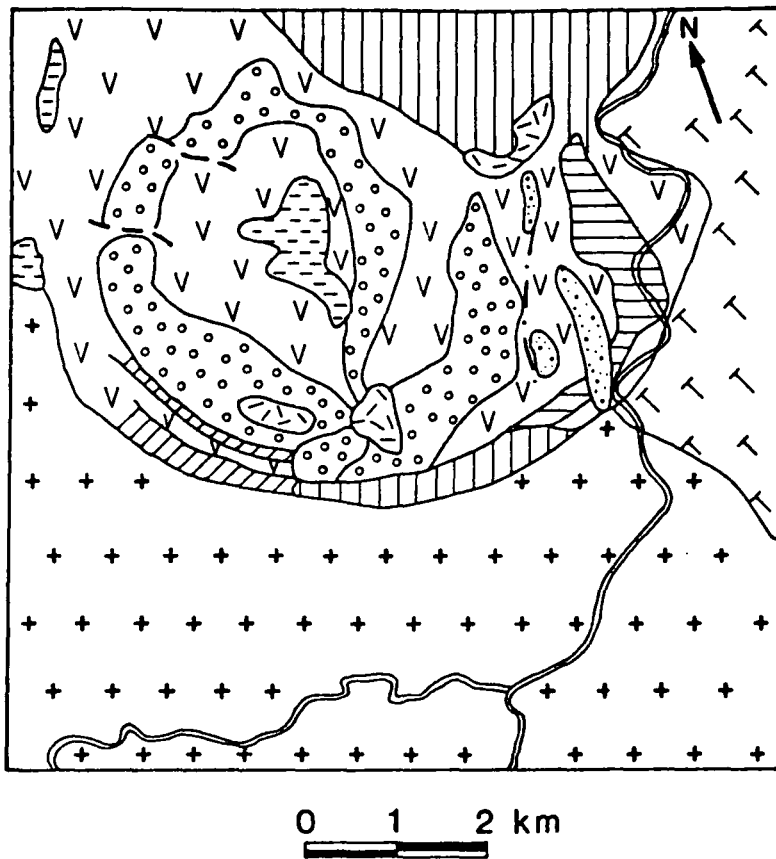
0   1   2 km

MID-UPPER CARBONIFEROUS VOLCANIC ROCKS

[⬚] Undifferentiated Rhyolitic Rocks

[⬚] Rhyolitic Rocks

[⬚] Ignimbrite   Interbeds of Volcanic Breccia and Andesite, Dacite(Rhyolitic ?) Lavas

[V V] Volcanic Breccias

[⬚] Grey Dacite Lavas

[⬚] Andesite Lavas

[⬚] Andesite Lavas of the south

LOWER CARBONIFEROUS SEDIMENTS

[⬚] Red Mudstone

MID ORDOVICIAN TO LOWER DEVONIAN BASEMENT

[⬚] Quartz Feldspar Porphyry

[+ +] Granodiorite

Figure 4.5   Geology of the Camp Oven Test Site (after Lorraway 1976).
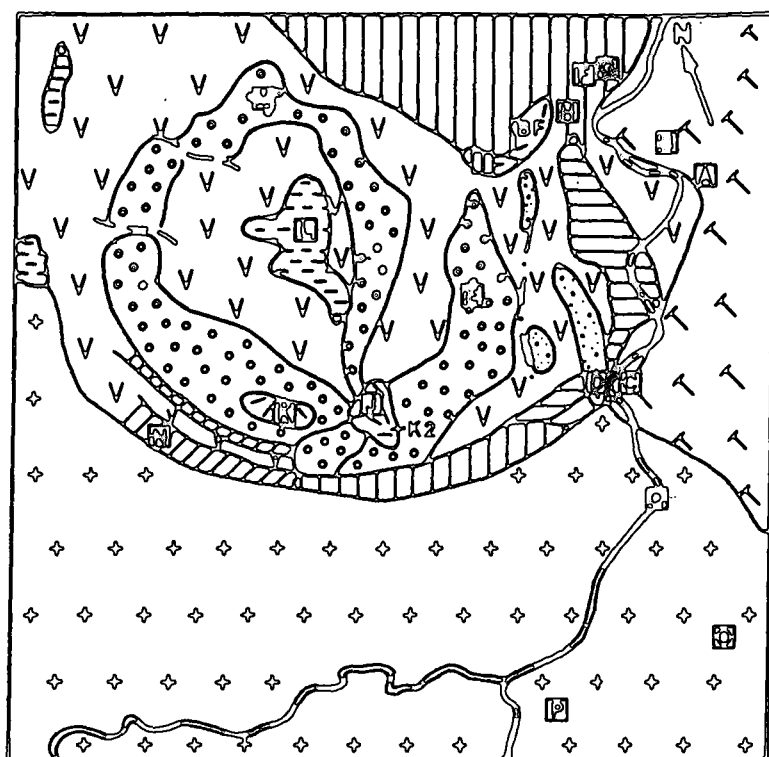
0   1   2 km

MID-UPPER CARBONIFEROUS VOLCANIC ROCKS

Undifferentiated Rhyolitic Rocks

Rhyolitic Rocks

Ignimbrite   Interbeds of Volcanic Breccia and Andesite, Dacite(Rhyolitic ?) Lavas

Volcanic Breccias

Grey Dacite Lavas

Andesite Lavas

Andesite Lavas of the south

LOWER CARBONIFEROUS SEDIMENTS

Red Mudstone

MID ORDOVICIAN TO LOWER DEVONIAN BASEMENT

Quartz Feldspar Porphyry

Granodiorite

BF   Blackfollow Mountain

K2

Figure 4.6   Location of the subsites within the Camp Oven Test Site.

147
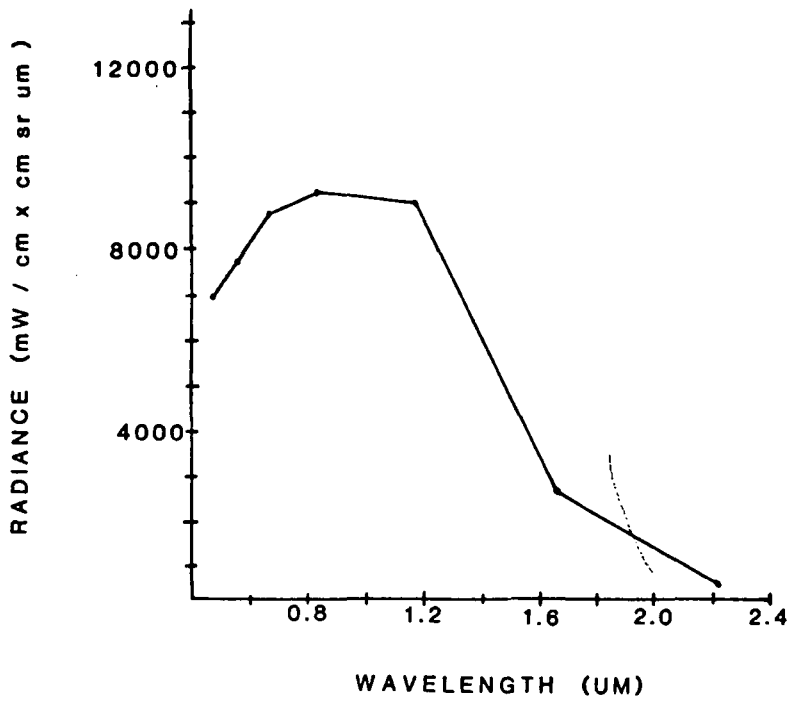
Figure 4.7   Radiance spectrum from subsite A.
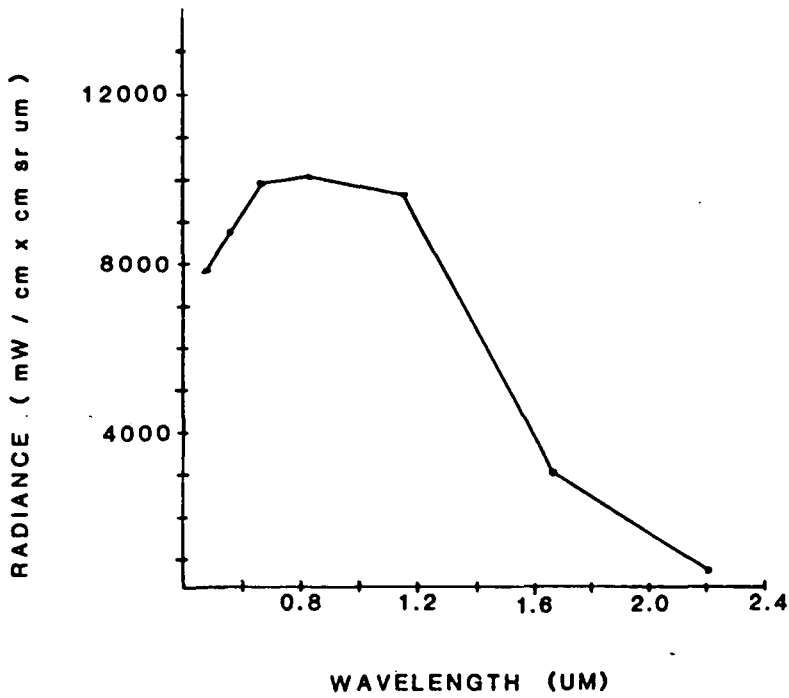
Figure 4.8   Radiance spectrum from subsite B.

148
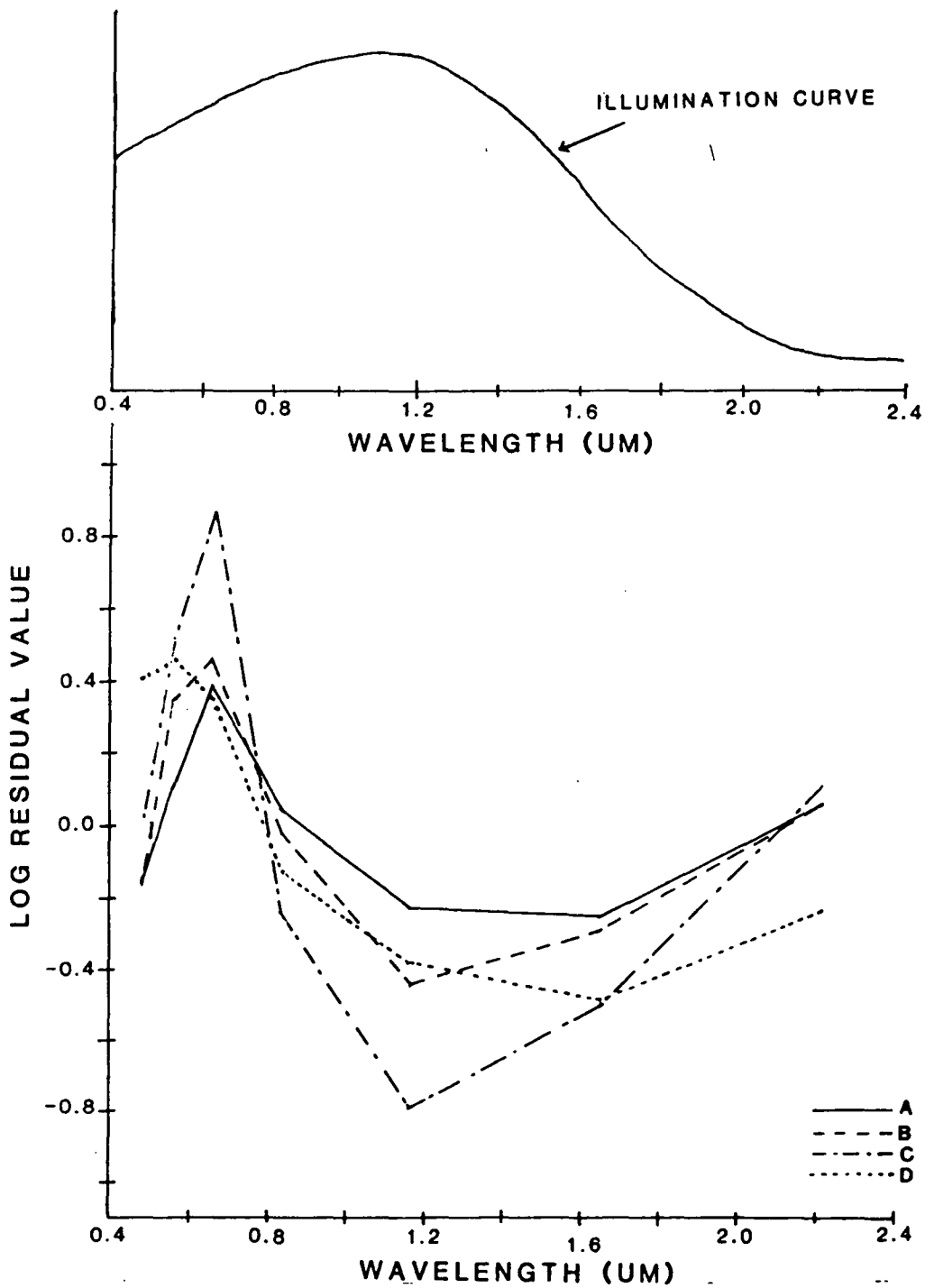
Figure 4.9 Log residual spectra from subsite A-D and solar illumination curve derived using channel means.
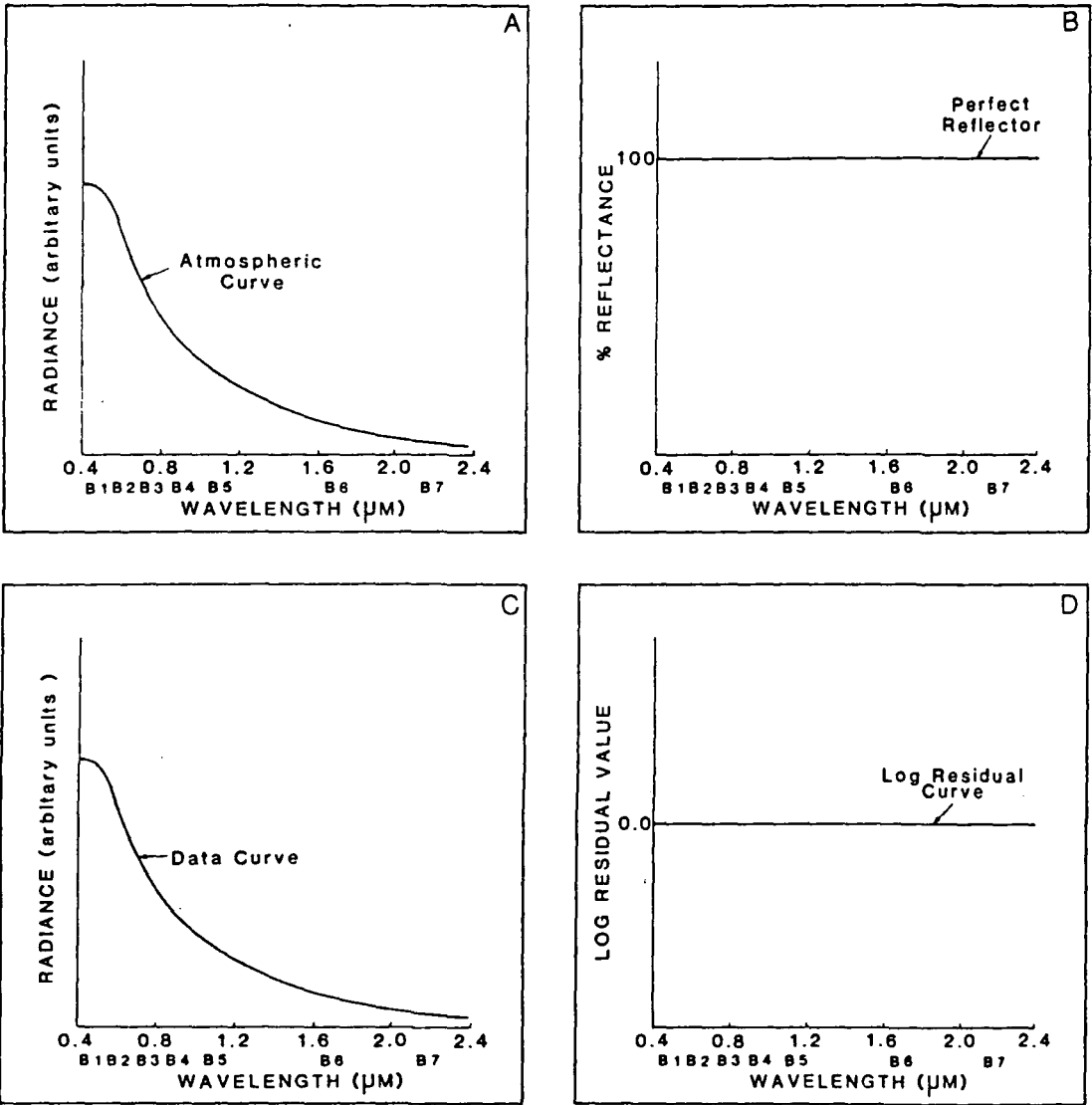
Figure 4.10   Illustration of part of the log residual calculation for a perfect reflector.
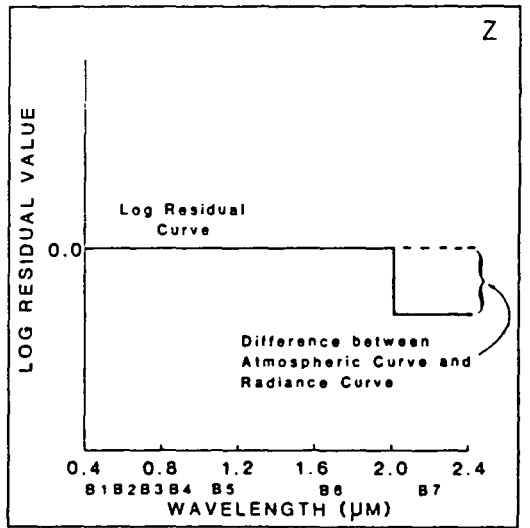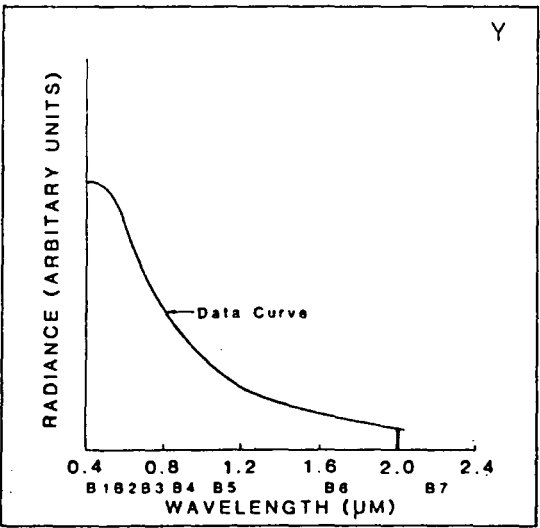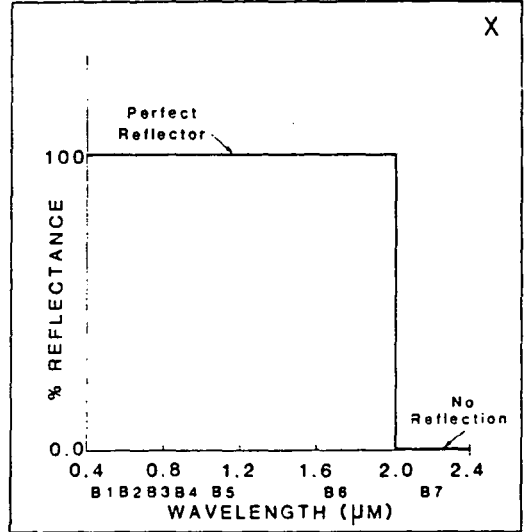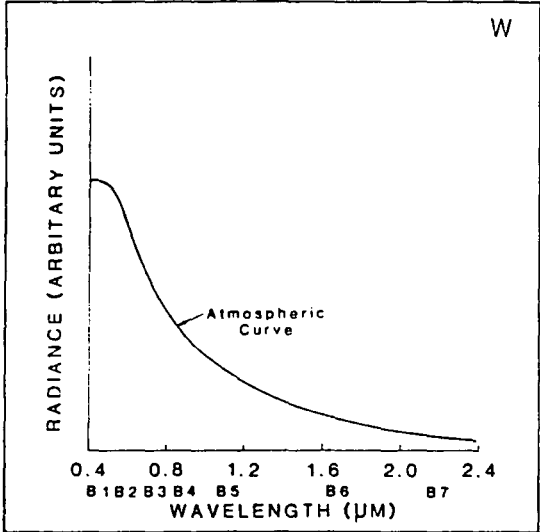
Figure 4.11   Illustration of part of the log residual calculation for a non perfect reflector.

151
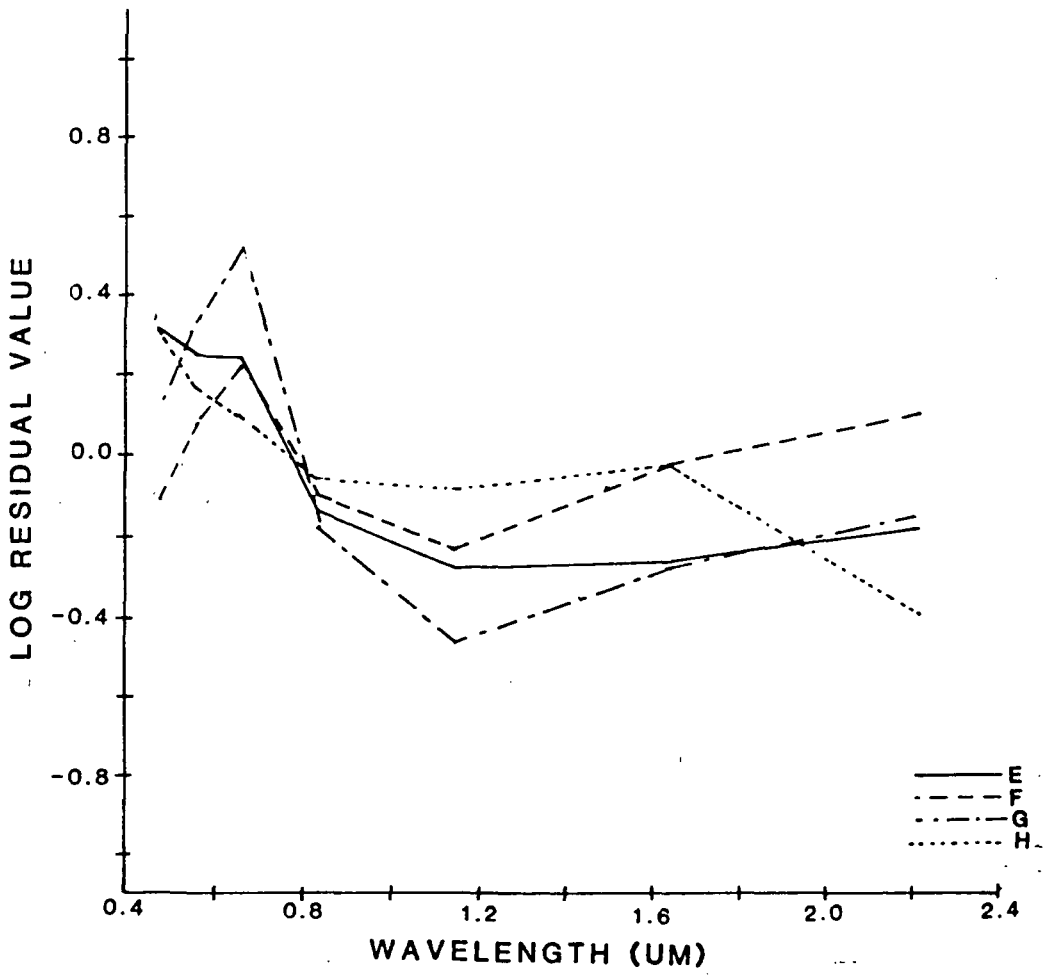
Figure 4.12   Log residual spectra from subsites E-H.
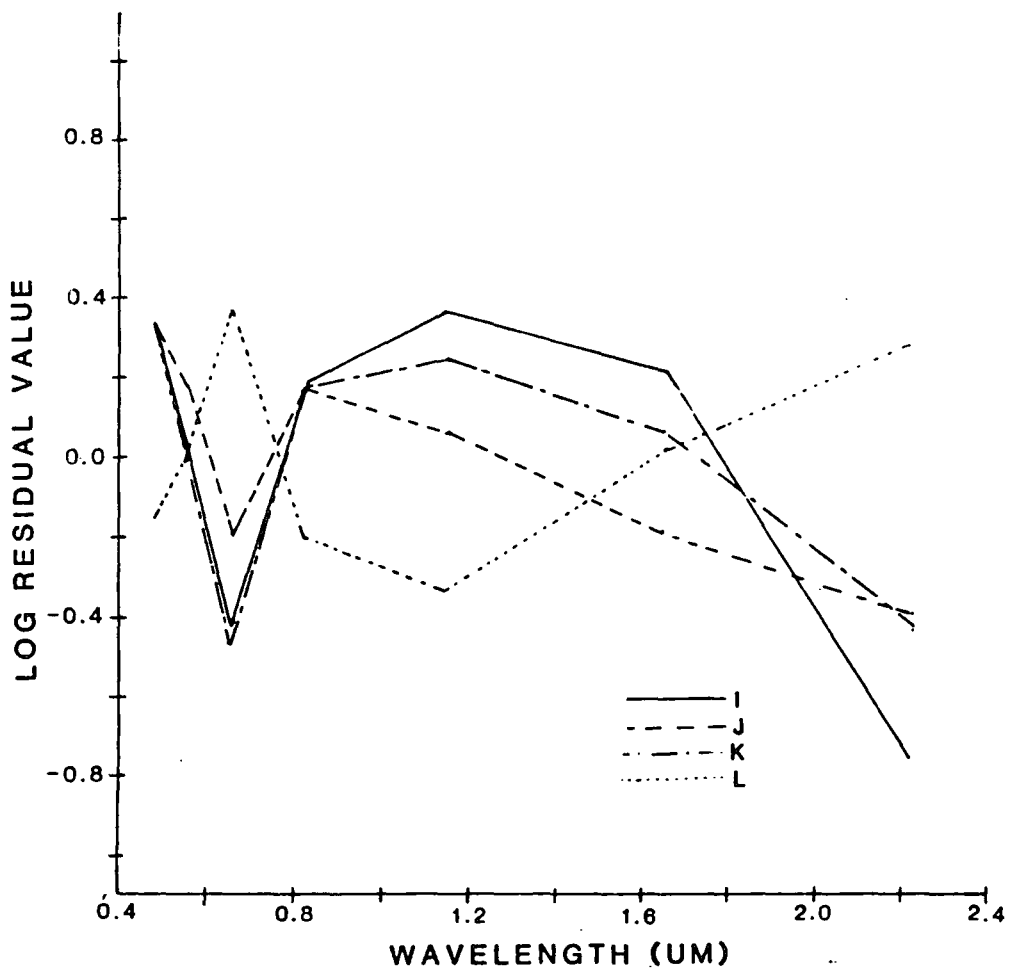
Figure 4.13   Log residual spectra from subsites I-L.
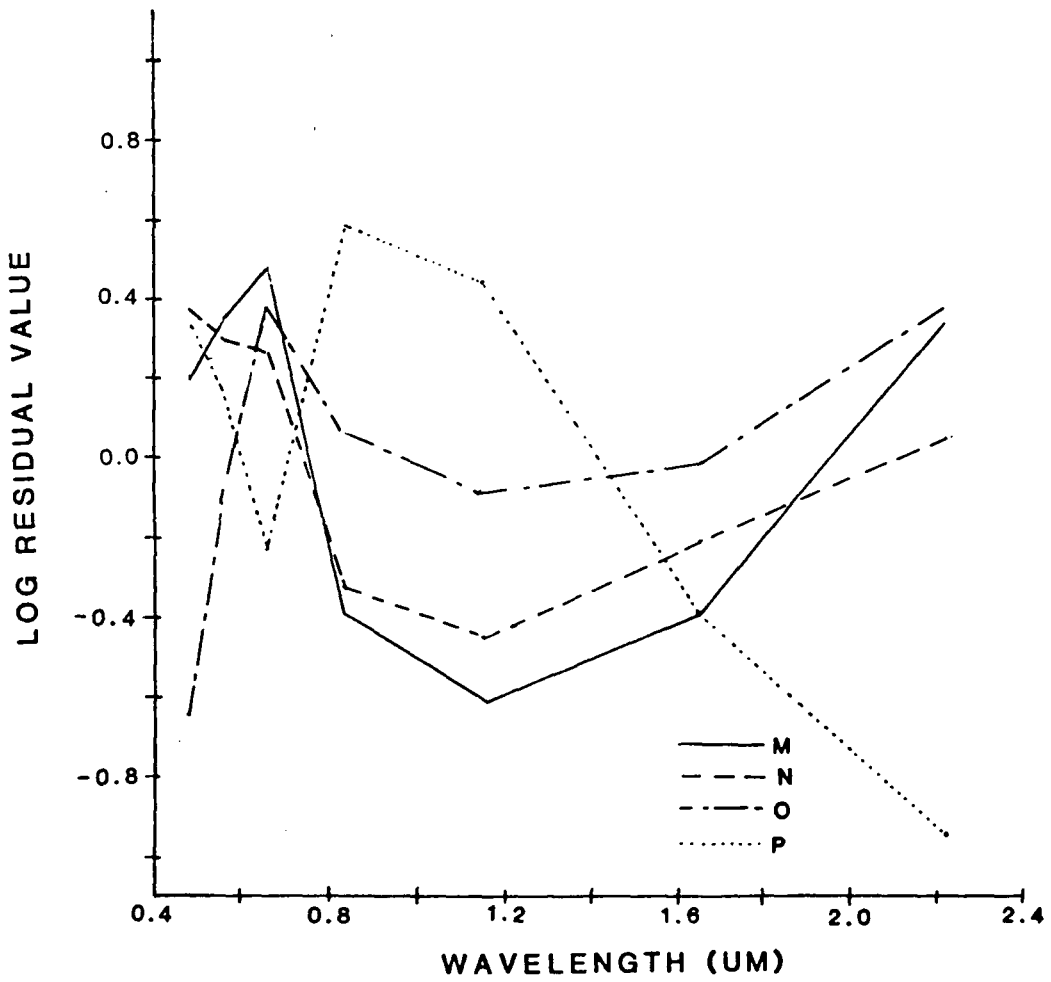
Figure 4.14   Log residual spectra from subsites M-P.
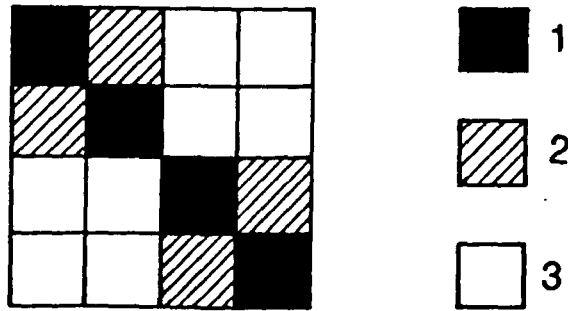
Figure 4.15 Schematic representation of mixing at the sub-pixel level for one pixel (after Green pers. comm. 1987).
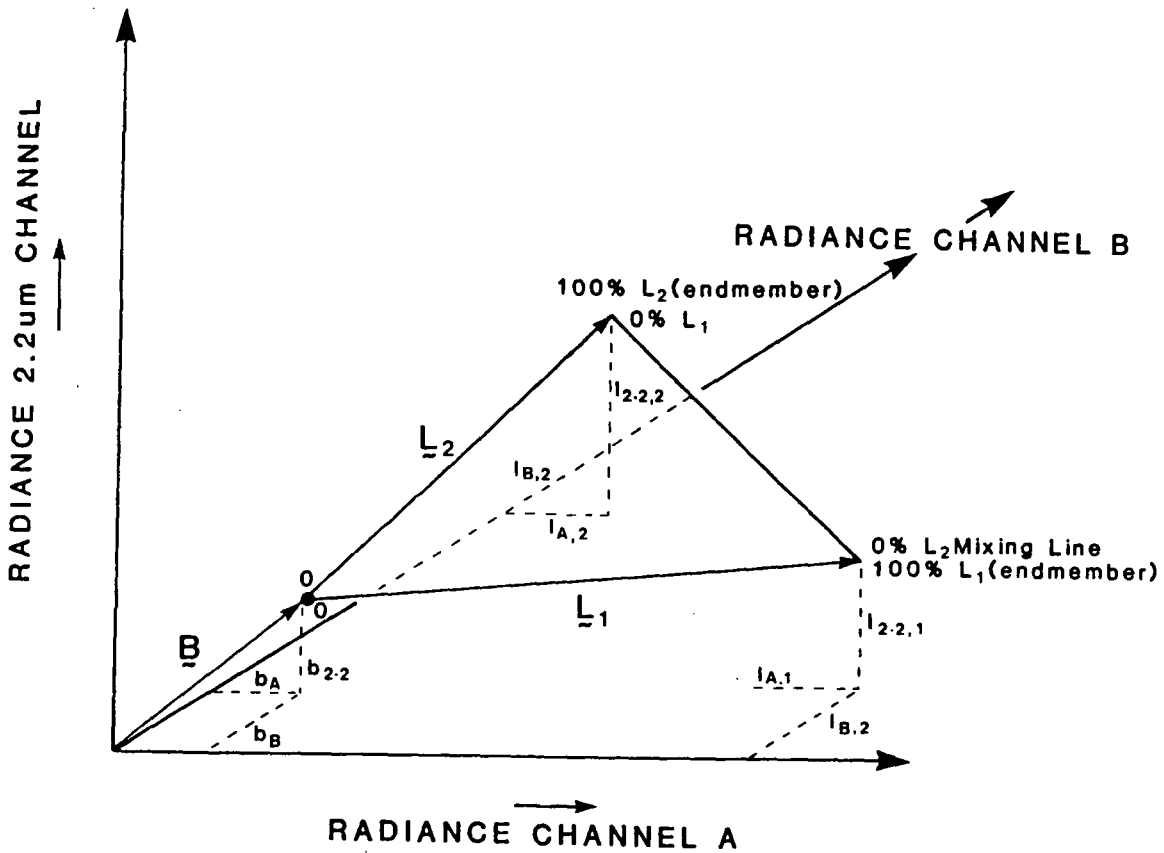
Figure 4.16 Schematic representation of mixing involving two materials and three channels (after Green pers. comm. 1987).
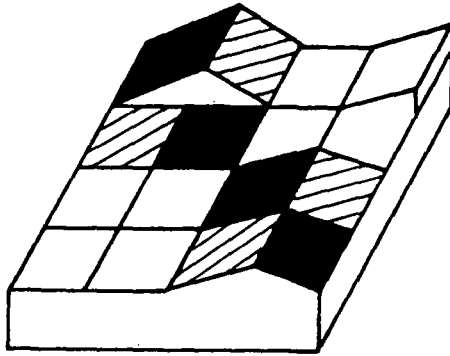
Figure 4.17   Schematic representation of mixing with varying exposure
at the sub-pixel level for one pixel (after Green pers. comm. 1987).
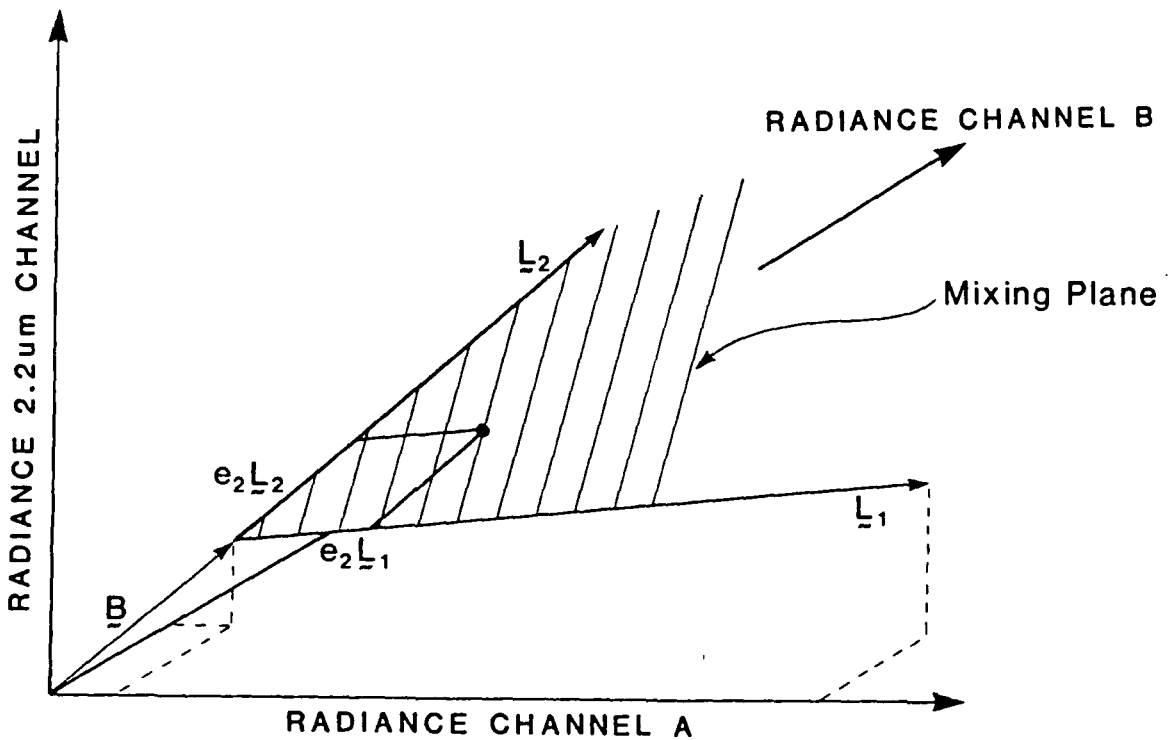
Figure 4.18   Schematic representation of mixing involving two materials
and three channels with varying exposure (after Green pers. comm.
1987).
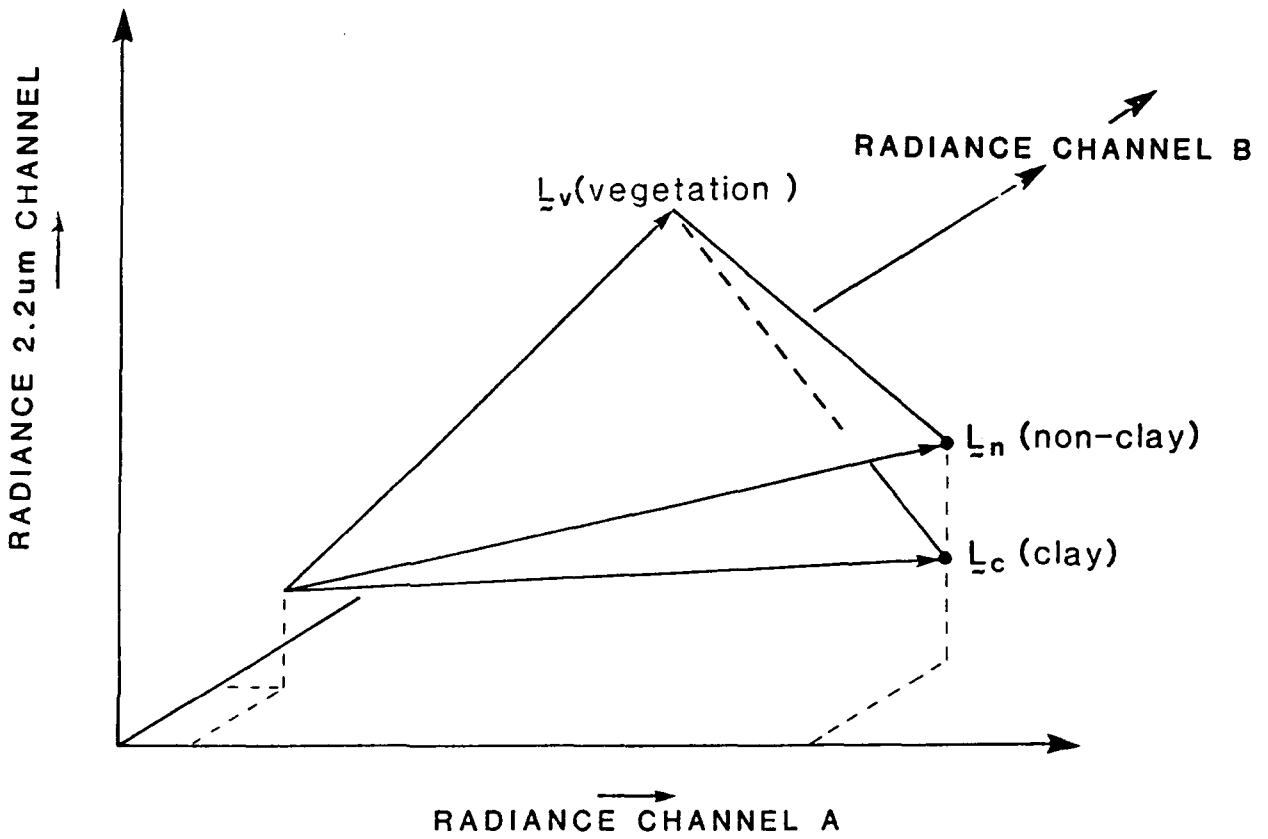
Figure 4.19 Schematic representation of mixing involving three materials and three channels with varying exposure (after Green pers. comm. 1987).
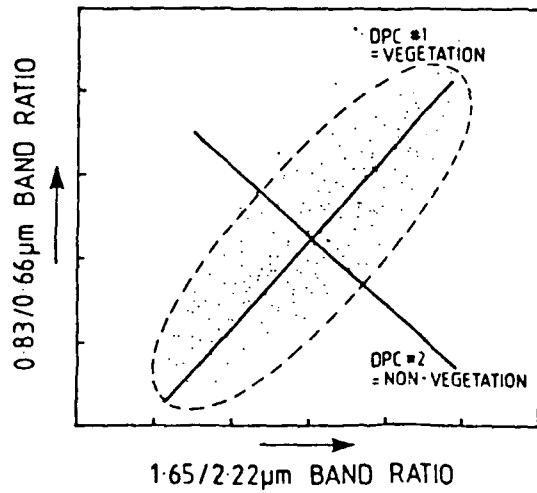
Figure 4.20   Schematic representation of the DPC method (after Fraser and Green 1987).
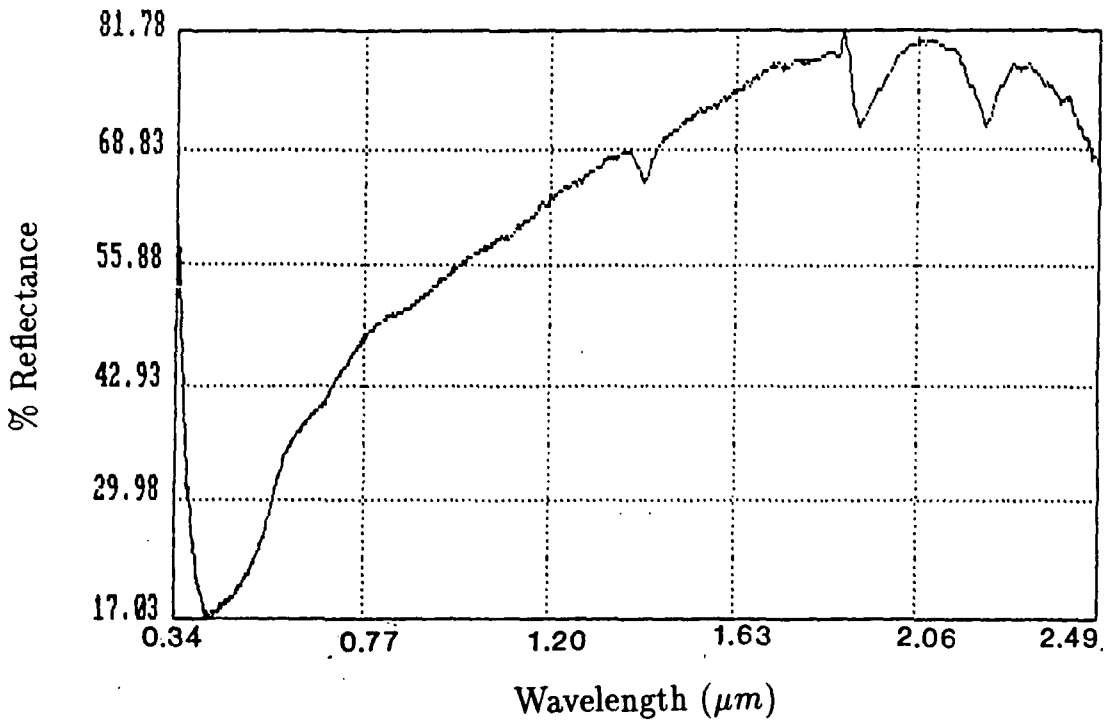
Figure 4.21   Lab. spectrum of the external surface of a sample collected at subsite A.
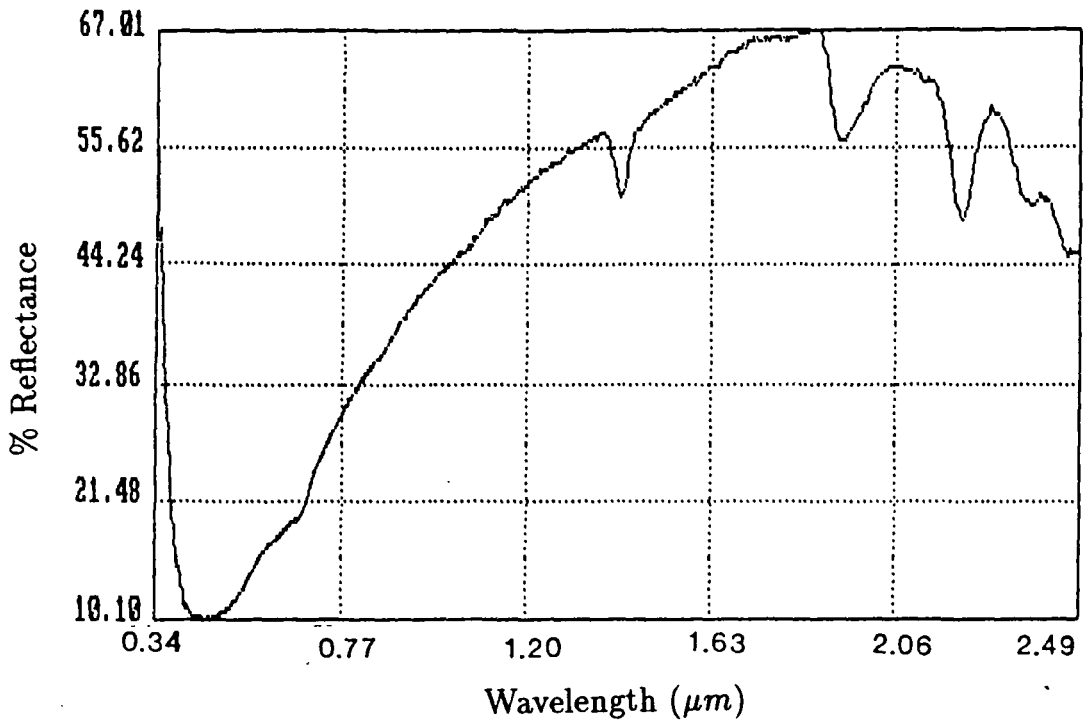
Figure 4.22   Lab. spectrum of the external surface of a sample collected at subsite A.
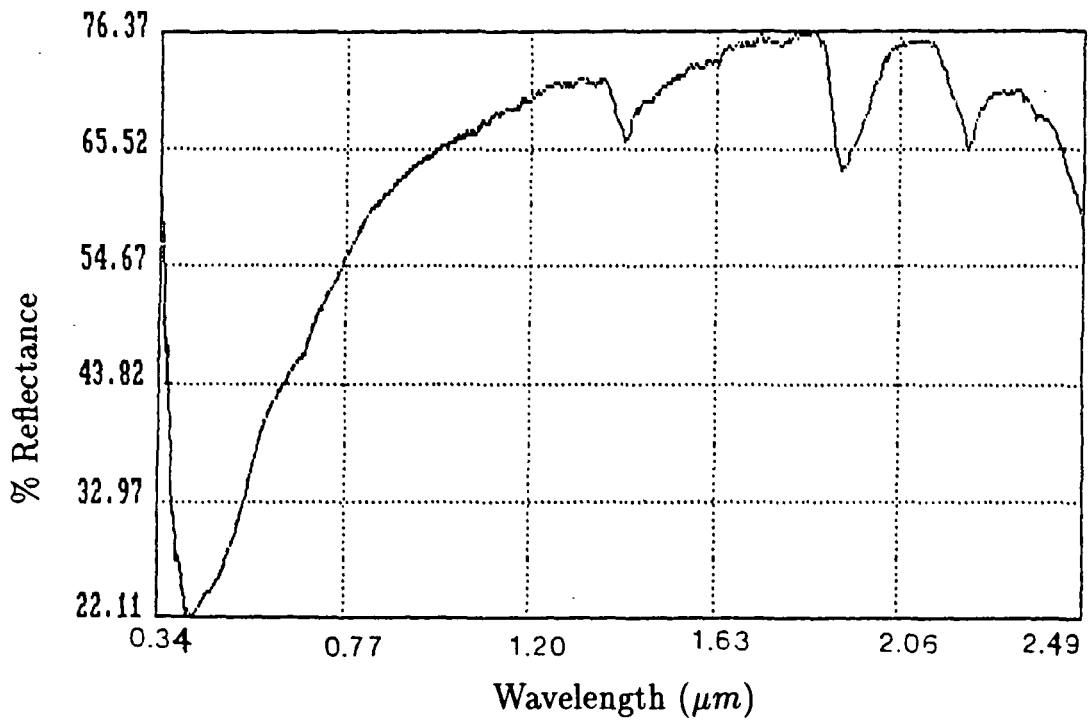
Figure 4.23   Lab. spectrum of the external surface of a sample collected at subsite B.

159
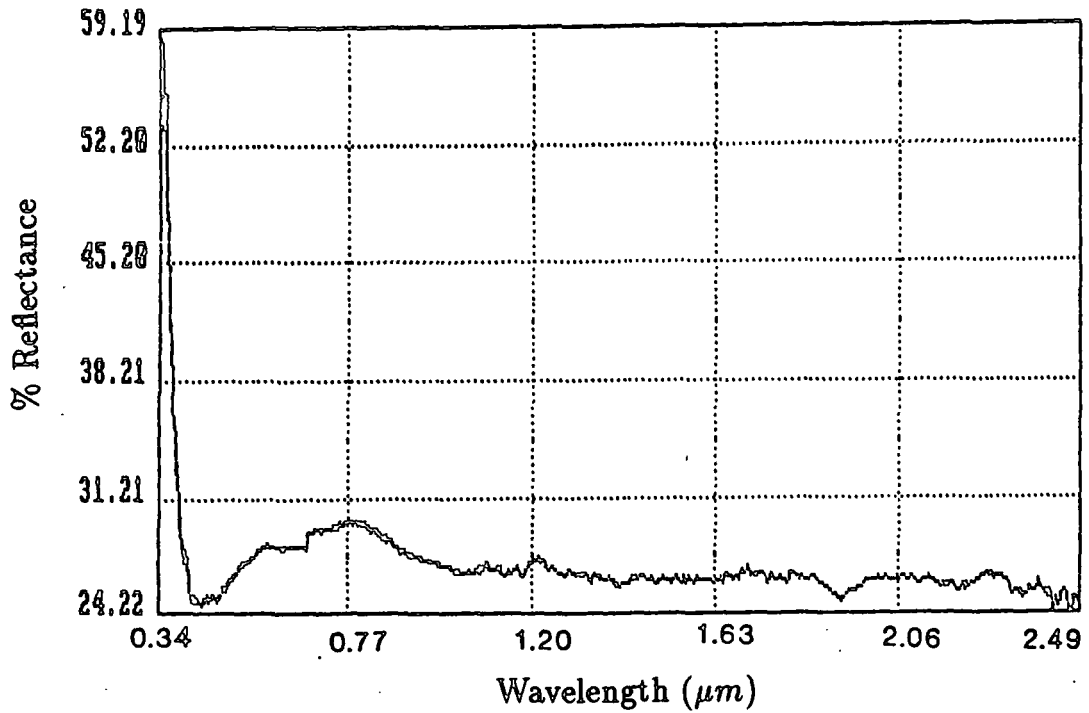
Figure 4.24   Lab. spectrum of the internal surface of a sample collected
at subsite B
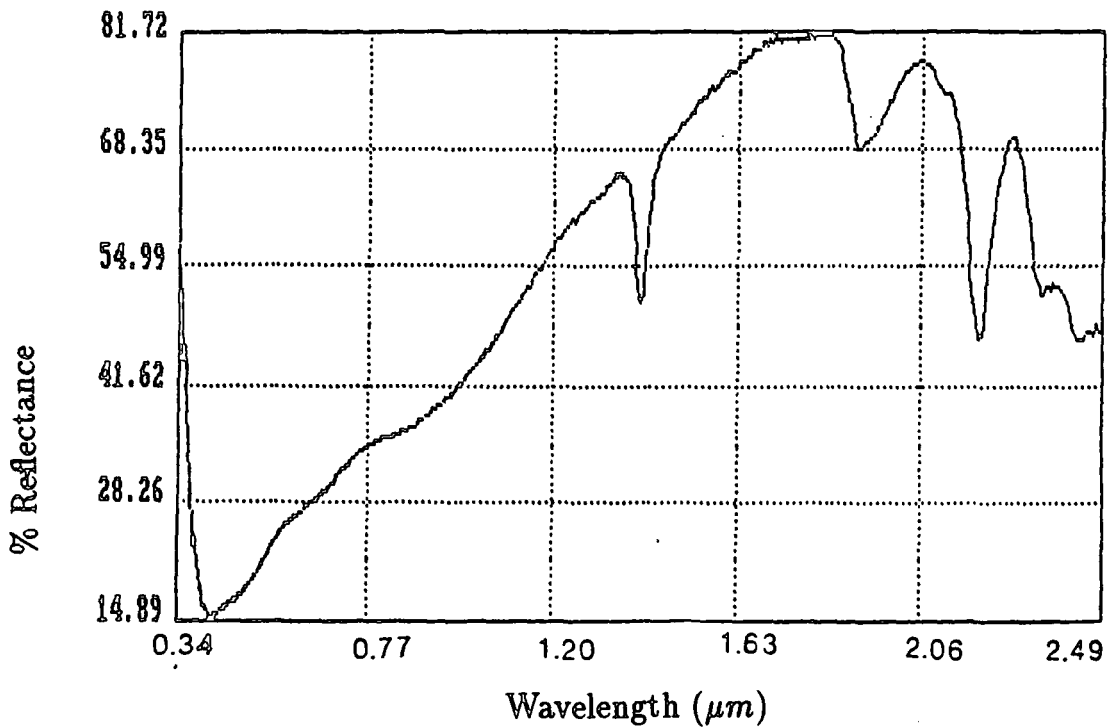
Figure 4.25   Lab. spectrum of the external surface of a sample collected
at subsite C.
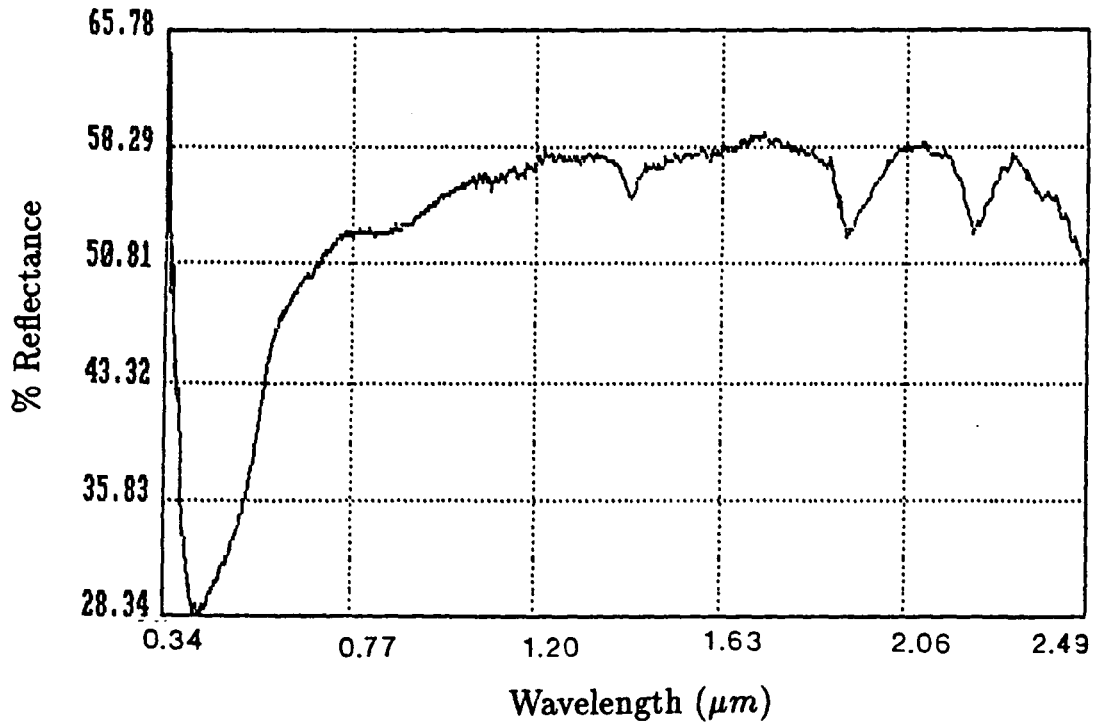
Figure 4.26 Lab. spectrum of the external surface of a sample collected
at subsite D.
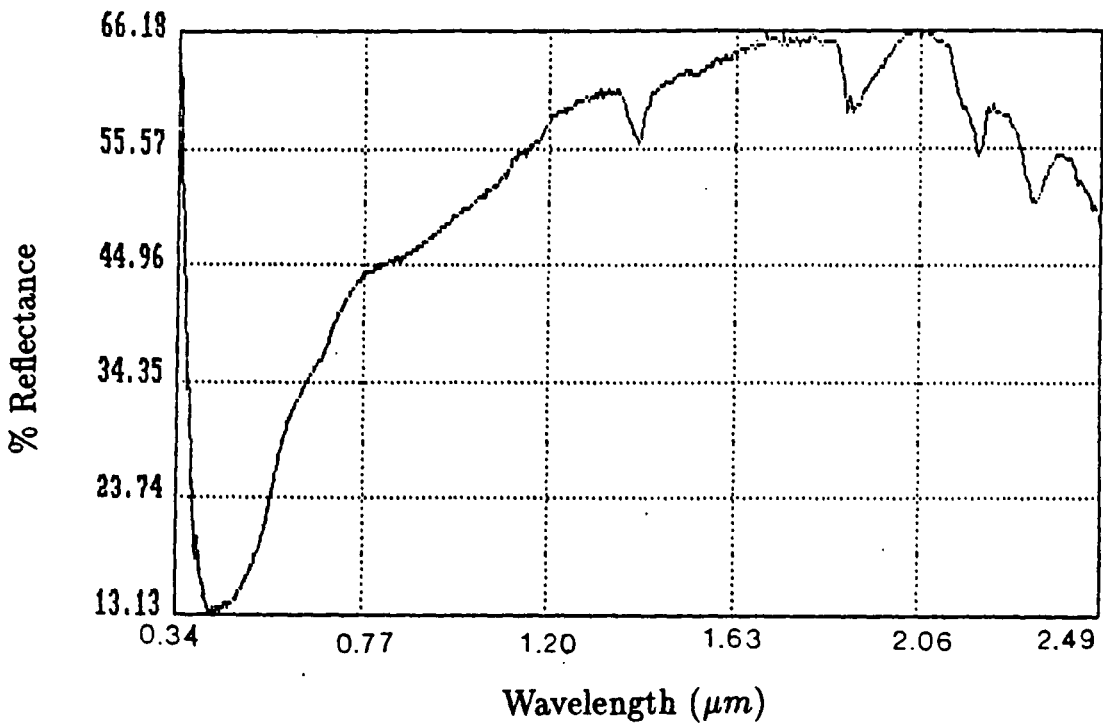
Figure 4.27 Lab. spectrum of the external surface of a sample collected
at subsite E.
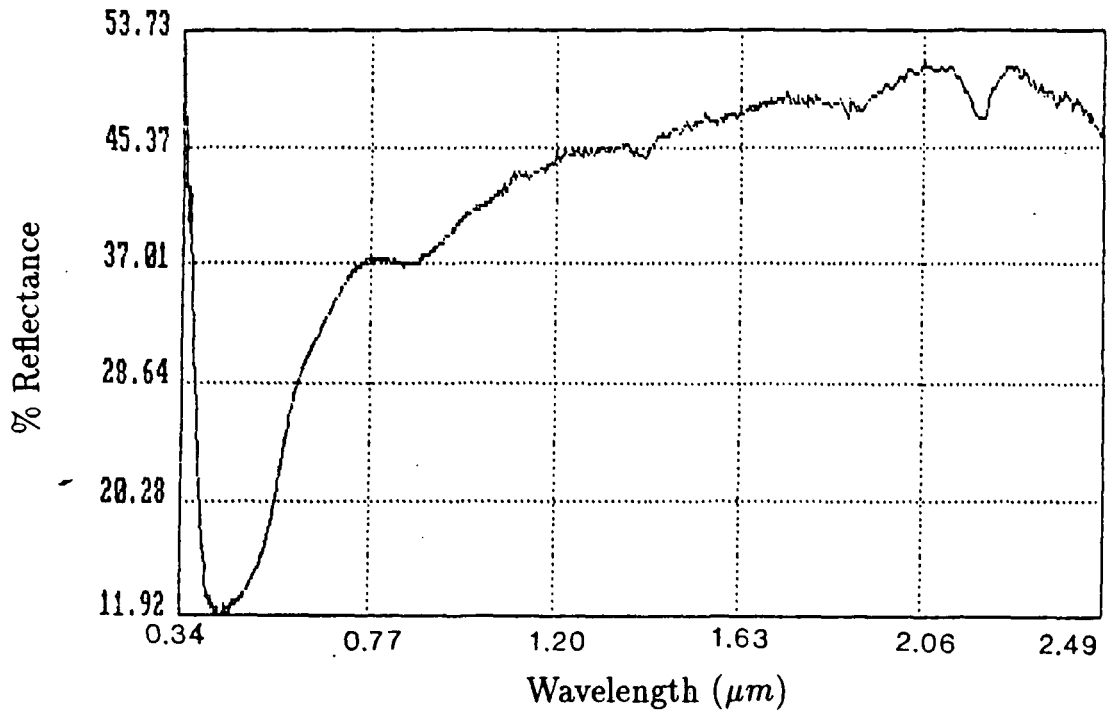
Figure 4.28   Lab. spectrum of the external surface of a sample collected
at subsite E.
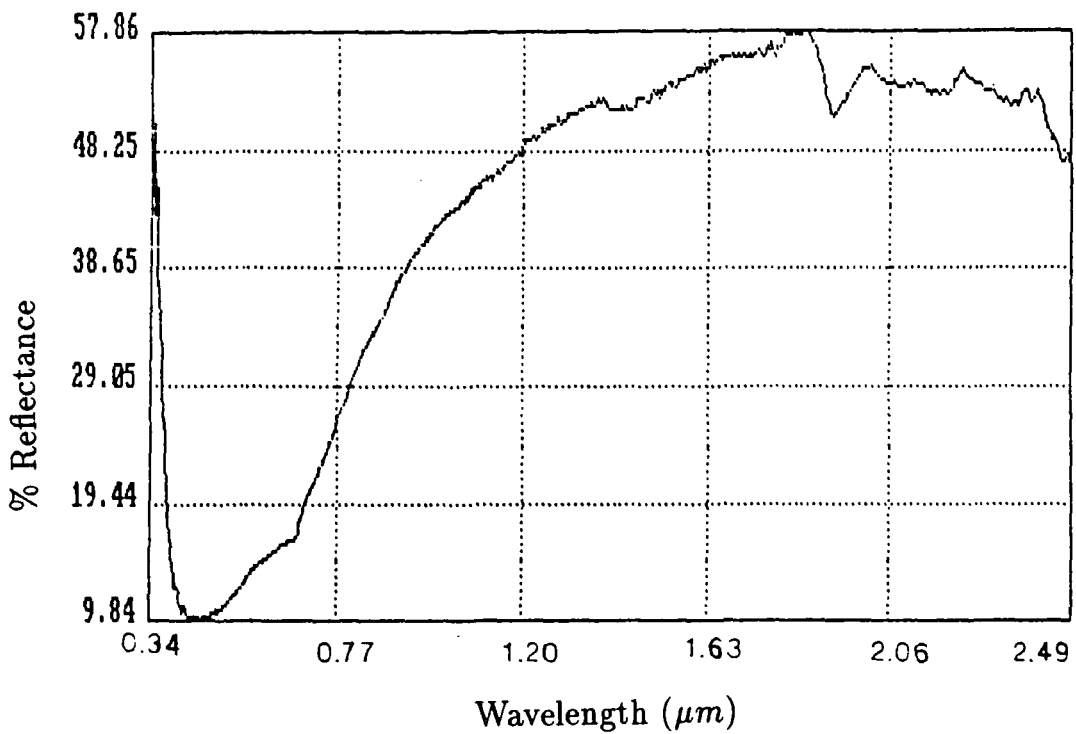
Figure 4.29   Lab. spectrum of the external surface of a sample collected
at subsite F.
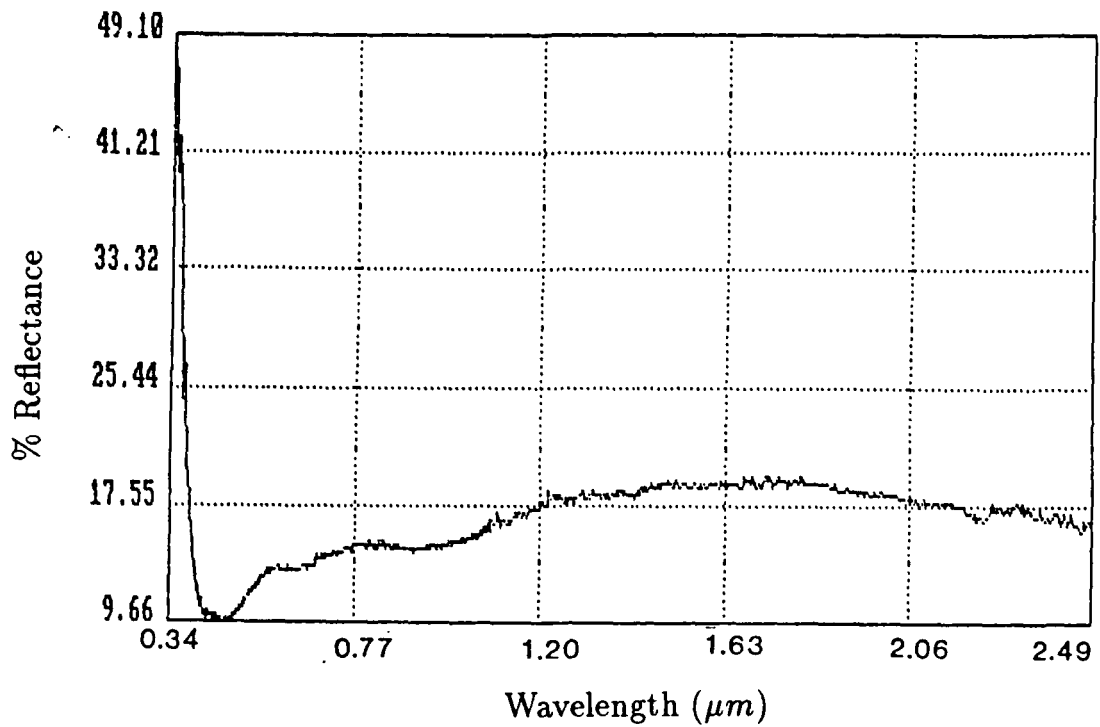
Figure 4.30 Lab. spectrum of the external surface of a sample collected at subsite G.
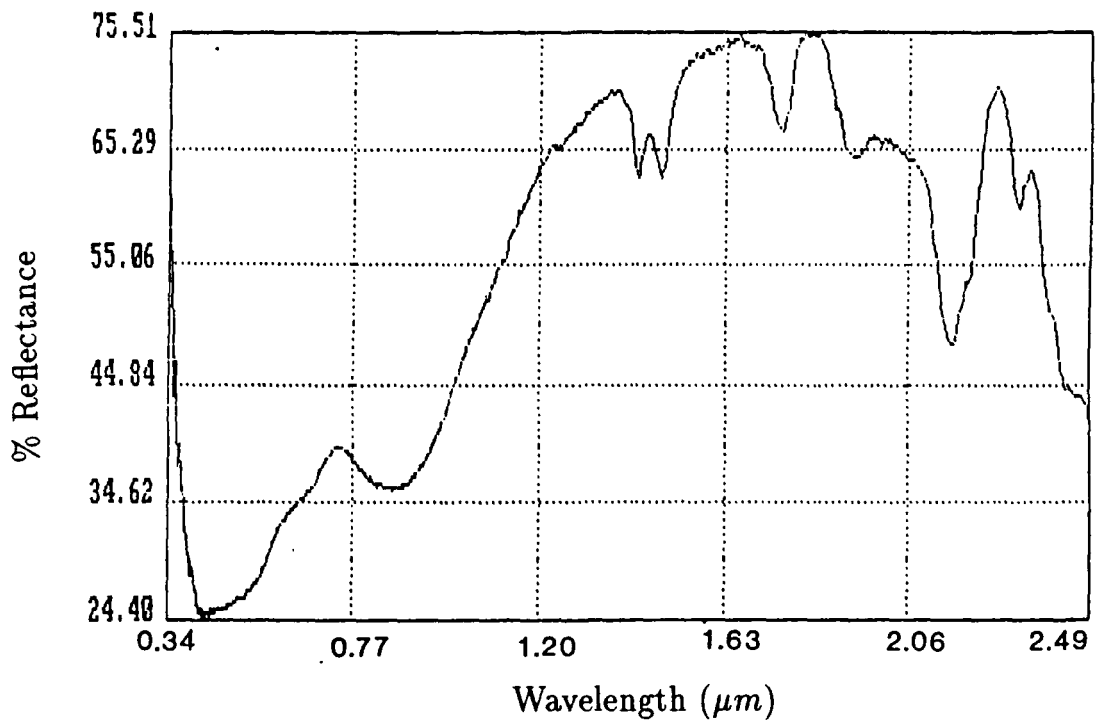
Figure 4.31 Lab. spectrum of the external surface of a sample collected at subsite H.
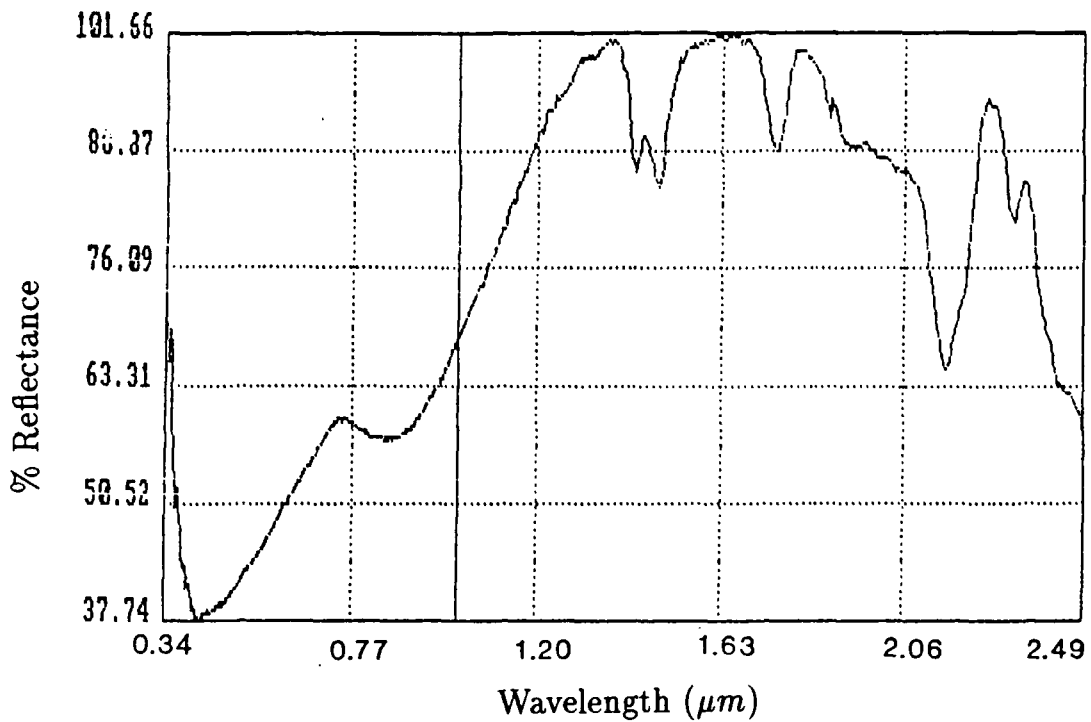
Figure 4.32   Lab. spectrum of the internal surface of a sample collected at subsite H.
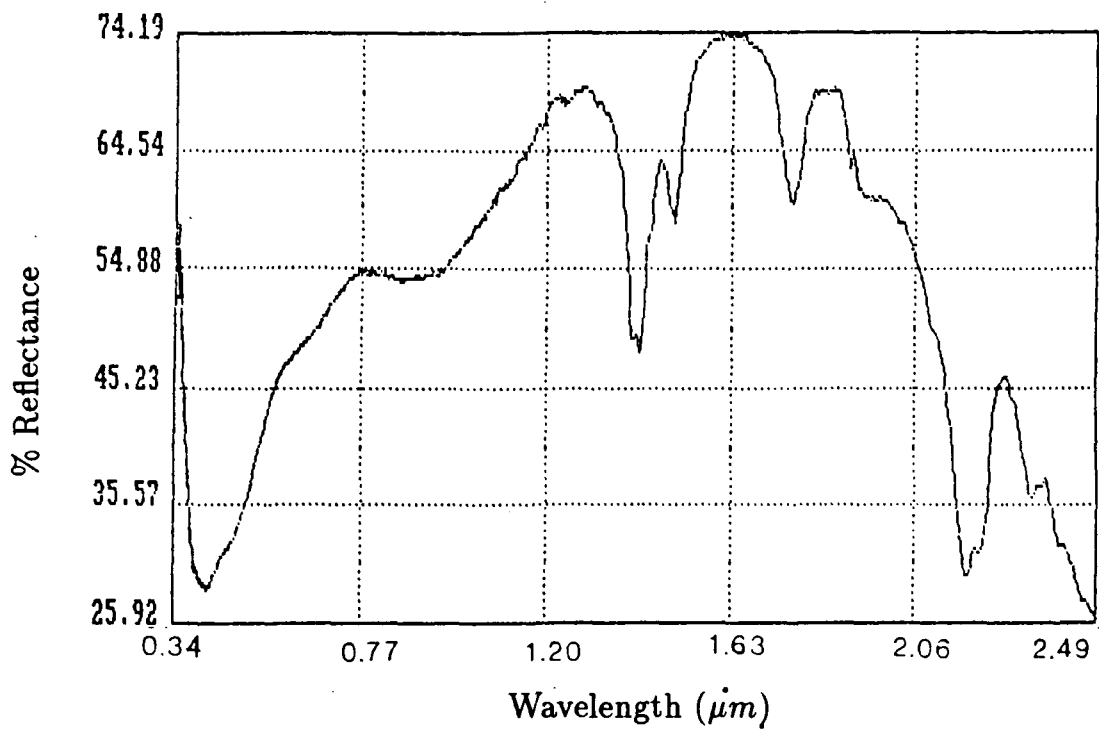
Figure 4.33   Lab. spectrum of the external surface of a sample collected at subsite I.
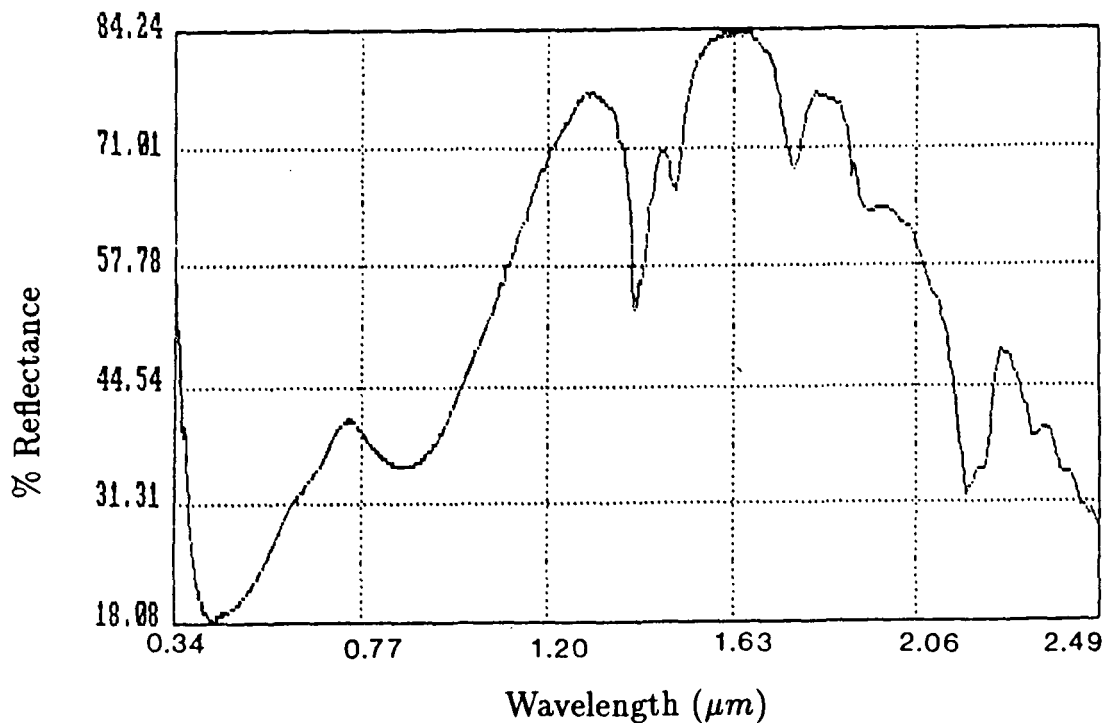
Figure 4.34   Lab. spectrum of the internal surface of a sample collected
at subsite I.
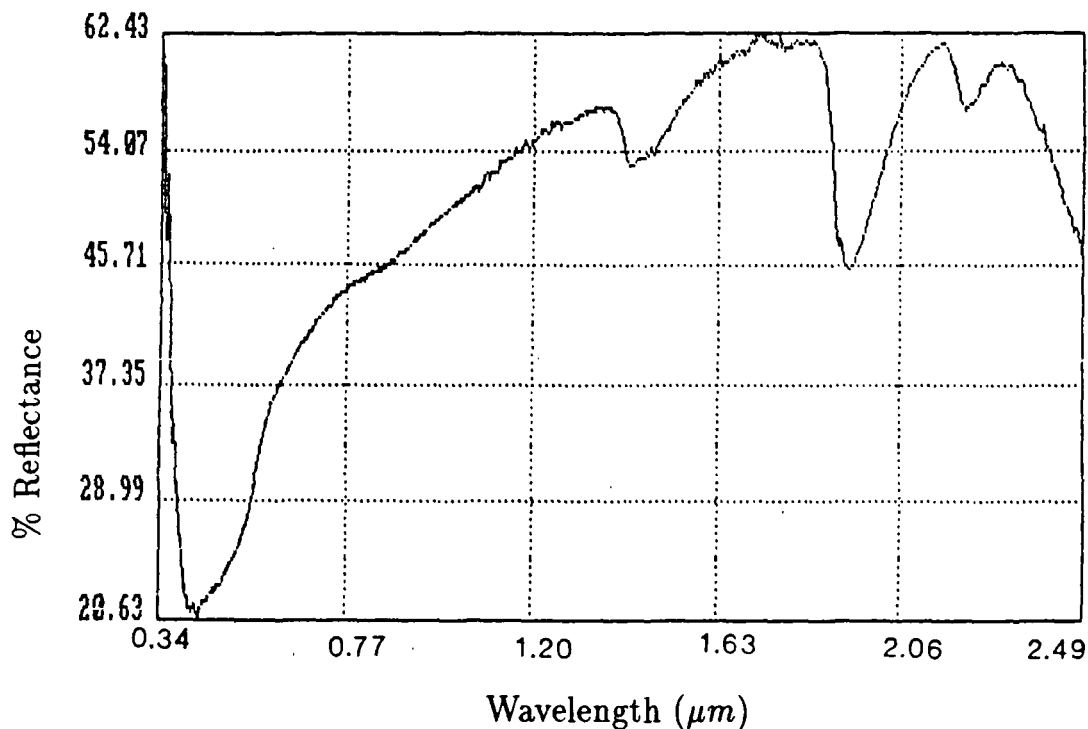
Figure 4.35   Lab. spectrum of the external surface of a sample collected
at subsite J.
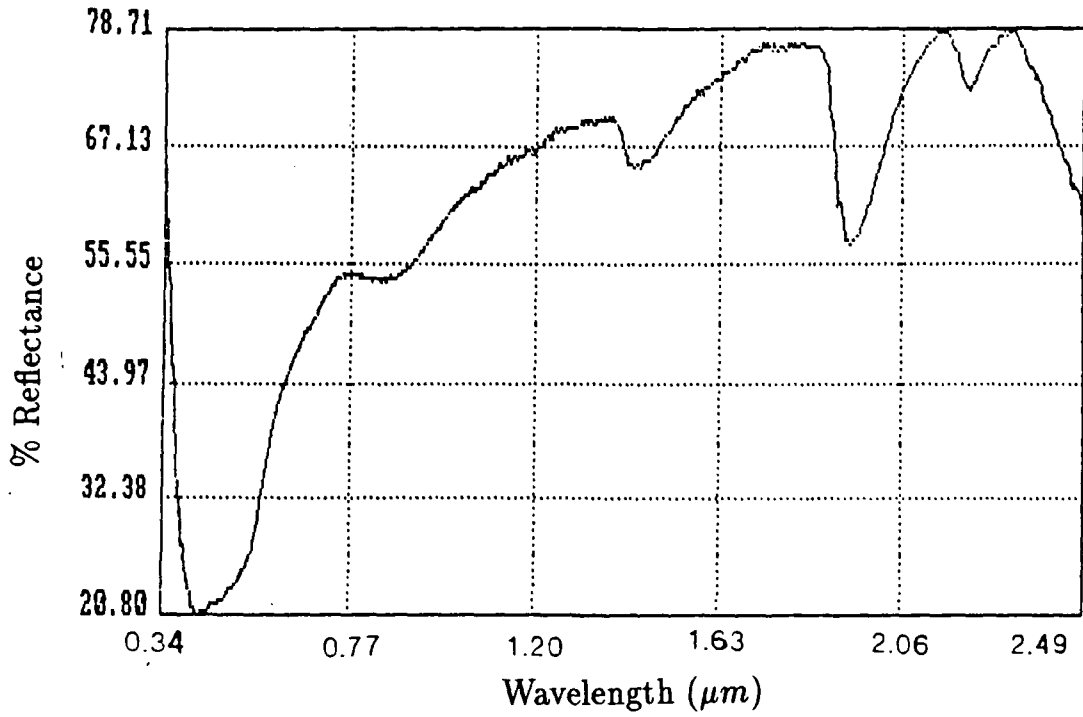
Figure 4.36   Lab. spectrum of the internal surface of a sample collected at subsite J.
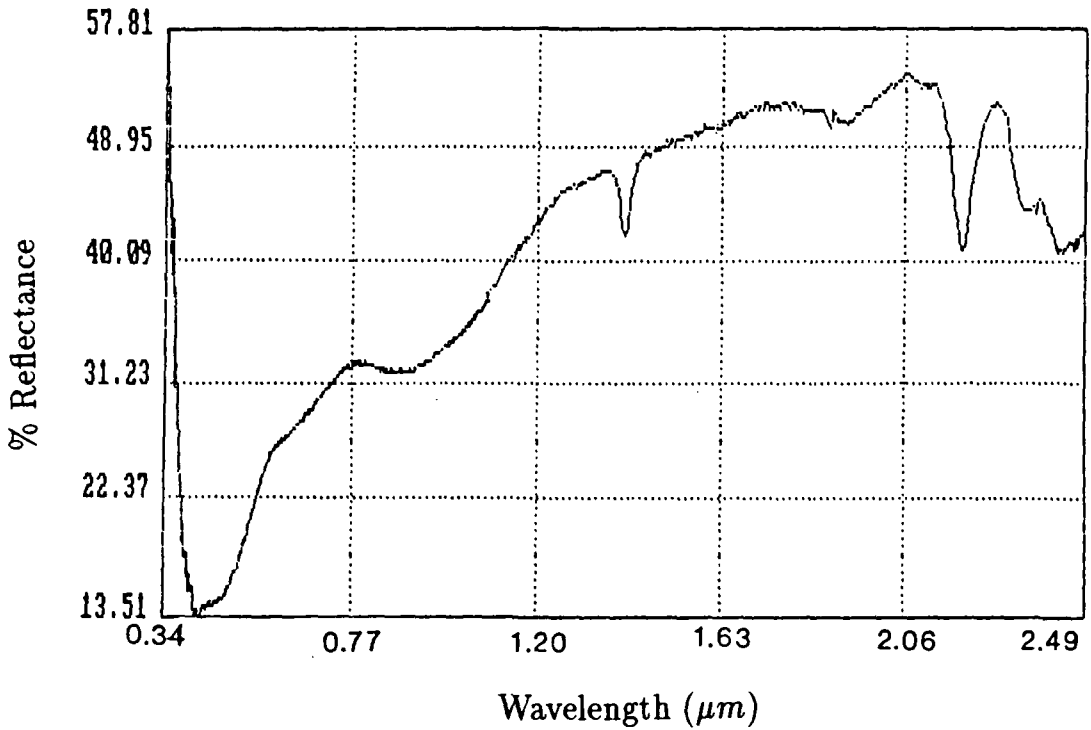
Figure 4.37   Lab. spectrum of the external surface of a sample collected at subsite K.
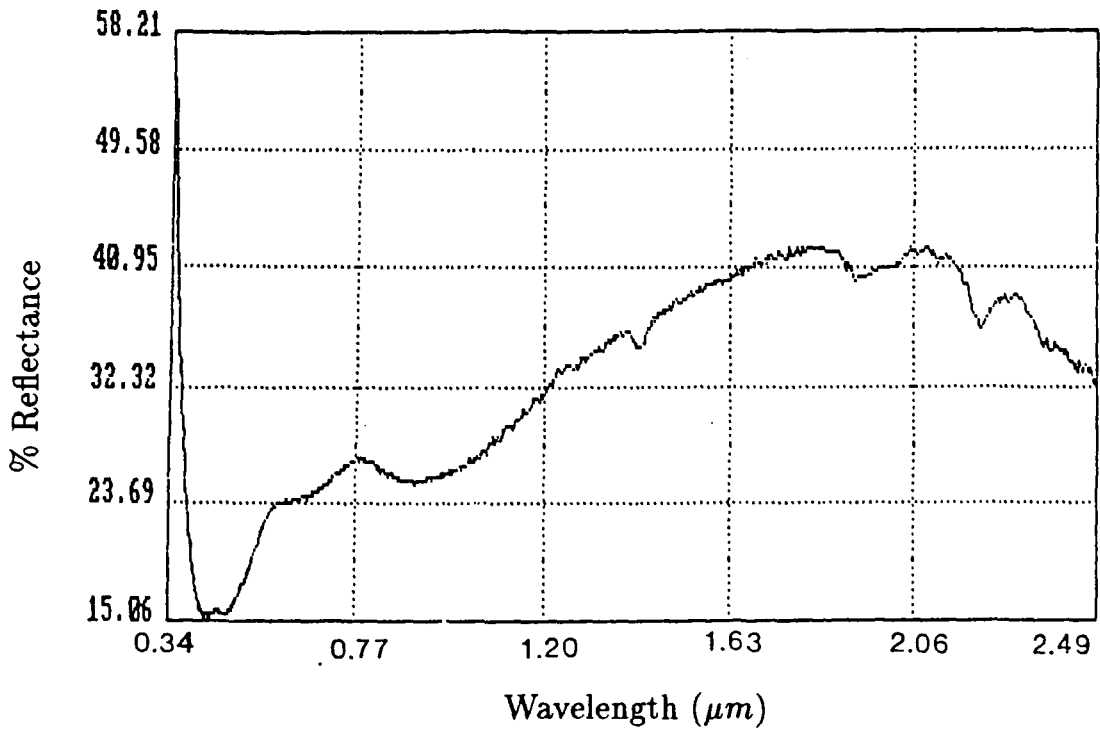
Figure 4.38   Lab. spectrum of the external surface of a sample collected at subsite L.
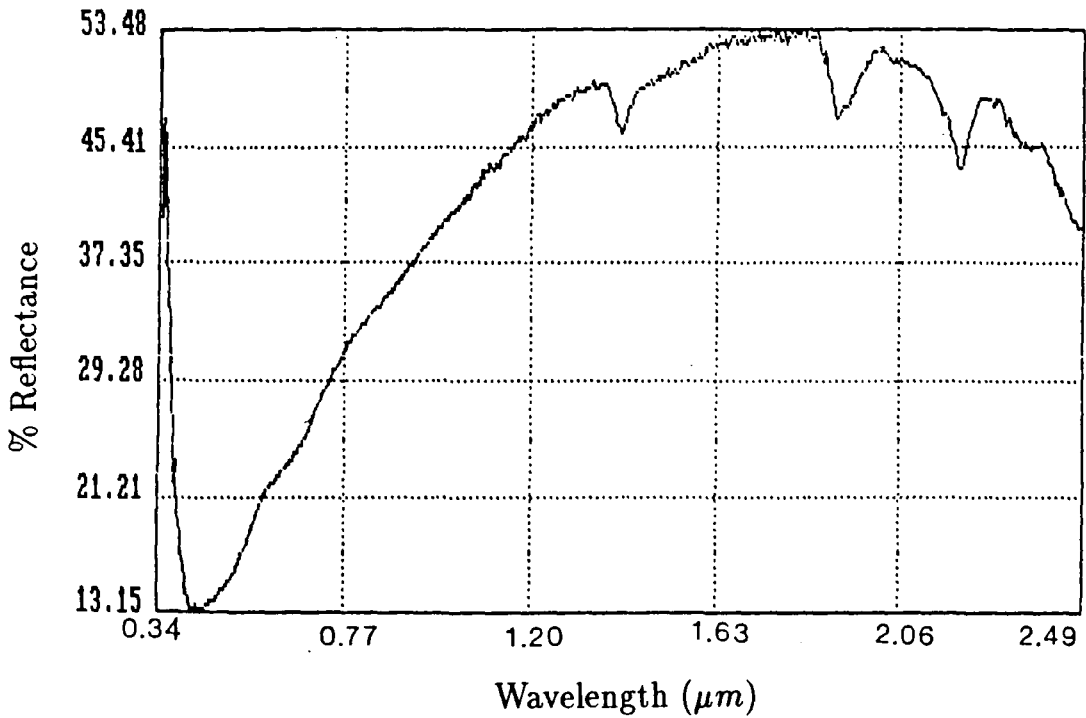
Figure 4.39   Lab. spectrum of the external surface of a sample collected at subsite M
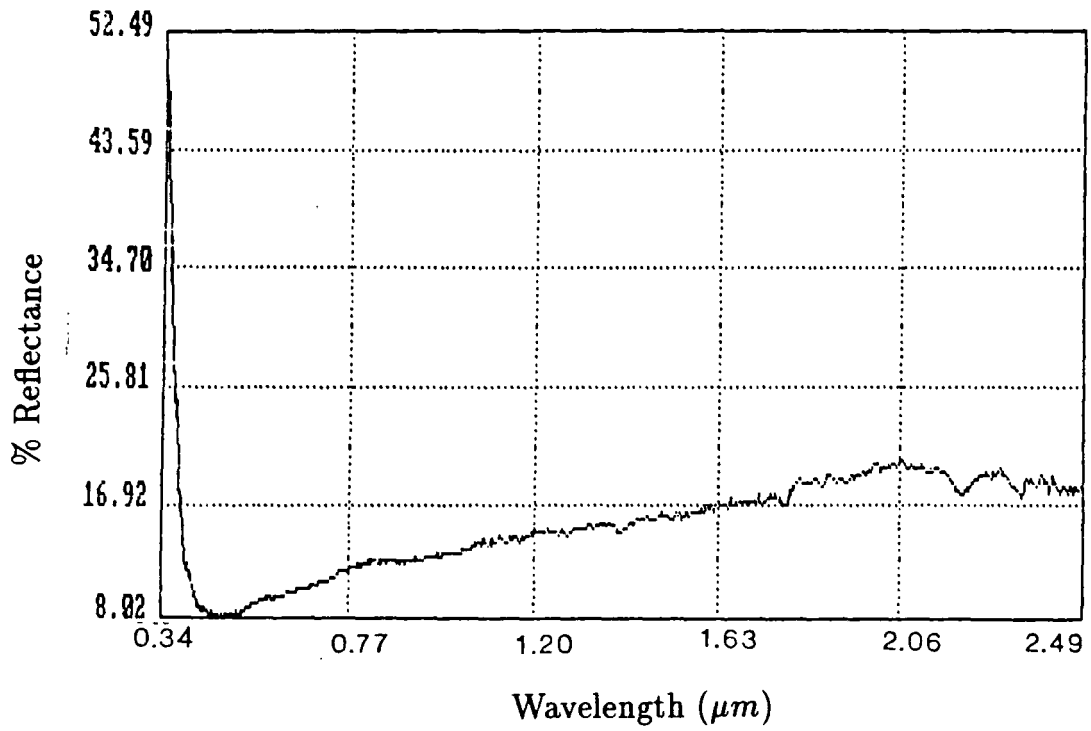
Figure 4.40   Lab. spectrum of the external surface of a sample collected at subsite N.
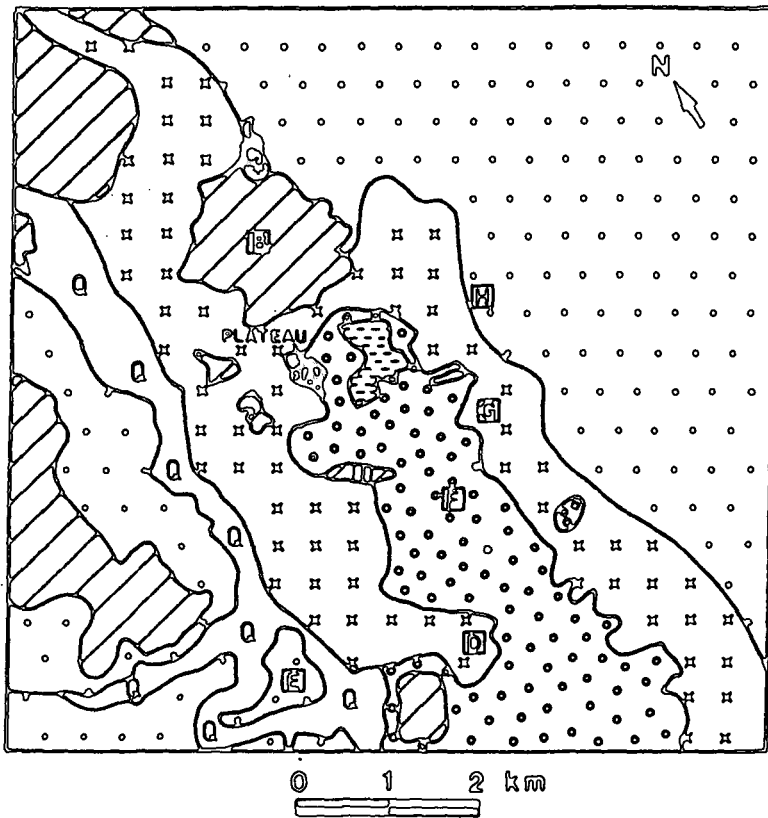
QUATERNARY

Q Alluvium

TERTIARY

Laterite

Campaspe sediments
poorly sorted, laterltized

TRIASSIC

Sandstone

PERMO CARBONIFEROUS

Granite

Rhyolite

CAMBRIAN TO ORDORVICIAN

Siliceous shales and cherts
(Cape River Beds)

Andesites
(Mount Windsor Volcanics)

Figure 4.41   Geology of the Plateau Test Site (after Beams 1986).
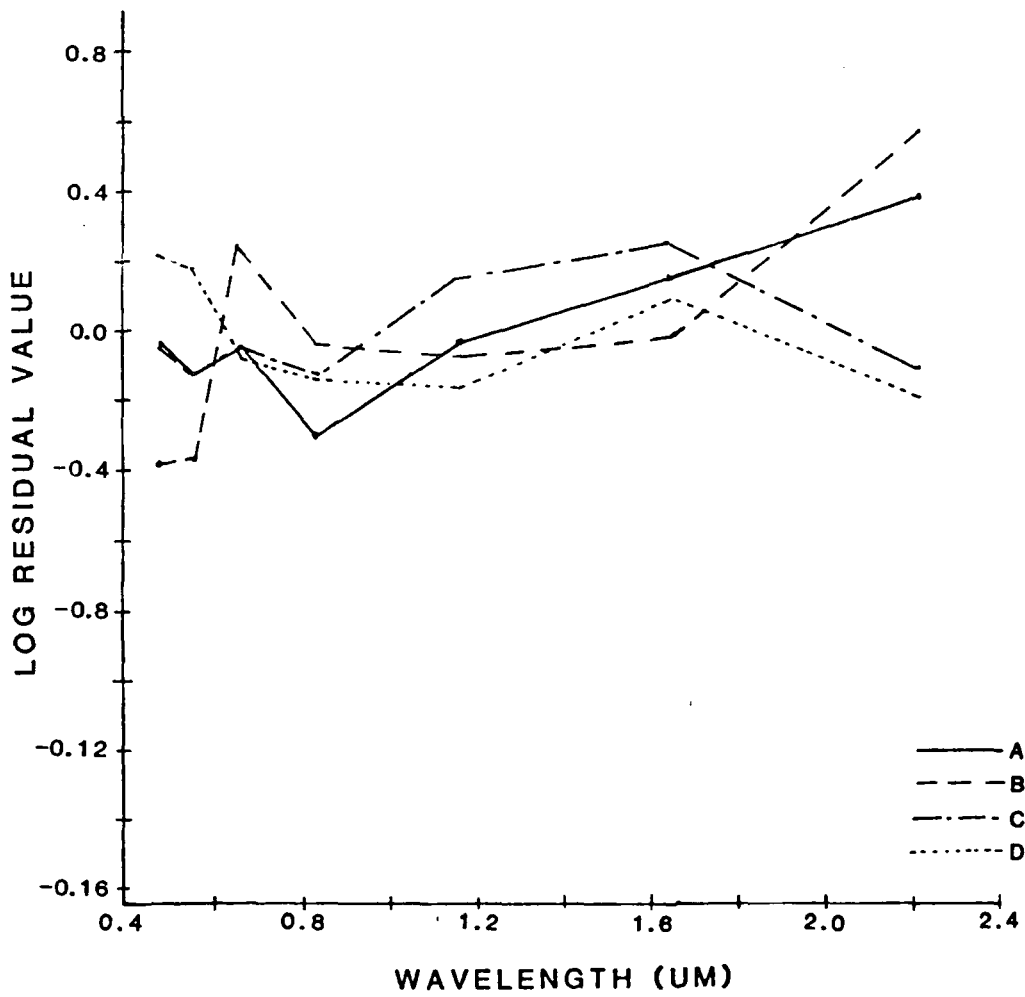
Figure 4.42   Log residual spectra from subsites A-D.
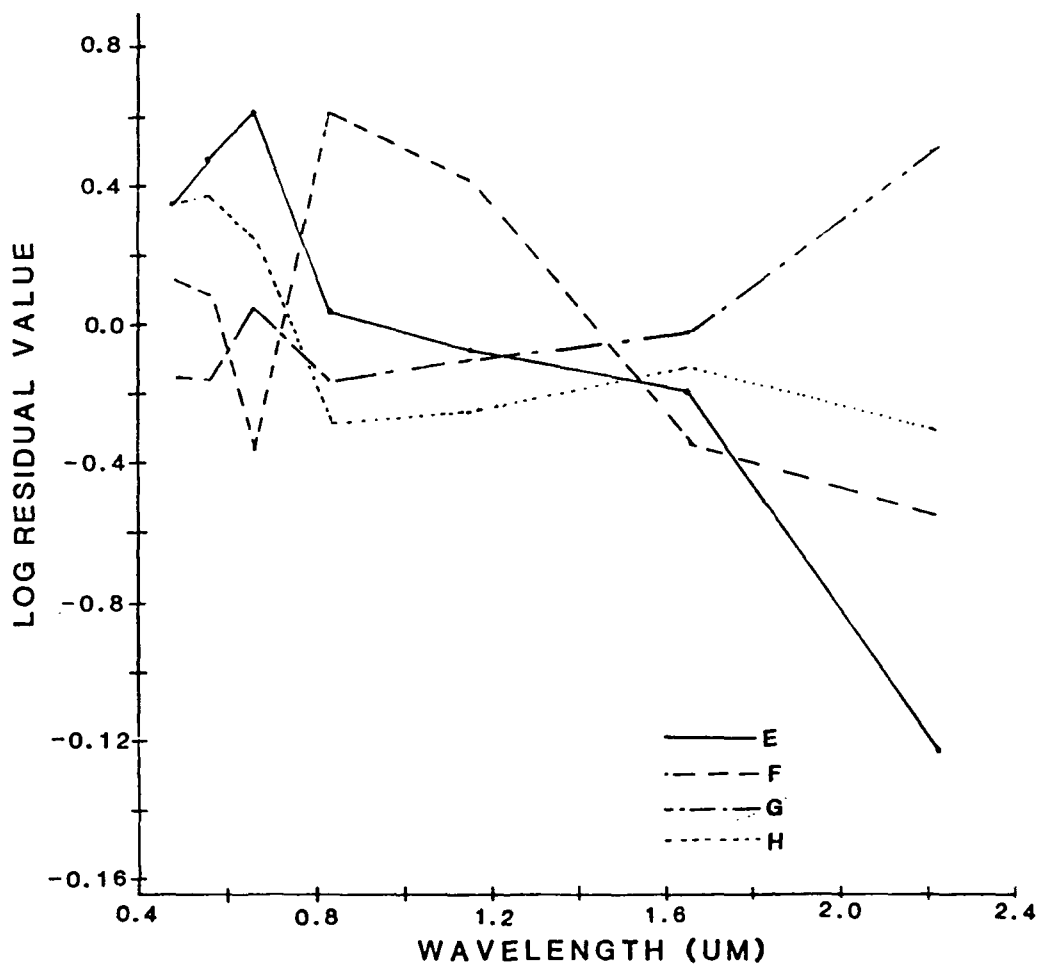
Figure 4.43   Log residual spectra from subsites E-H.
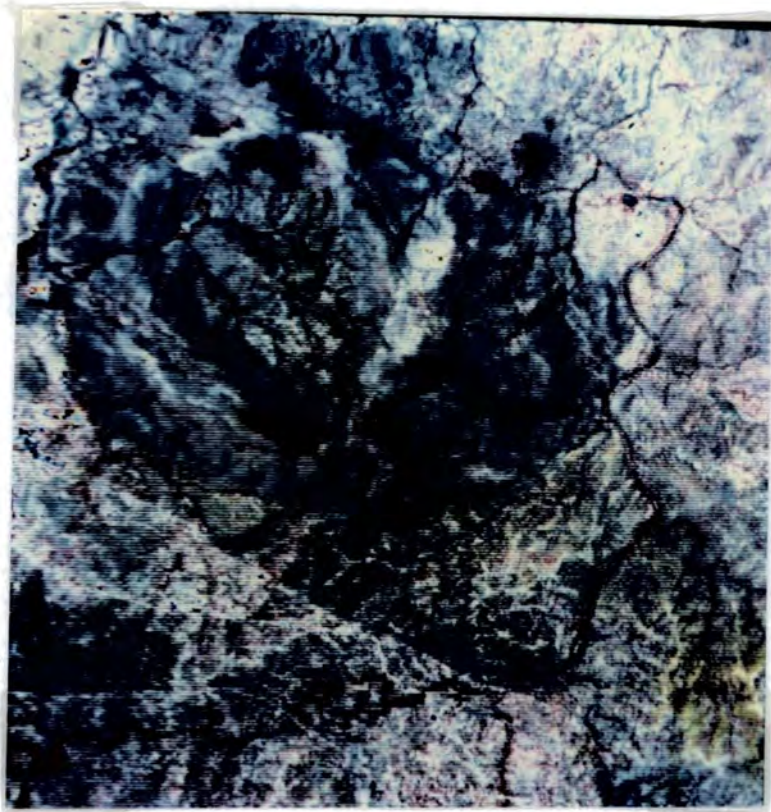
Plate 4.1   Colour Infrared Composite of the Camp Oven Test Site with the $0.83\mu m$, $0.66\mu m$ and $0.56\mu m$ channels displayed as red, green and blue respectively.
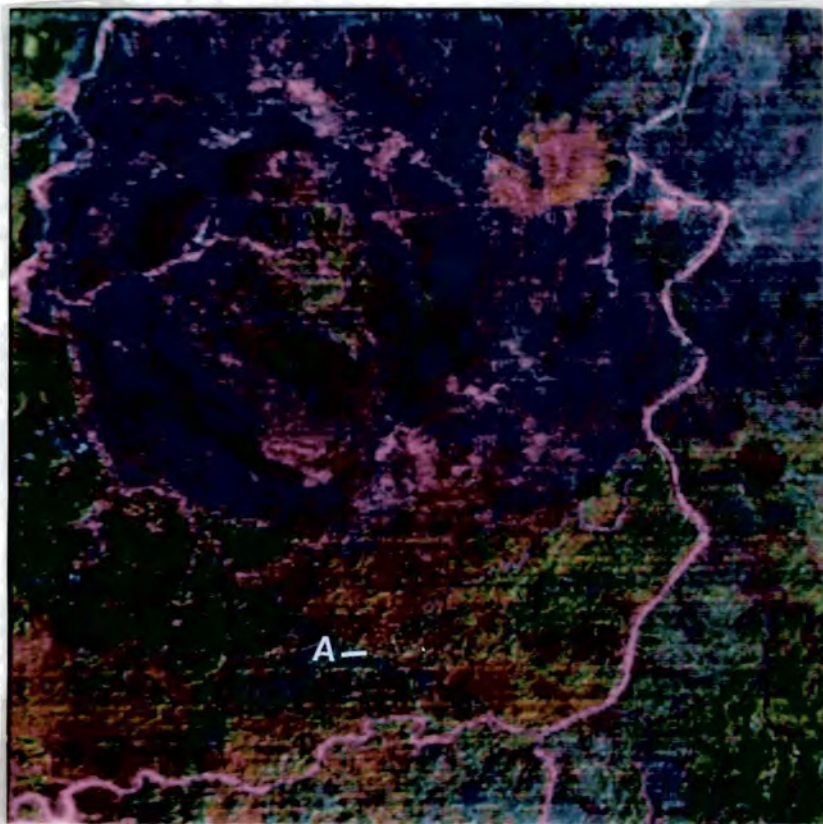
Plate 4.2   Channel Ratios $2.2\mu m$ /$1.65\mu m$, $0.66\mu m$ /$0.56\mu m$ and $0.83\mu m$ /1.65 displayed as red, green and blue respectively, Camp Oven Test Site.
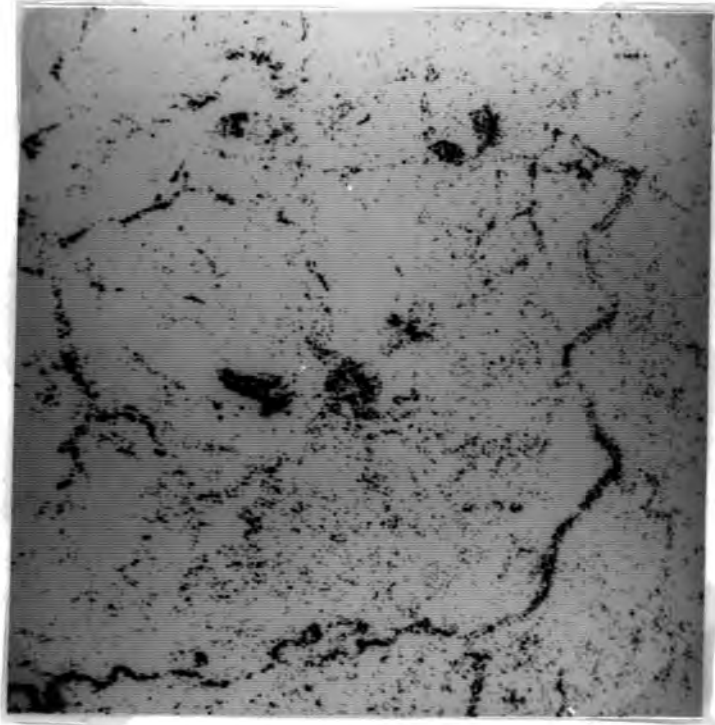
Plate 4.3   Vegetation Mask, over the Camp Oven Test Site.
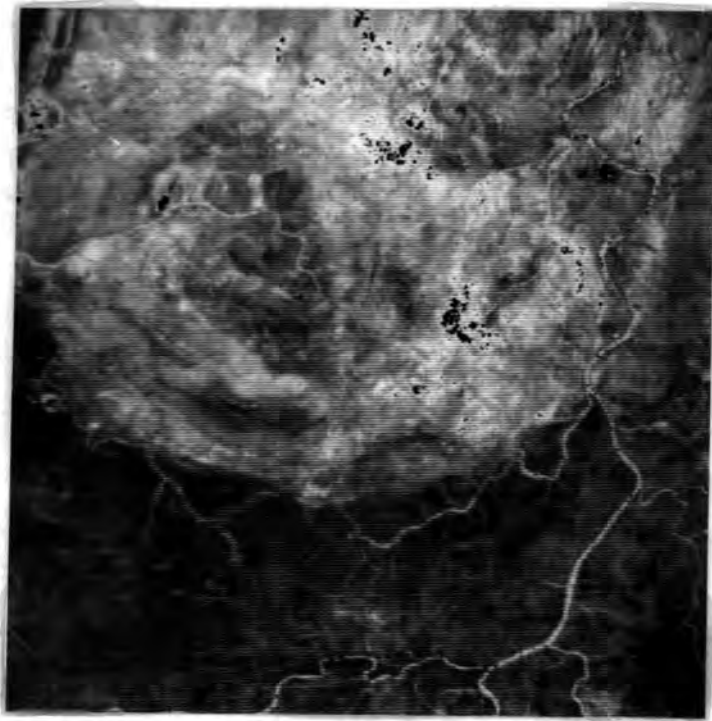
Plate 4.4   0.48μm Log Residual Channel, Camp Oven Test Site.
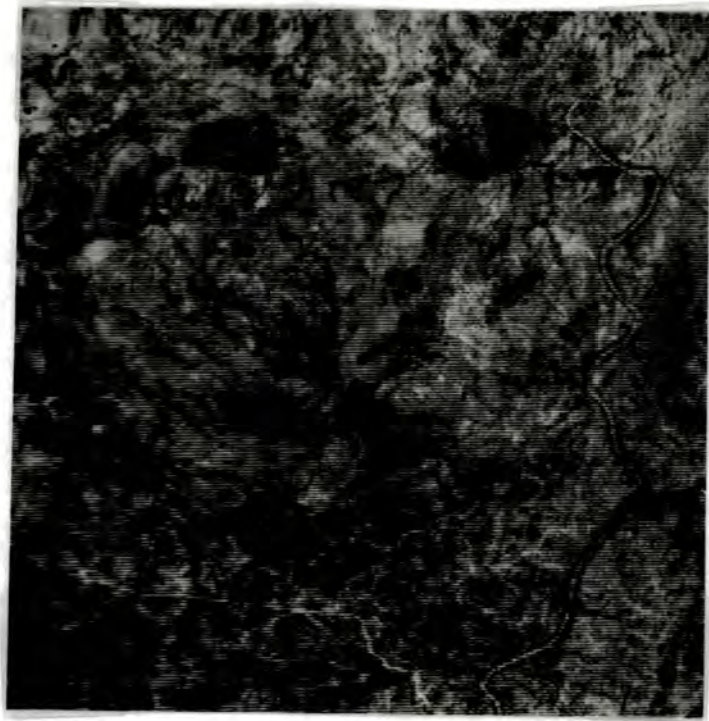
Plate 4.5   0.56μm Log Residual Channel, Camp Oven Test Site.
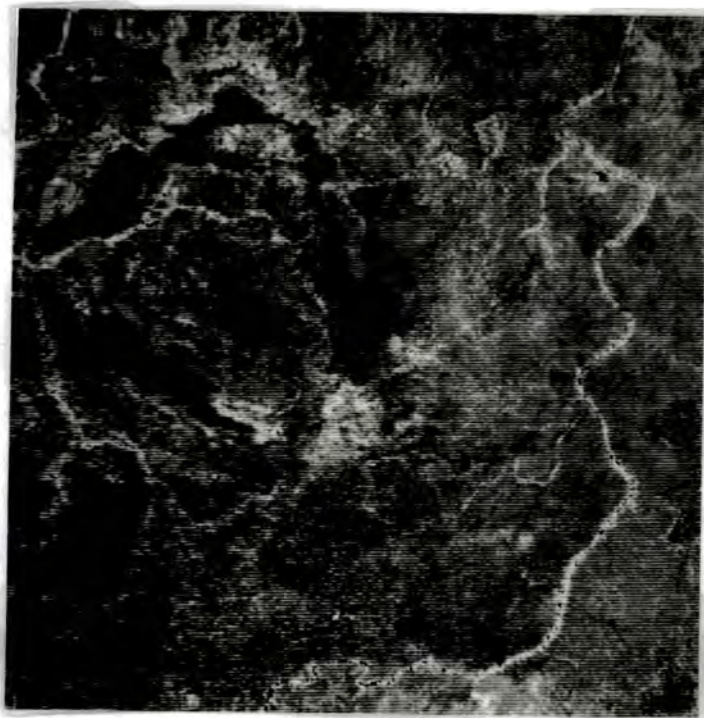
Plate 4.6   0.66μm Log Residual Channel, Camp Oven Test Site.
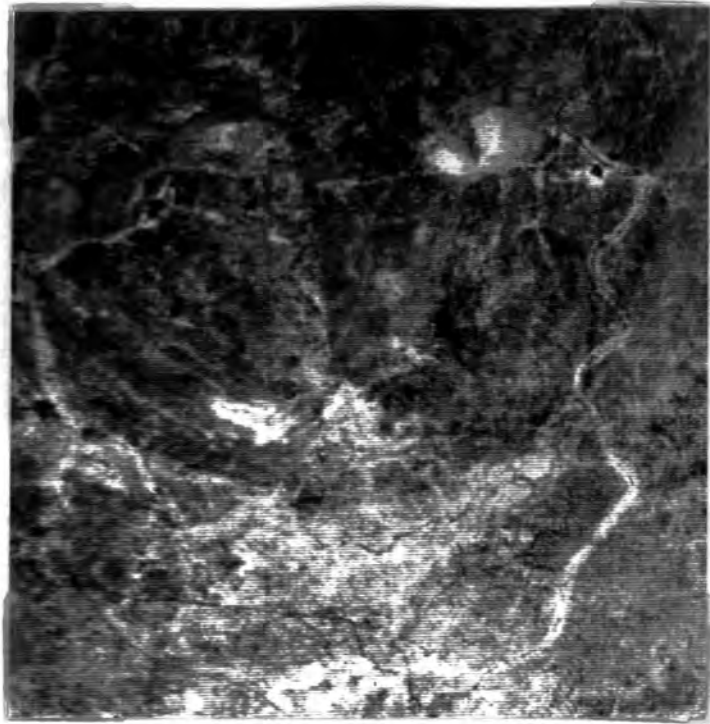
Plate 4.7 $0.83\mu m$ Log Residual Channel, Camp Oven Test Site.
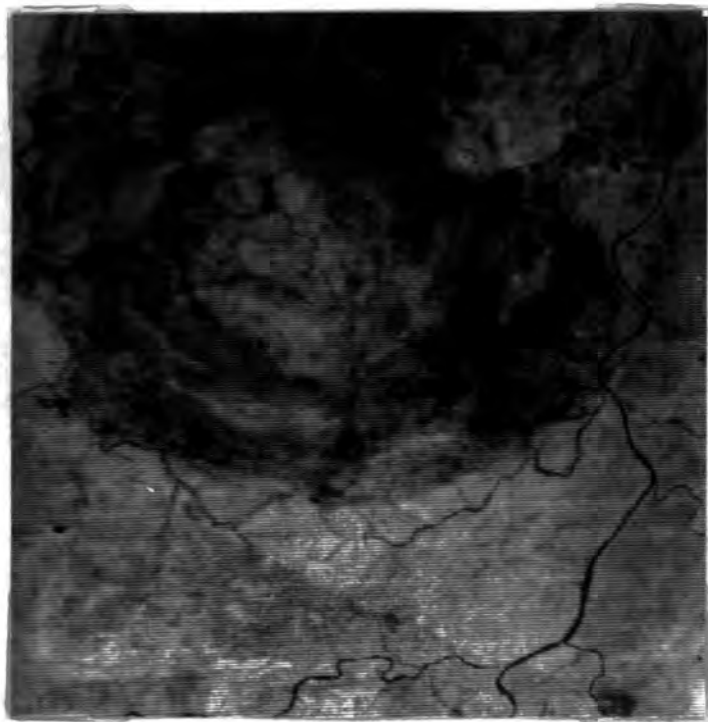
Plate 4.8 $1.13\mu m$ Log Residual Channel, Camp Oven Test Site.
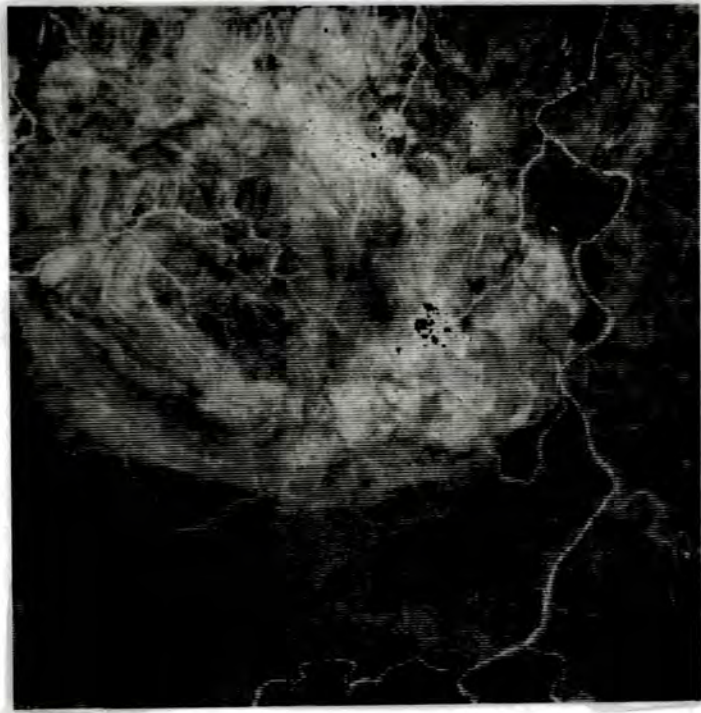
Plate 4.9   1.65μm Log Residual Channel, Camp Oven Test Site.
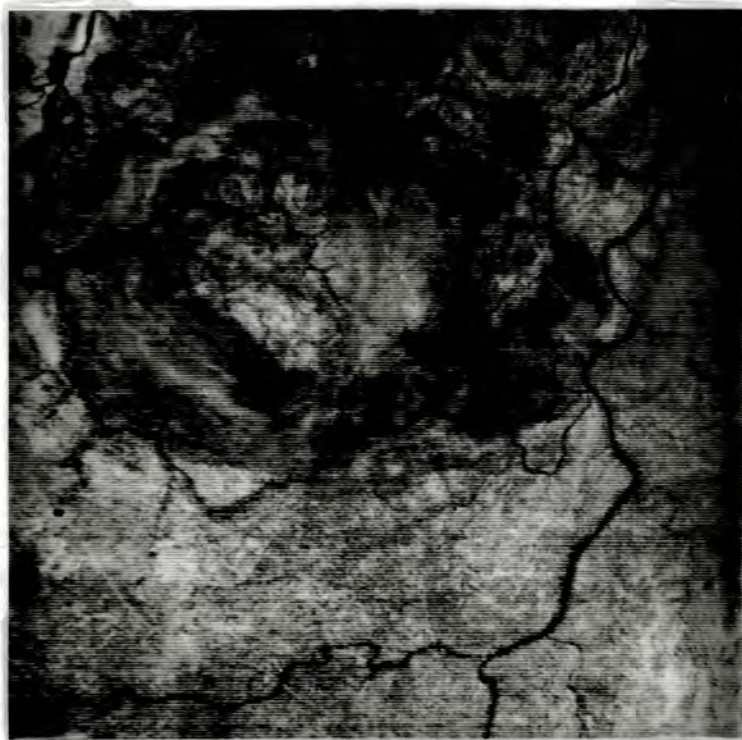
Plate 4.10   2.22μm Log Residual Band over the Camp Oven Test Site.
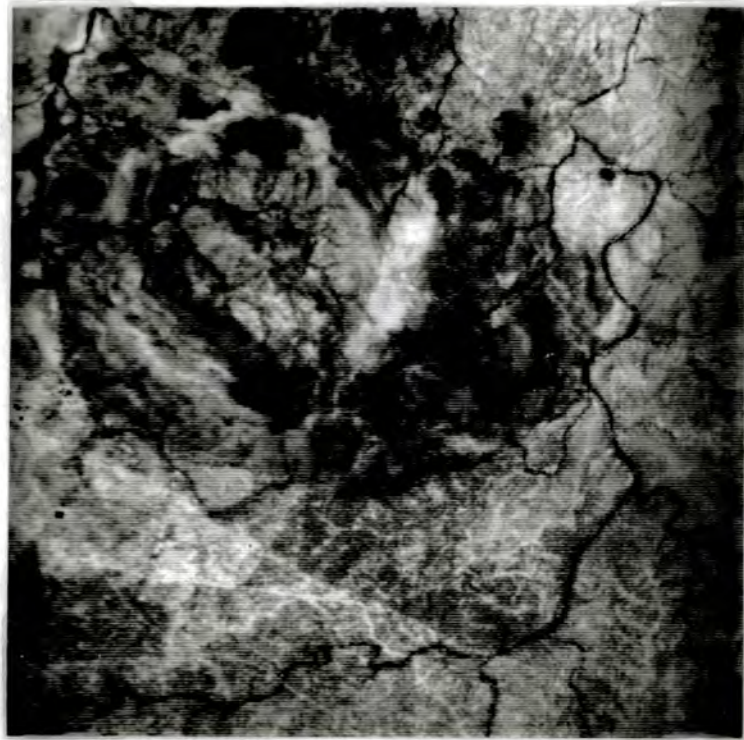
Plate 4.11   Albedo Channel, Camp Oven Test Site.
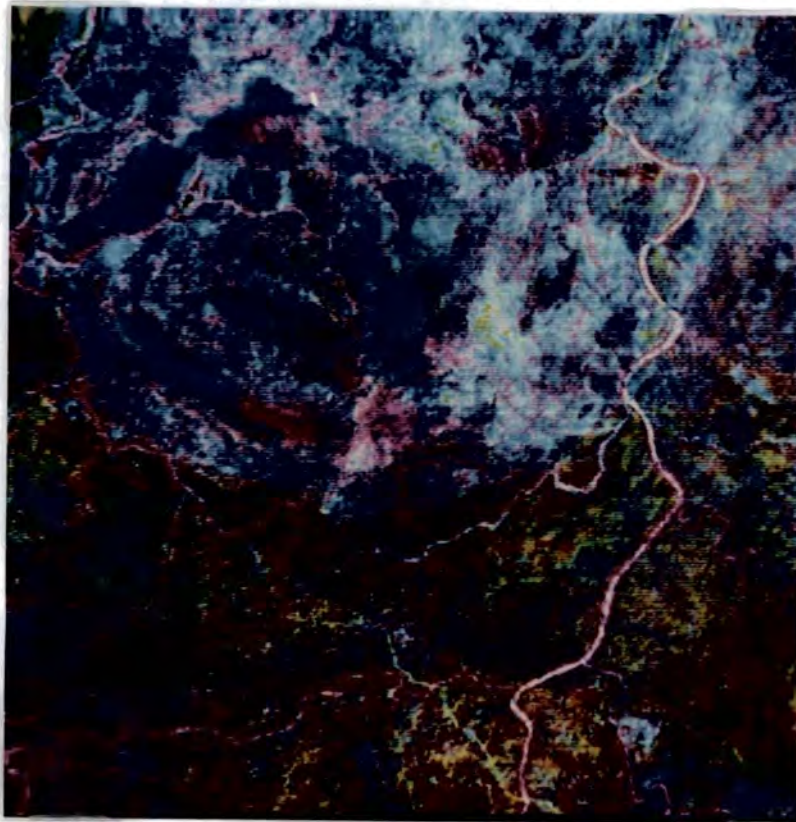
Plate 4.12   Colour Infrared Composite of the Log Residual Channels
$0.83\mu m$, $0.66\mu m$ and $0.56\mu m$ displayed as red, green and blue, Camp
Oven Test site.

177
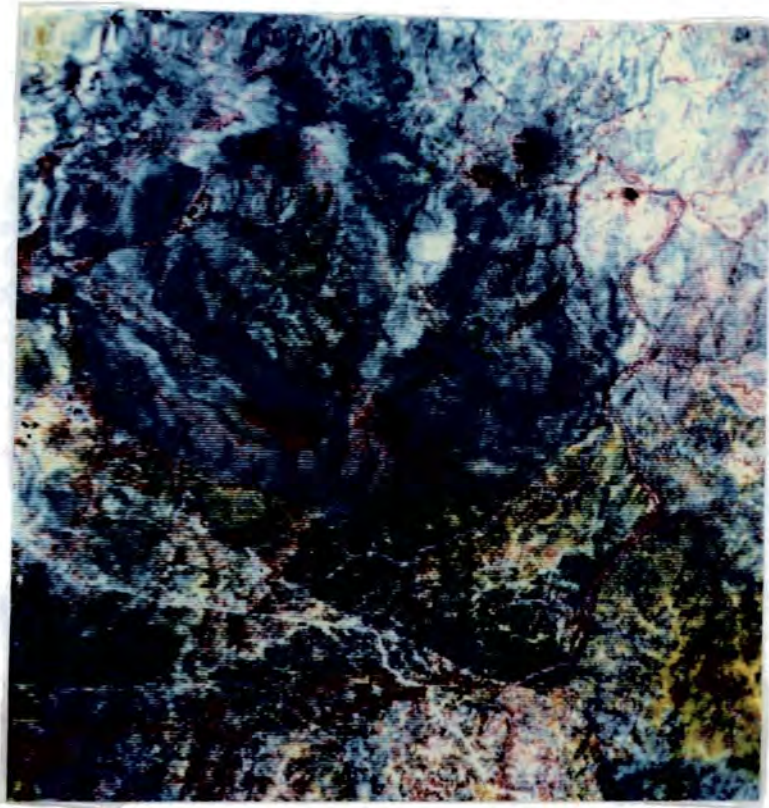
Plate 4.13   Colour Infrared Composite of the Log Residual Channels
0.83μm , 0.66μm and 0.56μm displayed as red, green and blue with
the Albedo Channel added in, Camp Oven Test site.

Plate 4.14   Actual 2.2μm Channel, Camp Oven Test Site.
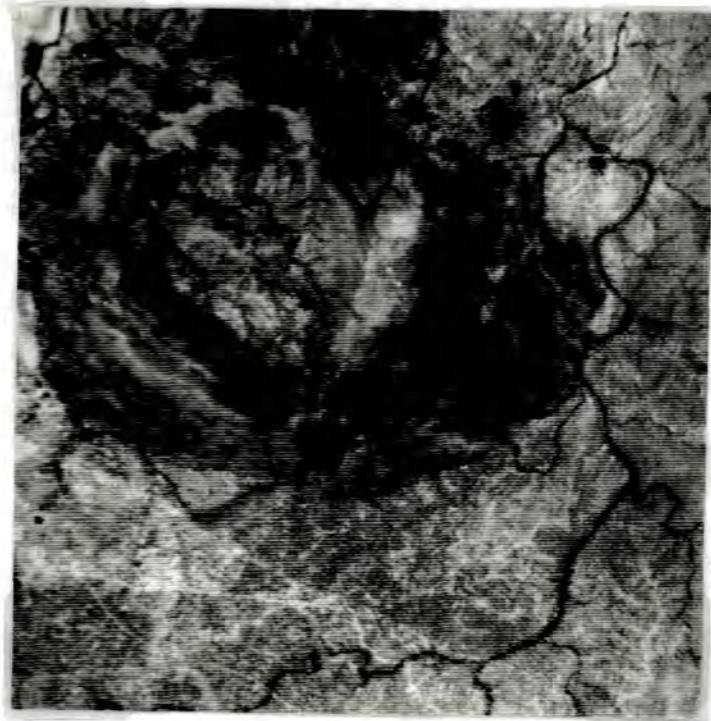
Plate 4.15   Predicted 2.2μm Channel, Camp Oven Test Site.
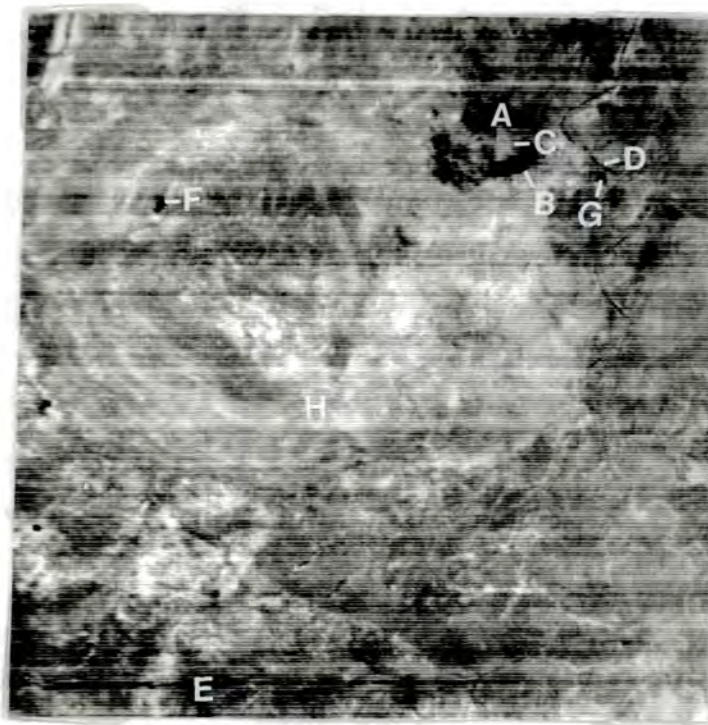
Plate 4.16   LRES 2.2μm Channel, Camp Oven Test Site.

Plate 4.17 Directed Principal Component 1, Camp Oven Test Site.
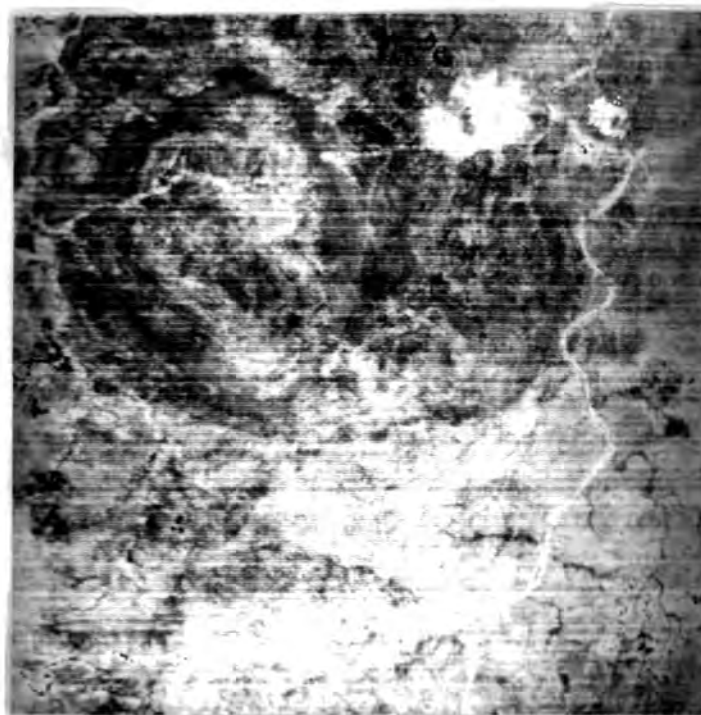
Plate 4.18 Directed Principal Component 2, Camp Oven Test Site.
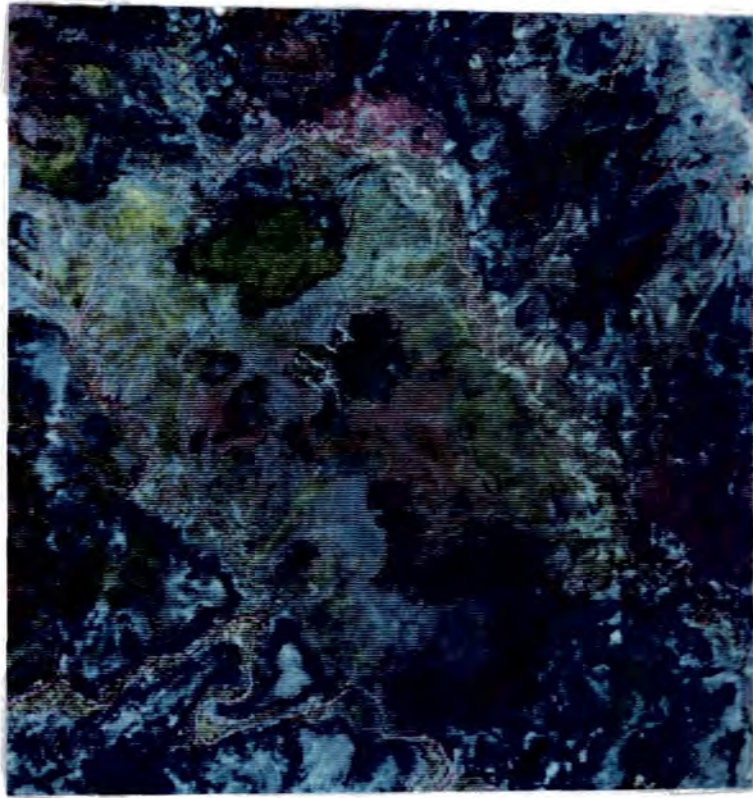
Plate 4.19   Colour Infrared Composite of the Log Residual Channels
0.83μm , 0.66μm and 0.56μm displayed as red, green and blue with
the Albedo Channel added in, Plateau Test site.
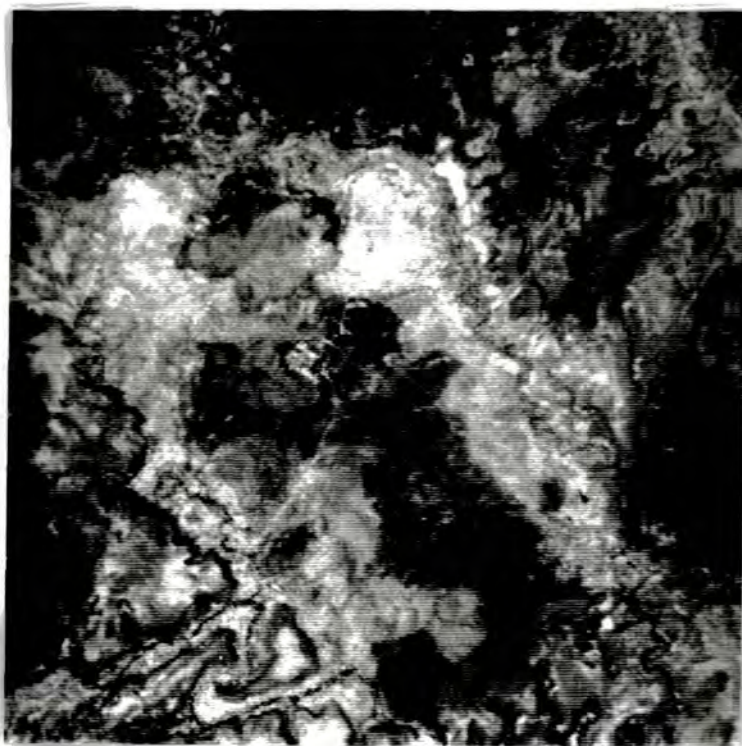
Plate 4.20   Actual 2.2μm Channel, Plateau Test Site.
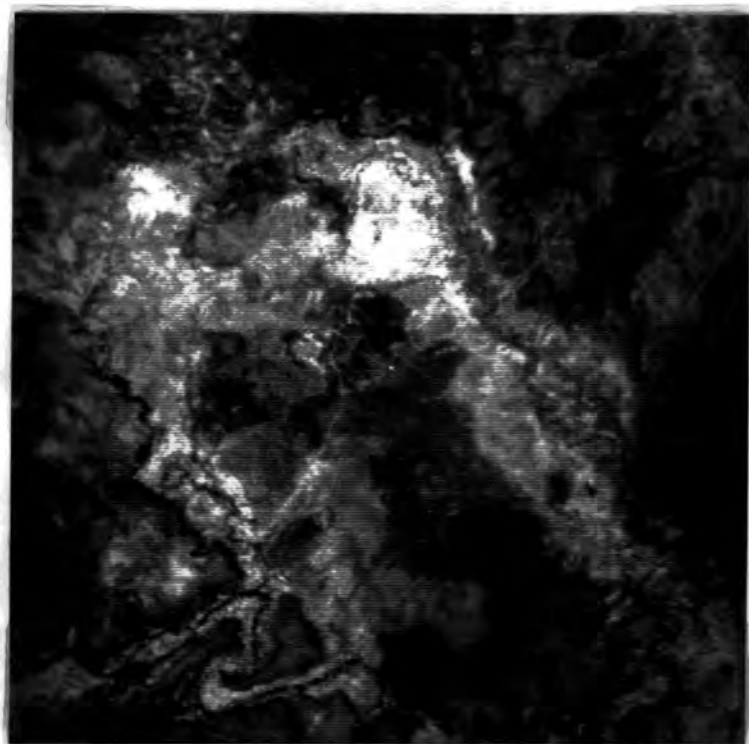
Plate 4.21   Predicted 2.2μm Channel, Plateau Test Site.
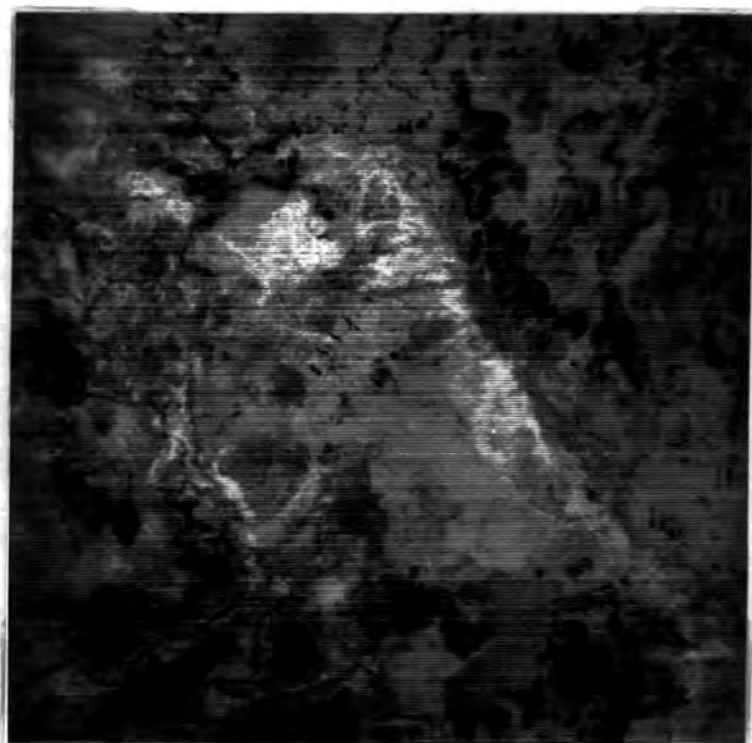
Plate 4.22   LSFIT 2.2μm Channel, Plateau Test Site.

CHAPTER 5

ANALYSIS AND INTERPRETATION OF DATA FROM THE

$8\mu m$ - $12\mu m$ WAVELENGTH REGION FOR

LITHOLOGICAL MAPPING AND MINERAL EXPLORATION

IN WEATHERED VEGETATED TERRAIN

5.1 Introduction

The principle objective of the analysis and interpretation of the data from the 8μm-12μm region was to evaluate its usefulness for lithological mapping and mineral exploration in deeply weathered vegetated terrain. The results from this study can then be compared with those from a similar study over the same area, using data from the 0.4μm-2.5μm wavelength region. This comparison should determine which wavelength region is most effective for geological studies such as this in weathered, vegetated terrain.

The data from the 8μm-12μm region were obtained by the Thermal Infrared Multispectral Scanner (TIMS). The TIMS acquires six discrete channels of data in this region. The exact wavelength range of each of these channels is given in Table 1.1. The TIMS data were radiometrically and geometrically corrected according to the methods described in Chapter Three.

In order to fully evaluate the geologic information present in the TIMS data it is desireable to reduce the data to physically meaningful parameters such as temperature and emittance. These data can then be compared with laboratory emittance data. A variety of image processing techniques were used to reduce these data including compositing the decorrelation stretch, the model emittance calculation, and thermal log residuals. The decorrelation stretch was developed by Soha and Schwartz (1978) and model emittance calculation was developed by Kahle (1980). The thermal log residual tech-

nique was developed by the author in collaboration with A. A. Green and A. R. Gabell of CSIRO, Sydney, Australia during a visit by author to CSIRO in 1987. The relative merits of each techniques are assessed in order to determine which is/are most effective at enhancing geological information in TIMS data in this terrain. The software to calculate model emittance from TIMS data was not available in the U.K. and was written and implemented by the author at Durham University. The software to calculate thermal log residuals was also written and implemented by the author at Durham University.

In order to fully evaluate the information obtained using these techniques, two test sites, each 512 x 512 pixels in size were selected from the TIMS data. The two test sites chosen were the same as used with the NS-001 data enabling comparison of the results from each wavelength region for mapping. These test sites are located at Camp Oven and Plateau (Figure 2.2). The lithologies and weathering history of these test sites is typical of much of NE Queensland. Therefore, the results from the study of these test sites should be widely applicable to other areas.

Initially, the physical basis for remote sensing of rocks, soils and vegetation in the 8μm-12μm region is reviewed. This provides an outline of the potential information available in this wavelength region for lithological mapping and mineral exploration.

This review is followed by the results from the analysis and interpetation of the TIMS data covering the Camp Oven test site using the three techniques (the decorrelation stretch, the model emittance calculation and thermal log residuals).

The geology of the test site has been described in section 4.3.1 Where appropriate, the methodology behind each technique is also given. The interpretations of the TIMS data were assessed through comparison with existing maps and field checking.

The results from the data obtained from the 0.4μm-2.5μm and 8μm-12μm wavelength regions at the Camp Oven test site are then compared to determine which region is most effective for lithological mapping and mineral exploration in deeply weathered vegetated terrain.

This is followed by the results from the analysis and interpretation of the TIMS data at the Plateau test site for lithological mapping and mineral

exploration. The geology of the Plateau test site has already been described in section 4.4.1. The TIMS data from Plateau were analysed using the techniques which were found to be most effective in the study at the Camp Oven test site.

The results from the data obtained from the 0.4μm-2.5μm and 8μm-12μm wavelength regions at the Plateau test site are then compared to determine which region is most effective for lithological mapping and mineral exploration in deeply weathered vegetated terrain.

The results from the application of thermal log residual (TLR) technique to data from a semi-arid sparsely vegetated terrain with little surface weathering are then presented. These data provide an indication of the wider applicability of the TLR technique developed as part of this study.

Finally, the conclusions are presented together with a brief summary.

5.2 Physical Basis for Remote Sensing in the 8μm-12μm Wavelength Region

The solar energy reflected by the earths surface falls rapidly to zero beyond 2.5μm (Figure 5.1). Any energy received from the earth at wavelengths longer than this is emitted by the earth. If a body is a perfect radiator, termed a blackbody, then the emitted radiation is a function of its temperature only and is given by Plancks Law:

$$R_{\lambda B} = \frac{C_1}{\lambda^5 (e^{(C_2/\lambda T)} - 1)} \qquad 5.1$$

where:

$R_{\lambda B}$ = Spectral Exitance

B = Blackbody

λ = wavelength in microns

T = Temperature in degrees Kelvin

C_1 = First Radiation Constant = $2\pi hc^2$ = 3.7413 $\times$ 10^{-4}watt microns^2

C_2 = Second Radiation Constant = $\frac{ch}{k}$ = 1.4388 $\times$ 10^4micron degrees

c = speed of light

h = Planck's Constant

k = Stefan-Boltzman Constant

Plancks Law indicates that the spectral exitance of a blackbody at a given temperature is not the same at all wavelengths. For very long and short wavelengths the spectral exitance is very low (Figure 5.2). For some wavelength in between, the spectral exitance reaches a maximum value depending on the temperature of the blackbody. The earths surface has an average temperature value of 290° K (Sabins, 1978). At this temperature the maximum spectral exitance occurs at 9.7μm (Sabins, 1978).

The ability of a body to emit radiation is expressed as the spectral exitance of the material to that of a blackbody at the same temperature. This is referred to as spectral emissivity and given the symbol (ϵ):

$$\epsilon_\lambda = \frac{R_\lambda(\text{material},K^o)}{R_\lambda(\text{blackbody},K^o)} \qquad 5.2$$

For a blackbody the emissivity is 1. If the emissivity is less than 1 but constant for all wavelengths the material is said to be a greybody. When the emissivity value varies with wavelength the material is called a selective radiator.

The spectral radiance of the surface of a blackbody L_λ can be related to the spectral exitance of a blackbody R_λ by:

$$L_\lambda \text{blackbody} = \frac{R_\lambda \text{blackbody}}{\pi} \qquad 5.3$$

Referring back to equation 5.1 C_1 becomes $2c^2h$.

The spectral radiance of a natural surface as opposed to a blackbody is given by:

$$L_\lambda = \epsilon_\lambda L_{\lambda B} \qquad 5.4$$

where:

L_λ = spectral radiance of a natural surface

ϵ_λ = emissivity of that surface at a given wavelength

$L_{\lambda B}$ = spectral radiance of the surface of a blackbody at that wavelength

Most natural surfaces have emissivities between 0.85 and 0.95 in the 8-12μm region (Suits, 1983). Variations in these emissivities are a function of the type of material and the composition of the emitting surface (Hunt, 1980).

This enables variations in emissivity to be used for lithological mapping and the causes of these emissivity variations are now discussed.

5.2.1 Rocks, Minerals and Soils

Emissivity variations of inorganic solids in the $8\mu m$-$12\mu m$ region are due to vibrational processes, and the most intense features result from excitation of the fundamental modes (Hunt, 1980).

Several publications are available on the spectra of rocks and minerals in this wavelength region including Lyon (1965), Salisbury et al. (1987c, 1988b) and references contained therein. Very little work has been undertaken on the spectra of soils in this region. This is due to interpetation being complicated by the abundant water and organic materials present in soils (Hunt, 1980). In the mid infrared the wavelength region between $8\mu m$ and $12\mu m$ has received the most attention since it contains evidence of the most intense Si-O stretching modes. This information relates to the bulk composition - the chemistry and structure of the material. It also coincides with an atmospheric window between $8\mu m$ and $12\mu m$ and the peak in spectral exitance for a blackbody at the temperature of the earths surface (see earlier discussion).

In silicates the most intense absorption features in the $8\mu m$-$12\mu m$ region occur near $10\mu m$, this region is referred to as the 'Si-O stretching region'. The absorption minimum in this region is termed the restrahlen band (Hunt, 1980). This minimum generally migrates to longer wavelengths as the material becomes more mafic with decreasing silica and increasing ferromagnesium minerals (Hunt, 1980). This minimum occurs at shorter wavelengths for framework silicates such as quartz and feldspars, and longer wavelengths for materials in which the tetrahedra are isolated as in orthosilicates (Figure 5.3). This effect is demonstrated for increasingly mafic rocks in Figure 5.4.

The other silicate feature in this wavelength range results from an H-O-Al stretching and produces a minimum near $11\mu m$ which is particularly apparent in the spectra of aluminium bearing clay minerals (Hunt, 1980; Figure 5.4).

In non-silicates a variety of absorptions occur in the $8\mu m$-$12\mu m$ region. These are demonstrated for the main non-silicate mineral groups in Figure 5.5. These include a carbonate, phosphate, sulphate, oxide and hydroxide. Of the non-silicate mineral groups carbonate is probably the most frequently encountered. Figure 5.6 illustrates the spectra of a variety of carbonates.

The top spectrum is similar to that of calcite, but with increasing amounts of clay and quartz seen in the lower spectra, additional features develop near 9μm and 13μm (Hunt, 1980).

5.2.2 Vegetation

A plant absorbs large amounts of solar radiation especially at visible wavelengths, and re-emits most of this energy in the thermal infrared (Raines and Canney 1980). In the 8μm-12μm region vegetation was considered spectrally flat within the sensitivity range of the TIMS, (Gillespie, 1986; Christensen *et al.*, 1986). However, more recent studies have shown vegetation does exhibit some subtle emittance differences in this region (Salisbury *et al.*, 1987a,b; 1988a; Elvidge, 1988). Salisbury and his co-workers consider these variations are within the detection limits of the TIMS, this remains to be proved.

5.3 Analysis and Interpretation of Data from the $8\mu m$-$12\mu m$ Wavelength Region for Lithological Mapping and Mineral Exploration over the Camp Oven Test Site

The Camp Oven test site is 512 x 512 pixels in size and located in the NE of the study area (Figure 2.2). The geology of the test site is described in section 4.3.1.

The data from the 8μm-12μm wavelength region were acquired by the TIMS. This sensor acquires six discrete channels of data between 8μm and 12μm. Data from this region can be used to map emissivity differences which relate to variations in the bulk silica content and presence of other non-silicate minerals in rocks (see section 5.2)

The TIMS data were processed using a variety of techniques to enhance emissivity variations for lithological mapping and mineral exploration. These included compositing, the decorrelation stretch, the model emittance calculation and thermal log residuals. The results from the analysis of the TIMS data from the Camp Oven test site using these techniques are now presented. Where appropriate the methodology behind each technique is also given.

5.3.1   Radiometrically Corrected Data

Plate 3.6 is a colour composite image of the TIMS channels centered on $10.7\mu m$, $9.2\mu m$ and $8.4\mu m$ displayed in red, green and blue respectively. These are henceforth referred to according to their centre wavelength positions (eg. the $8.4\mu m$ channel). The image appears grey due to the high correlation between channels. This high correlation results from the temperature component of the radiance measured dominating any emissivity variations (see equation 5.4). The decorrelation stretch model emittance calculation and thermal log residual techniques are all designed to enhance or extract these emissivity variations and suppress temperature effects to enable the former to be used for lithological mapping.

5.3.2   Decorrelation Stretch Data

Colour images are usually made be selecting three channels of data and displaying each in a different primary colour (red, green and blue) to form a colour additive picture. If the data used are highly correlated between channels the resultant images do not utilize the full colour space and the images appear monochromatic (as in Plate 3.6). The image histogram from such data occupies a long narrow region near the achromatic axis (Figure 5.7; Gillespie, 1987). Contrast stretching each component spreads the data out along the achromatic axis but still does not utilize the full colour space available (Figure 5.8; Gillespie, 1987). This results in an image in which the dark-light colour intensity range has been expanded, but does not increase the range of colours and the image retains a monochromatic appearance (Gillespie, 1987). A technique is required which selectively enhances the least correlated information thereby increasing the colour range.

Soha and Schwartz (1980), developed a technique which solved this problem by rotating the image to new coordinates, contrast stretching these, then rotating back to the original colour space. The spread of the resultant histogram for the data is maximized when the rotation employed is the principle component transformation (Soha and Schwartz, 1980). This results in an image in which the colour space is maximised (Figure 5.9). Also, if the principle component images are stretched to equalize the variance of all components, the final output images remain uncorrelated regardless of the amount of rotation. This produces an image in which the colour saturation has been exaggerated

independantly of brightness (Gillespie *et al.*, 1987).

The decorrelation stretch was first applied to data from the 8µm-12µm region by Kahle *et al.* (1980). The highly correlated temperature information is displayed as intensity variations while the uncorrelated emissivity information is displayed as colour variations (Kahle *et al.*, 1980). The technique has since been used by a variety of authors in sparsely vegetated terrain to enhance emissivity variations for lithological mapping (eg. Kahle and Goetz, 1983; Gillespie *et al.*, 1984; Gillespie, 1986; Macias *et al.*, 1987; Simpson *et al.*, 1987; Lahren *et al.*, 1988).

The decorrelation stretch was applied to all six TIMS bands and an image formed from the 10.7µm, 9.2µm and 8.4µm channels displayed in red, green and blue respectively (Plate 5.1). The previous studies found using this channel-colour combination that silica rich areas appeared red/orange, clay rich areas blue/purple and carbonates green. Kahle *et al.* (1980), attribute the red colour of the silica rich areas to the high emissivity of tectosilicates (quartz) in the wavelength region covered by the 10.7µm channel and low emissivities in the wavelength regions covered by the 8.4µm and 9.2µm channels (Figure 5.3). The physical basis for the colour of the other areas in decorrelation stretch data has not been published. It should be noted that variations in the colour of these different rock types will occur between scenes using this technique which is dependant on scene statistics.

Field mapping revealed that the red patches in Plate 5.1 did correspond to areas that were rich in silica. These were areas of sandy alluvium associated with the rivers and creeks and *in situ* weathering of certain units. These units were the Ravenswood Granodiorite and the sandstones in the centre of the Camp Oven Complex. (Plate 5.1, Figure 4.6). The development of this weathered material permitted the discrimination of the sandstones and Ravenswood Granodiorite relative to the surrounding rocks (Plate 5.1, Figure 4.6). No other units mapped by Wyatt *et al.* (1971), Lorraway (1976) or the author could be discriminated with these data (Plate 5.1, Figures 2.2 and 4.6).

The top left corner of Plate 5.1 has a green/yellow appearance. This area does not correspond to any mapped lithological units (Figure 4.6). It is thought to result from a temperature difference caused by a period of uneven

heavy rainfall prior to the flight. If this area received more rainfall than the surrounding area it would be cooler. This is further inferred by examining the decorrelation stretch data from the 8.4μm channel in which the area has distinctly lower values than the surroundings (Plate 5.2). It is not possible to state unequivocally that this is the result of temperature since the decorrelation stretch data consist of both temperature and emittance information although it does appear most likely.

The presumed temperature effect could have been caused by atmospheric effects such as uneven distribution of haze over the study area. This seems unlikely since the region was subject to a period of heavy rain prior to the flight which would have flushed the atmosphere of aerosols likely to cause haze. The atmosphere was extremely clear on the day of the overflight.

Clearly, the TIMS data, processed using the decorrelation stretch technique are of limited use for lithological mapping or mineral exploration at the Camp Oven test site compared to the data from the 0.4μm -2.5μm (see Chapter 4).

5.3.3 Model Emittance Data

Laboratory studies indicate that emissivity variations in rocks in the 8μm-12μm wavelength relate to differences in their bulk silica content and presence of other non-silicate minerals which should permit lithological discrimination with airborne data (see section 5.2).

Airborne data acquired in this region by the TIMS have been shown to be dominated by temperature effects which mask any emissivity variations (see section 5.3.1). Previous studies have shown these temperature effects can be subdued using the decorrelation stretch (see section 5.3.2). However, this technique proved limited with TIMS data from this study area in weathered vegetated terrain. An alternative method for enhancing emissivity variations is termed the model emittance calculation and was developed by Kahle *et al.* (1980). This method involves certain assumptions and so the resultant data are referred to as model emittance rather than emissivity data. The model emittance calculation together with the assumptions made are now described. The results from the application of this technique to the TIMS data are then presented.

Since neither the emissivity in each channel nor the temperature of the

ground is known, certain assumptions are necessary in order to calculate emissivity. The assumption typically made is that the emissivity ($\epsilon'_{11.7\mu m}$) in the channel centered on 11.7μm is known. The value for $\epsilon'_{11.7\mu m}$ is generally thought to be 0.93 (on a scale 0-1) for most silicate minerals (Lyon, 1965). This is not the case for mafic and ultramafic silicate rocks where the restrahlen band (Si-O vibration) has shifted to longer wavelengths (see section 5.2.1). In this case a better assumption would be $\epsilon'_{8.4\mu m} = 0.93$ (Lyon, 1965).

In this study the emissivity in the 11.7μm channel was assumed to be 0.93.

Initially the temperature at which the surface is radiating is calculated from Planck's Law using an assumed emissivity in the 11.7μm channel:

$$T_{11.7\mu m} = \frac{C_2}{\lambda_{11.7\mu m}} \left(ln(\frac{\epsilon'_{11.7\mu m}C_1}{R_{11.7\mu m}\lambda_{11.7\mu m}^5} + 1) \right)^{-1} \qquad 5.5$$

where:

$T_{11.7\mu m}$ = temperature in the 11.7μm channel

C_2 = second radiation constant

$\lambda_{11.7\mu m}$ = wavelength of 11.7μm channel

$\epsilon'_{11.7\mu m}$ = assumed emissivity (0.93)

C_1 = first radiation constant

c = speed of light

h = Planck's constant

k = Boltzmann's constant

$\lambda_{11.7\mu m}$ is not a single value because the channelpass of 11.7μm channel is from 11.2μm to 12.2μm. Therefore, Plancks's Law should be integrated over this wavelength range to obtain $R_{11.7\mu m}$. The method can be simplified by assuming a single value for this wavelength and has been done in this study.

R'_i values can then be calculated once $T_{11.7\mu m}$ is known for channels 1-5 according to:

$$R'_i(T_{11.7\mu m}) = \frac{C_1}{\lambda_i^5 \left(e^{\frac{C_2}{\lambda_i T_{11.7\mu m}}} - 1 \right)} \qquad 5.6$$

The model emittance values (ϵ_i') are calculated by:

$$\epsilon_i' = \epsilon_{11.7\mu m}' \frac{R_i}{R_i'} \qquad\qquad 5.7$$

Plate 5.3 is an image of the model emittance data extracted from the 8.4μm channel. The areas of sandy alluvium associated with the river channels, weathering of the granodiorite to the south and sediments in the centre of the Camp Oven Complex have low values compared with the surrounding area (Plate 5.3; Figure 4.6).

The borders of Pinnacle Creek and some other rivers have high values. These high values are associated with vegetation and also on the top and sides of Blackfellow Mountain (Plate 5.3; Figure 4.6). The granodiorite in the south can be separated from the volcanics of the Camp Oven Complex and the granite east of Pinnacle Creek (Plate 5.3; Figure 4.6). However, the granite and volcanics of the Camp Oven Complex cannot be separated. Four areas of high values surrounded by low values, labelled A-D, are discernable (Plate 5.3). These do not correspond to any mapped geological contacts and the cause for them has not been determined.

Plate 5.4 is an image of the model emittance data derived from the 8.8μm channel. The interpretation of these data is similar to that for the emittance data extracted from 8.4μm channel, except the areas of sandy material appear to have slightly lower values than the surroundings.

Plate 5.5 is an image of the model emittance data derived from the 9.2μm channel. Again the areas of sandy material have low values compared with the surroundings (Plate 5.5). It is still possible to separate the granodiorite to the south from the volcanics of the Camp Oven Complex and the granite east of Pinnacle Creek (Plate 5.5; Figure 4.6). The granite can also be separated from the volcanics of the Camp Oven Complex unlike with the model emittance data extracted from 8.4 and 8.8μm channels (Plates 5.3, 5.4, 5.5; Figure 4.6). There is also an area of moderate values east of Pinnacle Creek which can be separated from the granite further east (Plate 5.5; Figure 4.6). Fieldwork identified this as an area of siliceous breccias not previously mapped.

Plate 5.6 is an image of the model emittance data derived from the 9.8μm channel. The siliceous breccia east of Pinnacle Creek is easily dis-

criminated as an area of low values compared to the surroundings (Plate 5.6). It is no longer possible to separate the granodiorite from the volcanics of the Camp Oven Complex (Plate 5.6; Figure 4.6). The granite east of Pinnacle Creek can still be discriminated (Plate 5.6; Figure 4.6) The andesites north and east of Blackfellow Mountain have lower values than the surrounding area (Plate 5.6; Figure 4.6).

Plate 5.7 is an image of the model emittance data derived from the 10.7μm channel. These data are dominated by noise and of little use for lithological mapping. The noise results from the assumption that the radiance in the sixth channel only varies as a function of temperature and the emittance is constant. This assumption is incorrect and since the data from the 10.7μm channel are highly correlated with the 11.7μm channel data any differences between them relate to noise differences and these are extracted as model emittance data (Kahle, 1987).

Plate 5.8 shows the temperature data derived as part of the model emittance calculation. Most of the variation relates to changes in topography. The rivers are cooler than the surroundings as expected since they warm more slowly. Vegetation is also cooler than the surroundings.

Thse results indicate that greater qualitative discrimination is possible with the model emittance data than the decorrelation stretch data (see section 5.3.2). The observed difference in the model emittance data between known rock types, in certain cases, agrees with laboratory spectra from similar rock types. For example, the silica rich areas of sandy material. Unfortunately, this method does not permit the extraction of useful model emittance data from the sixth channel and the data obtained in the fifth is extremely noisy due to the incorrect assumptions in the model emittance calculation. Therefore, any model emittance differences in the wavelength regions covered by these channels, which may allow greater lithological discrimination are lost using this approach.

Since the emittance values for each cover type have been extracted rather than enhanced using this technique it should also be possible to plot pixel spectra from these data. The shape of these pixel emittance spectra can then be compared with laboratory emissivity spectra to infer possible rock types. This possibility is now examined by plotting graphs of wavelength against

model emittance for subsites covering similar areas to those selected with the NS-001 data (see section 4.3.2).

The images used for visual discrimination were produced by rescaling the values in that channel on to a 0-255 range using the mean ± 3 standard deviations as the maximum and minimum values respectively. This enabled maximum utilization of the 0-255 dynamic range of the image processing system for each channel. In order to examine relative variations in emittance between each channel it is necessary to rescale the data using the overall maximum and minimum of all channels.

Examination of the curves from subsites A and B reveal they are almost identical with the maximum absorption occuring in the 9.8μm channel (Figures 5.10 and 5.11). This is not the case in laboratory spectra obtained from similar rock types to these. This absorption is due to the presence of atmospheric effects which have not been removed from the data. In this case the atmospheric component which is present and causes the absorption in the 9.8μm channel is ozone (Figure 3.12).

Field measurements have shown that vegetation can be regarded as a blackbody in the 8μm-12μm region (Gillespie, 1986; Christensen *et al.,* 1986). Therefore, in the model emittance data any areas of vegetation should be spectrally flat. Any spectral variations in the TIMS data over areas of vegetation should relate purely to atmospheric effects. These effects can be removed by normalising the calculated emittances to the values found for vegetation in the same scene (Gillespie, 1986). This approach assumes the atmosphere has a multiplicative effect on the data. However, the atmosphere has both a multiplicative and additive effect associated with absorption and scattering respectively (Kahle *et al.,* 1980). Furthermore, the multiplicative effect is scan angle dependant. That is the greater the scan angle the greater the atmospheric column the radiated energy passes through and greater the multiplicative effect on the data. Therefore, vegetated areas at similar scan angles to the lithologies of interest should be used when normalising data extracted over these lithologies.

Examination of the spectra from subsites A and B after this flat field or vegetation normalisation correction reveals considerable variations in the emittance values at each test site (Figures 5.12 and 5.13). Most obvious is the

twin minima in the 8.4μm and 9.2μm channels at subsite A compared with the single minima at subsite B (Figures 5.12 and 5.13). Comparison of the pixel spectrum from subsite A with laboratory emission spectra indicates the pixel spectrum is not similar to any of these laboratory spectra (Figures 5.3, 5.4, 5.5 and 5.12). The spectrum from subsite A covers an area of granite (Figure 4.6). However, the pixel spectrum is not similar to laboratory emission curve for a granite (Figures 5.4 and 5.12). This suggests that the model emittance calculation coupled with the flat field correction has introduced artifacts into the spectrum making matching difficult.

The spectrum from subsite B is most similar to the laboratory emission spectrum of quartz (Figures 5.3 and 5.13). Fieldwork revealed the area mapped as subsite B had a layer of weathered silica-rich material.

Examination of the pixel spectra from all the remaining test sites indicated that with the exception of the pixel spectrum from subsite H, all the pixel spectra matched those obtained from either subsite A or B.

The spectrum from subsite H has minima in the 8.4μm, 9.2μm and 11.7μm channels (Figure 5.14). The minima in the 11.7μm channel is thought to result from the assumption that the emissivity is 0.93 in the 11.7μm channel. Field mapping had indicated the area covered by this subsite was rich in hydrous bearing minerals (see Chapter 4). Laboratory studies have shown the emissivity in the 11.7μm channel for hydrous minerals should be less than 0.93. If we assume an emissivity of 0.93 in the 11.7μm channel the temperature obtained through the model emittance calculation will be an under-estimate. As a result, the model emittance values obtained for the other channels will be over-estimates causing the value in the 10.7μm channel to be greater than the value in 11.7μm channel.

These results suggest the model emittance data allow greater visual discrimination than the decorrelation stretch data. Pixel spectra obtained from the subsites selected with the NS-001 data could be separated into two groups, with the exception of the spectrum from subsite H. The pixel spectrum of one of these groups was very similar to the laboratory emissivity spectrum of quartz. These spectra were of limited use for lithological discrimination. Unfortunately, useful model emittance data could only be derived from the first four TIMS channels.

5.3.4 Thermal Log Residual Data

Laboratory studies indicate that emissivity variations in rocks in the 8μm-12μm wavelength region relate to differences in their bulk silica content and presence of other non-silicate minerals which should permit lithological discrimination with airborne data (see section 5.2).

Airborne data acquired in this region by the TIMS have been shown to be dominated by temperature effects which mask any emissivity variations (see section 5.3.1). Previous studies have shown these temperature effects can be subdued using the decorrelation stretch to map emissivity variations (see section 5.3.2). However, this technique proved limited with TIMS data from this study area in weathered vegetated terrain. An alternative method for enhancing emissivity variations was then evaluated. This was termed the model emittance calculation (see section 5.3.3). Using the model emittance data it was possible to discriminate more of the mapped lithological units. An area of siliceous breccias was also discriminated which had not been previously mapped. However, the model emittance calculation only permitted the extraction of model emittance data from four of the six TIMS channels. Therefore, a new technique was developed as part of this study which permitted the extraction of relative emittance from all six TIMS channels. The technique is termed Thermal Log Residuals and was developed by the author in collaboration with A. A. Green and A. R. Gabell of CSIRO, Sydney, Australia. The methodology behind the technique is now described and the results from its application to the TIMS data presented.

The aim of the thermal log residual technique is to separate radiance measured by TIMS into its emissivity and temperature components in order to examine variations in emissivity as an aid to lithological mapping and mineral exploration. The radiance for a given sample measured by the TIMS can be related to the emittance and temperature of the surface by Plancks Law which can in turn be approximated to:

$$L_{ij} = \epsilon_{ij}\frac{A}{\lambda_j^5(e^{\frac{c_2}{\lambda_j T_i}} - 1)} \sim \epsilon_{ij}\frac{A}{\lambda_j^5}e^{\frac{-c_2}{\lambda_j T_i}} \qquad 5.8$$

where:

L_{ij} =radiance from a given pixel

$i =$ pixel

$j =$ wavelength

$\epsilon =$ emittance of that pixel

$C_2 =$ second radiation constant

$A = 2c^2h$

$c =$ speed of light

$h =$ Plancks constant

$\lambda_j =$ wavelength for a given TIMS channel

$T_i =$ temperature of a pixel (the same at all wavelengths)

Thermal Log Residuals are then calculated by undertaking the following steps :

(i) Take logs of TIMS data, gives (lnL_{ij})

(ii) Multiply by λ_j (gives $\lambda_j lnL_{ij}$)

(iii) Compute means of the $\lambda_j lnL_{ij}$

(iv) Subtract the means

After step (i) we obtain :

$$lnL_{ij} = Ln\epsilon_{ij} + lnA - 5ln\lambda_j - \frac{C_2}{\lambda_j T_i} \qquad 5.9$$

After step (ii) we obtain :

$$\lambda_j lnL_{ij} = \lambda_j ln\epsilon ij + \lambda_j lnA - 5\lambda_j ln\lambda_j - \frac{C_2}{T_i} \qquad 5.10$$

Note the λ and T terms are now separated.

Let $X_{ij} = \lambda_j lnL_{ij}$

The means are now calculated which when subtracted will result in the separation of the temperature and emittance information. The calculation in order to achieive this is given below:

$$Y_{ij} = X_{ij} - \bar{X}_{i\bullet} - \bar{X}_{\bullet j} + \bar{X}_{\bullet\bullet} \qquad 5.11$$

where:

$Y_{ij} =$ thermal log residual value for a given pixel (contains emittance only)

$\bar{X}_{i\bullet} =$ mean of all channels for a given pixel. This represents the scene temperature and is considered constant for all channels.

$\bar{X}_{\bullet j} =$ mean of all pixels in a given channnel

$\bar{X}_{\bullet\bullet}$ = mean of all pixels from all channels. This is scene constant and added to all values.

$$X_{ij} = \lambda_j ln\epsilon_{ij} + \lambda_j lnA - 5\lambda_j ln\lambda_j - \frac{C_2}{T_i}$$

$$\bar{X}_{i\bullet} = \frac{1}{6}\sum_j^6 \lambda_j ln\epsilon_{ij} + \frac{lnA}{6}\sum_j^6 \lambda_j - \frac{5}{6}\sum_j^6 \lambda_j ln\lambda_j - \frac{C_2}{T_i}$$

$$\bar{X}_{\bullet j} = \frac{1}{N}\sum_i^N \lambda_j ln\epsilon_{ij} + \lambda_j lnA - 5\lambda_j ln\lambda_j - \frac{C_2}{N}\sum_i^N \frac{1}{T_i}$$

$$\bar{X}_{\bullet\bullet} = \frac{1}{6N}\sum_i^N\sum_j^6 \lambda_j ln\epsilon_{ij} - \frac{lnA}{6}\sum_j^6 \lambda_j - \frac{5}{6}\sum_j^6 \lambda_j ln\lambda_j - \frac{C_2}{N}\sum_i^N \frac{1}{T_i}$$

Subtracting the means in equation 5.11 we obtain:

$$Yij = \lambda_j ln\epsilon ij - \frac{1}{6}\sum_j^6 \lambda_j ln\epsilon_{ij} - \frac{1}{N}\sum_i^N \lambda_j + \frac{1}{6N}\sum_i^N\sum_j^6 \lambda_j ln\epsilon_{ij} \qquad 5.12$$

If we let $l_j = \frac{\lambda_j}{\lambda_\bullet}$ and $e_{ij} = (\epsilon_{ij})^{lj}$, where $\overset{\sim}{\lambda_\bullet}$ is some mean of the wavelengths. Then:

$$\frac{Y_{ij}}{\overset{\sim}{\lambda_\bullet}} = lne_{ij} - \frac{1}{6}\sum_k lne_{ij} - \frac{1}{N}\sum_i lne_{ij} + \frac{1}{6N}\sum_{ij} lne_{ij} \qquad 5.13$$

Therefore:

$$\frac{Y_{ij}}{\overset{\sim}{\lambda_\bullet}} = ln\frac{e_{ij}\overset{\sim}{e_{\bullet\bullet}}}{\overset{\sim}{e_{\bullet j}}\overset{\sim}{e_{i\bullet}}} \qquad 5.14$$

Therefore:

$$exp\frac{Y_{ij}}{\overset{\sim}{\lambda_\bullet}} = \frac{e_{ij}\overset{\sim}{e_{\bullet\bullet}}}{\overset{\sim}{e_{\bullet j}}\overset{\sim}{e_{i\bullet}}} \qquad 5.15$$

Thus the thermal log residual reflects variations in some combination of emissivity for a given channel rather than variations of both temperature and emissivity. Initially, log residuals were calculated from the TIMS data by the author using the modified version of log residuals described by Roberts *et al.* (1985) and used with the data from the 0.45μm-2.35μm wavelength region (see previous chapter). These data gave promising results but were not mathematically sound since the effect of temperature still remained, although very subdued, in the log residual data. A. A. Green suggested the multiplication of each channel of data by the central wavelength of that channel which enabled the complete separation of temperature and emittance. The updated technique was then coded and implemented at Durham University upon the author's return to the U. K.

Examination of the relative temperature image obtained as part of the thermal log residual calculation reveals most of the temperature variation results from differences in topography (Plate 5.9). The rivers appear cold (dark). This is due to the water warming more slowly than the surrounding surfaces. No known geological contacts are apparent in the relative temperature image (Figure 4.6; Plate 5.9). The vegetated areas also appear cold since they warm more slowly than the surrounding rocks. This temperature image was correlated with the temperature image derived as part of the model emittance calculation and found to have an R value of greater than 9.0 (Plates 5.8 and 5.9).

Plate 5.10 is an image of the relative emissivity data derived from the channel centered on 8.4μm as part of the thermal log residual calculation. Henceforth all channels are referred to according to their centre wavelength (for example the 8.4μm channel).

Fieldwork determined the lowest values in this image were associated with areas rich in silica. These included the alluvium in and adjacent to the river channels and the weathered mantle produced by *in situ* weathering of the Ravenswood Granodiorite and sediments in the centre of the Camp Oven Complex (Figure 4.6; Plate 5.10) The top and sides of Blackfellow Mountain and K2 also have low values compared with the surroundings (Figure 4.6; Plate 5.10). These areas are also silica rich. Closer examination reveals the scree from Blackfellow Mountain does not have low values. Field mapping indicated the top and sides of Blackfellow Mountain and K2 were densely vegetated ($> 60\%$) compared with the surrounding terrain. These low values are attributed to the vegetation cover rather than the underlying substrate. No other known contacts were discriminated in the relative emissivity data derived from this channel (Plate 5.10; Figure 4.6).

Plate 5.11 is an image of the relative emissivity data derived from the 8.8μm channel as part of the thermal log residual calculation. The lowest values in the image are still associated with the silica rich areas described with the data from the 8.4μm channel. The surface of the dirt road is particularly distintive as an area of low values as it passes over the Ravenswood Granodiorite in the bottom left of the image (Plate 5.11; Figure 4.6). The contact between the Ravenswood Granodiorite and Camp Oven Complex is

easily discriminated (Plate 5.11; Figure 4.6). Parts of the rim of Camp Oven Mountain also have low values compared with the surrounding terrain (Figure 4.6; Plate 5.11). These do not correspond to any mapped lithological variations but may relate to the more siliceous parts of the rim.

Plate 5.12 is the relative emittance data derived from the 9.2μm channel as part of the thermal log residual calculation. The silica-rich areas described with the data from the 8.2μm channel still have the lowest values in this image (Plate 5.12) The rivers are bordered by high values attributed to the vegetation along their banks (Plate 5.12). The eastern flank of the caldera has distinctly low values (Plate 5.12; Figure 4.6). These do not correspond to any mapped lithological units but may indicate the more siliceous areas. The contacts between the Camp Oven Complex and Ravenswood Granodiorite and the late granitic phase of the Ravenswood Granodiorite are easily discriminated (Plate 5.12; Figure 4.6). The apron of scree surrounding Blackfellow Mountain is also apparent although not particularly distinct. There is an area of low values bordering the eastern edge of Pinnacle Creek. The contact between these values and the surrounding terrain had not been mapped. Subsequent fieldwork identified this as an area of siliceous breccia.

Plate 5.13 is an image of the relative emissivity data derived from the 9.8μm channel as part of the log residual calculation. The area of siliceous volcanics east of Pinnacle Creek is particularly distinct as an area of low values in this image (Plate 5.13). This contact had not been mapped and is not apparent in the NS-001 data. The silica rich areas described with the data from the 8.4μm channel now have high values in the image and are becoming less apparent. The areas mapped as andesite lavas can be discriminated having low values (Plate 5.13; Figure 4.6). Two areas labelled A and B can also be discriminated which have high values. Field mapping identified these areas as being silicified. Other silicified areas such as Blackfellow Mountain have high values in the relative emissivity data derived from this channel. (Plate 5.13; Figure 4.6).

Plate 5.14 is an image of the relative emissivity data derived from the 10.7μm channel as part of the log residual calculation. The contact between the Camp Oven Complex and Ravenswood Granodiorite is again clear (Plate 5.14; Figure 4.6). The silica-rich areas are easily discriminated and have high

values in this image (Plate 5.14; Figure 4.6). No other known geological contacts were apparent in this channel.

Plate 5.15 is an image of the relative emittance data derived from the 11.7μm channel as part of the log residual calculation. The interpretation of this data is similar to that for the relative emittance data derived from the 10.7μm channel except that Blackfellow Mountain appears more distinct and has high values in the image.

In general, the relative emissivity values of the different geological units in the thermal log residual data agrees with the expected values from laboratory studies. For example, quartz rich areas have low emissivity values relative to other materials in the first three channels then increasingly higher values in the remaining three channels. By contrast, the areas of basalt have high emissivity values relative to other materials in the scene in the first three channels and low values in the remaining three channels. This agrees with laboratory studies which show the minima associated with the restrahlen band moves to longer wavelengths with decreasing quartz and a concomitant increase in mafic minerals (Lyon, 1965; Figures 5.3 and 5.4). One exception to this is the area of hydrous minerals associated with Blackfellow Mountain. This area should have lower values than other materials in the wavelength region covered by the fifth TIMS channel (10.2μm-11.2μm) due to absorption associated with H-O-Al (see section 5.2.1). These anomalous high values may result from the presence of other minerals which raise the relative emissivity of this material. This hypothesis could be tested by obtaining laboratory spectra of field samples from this wavelength region. Unfortunately, no facilitites were available during this study and the exact cause of these anomalously high values remains undetermined.

5.3.5 Comparison of the Data from the 0.45μm-2.5μm and 8μm-12μm Wavelength Regions for Lithological Mapping and Mineral Exploration at the Camp Oven Test Site

It was possible to discriminate the main lithological units at the Camp Oven test sites using the data from the 0.45μm-2.35μm wavelength region after they were processed with the log residual and LRES techniques. These units included the Ravenswood Granodiorite and its late granitic phase, the Lower Carboniferous sediments and Upper Carboniferous volcanic complex. It was not possible to subdivide the volcanic complex into its mapped sub-units (Figure 4.6). This discrimination was achieved primarily through variations in the amount of iron oxide and Al-OH $\pm$ Mg-OH $\pm$ CO bearing minerals in each unit. The differences in the amount of these minerals present was largely related to the primary mineralogy and weathering history of each unit.

In addition, an area anomalously abundant in Al-OH $\pm$ Mg-OH $\pm$ CO bearing minerals was detected at Blackfellow Mountain. The increased abundance of these minerals is thought to result from hydrothermal alteration of an advanced argillic nature and has obvious significance for mineral exploration.

It was also possible to discriminate these same main lithological units with the multispectral data from the 8μm-12μm region after processing of the data with the thermal log residual technique. A further area of siliceous breccias was also discriminated east of Pinnacle Creek. This area had not been mapped and could not be discriminated with the data from the 0.45-2.35μm wavelength region. This illustrates the complimentary nature of data from the 8μm-12μm wavelength region for lithological mapping. This discrimination was achieved through variations in the Si-O content of these lithologies. It was not possible to discriminate the area of Al-OH $\pm$ Mg-OH $\pm$ CO bearing minerals at Blackfellow Mountain with the data from the 8μm-12μm region.

These results suggest the data from both wavelength regions are useful for lithological mapping and the data from the 8μm-12μm wavelength region provide complimentary information to the data from the 0.45μm-2.35μm wavelength region.

They further infer the data from the 0.45μm-2.35μm wavelength region are of more use in the dectection of areas of Al-OH $\pm$ Mg-OH $\pm$ CO bearing

minerals in this terrain which is particularly important for mineral exploration.

5.4 Analysis and Interpretation of Data from the $8\mu m$-$12\mu m$ Wavelength Region for Lithological Mapping and Mineral Exploration over the Plateau Test Site

The Plateau test site is 512 x 512 pixels in size and located in the SW of the study area (Figure 2.2). The geology of the test site was described in the previous chapter (see section 4.4.1; Figure 4.41).

Data from the 8μm-12μm wavelength region can be used to map emissivity variations which relate to the composition of the underlying material and allow lithological mapping (see section 5.2). Six channels of data were acquired by the TIMS in this wavelength region over the Plateau test site.

These data were processed using the thermal log residual technique. This technique proved the most effective means of enhancing these emissivity differences for lithological mapping with TIMS data from the Camp Oven test site.

The results from analysis of the TIMS with these techniques over the Plateau test site for lithological mapping and mineral exploration should provide an indication of the wider applicability of these techniques in more deeply weathered and vegetated terrain.

The geology of the Plateau test site has been described in section 4.4.1. The results from the interpretation of the thermal log residual data from the Plateau test site are now described.

5.4.1 Thermal Log Residual Data

Plate 5.16 is an image of the relative emissivity data derived from the 8.4μm channel as part of the thermal log residual calculation The andesites and kaolinite rich areas of the sandstones and laterites are easily discriminated and have the highest values in the image (Plate 5.16; Figure 4.41). The areas of sandy alluvium adjacent to the river beds and areas of siliceous shales and cherts can also be discriminated and have the lowest values in the image (Plate 5.16; Figure 4.41). The area mapped as andesite around subsite D appears to extend into the area mapped as siliceous shales and cherts (Plate 5.16; Figure

4.41).

The areas mapped as laterite show considerable variation in their relative emissivity values in this image (Plate 5.16; Figure 4.41). These variations may result from differences in the composition of the underlying material upon which they have developed. For example, the laterite to the northeast of Plateau has lower values than the laterites farther west (Plate 5.16; Figure 4.41). The laterite northeast of Plateau is underlain by the siliceous shales and cherts which also have low values in this image whilst the laterites further west are underlain by the kaolinitic sandstones which have high values in this image.

The grid lines which expose the underlying rock type are particularly useful for lithological discrimination with these data. The grid lines over the siliceous shales, cherts and rhyolite plug (labelled A - Plate 5.16). have far lower values than those over the Campaspe Beds (labelled B - Plate 5.16).

Plate 5.17 is an image of the relative emissivity data derived from the $8.8\mu m$ channel as part of the thermal log residual calculation. The area mapped as andesite around subsite D now clearly extends into the area mapped as siliceous shales and cherts (Plate 5.17; Figure 4.41). The areas of sandy alluvium adjacent to the river beds and siliceous shales and cherts still have the lowest values in the image (Plate 5.17; Figure 4.41). The values of the sandy alluvium are clearly lower than those of the siliceous shales and cherts, permitting the discrimination of these units.

The kaolinite rich areas of the sandstones and andesites still have the highest values in this image and cannot be discriminated from each other (Plate 5.17; Figure 4.41). The grid lines cutting the rhyolite are still visible and have low values compared to the surrounding rocks (Plate 5.19). The grid lines across the rhyolite are now very apparent having low values.

Plate 5.18 is an image of the relative emissivity data derived from the $9.2\mu m$ channel as part of the thermal log residual calculation. It is no longer possible to discriminate the siliceous shales and cherts, the andesite and the sandstones. The areas of sandy alluvium adjacent to the river beds can still be discriminated and have low values in the image (Plate 5.18). The kaolinite rich areas of the sandstones and laterites can be discriminated and have similar low values in the image (Plate 5.18; Figure 4.41). Only the grid lines cutting

the rhyolite are still apparent and have lower values than the surroundings (Plate 5.18; Figure 4.41).

Plate 5.19 is an image of the relative emissivity data derived from the 9.8μm channel as part of the thermal log residual calculation. The areas of sandy alluvium adjacent to the river beds have the highest values in the image (Plate 5.19). The siliceous shales and cherts have moderate values in the image and are easily distinguished from the areas of sandy alluvium (Plate 5.19; Figure 4.41). The lowest values in the image are associated with the kaolinite rich areas of the sandstones and laterites (Plate 5.19; Figure 4.41). The values in the andesites are variable, it appears the unaltered parts of the andesite have lower values than the altered parts (Plate 5.19; Figure 4.41).

Plate 5.20 is an image of the relative emissivity data derived from the 10.7μm channel as part of thermal log residual calculation. The areas of sandy alluvium and the laterite to the northeast of Plateau has the highest values in this image (Plate 5.20; Figure 4.41). The siliceous shales and cherts cannot be separated from the andesites, both have low values in the image (Plate 5.20; Figure 4.41). The lowest values occur in the andesites. The grid lines over the rhyolite have high values compared to the surroundings (Plate 5.20; Figure 4.41). The remainder of the grid lines are not easily distinguished. The kaolinite rich areas of the sandstones and laterite also cannot be discriminated in this image.

Plate 5.21 is an image of the relative emissivity data derived from the 11.7μm channel as part of the thermal log residual calculation. The andesites have the lowest values in this image and are easily distinguished from the siliceous shales and cherts which have moderate values (Plate 5.21; Figure 4.41). The area mapped as andesites now clearly extends into the area mapped as siliceous shales and cherts around subsite D (Plate 5.21; Figure 4.41). The areas of sandy alluvium, laterite northeast of Plateau and grid lines across the rhyolite have the highest values in the image (Plate 5.21; Figure 4.41). The kaolinite rich areas of the sandstones and laterite cannot be discriminated in this image.

Plate 5.22 is an image of the relative temperature data derived as part of the thermal log residual calculation. Variations in these data relate to topography and vegetation. The vegetated areas such as the siliceous shales

and cherts, Campaspe Beds, and river channels appear much cooler (darker) than the surrounding area. The kaolinite rich areas appear hot (light). The grid lines have a variety of values which no longer appear to relate to changes in the underlying lithology.

In general, the results from the thermal log residual data agree with the expected results from laboratory studies. For example, the siliceous areas associated with the rhyolite and certain laterites have lower values than other materials in the relative emissivity data derived from the first three TIMS channels and higher values than other materials in the latter three TIMS channels. By contrast, the andesites have higher values than other materials in the relative emissivity data derived from the first three TIMS channels and lower values in the remaining three TIMS channels. This concurs with laboratory studies which show the minima associated with the restrahlen band moves to longer wavelengths with decreasing quartz content and increasing mafic mineral content (Lyon, 1965; Figure 5.4)

The andesites do show some variation in relative emissivity data derived from a given TIMS channel and this may relate to the presence of additional minerals, in certain areas, such as epidote.

Of particular interest are the areas of kaolinite. These agree with the expected behaviour of pure kaolinite having a marked minima relative to other materials in the scene in the wavelength region covered by the 9.8μm channel (Figure 5.4) This conflicts with behaviour of the area of hydrous minerals at Blackfellow Mountain in the Camp Oven test site which included kaolinite but did not have a marked minima relative to other materials in this channel. This may be due to the presence of other minerals which increase the relative emissivity of the values from Blackfellow Mountain.

5.4.2 Comparison of the Data from the 0.45μm-2.5μm and 8μm-12μm Wavelength Regions for Lithological Mapping and Mineral Exploration at the Plateau Test Site

It was possible to discriminate all the mapped lithological units with the multispectral data from the 0.45μm-2.35μm region after processing with the log residual and LRES techniques. These units included the Cambro-Ordovician siliceous shales, cherts, and andesites, the Upper Carboniferous rhyolite and granite, the Triassic kaolinitic sandstones and the laterites and alluvium.

This discrimination was achieved largely through variations in the amount of iron oxides and Al-OH ± Mg-OH ± CO bearing minerals. Differences in these minerals were related to the weathering history and primary mineralogy of each unit.

It was also possible to discriminate these same units using multispectral data from the 8μm-12μm region. Discrimination in this wavelength region was achieved through variations in the Si-O content of each unit. The kaolinite rich areas were mapped through absorptions associated with H-O-Al bonding.

It was far easier to detect areas of Al-OH ± Mg-OH ± CO bearing minerals with the data from the 0.45μm-2.35μm wavelength region than the 8μm-12μm wavelength region For example, the epidote altered areas of the andesite.

These results concur with those from the Camp Oven test site and indicate the data from both wavelength regions are useful for lithological mapping. However, the data from the 0.45μm-2.35μm wavelength region allow greater discrimination of areas rich in Al-OH ± Mg-OH ± CO bearing minerals and are therefore more useful for mineral exploration.

5.5 Interpretation of Thermal Log Residual Data calculated from TIMS data acquired over the Cuprite Mining District Nevada, W. USA

The thermal log residual technique proved to be the most effective means of a variety of techniques for enhancing relative emissivity variations in TIMS data acquired over vegetated weathered terrain (sections 5.3.4 and 5.4.1).

This technique was developed as part of this study and the methodology behind it described in section 5.3.4. The results are now presented from the application of this technique to TIMS data from a semi-arid terrain with limited surface weathering at Cuprite, Nevada. These results are contrasted with decorrelation data already published from this data set to evaluate the wider applicability of this technique. The results from the analysis and interpretation of TIMS data using the decorrelation stretch were published by Kahle and Goetz (1983). Figure 5.15 shows the geology of this test site and Plate 5.23 is the decorrelation stretch of the 10.7μm, 9.2μm and 8.4μm channels displayed as red, green and blue respectively also taken from Kahle and Goetz (1983).

Plate 5.24 is an image of the relative emissivity data derived from the 8.4μm channel as part of the thermal log residual calculation. The relative differences in emissivity between a variety of rock types are now examined. The rock types and their notation is the same as that used for the Decorrelation Stretch data in Kahle and Goetz (1983). The silicified core (S) of the Siebert Tuff and Harkless Siltstone (SS) have the lowest values in the image (Plate 5.24; Figure 5.15). The next highest values in the image occur in the in the fan (Q), south of the eastern portion of the Siebert Tuff (Plate 5.24; Figure 5.15). The carbonates (C), clay-rich opalized units (O) and unaltered Thirsty Canyon Tuffs (T) have slightly higher values (Plate 5.24; Figure 5.15). The highest values in this image occur in the basalt (B) (Plate 5.24; Figure 5.15).

Plate 5.25 is an image of the relative emissivity data derived from the 8.8μm channel as part of the log residual calculation. The lowest values in the image are now associated with the clay-rich opalized zone (O) (Plate 5.25; Figure 5.15). The next highest values are associated with the fan (Q) then the silicified zone (S) (Plate 5.25; Figure 5.15). The Harkless Siltstone (SS) and Thirsty Canyon Tuff have slightly higher values (Plate 5.25; Figure 5.15). The highest values in the image occur in the carbonates (C) and basalt (B) (Plate 5.25; Figure 5.15).

Plate 5.26 is an image of the relative emissivity data derived from the 9.2μm channel as part of the thermal log residual calculation. The lowest values in the image are still associated with the clay-rich opalised zone (O),

unaltered Siebert Tuff and fans (Q) derived from this lithology (Plate 5.26; Figure 5.15). The next highest values are associated with the silicified zones (S) and Harkless Silstone (SS) (Plate 5.26; Figure 5.15). The Thirsty Canyon Tuff (T) has higher values and the carbonates (C) have slightly higher values (Plate 5.26; Figure 5.15). The highest values are associated with the basalt (B).

Plate 5.27 is an image of the relative emissivity values derived from the 9.8μm channel as part of the thermal log residual calculation. The lowest values in the image are now associated with the basalt (B) and Harkless Silstone (SS) (Plate 5.27; Figure 5.15). The next highest values are associated with the Thirsty Canyon Tuff (T) then carbonates (C) (Plate 5.27; Figure 5.15). The highest values in the image occur in the clay-rich opalised zone (O) (Plate 5.27; Figure 5.15). The fan (Q) also has high values (Plate 5.27; Figure 5.15).

Plate 5.28 is an image of the relative emissivity data derived from the 10.7μm channel as part of the log residual calculation. Both the carbonates (C) and basalt (B) have very low values in this image (Plate 5.28; Figure 5.15). The Harkless Silstone (SS) and Thirsty Canyon Tuff (T) have slightly higher values (Plate 5.28; Figure 5.15). The highest values in the image occur in the clay-rich opalised zone, with slightly lower values in the fan (Q) (Plate 5.28; Figure 5.15).

Plate 5.29 is an image of the relative emissivity data derived from the 11.7μm channel as part of the thermal log residual calculation. The lowest values in the image are associated with the carbonates (C) and the basalt (B) (Plate 5.29; Figure 5.15). The Harkless Siltsone (SS) has higher values followed by the Thirsty Canyon Tuff (T) (Plate 5.29; Figure 5.15). The highest values in the image occur in the silicified zone (S), the fan (Q) and opalised zone (O) have slightly lower values.

Table 5.1 summarises the relative postion of each unit in each channel in terms of brightness. These data show good agreement with published spectra from similar rock types (Figure 5.3 and 5.4). For example the silica rich areas have lower values in the first three TIMS bands and higher values in the latter three TIMS bands. By contrast, the silica poor areas (basalt) have high values in the first three TIMS channels and lower values in the

latter three channels. Laboratory studies show the restrahlen minima in the 8μm-12μm wavelength region moves to longer wavelengths with decreasing quartz content and increasing mafic mineral content (Lyon, 1965; Figure 5.4). The relative emissivity of the carbonate also agrees with laboratory studies which indicate such materials should have low values in the wavlength regions covered by the fifth and sixth TIMS channels (Figure 5.5).

Plate 5.30 is an image of the relative temperature data derived as part of the thermal log residual calculation. Again most of the variation appears to be related to topography as expected and was of limited use for lithological mapping.

If so desired the temperature information can be added back to each channel to produce an image very similar to that obtained using the Decorrelation Stretch (Plates 5.31 and 5.23).

5.6 Conclusions

1. The decorrelation stretch data were of little use for mapping known or new lithological units at the Camp Oven test site.

2. It was possible to discriminate most of the mapped lithological units with the model emittance data.

3. An additional area was discriminated with the model emittance data which was subsequently identifed as siliceous breccia. This area had not been mapped previously.

4. The model emittance calculation resulted in the loss of useful emittance data from the last two TIMS channels.

5. Matching of model emittance pixel spectra to laboratory emissivity spectra proved difficult. This is thought to be due to assumptions in the model emittance calculation and flat field correction.

6. It was possible to map most of the known lithological units with the thermal log residual data.

7. An additional area was discriminated with the thermal log residual data which was subsequently identifed as siliceous breccia. This area had not been mapped previously and was more apparent than in the model emit-

tance data.

8. The thermal log residual data allowed the extraction of relative emissivity variations in all six TIMS channels.

9. The thermal log residual data permitted the greatest discrimination of the three techniques which also included the decorrelation stretch and model emittance calculation at the Camp Oven test site.

10. The multispectral data from the $8\mu m$-$12\mu m$ wavelength region proved just as effective as data from the $0.45\mu m$-$2.35\mu m$ wavelength region for lithological mapping at the Camp Oven test site. An additonal unit was discriminated with the data from the $8\mu m$-$12\mu m$ wavelength region illustrating the complimentary nature of the two data sets.

11. The data from the $0.45\mu m$-$2.35\mu m$ wavelength region proved more effective than the data from the $8\mu m$-$12\mu m$ wavelength region for the detection of areas of Al-OH $\pm$ Mg-OH $\pm$ CO bearing minerals and were therefore considered more useful for mineral exploration.

12. It was possible to discriminate most of the mapped lithological units with the thermal log residual data from the Plateau test site.

13. Comparison of the data from the 0.45-$2.35\mu m$ and $8\mu m$-$12\mu m$ wavelength regions at the Plateau test site obtained similar results to the same data types from the Camp Oven test site (conclusions 10 and 11).

14. It was possible to discriminate most of the mapped lithological units with thermal log residual data derived from TIMS data acquired over a semi-arid sparsely vegetated area with little surface weathering at Cuprite, Nevada, W. USA.

15. Greater discrimination was achieved with the thermal log residual data than with the decorrelation stretch data calculated from the TIMS data acquired over this test site.

16. The relative emissivity values of a group of rock types in each channel at the Cuprite test site agrees with those expected from laboratory emissivity data.

17. The thermal log residual technique appears to be widely applicable to TIMS data from a variety of terrains and permits greater discrimination than the decorrelation stretch or model emittance calculation.

5.7 Summary

Laboratory studies have demostrated that the energy emitted in the 8μm-12μm wavelength region is a function of temperature and emissivity variations. These emissivity variations relate to the type of material and composition of the emitting surface and should permit the discrimination of certain lithologies.

Airborne multispectral data acquired from the 8μm-12μm wavelength region by the TIMS were found to be dominated by temperature effects which inhibited the examination of any emissivity differences. Previous studies had shown these emissivity differences could be enhanced or extracted using either the decorrelation stretch or model emittance calculation sufficiently for lithological discrimination. In this study area the data extracted using the model emittance calculation enabled greater discrimination than the decorrelation stretch data. It was possible to discriminate an area which was subsequently identifed as siliceous breccia with the model emittance data which had not been previously mapped. Unfortunately, assumptions made in the model emittance calculation meant it was only possible to extract useful model emittance data from the first four TIMS channels.

Therefore, a new technique was developed termed thermal log residuals which permited the extraction of relative emissivity data in all six TIMS channels. It was possible to map all the contacts identified with the model emittance data with thermal log residual data. The area of silceous breccia was also more apparent in the thermal log residual data. The relative emissivity differences of a variety of rock types in a given channel obtained with the thermal log residual calcualtion showed good agreement with the differences expected from laboratory studies.

Comparison of data from the 0.45μm-2.35μm and 8μm-12μm wavelength regions over the Camp Oven and Plateau test sites indicate the longer wavelength data provide complimentary information to the shorter wavelength data which can improve lithological discrimination. The data from the 0.45μm-2.35μm wavelength region permitted greater discrimination of areas of Al-OH $\pm$ Mg-OH $\pm$ CO bearing minerals than the 8μm-12μm wavelength data, and as a result are considered more useful for mineral exploration.

The thermal log residual technique was then applied to TIMS data from a semi-arid sparsely vegetated terrain with little surface weathering at Cuprite, Nevada, USA. These TIMS data had already been interpreted using the decorrelation stretch technique. Comparison of the intepretations obtained using the two techiques indicated greater discrimination was possible with the thermal log residual data. The relative emissivity differences of a group of rocks in a given channel obtained with the thermal log residual calculation again showed good agreement with the expected differences from laboratory studies.

Channel 1 8.2-8.6μm	Channel 2 8.6-9.0μm	Channel 3 9.0-9.4μm	Channel 4 9.6-10.2μm	Channel 5 10.3-11.1μm	Channel 6 11.3-11.7μm
B	B	B	O	O	O
C, O, T	C	C	Q	Q	Q
Q	SS, T	T	S	S	S
S, SS	S	S, SS	C	SS	T
	Q	Q	T	T	SS
	O	O	B, SS	B, C	B, C

Table 5.1 Comparison of the relative emissivity of a variety of rock types in each channel of thermal log residual data over Cuprite, Nevada, USA. Relative emittance increases in direction of arrow. B -basalt, C - carbonates, O - opalised zone, S - silicified zone, SS - Harkless Silstone, Q - fan, T - unaltered tuffs
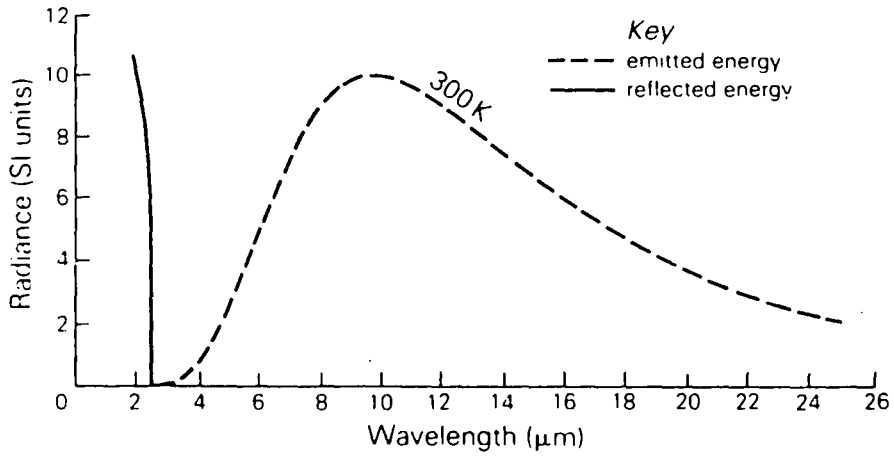
Figure 5.1 Energy received from the Earth's Surface at wavelengths longer than $2.5\mu m$ (from Drury 1987).
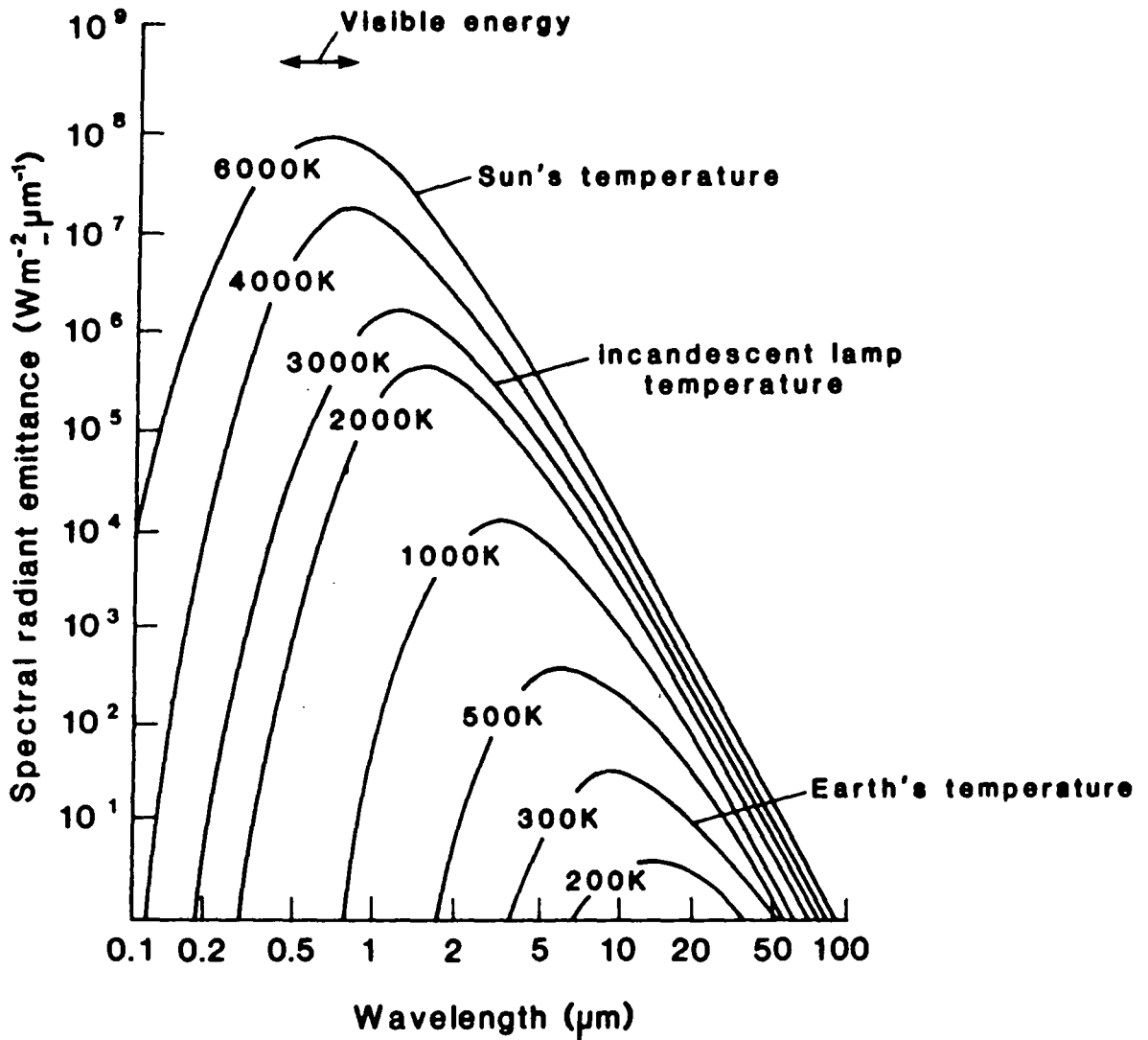
Figure 5.2 Spectral exitance of a Blackbody at various temperatures (from Drury 1987).
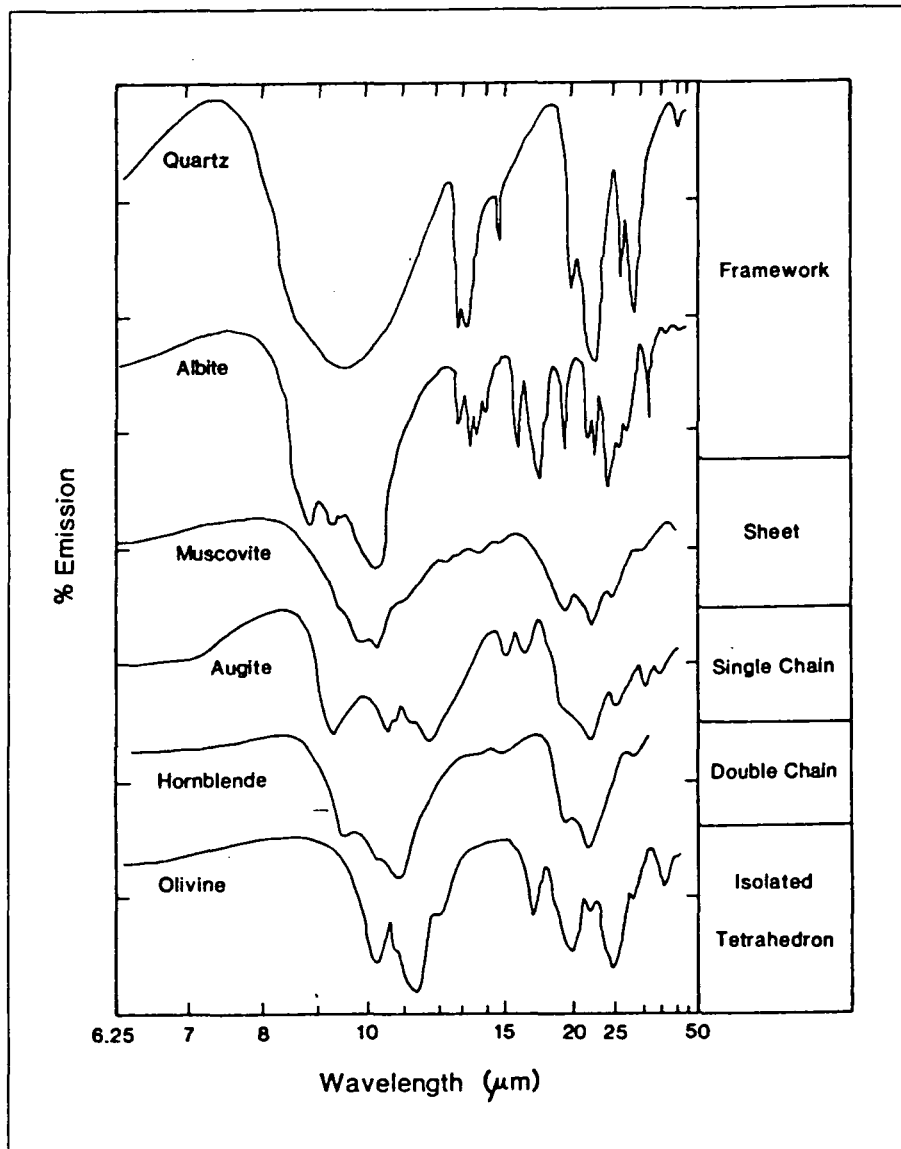
Figure 5.3   Thermal Infrared Spectra of Silicate Minerals. Spectra were
converted from reflectance to emission using Kirchoffs Law. The ver-
tical axis divisions are placed 0.1 in emissivity (from Christensen *et
al.*, 1986).

217
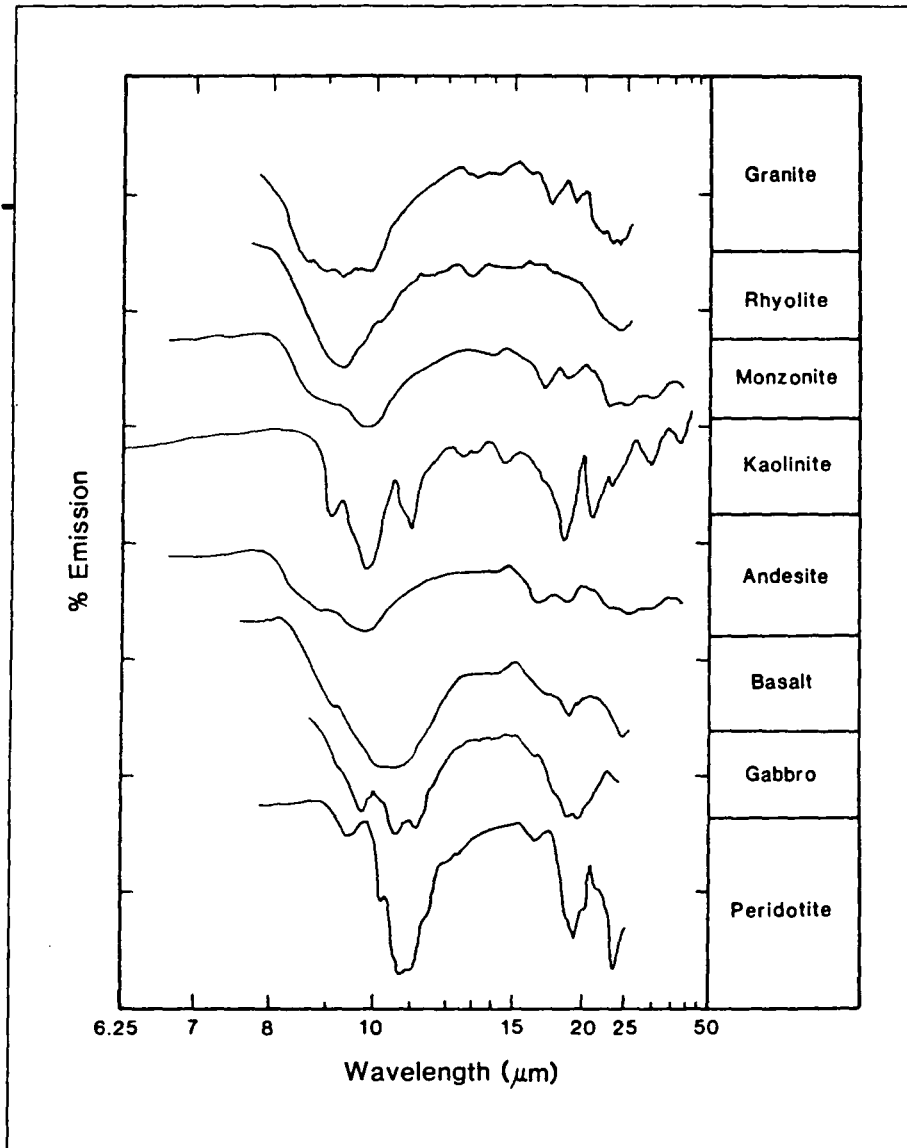
Figure 5.4   Thermal Infrared Spectra of the Rocks varying from high
SiO$_2$ (granite) to low SiO$_2$ (peridotite). Spectra were converted from
reflectance to emission using Kirchoffs Law. The vertical axis divisions
are placed 0.1 in emissivity (from Christensen *et al.*, 1986).
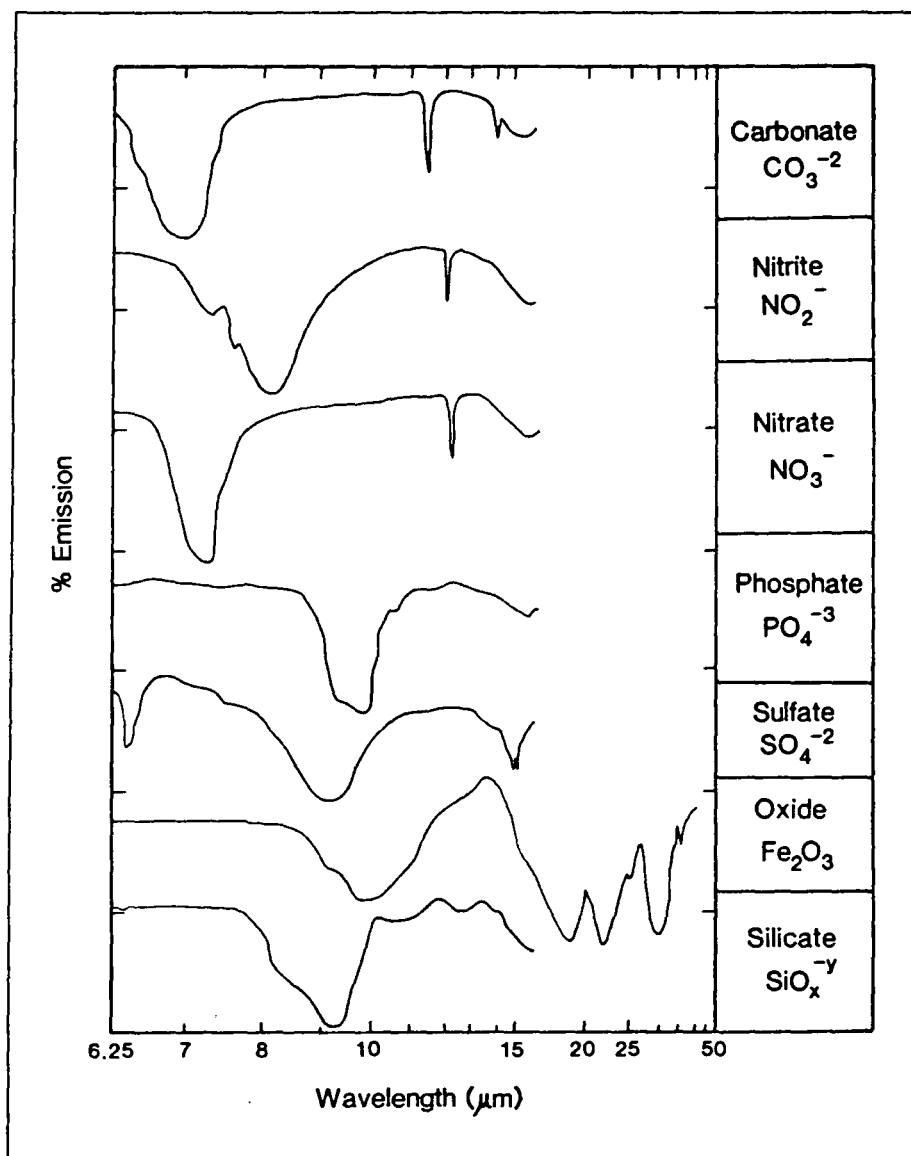
Figure 5.5 Thermal Infrared Spectra of the Major Mineral Groups. Spectra were converted from reflectance to emission using Kirchoffs Law. The vertical axis divisions are placed 0.1 in emissivity (from Christensen *et al.*, 1986).
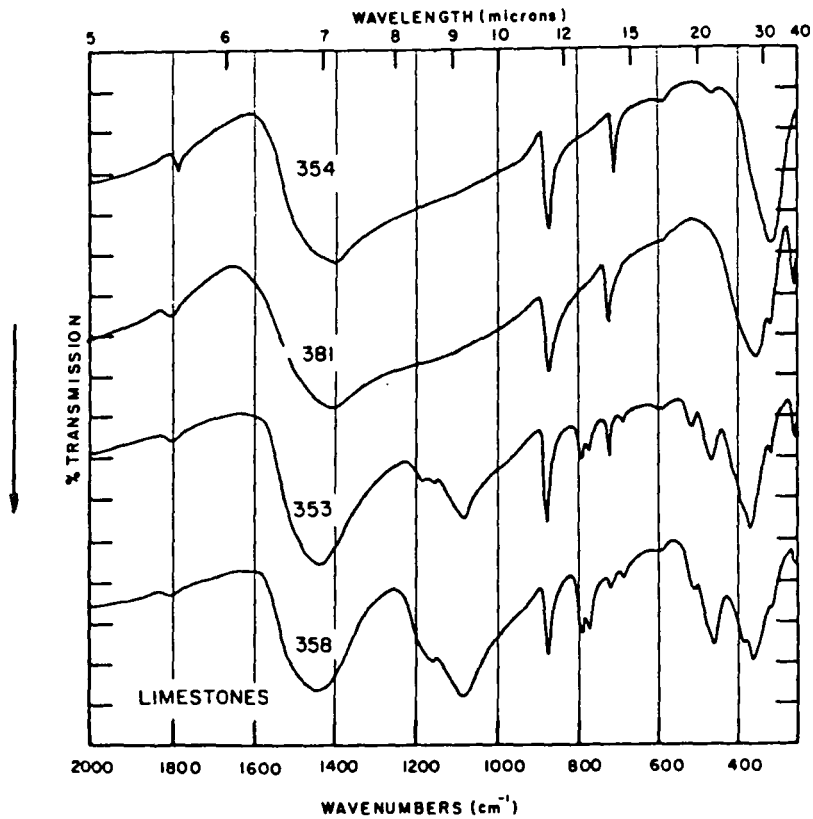
Figure 5.6   Midinfrared transmission spectra of a series of limestones with increasing quartz and clay content in direction of arrow (after Hunt, 1980).
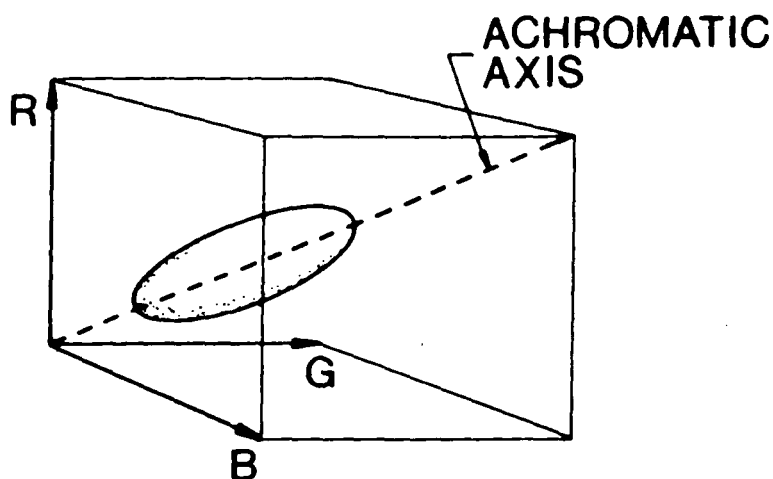
Figure 5.7   Illustration of the effect of high interband correlation on the scattergram of two bands.

UNDERUTILIZED
REGION OF
HISTOGRAM
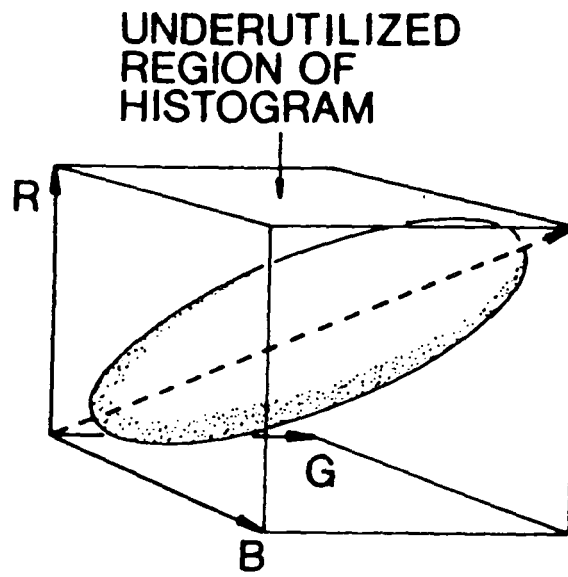
Figure 5.8   Illustration of the effect of contrast stretching on two bands
with a high interband correlation.
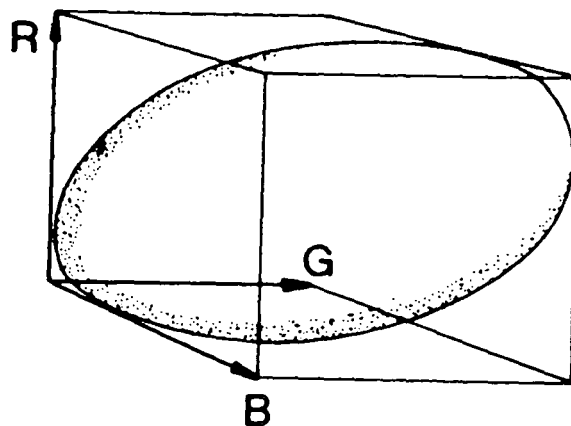
Figure 5.9   Illustration of colour space utilised after Decorrelation Stretch-
ing
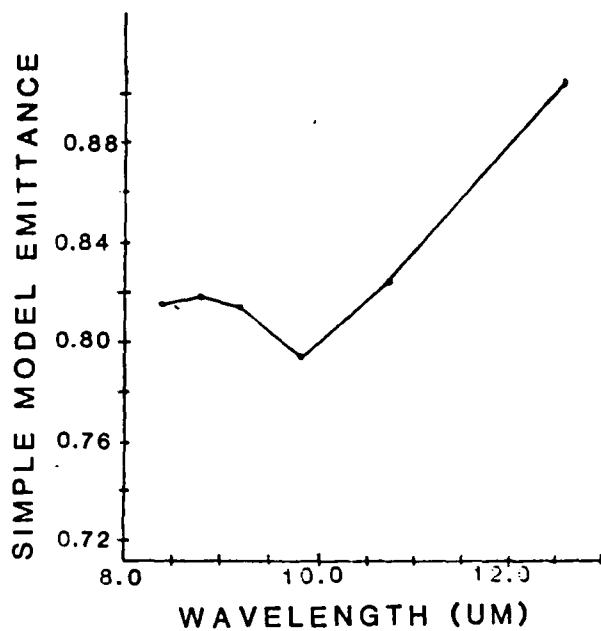
Figure 5.10   Six point emittance spectrum extracted from subsite A.
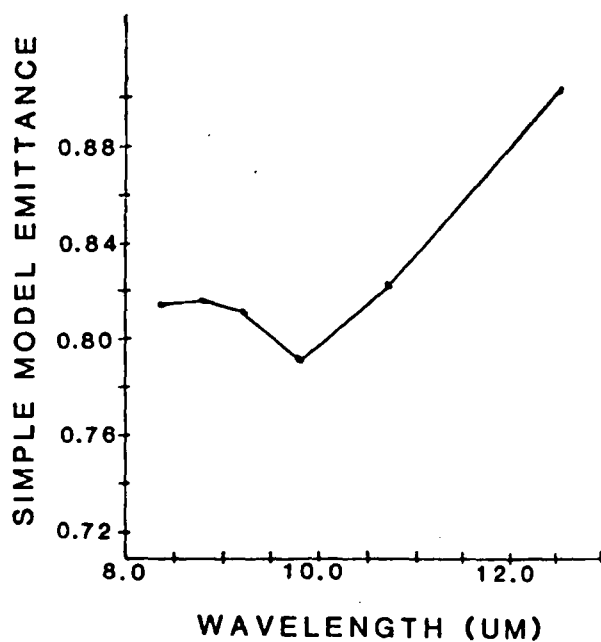
Figure 5.11   Six point emittance spectrum extracted from subsite B.
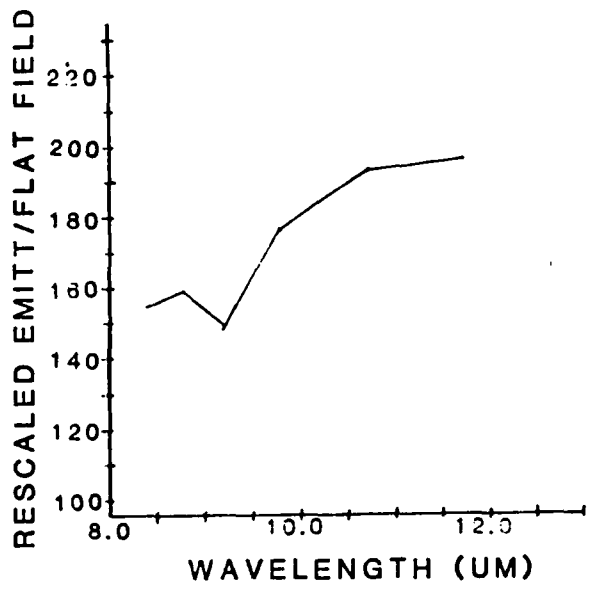
Figure 5.12   Six point emittance spectrum with flat field correction extracted from subsite A.
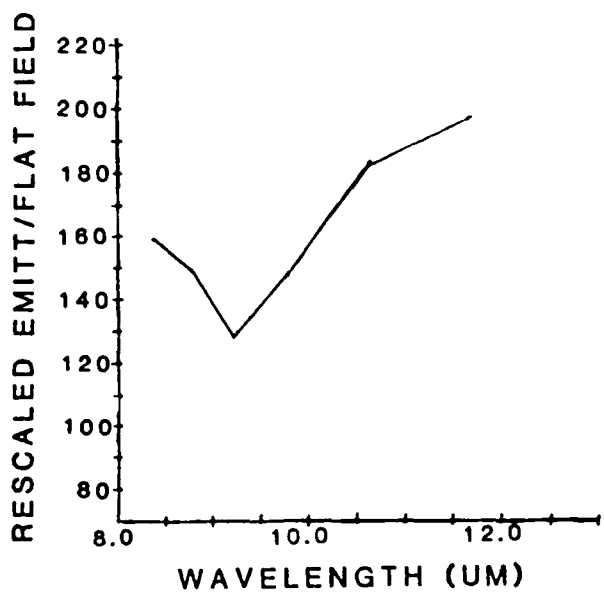
Figure 5.13   Six point emittance spectrum with flat field correction extracted from subsite B.
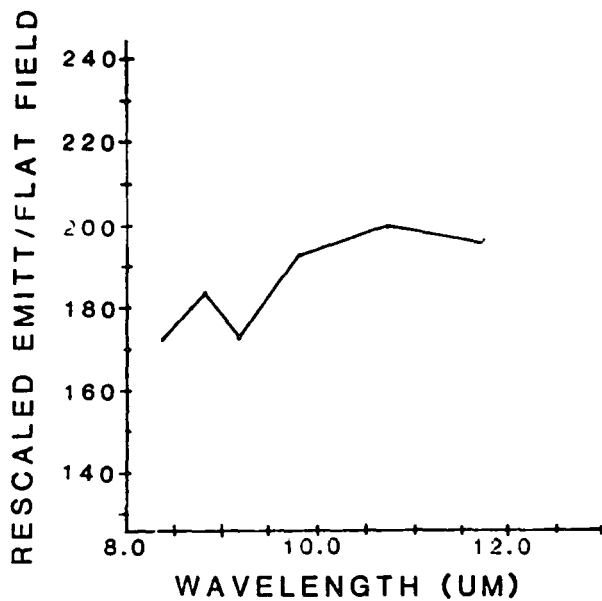
Figure 5.14   Six point emittance spectrum with flat field correction extracted from subsite H.
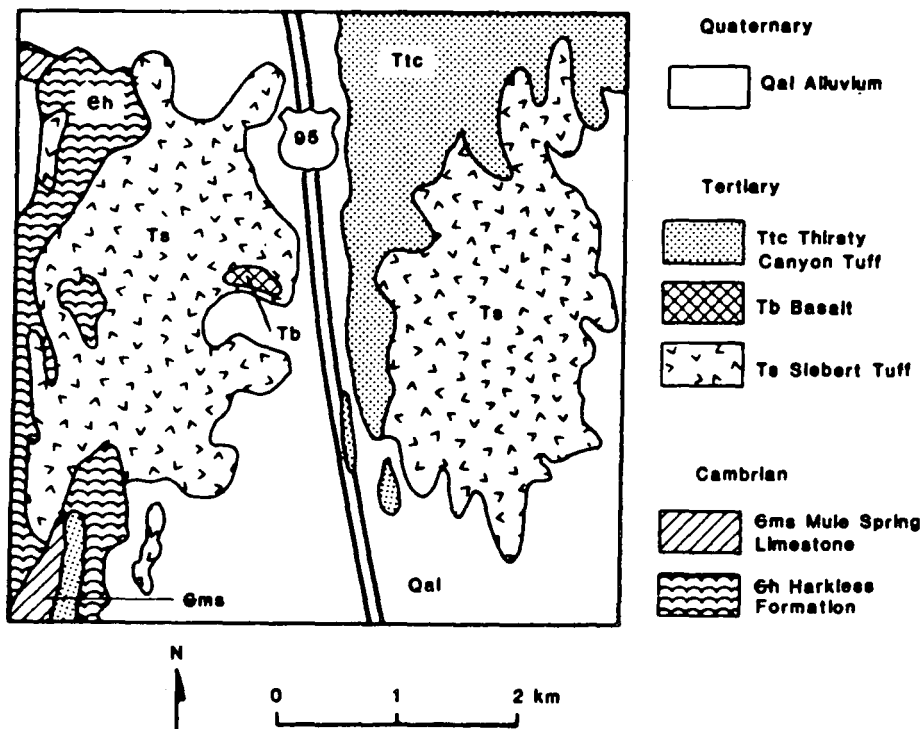
Figure 5.15   Generalised lithologic map of the Cuprite Mining District (from Kahle and Goetz 1983).

224
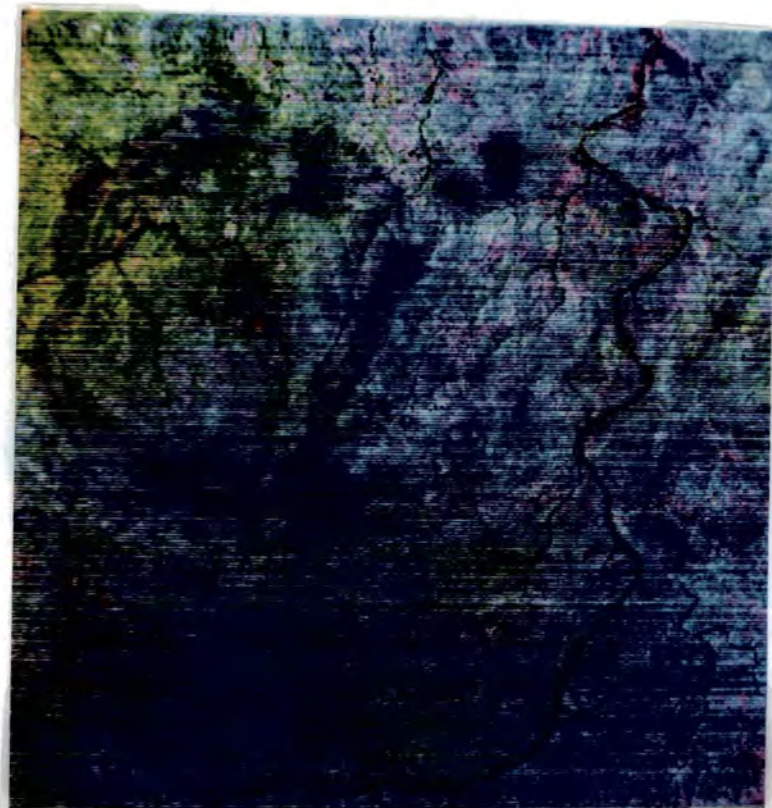
Plate 5.1   Composite of the 10.7μm , 9.2μm and 8.4μm Decorrelation
Stretch   Channels Displayed as Red, Green and Blue Respectively,
Camp Oven Test Site.
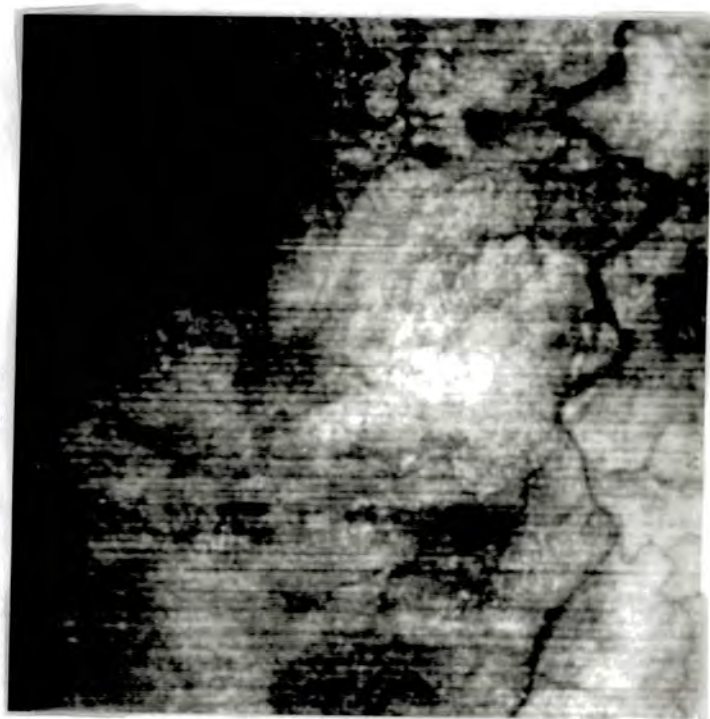
Plate 5.2   Decorrelation Stretch of the 8.4μm Channel, Camp Oven Test
Site.
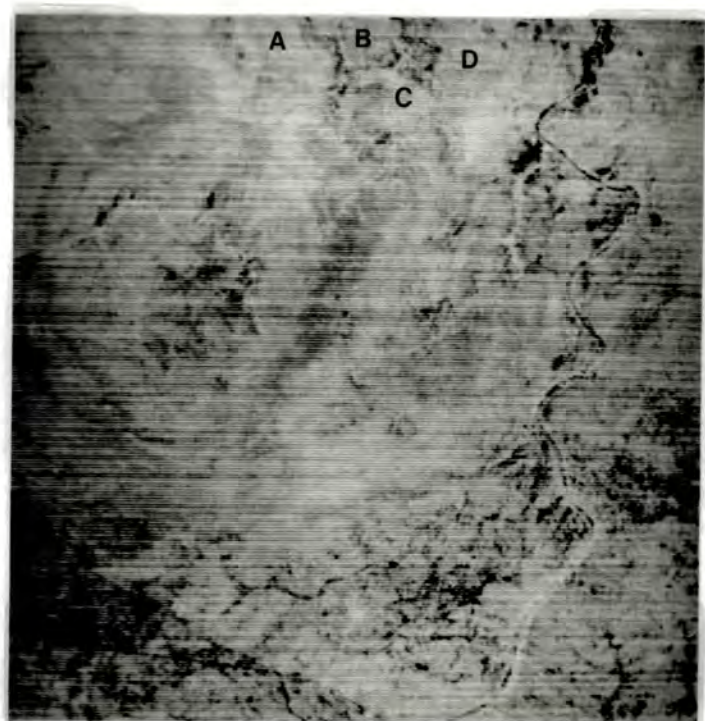
Plate 5.3   Model Emittance Data Derived from 8.4µm Channel, Camp
Oven Test Site.
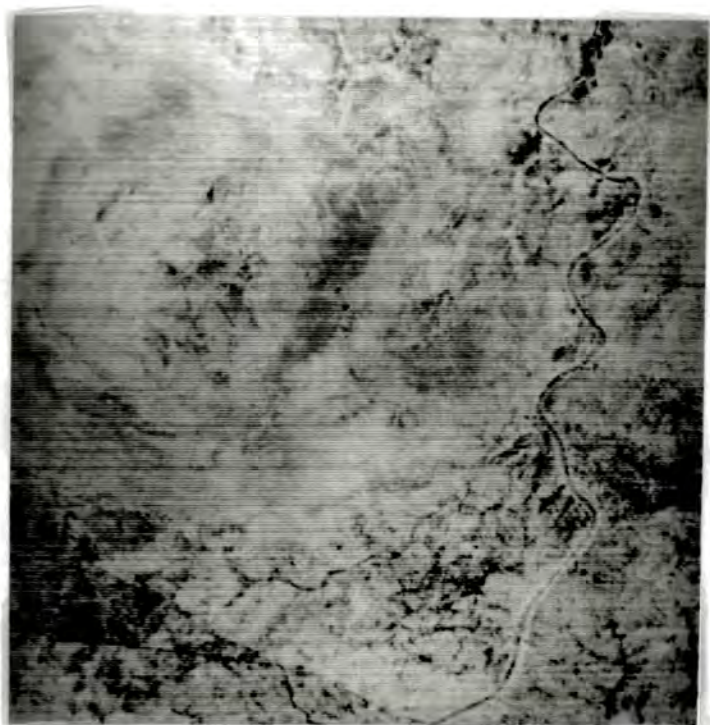
Plate 5.4   Model Emittance Data Derived from 8.8µm Channel, Camp
Oven Test Site.
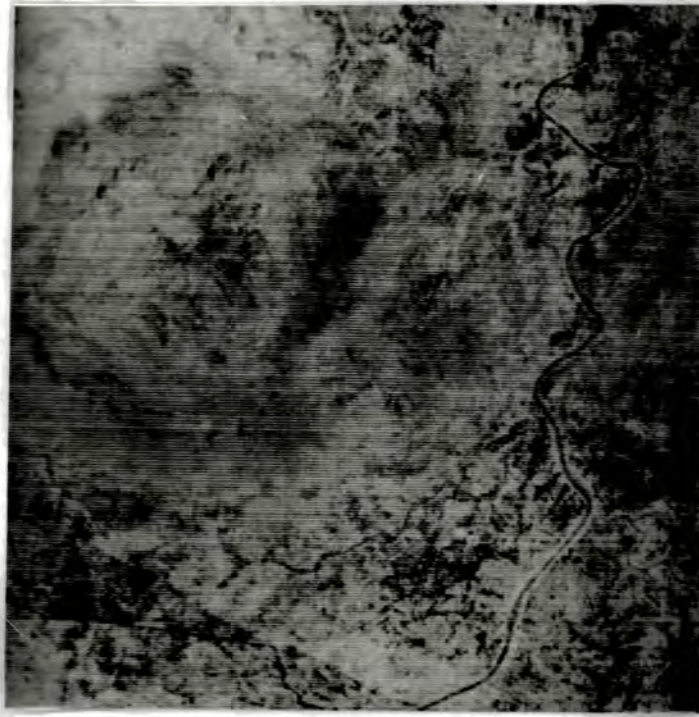
Plate 5.5   Model Emittance Data Derived from 9.2μm Channel, Camp
Oven Test Site.
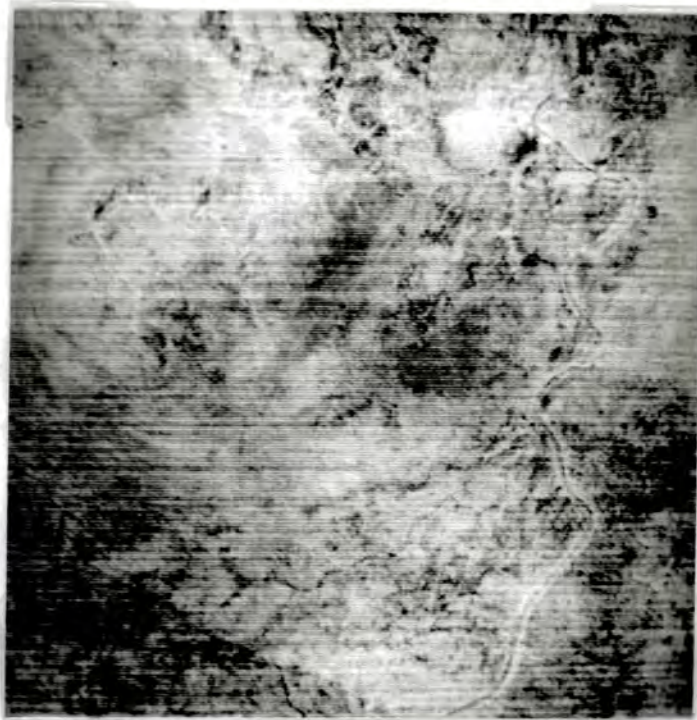
Plate 5.6   Model Emittance Data Derived from 9.8μm Channel, Camp
Oven Test Site.
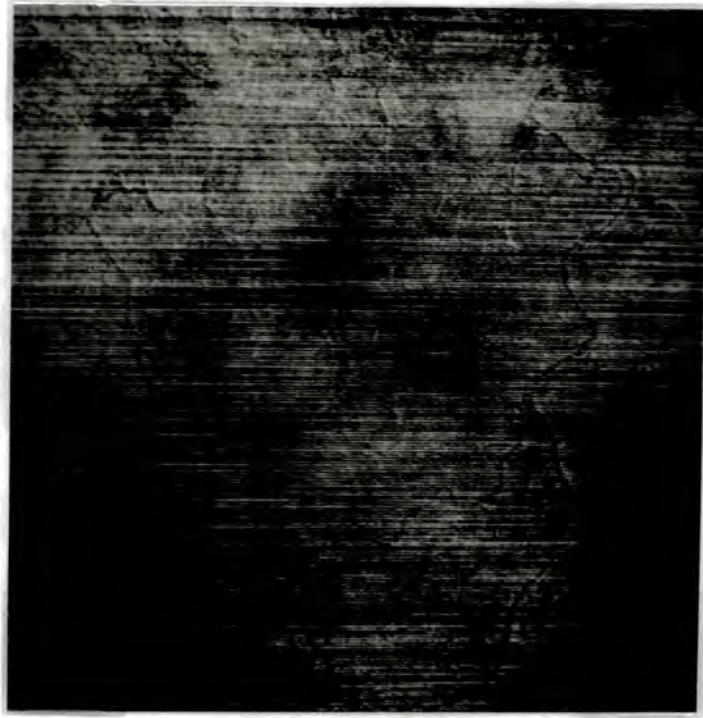
Plate 5.7　Model Emittance Data Derived from 10.7μm Channel, Camp Oven Test Site.
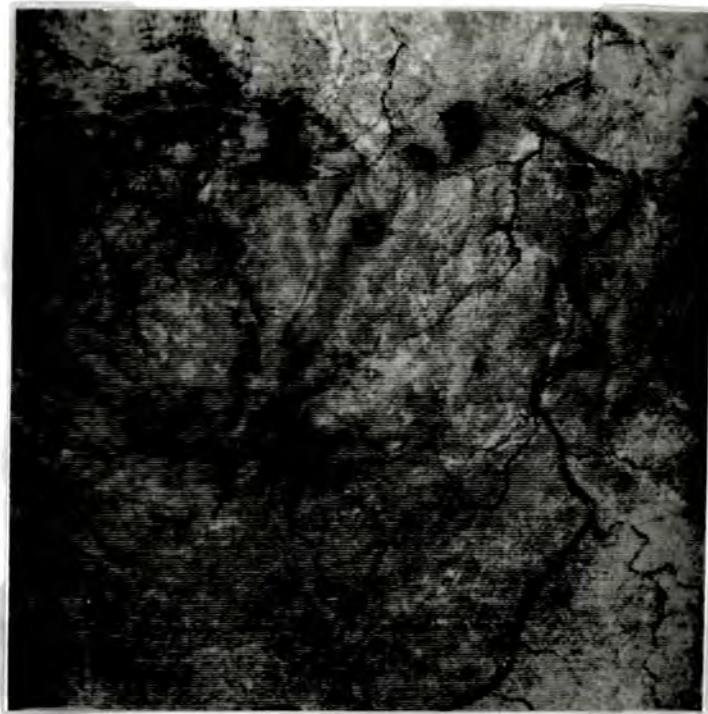
Plate 5.8　Temperature Data Derived as Part of the Model Emittance Calculation, Camp Oven Test Site.

Plate 5.9   Relative Temperature Data Derived as Part of the Thermal
Log Residual Calculation, Camp Oven Test Site.

Plate 5.10   Thermal Log Residual of the 8.4μm Channel, Camp Oven
Test Site.

Plate 5.11   Thermal Log Residual of the 8.8μm Channel, Camp Oven
Test Site.
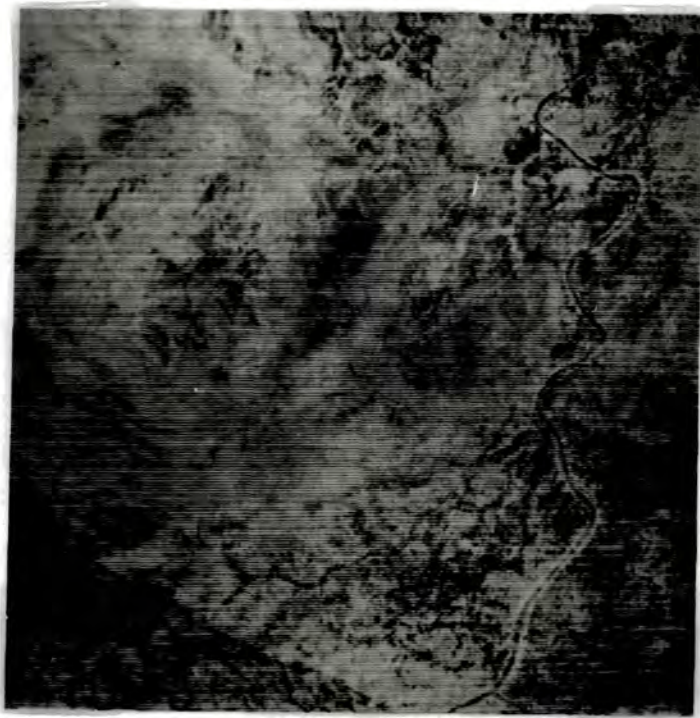
Plate 5.12   Thermal Log Residual of the 9.2μm Channel, Camp Oven
Test Site.
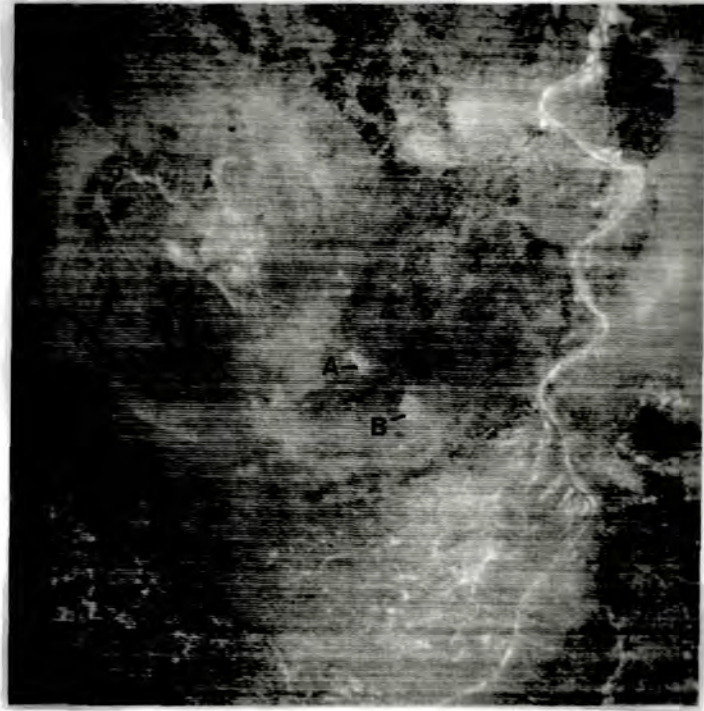
Plate 5.13   Thermal Log Residual of the 9.8μm Channel, Camp Oven
Test Site.
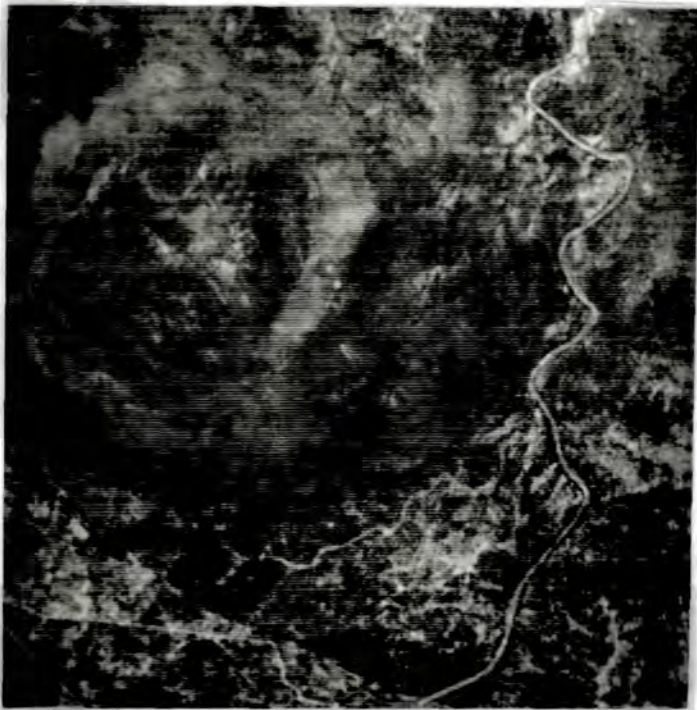
Plate 5.14   Thermal Log Residual of the 10.7μm Channel, Camp Oven
Test Site.

Plate 5.15   Thermal Log Residual of the 11.7µm Channel, Camp Oven
    Test Site.
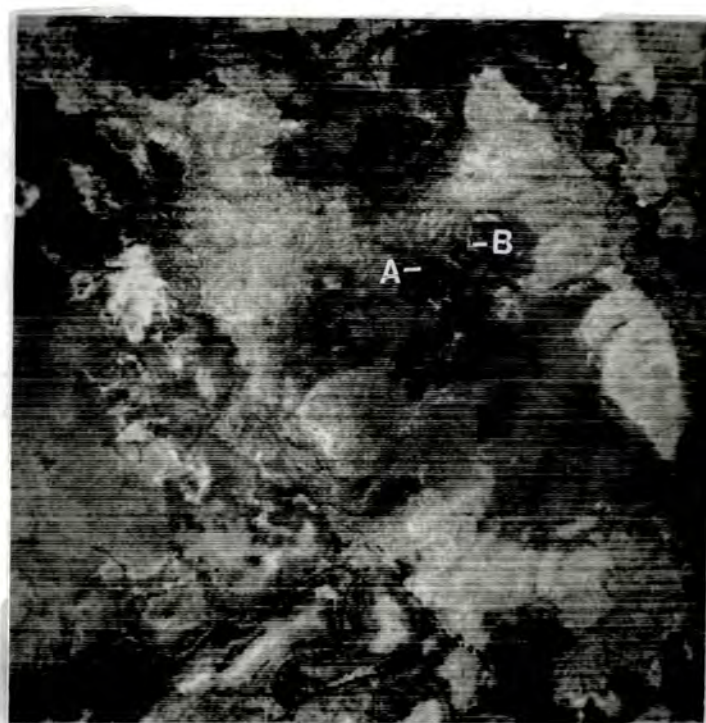
Plate 5.16   Thermal Log Residual of the 8.4µm Channel, Plateau Test
    Site.
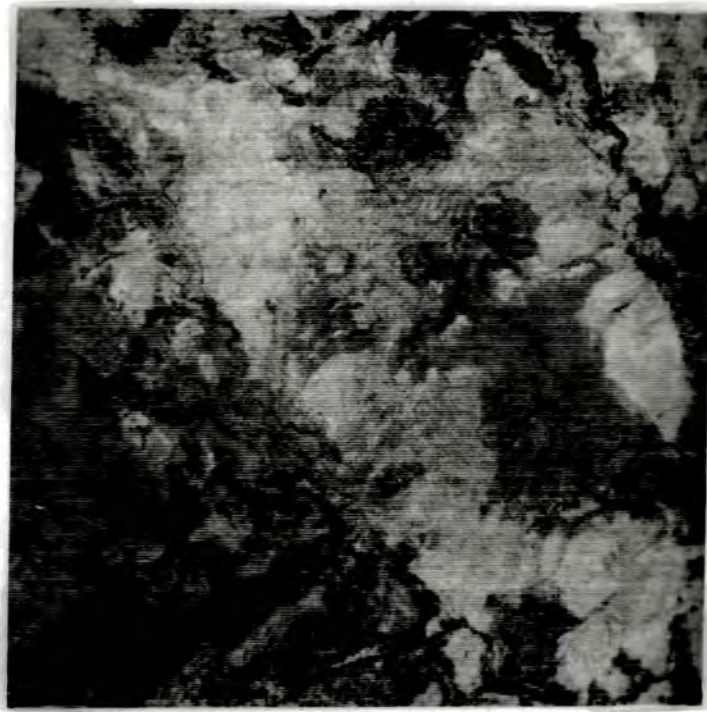
Plate 5.17   Thermal Log Residual of the 8.8μm Channel, Plateau Test
Site.
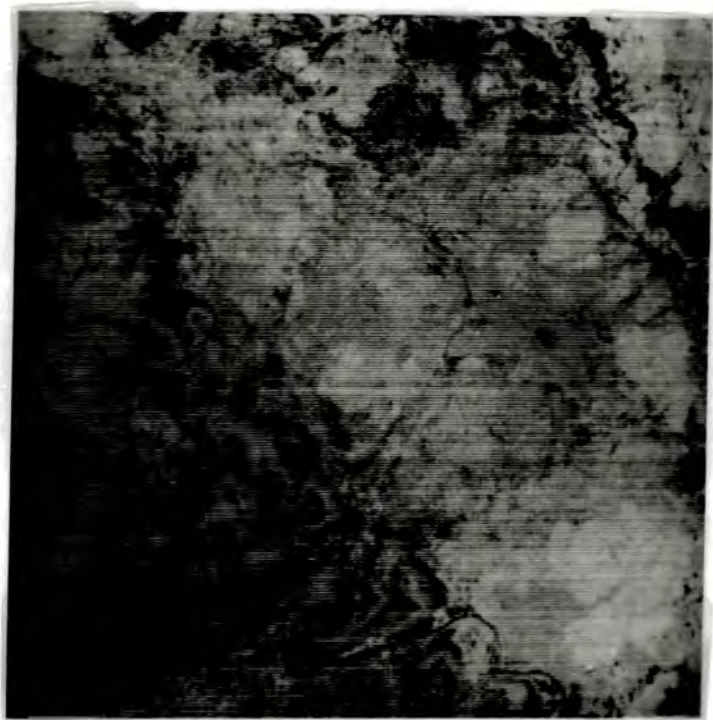
Plate 5.18   Thermal Log Residual of the 9.2μm Channel, Plateau Test
Site.
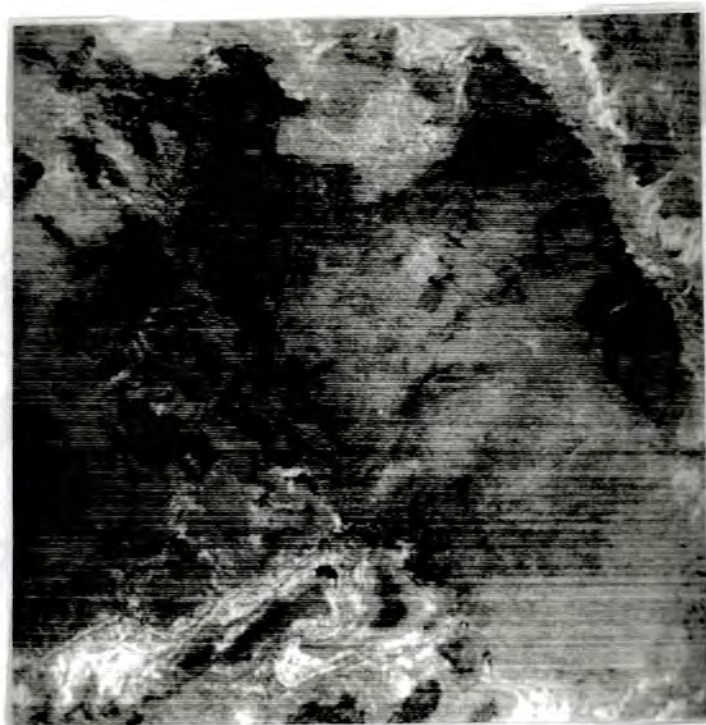
Plate 5.19   Thermal Log Residual of the 9.8μm Channel, Plateau Test
Site.
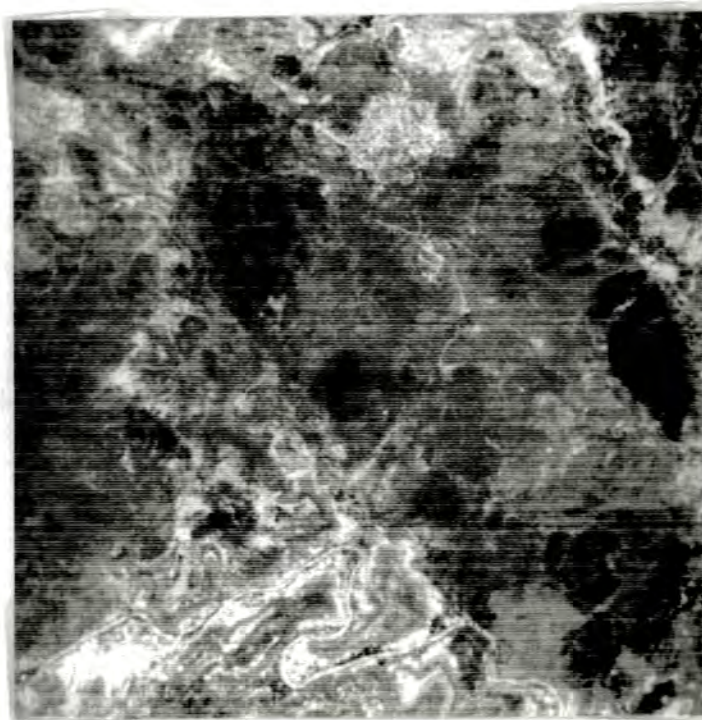
Plate 5.20   Thermal Log Residual of the 10.7μm Channel, Plateau Test
Site.

234
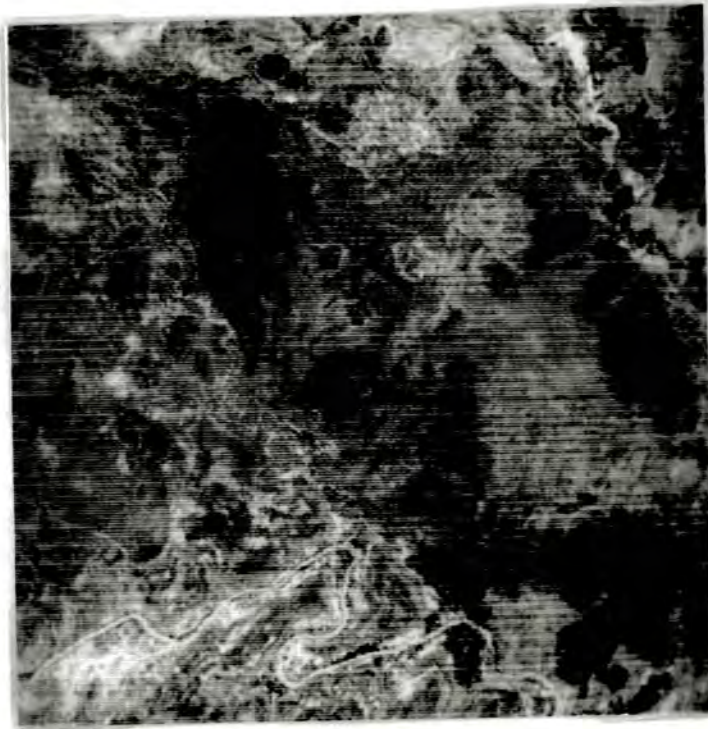
Plate 5.21   Thermal Log Residual of the 11.7μm Channel, Plateau Test Site.
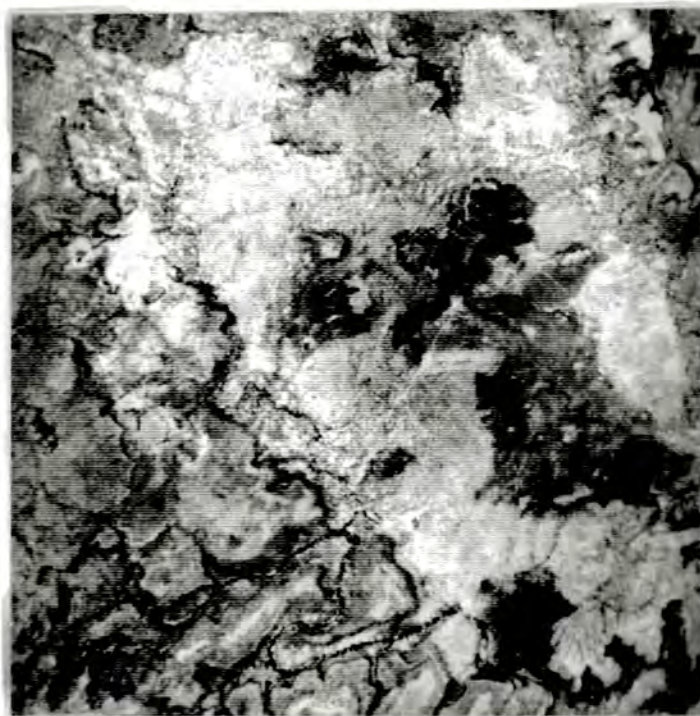
Plate 5.22   Relative Temperature Data Derived as Part of the Thermal Log Residual Calculation, Plateau Test Site.
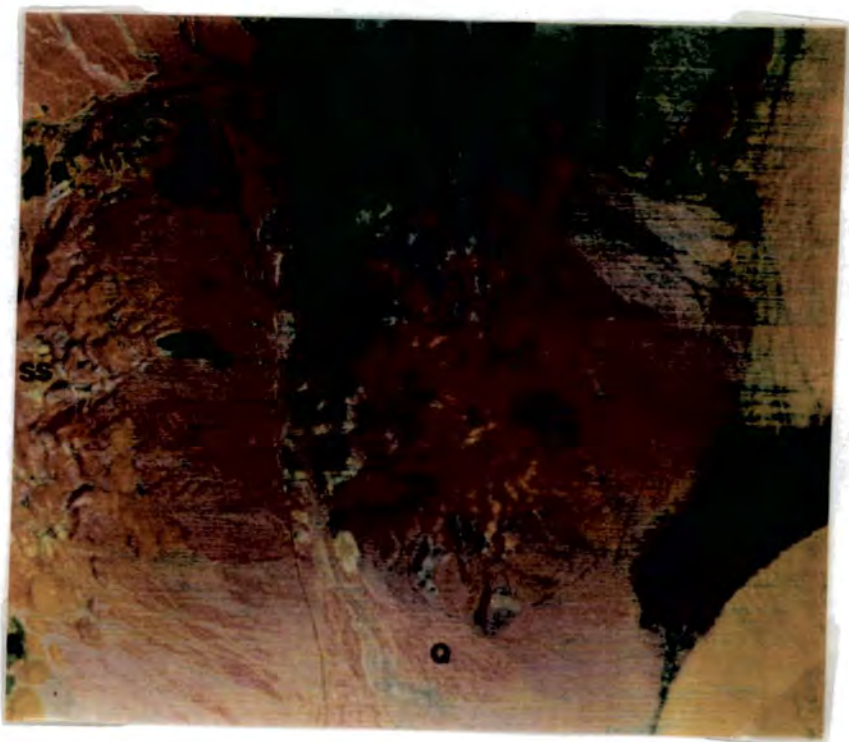
Plate 5.23   Colour Composite of Decorrelation Stretch 10.7μm ,
9.2μm and 8.4μm Channels Displayed as Red, Green and Blue,
Cuprite Test Site (from Kahle and Goetz 1983).
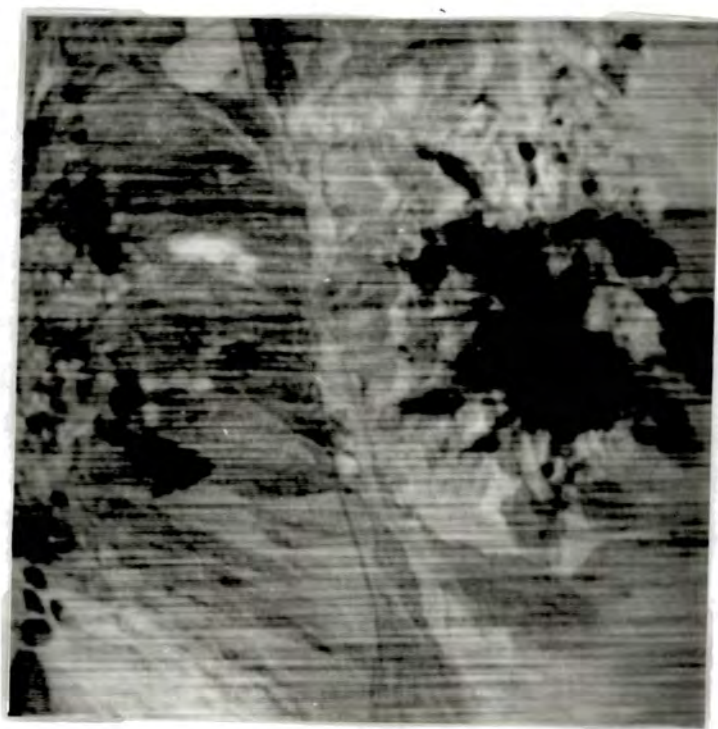
Plate 5.24   Thermal Log Residual of the 8.4μm Channel, Cuprite Test
Site.

Plate 5.25   Thermal Log Residual of the 8.8μm Channel, Cuprite Test
Site.

Plate 5.26   Thermal Log Residual of the 9.2μm Channel, Cuprite Test
Site.
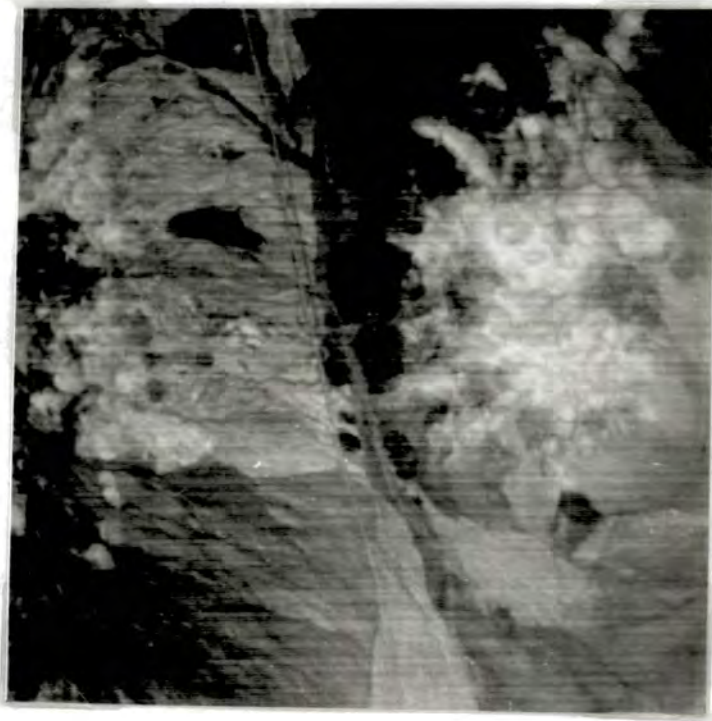
Plate 5.27   Thermal Log Residual of the 9.8μm Channel, Cuprite Test
Site.
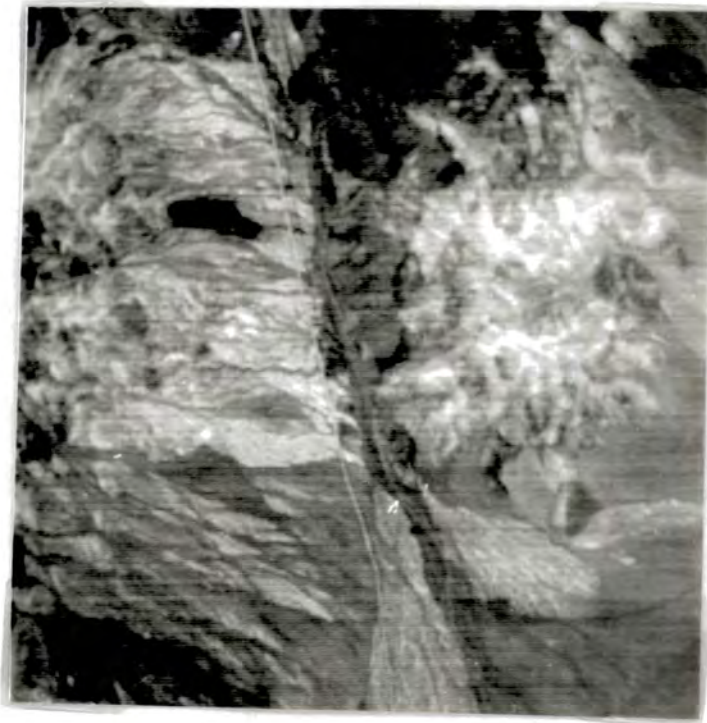
Plate 5.28   Thermal Log Residual of the 10.7μm Channel, Cuprite Test
Site.
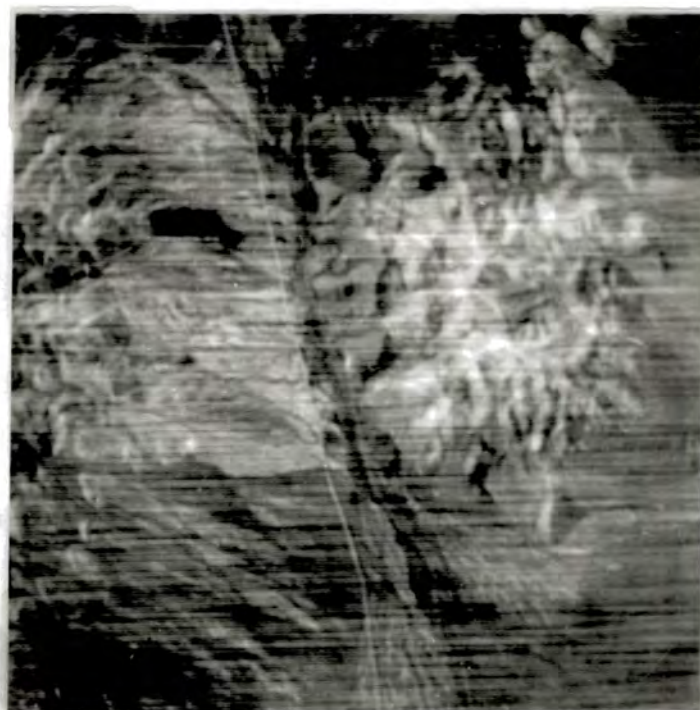
Plate 5.29   Thermal Log Residual of the 11.7μm Channel, Cuprite Test
Site.
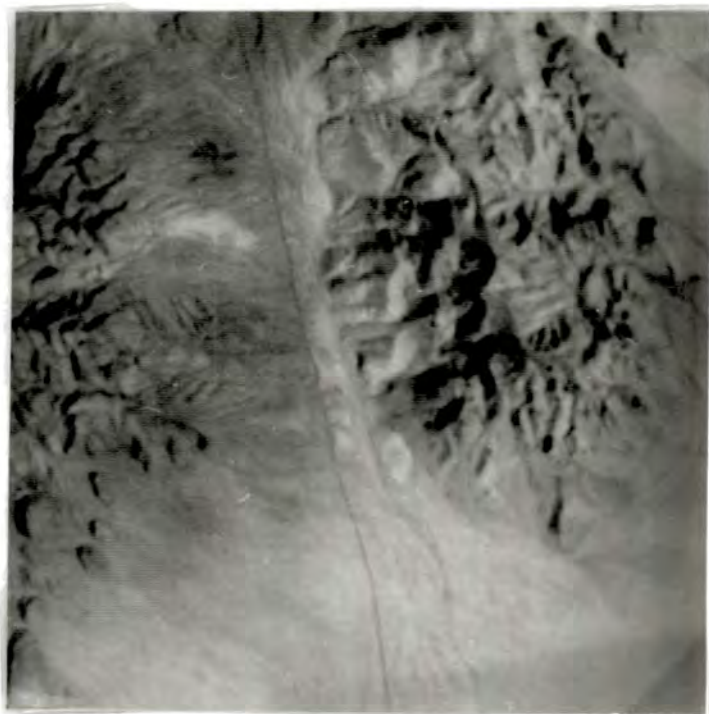
Plate 5.30   Relative Temperature Data Derived as Part of the Thermal
Log Residual Calculation, Cuprite Test Site.
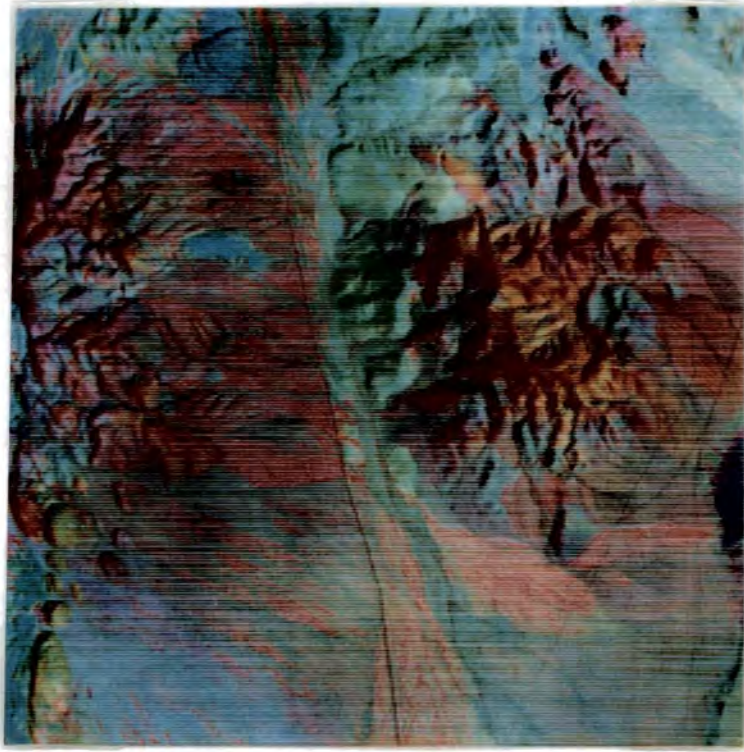
Plate 5.31   Colour Composite of the Thermal Log Residuals from the
10.7μm 9.2μm and 8.4μm Channels with Relative Temperature Added
to each Channel and Displayed as Red, Green and Blue Respectively.

CHAPTER 6

ANALYSIS AND INTERPRETATION OF SAMPLES

COLLECTED FROM BLACKFELLOW MOUNTAIN

BY X-RAY DIFFRACTION AND

LABORATORY SPECTROMETRY

6.1 Introduction

Blackfellow Mountain and the Pinnacles were identifed as areas of intense alteration with airborne multispectral data from the $0.45\mu m$-$2.35\mu m$ wavelength region (see chapter 4). Samples were collected from this area for analysis by laboratory spectrometry and X-ray diffraction. These samples were collected both *in situ* and from the surrounding scree (Plates 6.1 and 6.2).

The principle objective of the interpretation of these analyses was to identify which alteration minerals were present in the samples. These data could then be combined with field data to determine which general hydrothermal alteration model best fits observed alteration. Comparison of the result obtained by each technique also provides an indication of whether laboratory spectrometry offers a viable accurate alternative to X-ray diffraction as a rapid means for the identification of Al-OH $\pm$ Mg-OH $\pm$ CO bearing minerals. The increased spectral resolution of these measurements in the $0.45\mu m$-$2.4\mu m$ wavelength region compared with the NS-001 data also provides an indication of which minerals should be identifiable from new sensors with similar increased spectral resolutions such as the NASA Airborne Imaging Spectrometer (AIS) and the GER II Airborne Scanner in this wavelength region (Goetz and Srivastava, 1985; Huntington, 1988).

Initally the laboratory spectra are interpreted. These results are compared

with those obtained by X-ray diffraction. The resultant data, together with field observations, are then used to propose a hydrothermal model to explain the alteration pattern and mineralogy. Finally the conclusions are presented together with a brief summary.

6.2 Interpretation of Laboratory Spectra

Figure 6.1 shows the distribution of the sampling points over Blackfellow Mountain and the adjacent areas. Locality 1 coincides with subsite H and the laboratory spectrum from this area has been described and interpreted in section 4.3.7. The minerals haematite and alunite were identified in these spectra.

Three grab samples (2a-c) were collected from the scree between locality 1 and the groove in the centre of Blackfellow east (Figure 6.1). Figures 6.2 and 6.3 illustrate the laboratory spectra from the external and internal surfaces of the first grab sample (2a). Figure 6.2 has absorptions at 0.86μm, 1.44μm, 1.49μm, 1.77μm, 1.95μm, 2.18μm and 2.35μm. There is also a reflectance maximum at 0.75μm and a rapid fall in reflectance from this point to 0.43μm. Below 0.43μm there is a rapid increase in reflectance to shorter wavelengths. This rapid increase in reflectance from 0.43μm is an instrumental effect and is henceforth ignored. The fall in reflectance from 0.75μm to 0.43μm indicates the presence of Fe-O (Hunt *et al.*, 1971a). The maximum at 0.75μm and absorption at 0.86μm relate to ferric iron in haematite (Hunt *et al.*, 1971a). The longer wavelength absorptions are all attributed to OH and Al-OH combinations and are typical of alunite (Hunt *et al.*, 1971b). The reflectance spectrum from the internal surface closely matches the spectrum from the external surface and is interpreted similarly. The presence of alunite features on both the internal and external surfaces suggests that this mineral results from hydrothermal alteration rather than from weathering. If this mineral was only the result of weathering it would be restricted to the external surface. The sample was mapped as a bleached altered rock with red veins. The red veins are typical of haematite.

Figure 6.4 shows the laboratory spectrum from the external surface of the second grab sample (2b) collected between locality 1 and 2 (Figure 6.1). The

spectrum has absorptions at 0.85μm, 1.42μm, 1.93μm and 2.22μm. There is also a reflectance maximum at 0.77μm and a rapid decrease in reflectance from this point to 0.43μm. The absorption at 0.85μm and reflectance maximum at 0.77μm relate to ferric iron present in haematite (Hunt *et al.,* 1971a). The rapid decrease in reflectance from 0.77μm to 0.43μm results from the presence of Fe-O (Hunt *et al.,* 1971a). The twin absorptions at 1.42μm and 1.93μm indicate that molecular water is present (Hunt, 1980). The 2.22μm absorption indicates an Al-OH bearing mineral is present (Hunt *et al.,* 1973a); these could be sericite, montmorillonite or illite. Montmorillonite and illite also contain molecular water, which sericite does not, but this molecular water could also result from other minerals such as quartz. Sericite has additional absorptions at 2.35μm and 2.44μm, but these are small and may not develop if only small amounts of sericite are present. The sample was mapped as a breccia and had not been strongly altered. Thin section analysis revealed the feldspars were altering to sericite.

Figure 6.5 illustrates the laboratory spectrum from the external surface of the final grab sample (2c) collected between localities 1 and 2 (Figure 6.1). The spectrum has absorptions at 1.42μm, 1.94μm and 2.21μm. There is also a positive inflection in the spectrum at 0.68μm and a general decrease in reflectance from 1.9μm to 0.43μm. The positive inflection in the spectrum at 0.68μm indicates lichen is present (Ager and Milton, 1987). The general decrease in reflectance is typical of the the presence of Fe-O (Hunt *et al.,* 1971a). The twin absorptions at 1.42μm and 1.94μm indicate molecular water is present (Hunt, 1980). The 2.22μm absorption suggests an Al-OH bearing mineral is present. This could be sericite, illite or montmorillonite for the reasons stated for the previous sample. The sample was bleached and altered, but had a thick ($>$1mm) weathering rind which masked any absorption features from other minerals.

Figures 6.6 and 6.7 illustrate the laboratory spectra obtained from the external and internal surfaces of sample 2d, collected at locality 2 (Figure 6.1). Figure 6.6 has absorptions at 0.88μm, 1.40μm, 1.42μm, 1.49μm, 1.78μm, 1.95μm, 2.19μm, 2.34μm and a shoulder at 2.2μm. There is also a reflectance maximum at 0.75μm and a fall in reflectance from this point to 0.43μmwhich indicates Fe-O is present (Hunt *et al.,* 1971a). The absorp-

tion at $0.88\mu m$ and reflectance maximum at $0.75\mu m$ indicates the presence of ferric iron in haematite (Hunt *et al.*, 1971a). The longer wavelength absorption features all result from Al-OH, OH combinations and molecular water (Hunt, 1980). These absorptions cannot be explained by any given mineral, rather a mixture of minerals are responsible. The absorptions at $1.42\mu m$, $1.49\mu m$, $1.78\mu m$, $2.2\mu m$ and $2.34\mu m$ match closely those seen in alunite (Hunt *et al.*, 1973b). The absorption around $1.49\mu m$ is normally deeper than the $1.42\mu m$ absorption the reverse of which is true in this spectrum (Hunt *et al.*, 1973b, Figure 6.6). This could be explained if an additional mineral was present which absorbed strongly at $1.42\mu m$ and not at $1.49\mu m$. Such a mineral could be kaolinite or dickite. These minerals have additonal features which explain those outstanding absorptions which do not match those seen in alunite. It should be noted, however, that these absorptions do not exactly match those of alunite, kaolinite or dickite (Hunt and Ashley, 1977). This discrepency is thought to arise through the mixing of the spectral features of these minerals causing small shifts in their diagnostic absorption positions. Figure 6.7, the spectrum from the internal surface, closely resembles that from the external surface and is interpreted similarly.

Figure 6.8 illustrates the laboratory spectrum from the external surface of a second sample (2e) collected from locality 2. The spectrum has absorptions at $0.85\mu m$, $1.42\mu m$, $1.95\mu m$, $2.19\mu m$, $2.22\mu m$ and a shoulder at $1.40\mu m$. There is also a reflectance maximum at $0.75\mu m$ and a drop in reflectance from this maxima to shorter wavelengths. The drop in reflectance indicates Fe-O is present (Hunt *et al.*, 1971a). The absorption at $0.85\mu m$ and reflectance maximum at $0.75\mu m$ is indicative of ferric iron in haematite (Hunt *et al.*, 1971a) and the longer wavelength absorption features result from Al-OH, OH combinations or molecular water. They closely match those of either kaolinite or dickite (Hunt *et al.*, 1973a). Kaolinite has absorptions at $1.40\mu m$, $1.41\mu m$, and $2.22\mu m$ and a shoulder at $2.16\mu m$, whilst dickite has absorptions at $1.38\mu m$, $1.41\mu m$, $2.19\mu m$ and $2.2\mu m$. The presence of absorptions around $1.4\mu m$ and $1.95\mu m$ indicates molecular water is also present (Hunt, 1980). The sample was mapped as bleached and altered and was cut by red veins.

Figure 6.9 illustrates the laboratory spectrum from the internal surface of the previous sample. The spectrum has absorptions at $0.85\mu m$, $1.40\mu m$,

1.42μm, 1.83μm, 1.96μm, 2.22μm and 2.40μm. The absorptions closely match those in the spectrum from the external surface and this spectrum is interpreted similarly. The additional absortion features at 1.83μm and 2.40μm can occur in kaolinite or dickite (Hunt et al., 1973a).

Figure 6.10 illustrates the laboratory spectrum from the external surface of the first of four samples (3a) collected at locality 3 (Figure 6.1). The spectrum has absorptions at 1.06μm, 1.54μm, 2.25μm and 2.34μm. There is also a reflectance maximum at 0.55μm and a sharp falloff in reflectance from this point to shorter wavelengths. The falloff in reflectance is typical of the presence of Fe-O (Hunt et al., 1971a). The longer wavelength absorption features result from Al-OH and OH combinations and are all typical of epidote (Hunt et al., 1973a). The maximum at 0.55μm explains the green appearance of the sample and is typical of epidote. The sample was mapped as an epidote nodule.

Figure 6.11 is the laboratory spectrum from the external surface of the second sample (3b) collected at locality 3 (Figure 6.1). The spectrum has absorptions at 1.41μm, 1.55μm, 1.91μm, 2.25μm and 2.34μm. There is also a sharp decrease in reflectance from 0.77μm to shorter wavelengths typical of Fe-O (Hunt et al., 1971a). The absorptions at 1.41μm and 1.91μm indicate that molecular water is present (Hunt, 1980). The remainder of the absorptions relate to Al-OH and OH combinations and are all typical of epidote (Hunt et al., 1973a). This sample was also interpreted as an epidote nodule but had a light brown stain and some felspar which probably contained the liquid water.

Figure 6.12 illustrates the laboratory spectrum from the external surface of the third sample (3c) collected at locality 3 (Figure 6.1). The spectrum has absorptions at 0.84μm, 1.39μm, 1.41μm, 1.81μm, 1.92μm, 2.17μm, 2.2μm and 2.38μm. There is also a reflectance maximum at 0.77μm and a sharp fall in reflectance from this point to 0.43μm, which is typical of Fe-O (Hunt et al., 1973a). The reflectance maximum and absorption at 0.84μm relate to ferric iron present in haematite (Hunt et al., 1971a). The 1.41μm and 1.92μm absorptions indicate molecular water is present (Hunt, 1980). The remaining absorptions including the 1.41μm absorption result from Al-OH or OH combinations and closely match those of dickite. The sample was mapped as altered and bleached and was riddled with red veins.

Figure 6.13 illustrates the laboratory spectrum from the external surface of the fourth sample (3d) collected from locality 3 (Figure 6.1). The spectrum has absorptions at $0.85\mu m$, $1.41\mu m$, $1.92\mu m$ and $2.2\mu m$. There is also a reflectance maximum at $0.77\mu m$ and a rapid fall in reflectance from this point to shorter wavelengths. The fall in reflectance indicates Fe-O is present (Hunt et al., 1971a). The maximum at $0.77\mu m$ and the absorption at $0.85\mu m$ result from ferric iron in haematite (Hunt et al., 1971a). The $1.42\mu m$ and $1.92\mu m$ absorptions indicate molecular water is present (Hunt, 1980). The $2.2\mu m$ absorption infers an Al-OH bearing mineral is present (Hunt, 1980). This could be sericite, montmorillonite or illite for the reasons stated with the interpretation of spectrum from sample 2b (Figure 6.4).

Figure 6.14 illustrates the laboratory spectrum from the internal surface of the previous sample. The spectrum has absorptions at $1.39\mu m$, $1.41\mu m$, $1.80\mu m$, $1.93\mu m$, $2.18\mu m$, $2.2\mu m$ and $2.38\mu m$. There is also a fall in reflectance from $1.2\mu m$ to shorter wavelengths. The fall in reflectance indicates Fe-O is present (Hunt et al., 1971a). The $1.41\mu m$ and $1.93\mu m$ absorptions indicate that molecular water is present (Hunt, 1980). The remaining absorptions including the $1.42\mu m$ absorption result from Al-OH and OH combinations and closely match those of dickite. The sample was mapped as altered and bleached.

Figure 6.15 illustrates the laboratory spectrum from the external surface of a sample collected at locality 4. The spectrum appears to be somewhat unique. The reflectance is very low in the visible and high in the infrared with two well developed absorptions bands at $1.46\mu m$ and $1.96\mu m$. The spectrum results from the sample having a thick ($> 2mm$) weathering rind of what is thought to be manganese oxide. The twin absorptions at $1.46\mu m$ and $1.96\mu m$ indicate molecular water is present (Hunt, 1980). The sample was mapped as altered and bleached.

Figure 6.16 illustrates the laboratory spectrum from the internal surface of the previous sample. The spectrum has absorptions at $1.42\mu m$, $1.94\mu m$, $2.10\mu m$, $2.2\mu m$ and a shoulder at $2.18\mu m$. There is also a decrease in reflectance from $1.2\mu m$ to shorter wavelengths. The decrease in reflectance indicates that Fe-O is present (Hunt et al., 1971a) and the $1.42\mu m$ and $1.94\mu m$ absorptions indicate that molecular water is present (Hunt, 1980).

The 2.2μm absorption indicates that an Al-OH bearing mineral is present (Hunt, 1980), which could be sericite, montmorillonite or illite for the reasons discussed for the laboratory spectrum from sample 2b (Figure 6.4). The well developed absorption at 2.10μm has not been accounted for but probably results from mineral mixing.

Figure 6.17 illustrates the laboratory spectrum from the external surface of a sample collected from locality 5 (Figure 6.1). The spectrum has absorptions at 0.86μm, 1.39μm, 1.41μm, 1.93μm, 2.18μm, 2.2μm and 2.38μm. There is also a reflectance maximum at 0.75μm and a decrease in reflectance from this point to shorter wavelengths. The decrease in reflectance indicates that Fe-O is present (Hunt *et al.*, 1971a). The maximum at 0.75μm and absorption at 0.86μm results from ferric iron in haematite (Hunt *et al.*, 1971a). The 1.41μm and 1.93μm absorptions indicates that molecular water is present (Hunt, 1980). The remaining absorptions result from Al-OH and OH combinations and closely match those of dickite. The sample was mapped as altered and bleached and was riddled with red veins.

Figure 6.18 illustrates the laboratory spectrum from the external surface of a sample collected from locality 6 (Figure 6.1). The spectrum has absorptions at 0.85μm, 1.41μm, 1.94μm, 2.18μm and 2.22μm. there is also a reflectance maximum at 0.77μm and a rapid fall in reflectance from this point to 0.43μm. The decrease in reflectance results from Fe-O (Hunt *et al.*, 1971a). The maximum at 0.77μm and absorption at 0.85μm relates to ferric iron in haematite (Hunt *et al.*, 1971a). The 1.41μm and 1.94μm indicate that molecular water is present (Hunt, 1980). The 2.18μm and 2.22μm absorptions are typical of dickite. Dickite has further absorptions at 1.39μm and 1.41μm which may be confused by the molecular water absorption bands. The sample was mapped as bleached and altered and contained red veins.

Figure 6.19 illustrates the laboratory spectrum from a sample collected at locality 7. The spectrum has a low overall reflectance and there is a rapid fall in reflectance from 0.77μm to shorter wavelengths. There are absorptions at 1.42μm, 1.91μm, 2.22μmand 2.37μm. The fall in reflectance is typical of the presence of Fe-O (Hunt *et al.*, 1971a). The 1.42μm and 1.91μm absorptions indicate that molecular water is present (Hunt, 1980). The 2.22μm absorption and deeper 2.37μm absorption result from Al-OH and Mg-OH combinations

and are typical of chlorite (Hunt *et al.*, 1971b). The sample was mapped and identified by thin section analysis as andesite. It represents the background to the altered area. Andesites are typically spectrally flat and any variations in their spectra result from alteration minerals (Hunt *et al.*, 1974).

The sample collected at locality 8 coincided with subsite I and the spectrum from it was interpreted with the spectra from the Camp Oven test site (see section 4.3.7).

Figure 6.20 illustrates the laboratory spectrum from the external surface of a sample collected at locality 9 (Figure 6.1). The spectrum has absorptions at 0.89μm, 1.39μm, 1.41μm, 1.92μm, 2.16μm and 2.2μm. There is also a reflectance maximum at 0.75μm and a fall in reflectance from this point to shorter wavelengths. The fall in reflectance indicates that Fe-O is present (Hunt *et al.*, 1971a). The absorption at 0.89μm relates to ferric iron in limonite (Hunt *et al.*, 1971a). The 1.41μm and 1.92μm absorptions indicate molecular water is present (Hunt, 1980). The remaining absorptions, including the 1.41μm absorptions result from Al-OH and OH combinations (Hunt, 1980) They are not typical of any given mineral rather a mixture of minerals. Kaolinite typically has absorptions at 1.40μm, 1.41μm and 2.2μm with a shoulder at 2.18μm (Hunt *et al.*, 1973a). The lack of an absorption at 1.40μm coupled with the absorption at 1.39μm and 2.16μm may indicate that pyrophyllite is present. This mineral has absorptions at 1.39μm and 2.16μm (Hunt *et al.*, 1973a). The sample was mapped as altered, bleached and had a light brown stain.

Figure 6.21 illustrates the laboratory spectrum from the internal surface of the previous sample. The spectrum has absorptions at 0.86μm, 1.41μm, 1.42μm, 1.95μm, 2.19μm, 2.2μm and 2.40μm. There is also a fall in reflectance from 0.77μm to 0.43μm. The fall in reflectance indicates Fe-O is present (Hunt *et al.*, 1971a). The absorption at 0.86μm relates to ferric iron in haematite (Hunt *et al.*, 1971a). The absorptions around 1.40μm and 1.95μm indicate that molecular water is present (Hunt, 1980). The remaining absorptions including those around 1.4μm result from Al-OH and OH combinations (Hunt, 1980). The 1.41μm, 1.42μm, 2.2μm and 2.40μm absorptions all occur in kaolinite (Hunt *et al.*, 1973a). The additional absorption at 2.19μm indicates that a further mineral is present, possibly pyrophyllite for the reasons stated above

for the external surface. The sample was mapped as altered and bleached and was cut by red veins.

Figure 6.22 illustrates the laboratory spectrum from the external surface of a sample collected from locality 10 (Figure 6.1). The spectrum has absorptions at 0.86μm, 1.41μm, 1.43μm, 1.48μm, 1.76μm, 1.92μm, 2.08μm, 2.16μm and 2.35μm. There is also a maximum at 0.75μm and a decrease in reflectance from this point to shorter wavelengths. The decrease in reflectance indicates that Fe-O is present (Hunt 1971a). The maximum at 0.75μm and absorption at 0.86μm relates to ferric iron in haematite (Hunt *et al.*, 1971a). The absorptions in the regions of 1.4μm and 1.92μm indicate molecular water is present (Hunt, 1980). The remaining absorptions including those around 1.4μm result from Al-OH and OH combinations (Hunt, 1980). The feature at 1.76μm is typical of alunite (Hunt and Ashley 1977). The presence of alunite also accounts for the absorptions at 1.41μm, 1.48μm and 2.35μm. Alunite also has a marked absorption at 2.19μm. This is thought to be masked by the presence of an additional mineral which would also account for the 1.43μm absorption. This mineral may be kaolinite or dickite. Both minerals have additional absorptions which are masked by those of alunite. Identification of this additional mineral is further complicated by the fact that mixing of minerals subtly shifts their diagnostic absorption features. The absorption at 2.08μm does not occur in alunite, kaolinite or dickite and is thought to arise through mixing. The sample was mapped as altered and was bleached and was cut by red veins.

Figure 6.23 illustrates the laboratory spectrum from the external surface of one of three samples collected from locality 11, a knoll to the north of Blackfellow west (Figure 6.1). The spectrum has absorptions at 1.41μm, 1.50μm, 1.78μm, 2.19μm, 2.22μm and 2.34μm. There is also a general decrease in reflectance from 1.2μm to shorter wavelengths. The decrease in reflectance indicates that Fe-O is present (Hunt *et al.*, 1971a). The remaining absorptions all result from Al-OH and OH combinations (Hunt, 1980). The 1.78μm indicates that alunite is present (Hunt and Ashley, 1977). This mineral would also account for the 1.50μm, 2.19μm and 2.35μm absorptions. Alunite also has an absorption at 1.44μm which is thought to be masked by the presence of another mineral, which also deepens the 1.41μm absorption

and introduces an absorption at 2.22μm. Such a mineral could be kaolinite. The sample was mapped as altered and was strongly bleached.

Figure 6.24 illustrates the laboratory spectrum from the internal surface of the previous sample. The spectrum has absorptions at 0.91μm, 1.25μm, 1.41μm, 1.5μm, 1.78μm, 2.18μm, 2.21μm and 2.40μm. There is also a fall in reflectance from a maximum at 0.77μm to shorter wavelengths. The fall in reflectance indicates Fe-O is present (Hunt *et al.*, 1971a). The absorption at 0.91μm and maximum at 0.77μm relates to ferric iron in limonite (Hunt *et al.*, 1971a). The remaining absorptions all result from Al-OH and OH combinations (Hunt, 1980). The 1.78μm absorption indicates that alunite is present (Hunt and Ashley, 1977). These absorption features are thought to result from a mixture of alunite and kaolinite for the reasons stated with the previous sample. The 1.78μm absorption is far more marked in this spectrum than in the spectrum from the external surface. This infers that more alunite is present on the internal surface. If we assume that kaolinite and alunite were initially evenly distributed in the sample, then alunite has been preferentially weathered from the external surface of the sample, thus increasing the kaolinite abundance. This is to be expected since kaolinite is frequently the product of extensive weathering (see Figure 2.4).

Figure 6.25 illustrates the laboratory spectrum from the external surface of a second sample collected at locality 11 (Figure 6.1). The spectrum has absorptions at 0.96μm, 1.25μm, 1.41μm, 1.50μm, 1.79μm, 2.18μm, 2.2μm, 2.34μm and 2.40μm. There is also a fall in reflectance from 1.2μm to shorter wavelengths which results from the presence of Fe-O (Hunt *et al.*, 1971a). The remaining absorption features all result from Al-OH and OH combinations (Hunt, 1980). They can all be explained by a mixture of alunite and kaolinite for the reasons discussed with the spectrum from the previous sample. The feature at 0.96μm occurs in kaolinite, but is commonly masked by iron oxide mineral features. The potential of this feature for mineral identification has been discussed by Gabell *et al.* (1986).

Figure 6.26 illustrates the laboratory spectrum from the internal surface of the previous sample. This spectrum closely resembles that acquired from the external surface and is interpreted similarly.

Figures 6.27 and 6.28 illustrate the laboratory spectra from the external

and internal surfaces a third sample collected at locality 11. The spectra closely resemble those obtained from the other samples and are interpreted similarly; that is as a mixture of kaolinite and alunite.

Figure 6.29 illustrates the laboratory spectrum from the external surface of one of two samples collected at locality 12 (Figure 6.1). The spectrum has absorptions at $1.92\mu m$, $2.26\mu m$ and $2.36\mu m$. There is also a positive inflection in the curve at $0.65\mu m$ and a general decrease in reflectance from $1.7\mu m$ to shorter wavelengths. The positive inflection in the curve indicates that lichen is present (Ager and Milton, 1987). The general decrease in reflectance indicates Fe-O is present (Hunt *et al.*, 1971a). The remaining absorptions all result from OH and Mg-OH combinations and are typical of chlorite (Hunt *et al.*, 1973a). The sample was not mapped as altered and represents the background andesite.

Figure 6.30 illustrates the laboratory spectrum from the internal surface of the previous sample. The spectrum has an absorption at $2.36\mu m$ typical of chlorite (Hunt *et al.*, 1973a). Chlorite, however, has additional absorption features which would be absent if chlorite was present in small quantitites. The presence of chlorite was confirmed by thin section analysis.

Figure 6.31 illustrates the laboratory spectrum from a second sample collected at locality 12 (Figure 6.1). The sample was taken from the scree associated with Blackfellow West. The spectrum has weak absorptions at $0.85\mu m$, $1.39\mu m$, $1.41\mu m$, $1.48\mu m$, $1.77\mu m$, $1.94\mu m$, $2.16\mu m$, $2.2\mu m$ and $2.38\mu m$. There is also a reflectance maximum at $0.77\mu m$ and a decrease in reflectance from this point to shorter wavelengths. The decrease in reflectance indicates the presence of Fe-O (Hunt *et al.*, 1971a). The absorption at $0.85\mu m$ and maximum at $0.77\mu m$ relate to ferric iron in haematite (Hunt *et al.*, 1971a). The absorptions around $1.4\mu m$ and $1.94\mu m$ indicate that molecular water is present (Hunt, 1980). The remaining absorptions including those around $1.4\mu m$ all result from Al-OH and OH combinations (Hunt, 1980). The longer wavelength features suggest a mixture of alunite and kaolinite for the reasons stated with similar spectrum acquired from samples collected at locality 10. The sample was mapped as altered and was riddled with red veins.

6.3 Comparison of Minerals Identified by X-ray diffraction with those Identified by Laboratory Spectral Analysis

Table 6.1 provides a summary of minerals identified by laboratory spectral analysis of the samples collected at each locality and those identified by X-ray diffraction. The X-ray diffraction pattern for each sample was obtained with a PW 1130 2kW X-ray Generator/Diffractometer Assembly using Co $K\alpha$ radiation. The X-ray diffraction pattern relates to the crystal structure of the minerals present in the sample and comparison of diffraction patterns of unknown minerals with a set of standard patterns permits their identification (Hardy and Tucker, 1988). These standard patterns have been compiled by an international organization called the Joint Committee on Powder Diffraction Standards (JCPDS) which collects and updates powder diffraction data.

The slide for X-ray diffraction was prepared by grinding the rock to a fine powder with a mortar and pestle. One gram of this powder was dispersed in 150ml of distilled water and the clay suspension decanted off and allowed to settle on a glass slide in a beaker placed in an oven.

In all cases, laboratory spectral analyses permitted the identification of iron oxide minerals from both the external and internal surfaces of samples, which were not identified by X-ray diffraction. These minerals were not present in sufficient quantities or they lacked sufficient crystallinity to be detected by X-ray diffraction. Such minerals included haematite, limonite goethite and amorphous iron oxide.

The Al-OH $\pm$ Mg-OH $\pm$ CO bearing minerals identified by laboratory spectrometry showed good agreement with those identified by X-ray diffraction although there were some exceptions. Alunite and the kandite group minerals when identified by laboratory spectrometry were nearly always identified by X-ray diffraction. There were some samples where alunite or a kandite was identified by X-ray diffraction and not by laboratory spectral analysis. The peaks in the X-ray diffraction charts for these samples were always small suggesting the amount of these minerals present in the sample was also small. Therefore, these minerals were thought not to be present in sufficient quantity to be detected by laboratory spectrometry.

In most cases it was possible to identify the specific kandite present by laboratory spectrometry. Usually, this was either kaolinite or dickite although

it was difficult to separate these in the laboratory spectra from some samples.

In the majority of samples where pyrophyllite was identified by X-ray diffraction it was not identified in the laboratory spectra. The main problem with the laboratory spectral analyses was the presence of other minerals whose spectral absorptions coincided with those of pyrophyllite, thus making it difficult to establish if the mineral was present. Further work is needed to determine rules for separating mineral mixtures.

In general, laboratory spectrometry offers a more rapid cost effective alternative to X-ray diffraction for the identification of Al-OH $\pm$ Mg-OH $\pm$ CO bearing minerals provided that relatively few of these minerals are present in any given sample. If several minerals are present with absorptions at similar positions then their diagnostic absorption features are masked and confused and X-ray diffraction then provides a more effective means of mineral identification.

These laboratory spectral data indicate that using airborne spectrometry data it should be possible to identify any Al-OH $\pm$ Mg-OH $\pm$ CO bearing minerals present and how they are distributed in the alteration zone at Blackfellow Mountain. This information can be used to separate areas of hydrothermal alteration from those resulting from weathering which have different Al-OH $\pm$ Mg-OH $\pm$ CO bearing minerals. . For example, alunite is more commonly associated with hydrothermal alteration than weathering.

6.4 Model for the development of the observed alteration at Blackfellow Mountain

Analysis of the NS-001 data revealed an alteration zone at and around Blackfellow Mountain. Subsequent laboratory spectrometry and X-ray diffraction measurements of samples collected from this zone identified a suite of minerals characteristic of argillic and advanced argillic alteration. These minerals can be separated into two groups, iron oxide minerals and hydrous minerals. The hydrous minerals include kaolinite or dickite, alunite, sericite and pyrophyllite. The iron oxide minerals included haematite, limonite and goethite. Alunite occurred throughout the alteration zone in varying quan-

tities. Kaolinite or dickite and pyrophyllite appeared to be more abundant in Blackfellow West than Blackfellow East and in the knoll to the north of Blackfellow West.

The host lithology adjacent to the alteration consisted of andesitic lavas which were brecciated and contained chlorite and epidote typical of background propylititic alteration. The andesites were part of a suite of intrusive intermediate to acidic lavas and pyroclastics.

This style of volcanic-hosted alteration is very similar to that seen in epithermal deposits. More specifically, high sulphur or enargite-precious metal deposits.

The models proposed for the development of these deposits have been reviewed by Bonham (1986). The following is based on a general model for the development of high sulphur or enargite-precious metal deposits by Bonham (1986).

The host rocks for these deposits are typically calc-alkaline andesite, dacite, rhyodacite and more rarely low silica rhyolite. All of these rocks have been identified within the Camp Oven Complex. Ashley, (1982) points out that the intermediate rocks spatially and temporally associated with these rocks are commonly porphyritic. Typical phenocrysts include plagioclase, orthoclase, hornblende, biotite and pyroxene, all of which occurred in these rocks.

Figure 6.32 gives a general occurrence model for high-sulphur volcanic-hosted, epithermal precious metal deposits, based upon the features of several known deposits (Bonham 1986). The alteration in these deposits is dominantly argillic. Argillic alteration assemblages include quartz - kaolinite-K mica, quartz-illite-montmorillonite and quartz-kaolinite. The adavanced argillic alteration assemblages include quartz-alunite- kaolinite, quartz-alunite-native sulphur, quartz-diaspore and quartz-alunite-sericite, quartz-kaolinite-pyrophyllite-alunite. Not all these assemblages are always present. At the Blackfellow Mountain alteration zone quartz-alunite-sericite quartz-alunite-kaolinite and quartz-kaolinite-pyrophyllite-alunite were the most commonly observed alteration assemblages.

Table 6.2 summarises the alteration and ore mineralogy of the high- sulphur epithermal system. The enargite group minerals are characteristic of

these deposits. These minerals are restricted to the silicified breccias and zones beneath the acid leached cap. The argillic zones are usually barren of ore minerals although they may contain some pyrite.

Clearly, the Blackfellow Mountain alteration zone and associated host rocks are very similar to the acid-leached cap of the high-sulphur epithermal system. The presence of mineralisation at Blackfellow Mountain and the identification of the ore minerals which would confirm this hypothesis requires the area to be drilled. To date this has not been undertaken.

6.5   Conclusions

1. The iron oxide minerals haematite, limonite, goethite, and amorphous iron oxide were identified using laboratory spectrometry.

2. None of these iron oxide minerals were identified by X-ray diffraction possibly due to their lack of abundance or crystallinity.

3. The Al-OH $\pm$ Mg-OH $\pm$ CO bearing minerals alunite, kaolinite, dickite, pyrophyllite (and sericite, montmorillonite, illite) were identifed by laboratory spectrometry.

4. The Al-OH $\pm$ Mg-OH $\pm$ CO bearing minerals alunite, a kandite (kaolinite, dickite, halloysite, nacrite) and pyrophyllite were identified by X-ray diffraction.

5. For any given sample there was good agreement between the minerals identified by laboratory spectrometry and X-ray diffraction provided that the spectral features of any one mineral did not mask those of another mineral in the laboratory spectra.

6. X-ray diffraction permitted the detection of smaller amounts of Al-OH $\pm$ Mg-OH $\pm$ CO bearing minerals than laboratory spectrometry

7. In certain cases laboratory spectrometry permitted the identification of the type of kandite present (kaolinite, dickite, halloysite, nacrite). This was not possible by X-ray diffraction.

8. The Al-OH $\pm$ Mg-OH $\pm$ CO bearing minerals were identified in the spectra from both the external and internal surfaces of samples suggesting they were the result of hydrothermal alteration rather than weathering

where they would have been restricted to the external surfaces.

9. The background rocks to this alteration were identified as andesites which had be propylitically altered.

10. The propylitic alteration minerals chlorite and epidote were identified in samples from the background by both laboratory spectrometry and X-ray diffraction.

11. The style of alteration together with the host rocks suggest that Blackfellow Mountain is the cap of a high sulphur epithermal system. This can only be confirmed if the site is drilled.

6.6   Summary

Laboratory spectrometry and X-ray diffraction permitted the identification of Al-OH $\pm$ Mg-OH $\pm$ CO bearing minerals present in samples collected from Blackfellow Mountain. It was also possible to identify any iron oxide minerals present by laboratory spectrometry. In general, there was good agreement between the Al-OH $\pm$ Mg-OH $\pm$ CO bearing minerals identified by laboratory spectrometry and X-ray diffraction in any given sample provided a limited number of these minerals were present. If several Al-OH $\pm$ Mg-OH $\pm$ CO bearing minerals were present, the diagnostic absorption features of a given mineral were often masked and shifted by other minerals present making identification difficult. It was also possible to identify smaller amounts of certain Al-OH $\pm$ Mg-OH $\pm$ CO bearing minerals by X-ray diffraction than by laboratory spectrometry. These results suggest laboratory spectrometry offers a rapid and cost effective alternative to X-ray diffraction for the identification of Al-OH $\pm$ Mg-OH $\pm$ CO bearing minerals.

The iron oxide minerals identified were haematite, goethite, limonite and amorphous iron oxide. Of these, haematite appeared to result from hydrothermal alteration and occurred in veins which cross cut the altered area. The Al-OH $\pm$ Mg-OH $\pm$ CO bearing minerals identifed were alunite, kaolinite, dickite pyrophyllite and (sericite, montmorillonite and illite). The latter bracketed group typically occurred on the external surfaces of samples and were thought to result from weathering. The remaining minerals occurred on both the external and internal surfaces of samples suggesting they were

the result of hydrothermal alteration. These minerals are typical of areas of advanced argillic alteration.

The area of intense alteration was hosted in andesites which had been propylitically altered. This alteration produced the minerals chlorite and epidote both of which were detected using laboratory spectrometry and X-ray diffraction. The laboratory spectral data imply it should be possible to map the type of alteration minerals present and their relative distribution at Blackfellow Mountain using airborne imaging spectrometers with better resolution than used here.

The alteration mineralogy and pattern suggests Blackfellow Mountain represents the cap of a high sulphur epithermal system.

Sample Number	Minerals identied by Lab. Spectral Analysis	Minerals identified by X. Ray Diffraction
1	E - Fe-O, ha, al	al, kan
2a	E - al,	al, kan
2a	I - Fe-O, ha, al	
2b	E - Fe-O, ha, (mi,mo,il)	mo
2c	E - Fe-O, (mi,mo,il)	al, mi
2d	E - Fe-O, ha, al, ka/di	al, kan
2d	I - Fe-O, ha, al, ka/di	
2e	E - Fe-O, ha, ka/di	al,kan
2e	I - Fe-O, ha, ka/di	
3a	E - Fe-O, ep	ep
3b	E - Fe-O, ep	ep
3c	E - Fe-O, ha, di	py, kan, mi
3d	E - Fe-O, ha, (mi,mo,il)	
4	E - Manganese coat	kan
4	I - Fe-O, di, (mi,mo,il)	
5	E - Fe-O, ha, di	kan
6	E - Fe-O, ha, di	py, kan
7	E - Fe-O, ch	ch, mi
8	E - go/li, al, ka/di	al, kan py
8	I - Fe-O, li, al, ka, mi/py	
9	E - Fe-O, ha, li, ka, py	kan, py, mi, ja, gy
9	I - Fe-O, ha, ka, py	
continued on next page		

10	E - Fe-O, ha, al, ka/di	kan
11a	E - Fe-O, al, ka	al, kan, py
11a	I - Fe-O, li, ka, al	
11b	E - Fe-O, ka, al	py, kan, al
11b	I - Fe-O, ka, al	
11c	E - Fe-O, ka, al	py, kan, al
11c	I - Fe-O, ka, al	
12a	E - Fe-O, ch,	ch, mi
12a	I - Fe-O, ch	ch, mi
12b	E - Fe-O, ha, al, ka	py, kan, al

E = external surface, I = internal surface

ha = haematite, li = limonite, go = goethite, ja = jarosite

al = alunite, di = dickite, ka = kaolinite, kan = kandite

mo = montmorillonite, il = illite, py = pyrophyllite

gy = gypsum, ep = epidote, ch = chlorite, mi = mica

Table 6.1   Comparison of minerals identified by lab spectral analysis with those identified by X. Ray Diffraction for samples collected at and around Blackfellow Mountain.

Ore minerals: mercury and antimony sulphides, enargite-luzonite group minerals, tennantite-tetrahedrite group minerals, covellite, native gold and/or electrum, silver sulphide and sulphosalts, bismuthinite, base metal sulphides, tellurides including Au-Ag tellurides.

Advanced argillic assemblages in and adjacent to mineralised structures, including veins, ledges and pipes: quartz-alunite-kaolinite, quartz-alunite-native sulfur-barite, quartz-pyrophyllite-zunyite-diaspore, quartz-diaspore, quartz-alunite-pyrophyllite-diaspore, quartz-alunite-sericite.

Intermediate argillic alteration adjacent to advanced argillic altera - tion: kaolinite, sericite, smectite.

Regional propylitic alteration.

Table 6.2   Typical Alteration and Ore Mineralogy of High Sulpher Epithermal Systems : source Bonham, 1986.
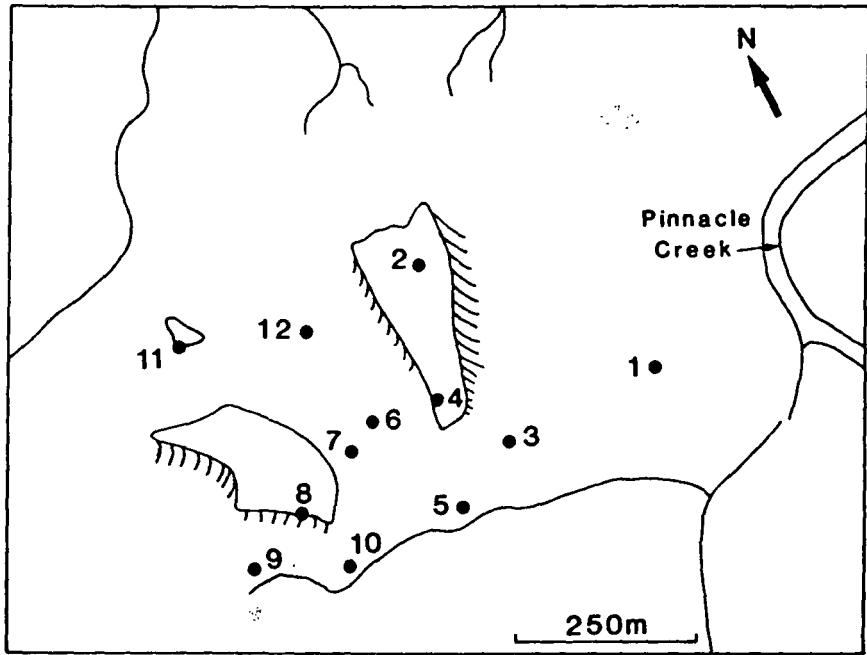
Figure 6.1   Location of the sampling points at Blackfellow Mountain and
the adjacent areas
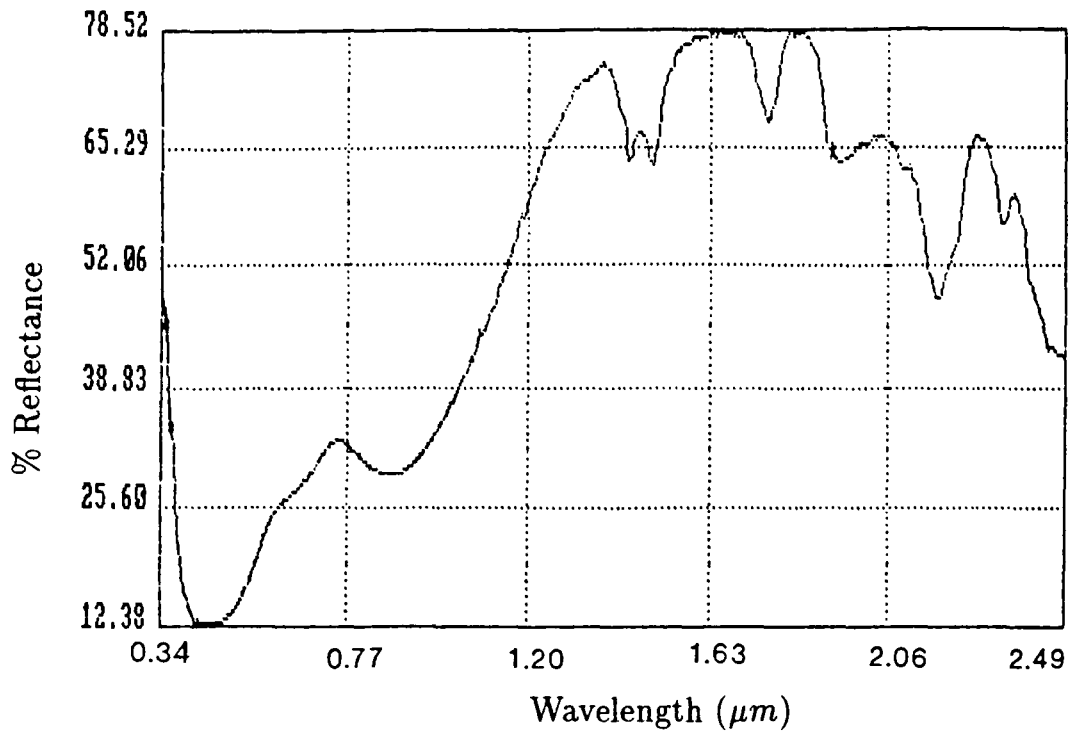
Figure 6.2   Lab spectrum from the external surface of a sample 2a
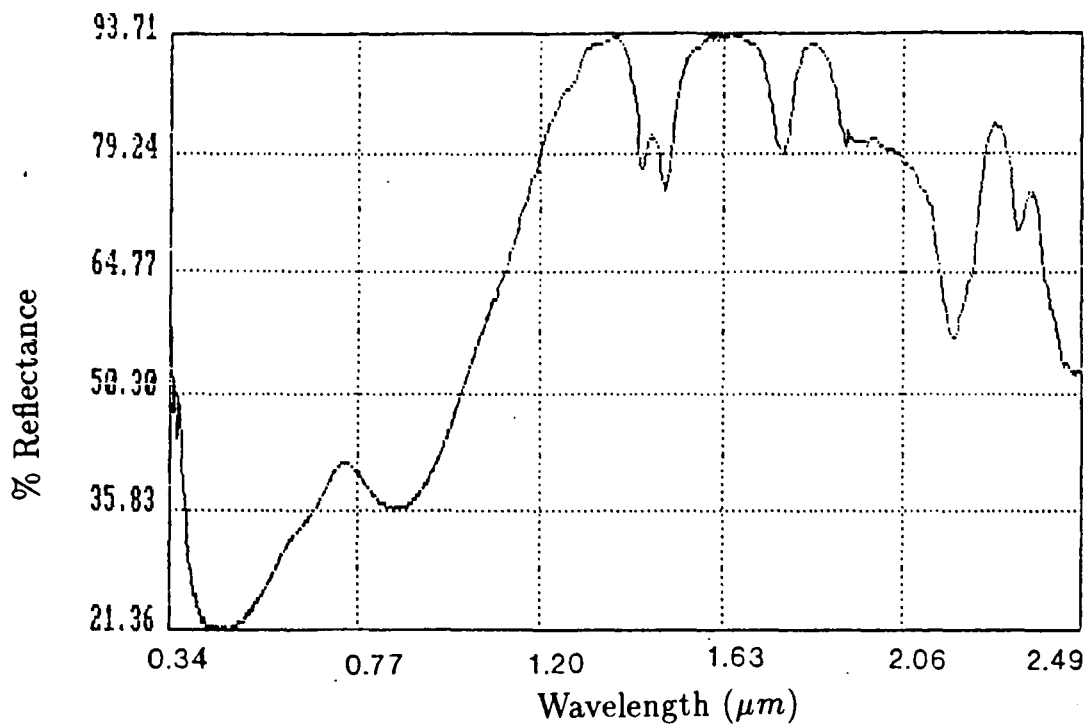
Figure 6.3   Lab spectrum from the internal surface of a sample 2a
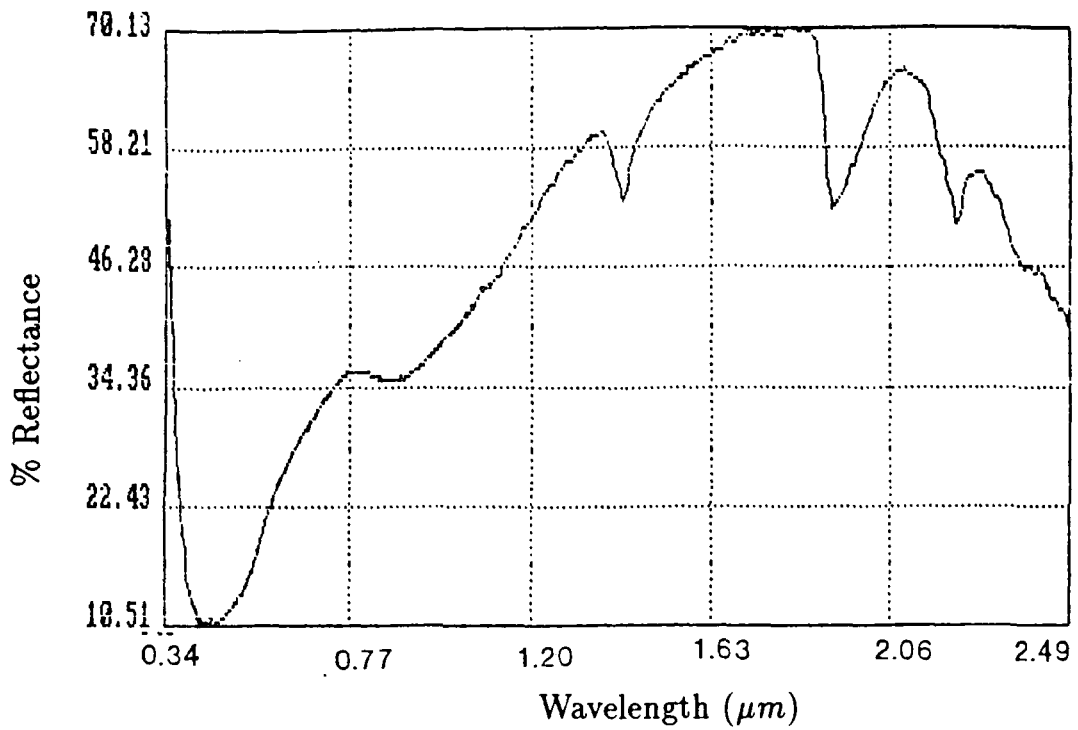
Figure 6.4   Lab spectrum from the external surface of a sample 2b
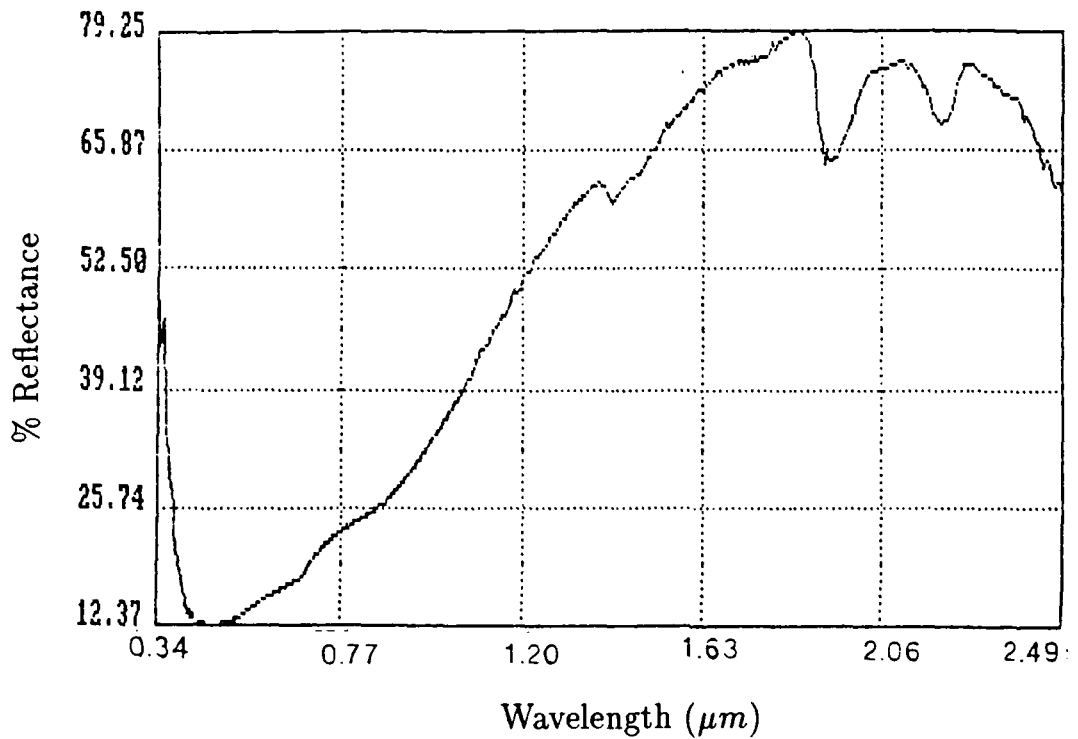
Figure 6.5   Lab spectrum from the external surface of a sample 2c
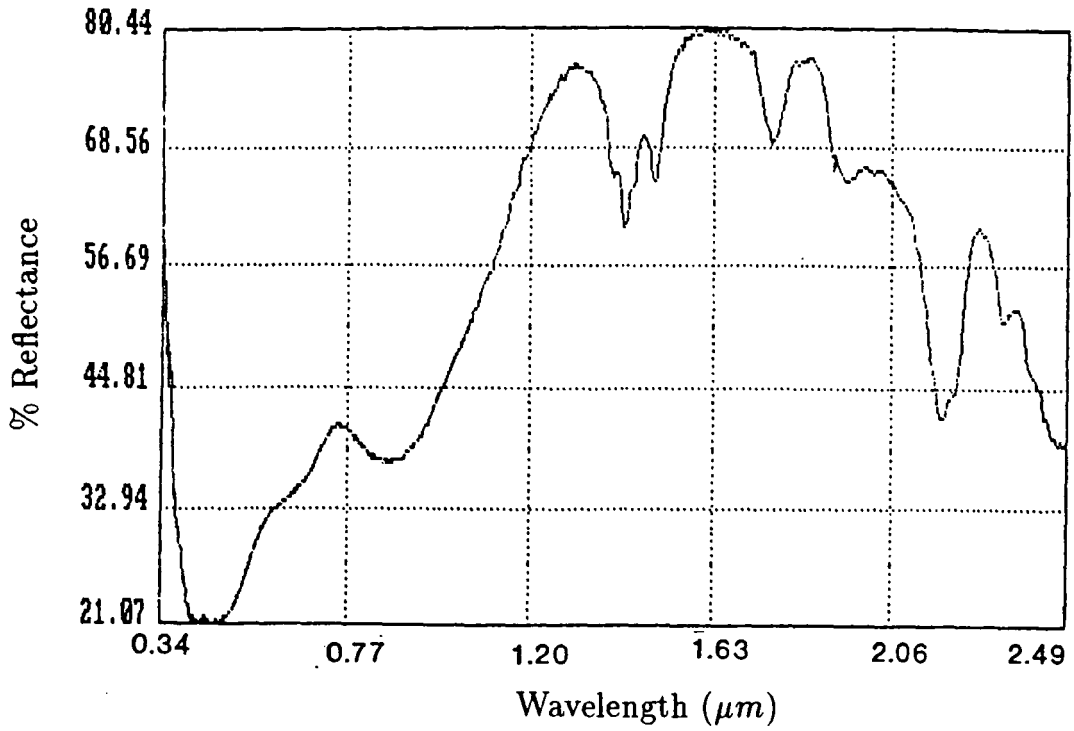
Figure 6.6   Lab spectrum from the external surface of a sample 2d
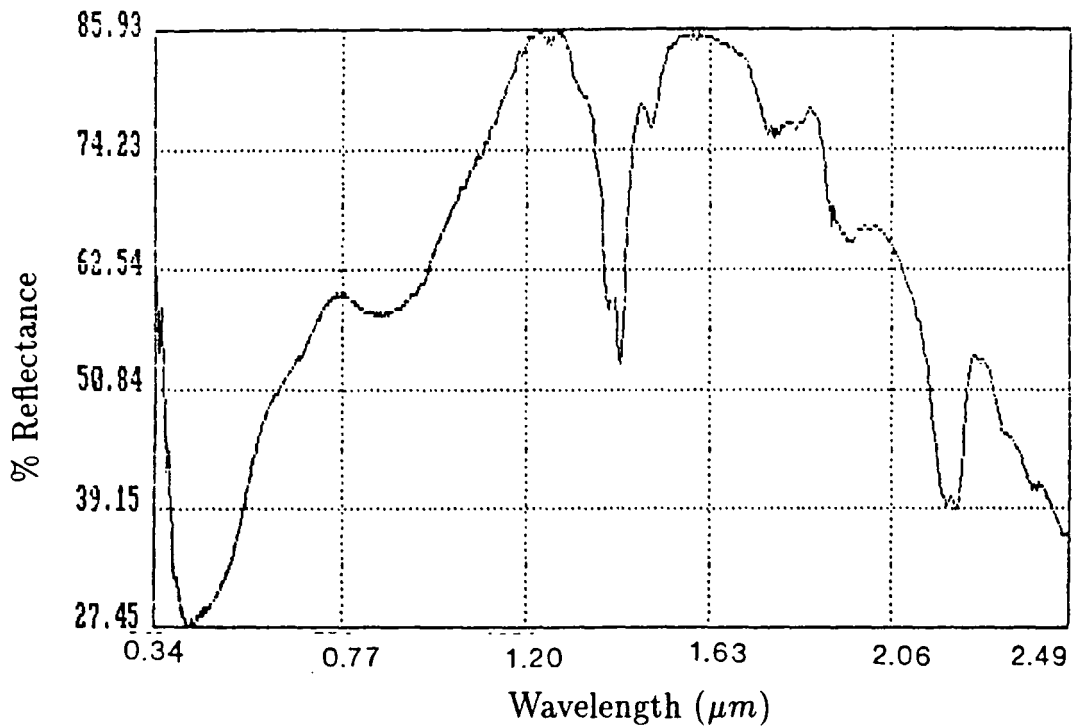
Figure 6.7   Lab spectrum from the internal surface of a sample 2d

264
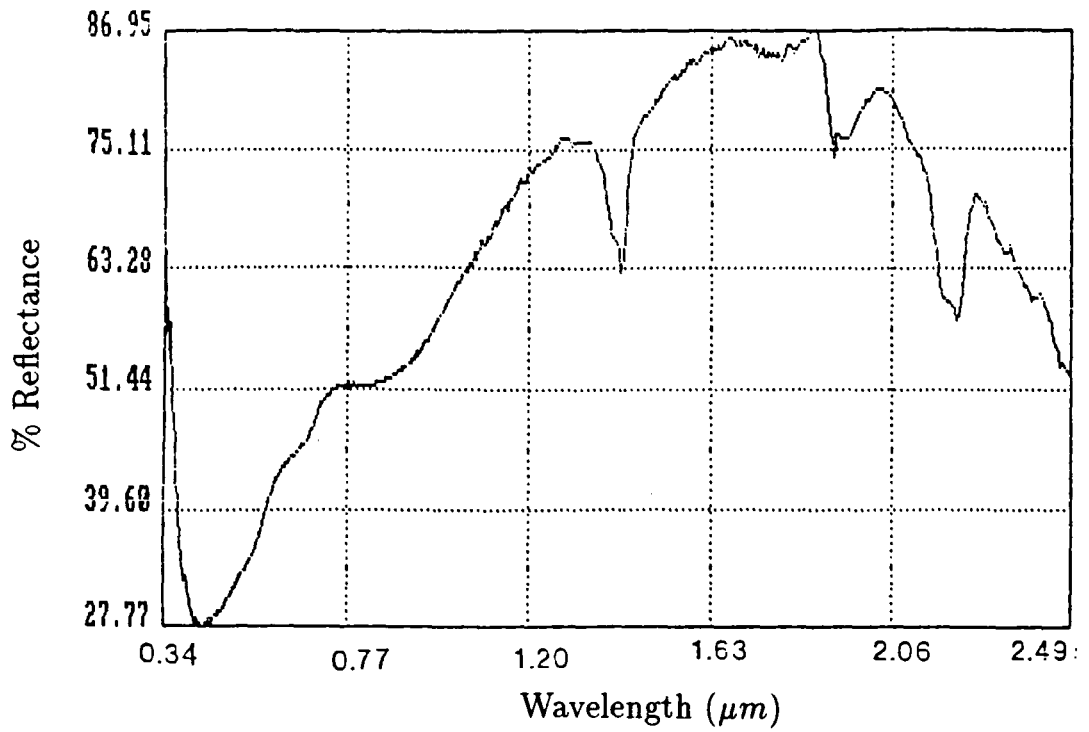
Figure 6.8 Lab spectrum from the external surface of a sample 2e
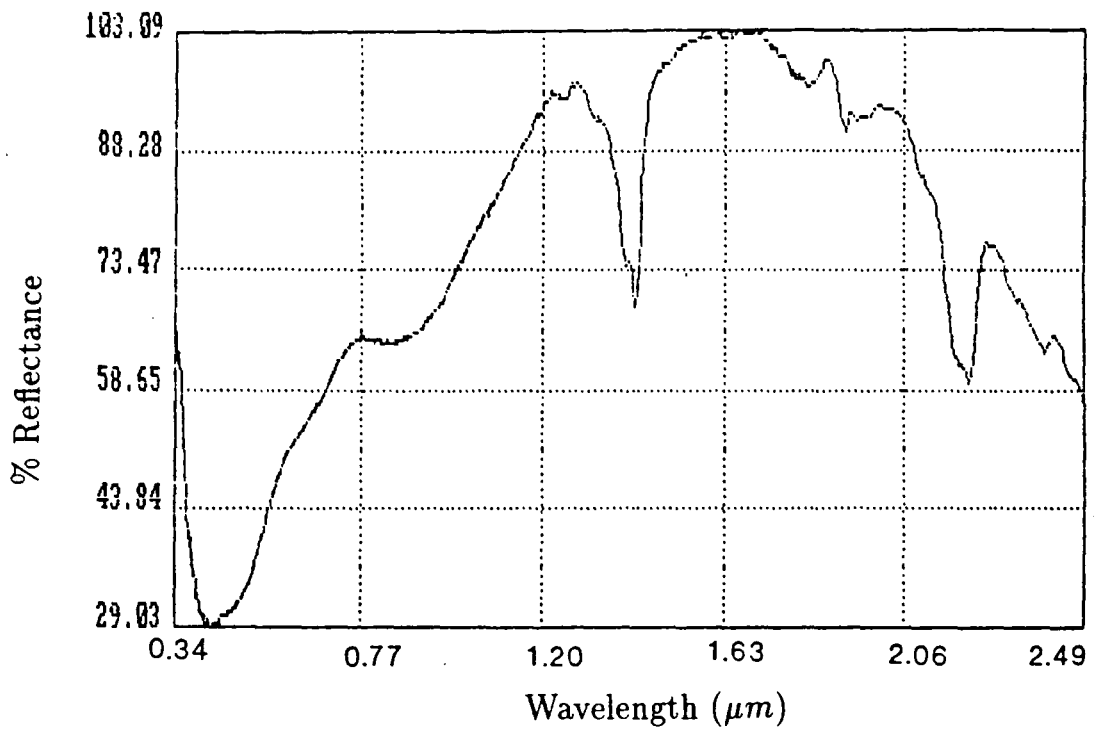
Figure 6.9 Lab spectrum from the internal surface of a sample 2e
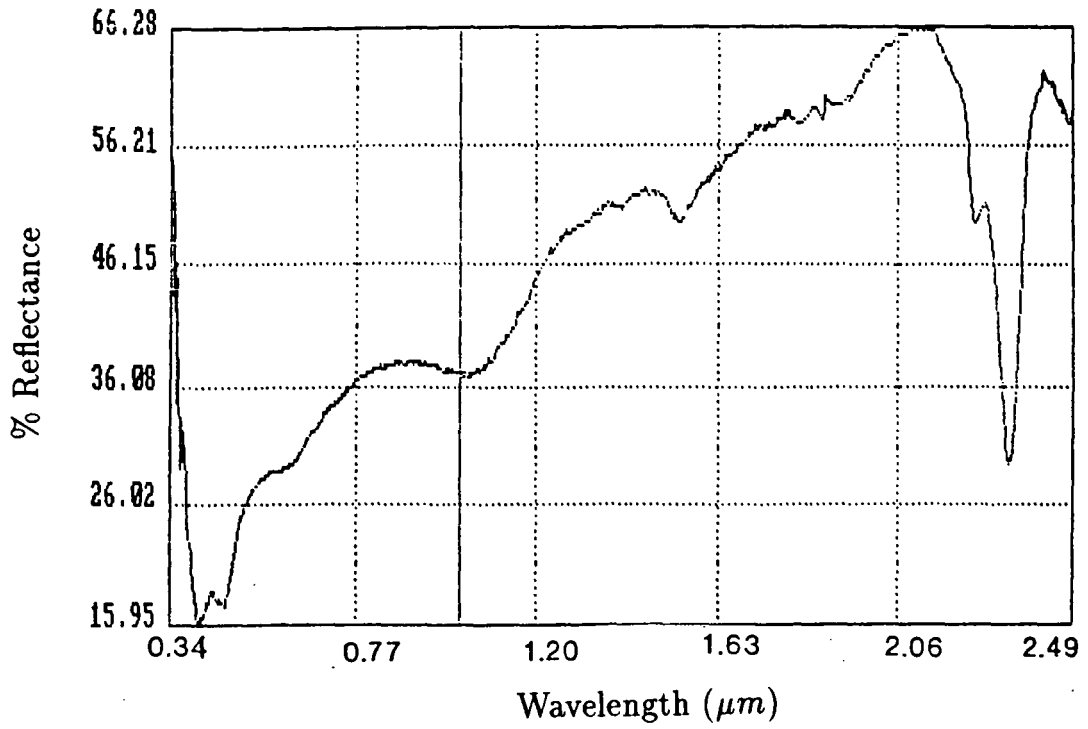
Figure 6.10 Lab spectrum from the external surface of a sample 3a
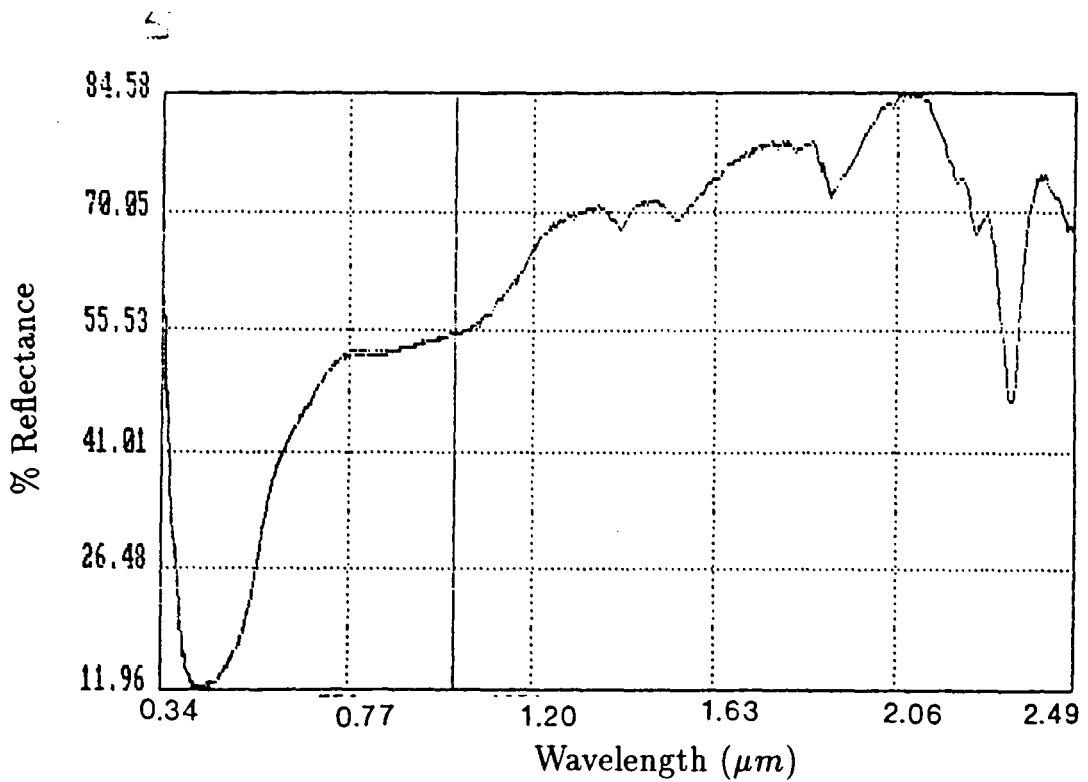
Figure 6.11 Lab spectrum from the external surface of a sample 3b
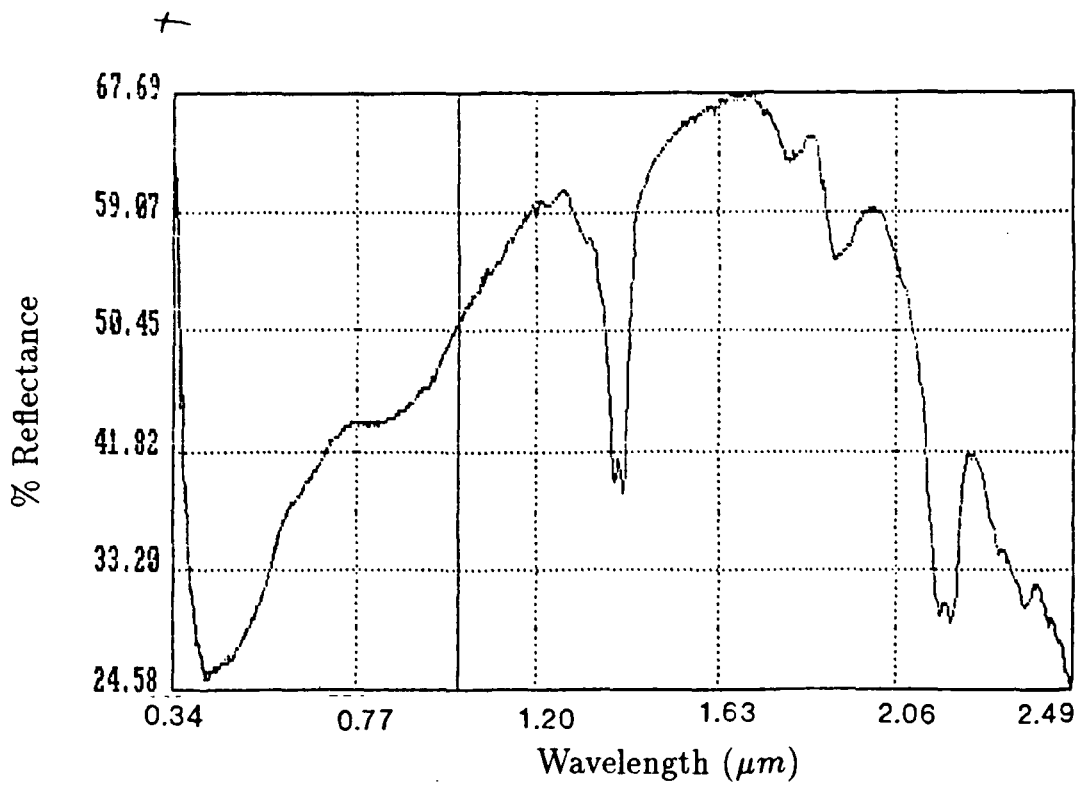
Figure 6.12   Lab spectrum from the external surface of a sample 3c
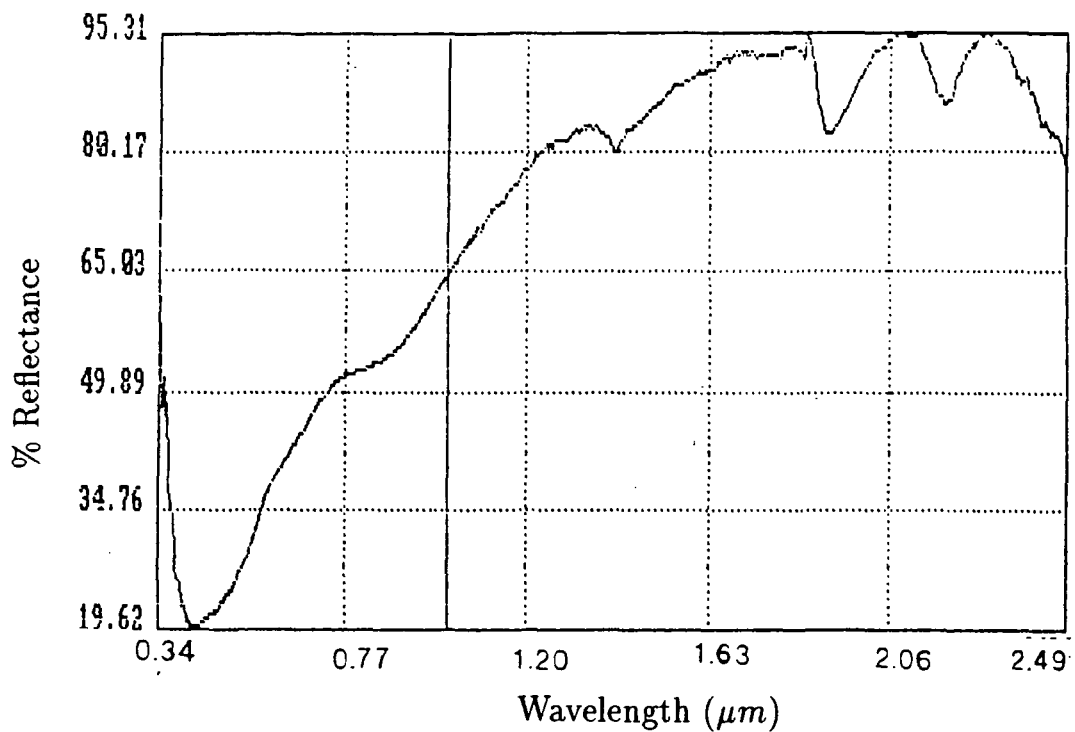
Figure 6.13   Lab spectrum from the external surface of a sample 3d
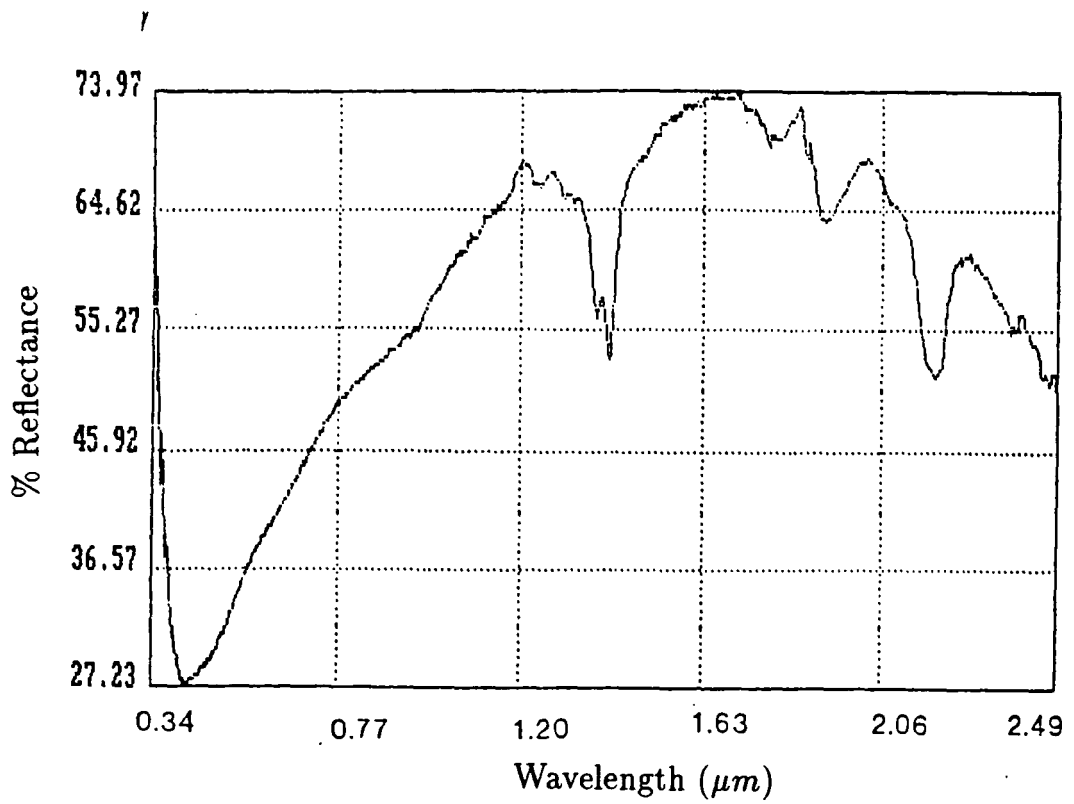
Figure 6.14   Lab spectrum from the internal surface of a sample 3d
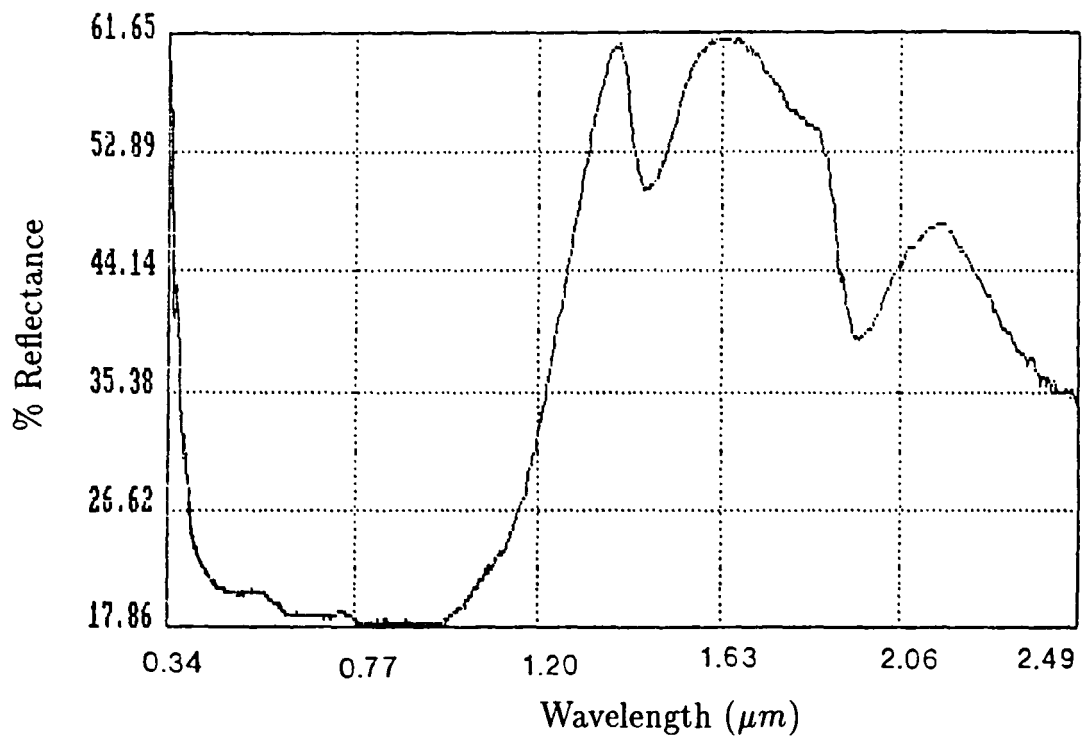
Figure 6.15   Lab spectrum from the external surface of a sample 4
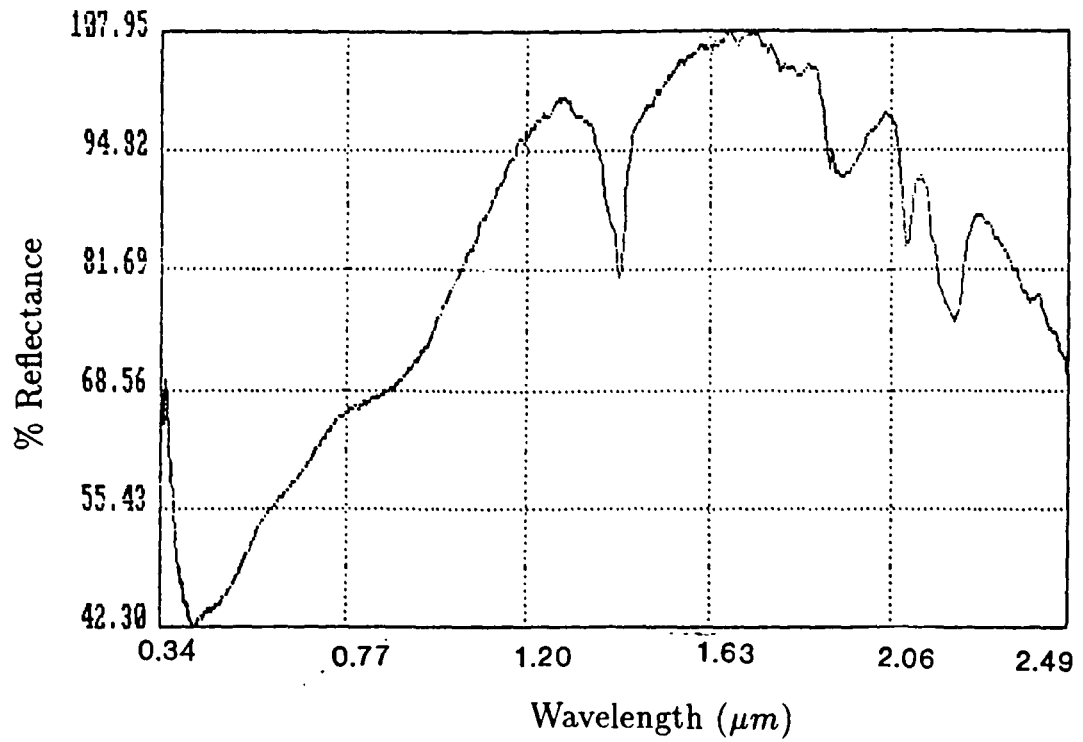
Figure 6.16 Lab spectrum from the internal surface of a sample 4
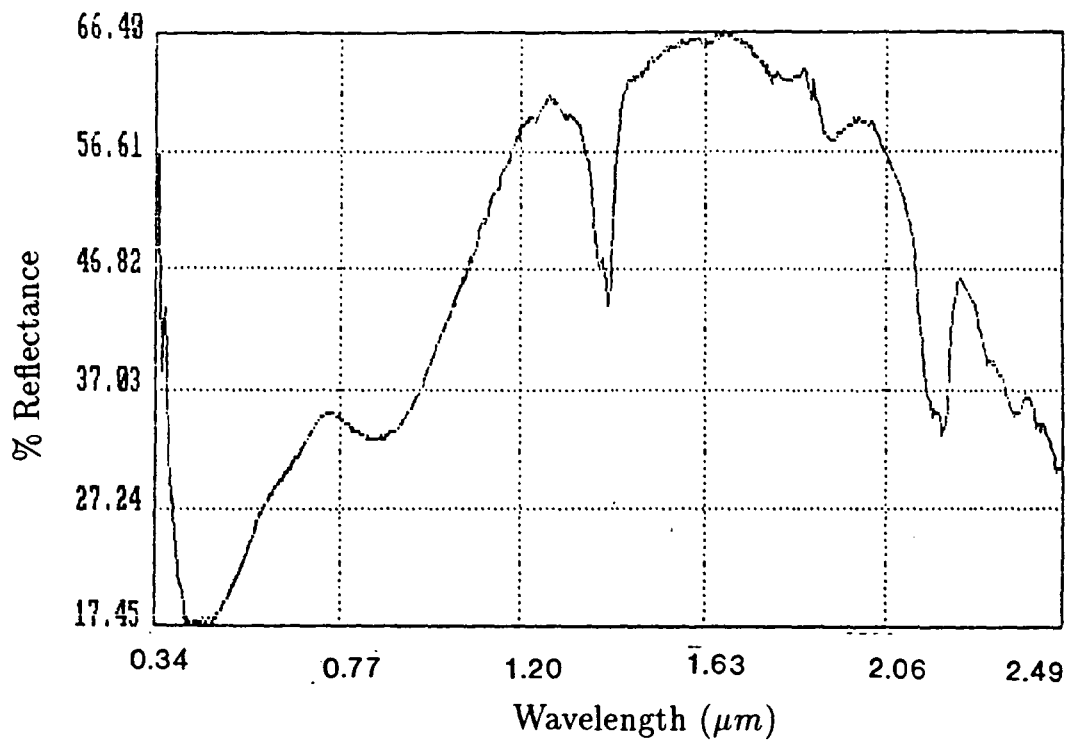
Figure 6.17 Lab spectrum from the external surface of a sample 5
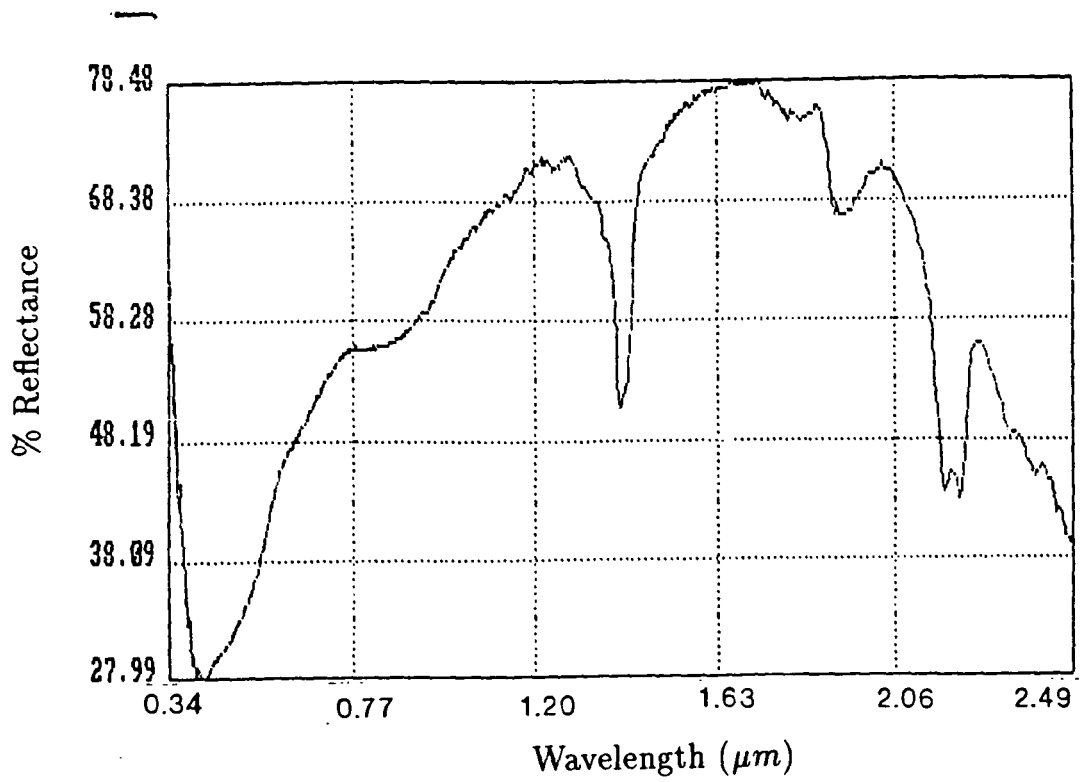
Figure 6.18   Lab spectrum from the external surface of a sample 6
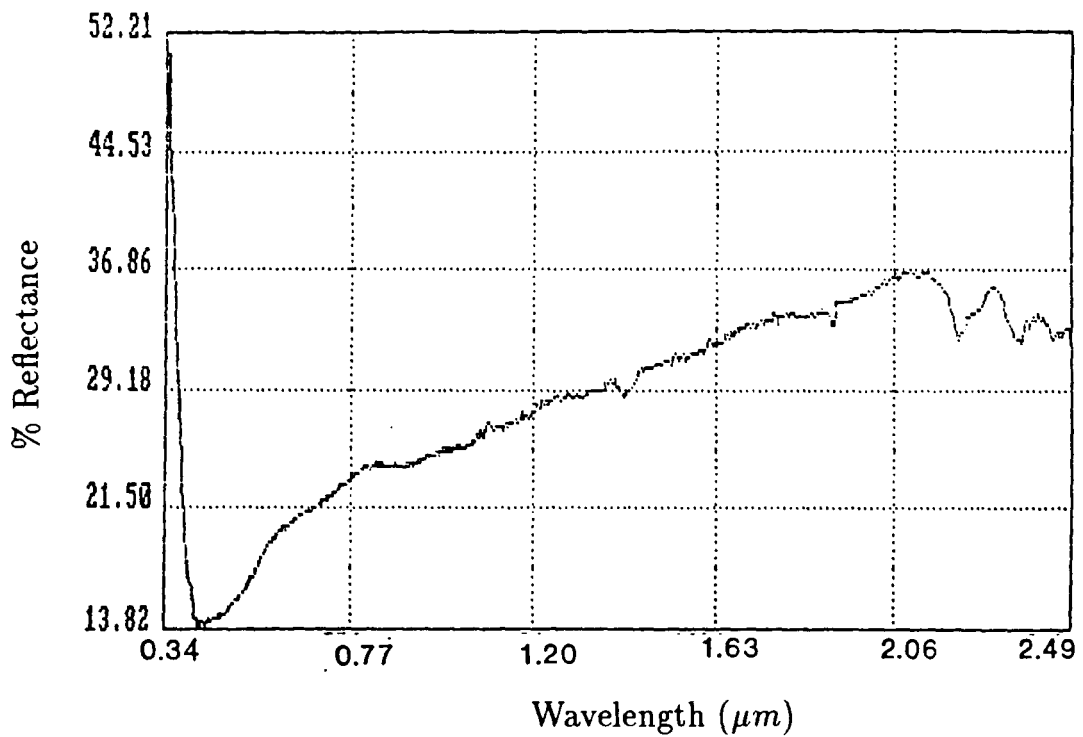
Figure 6.19   Lab spectrum from the external surface of a sample 7
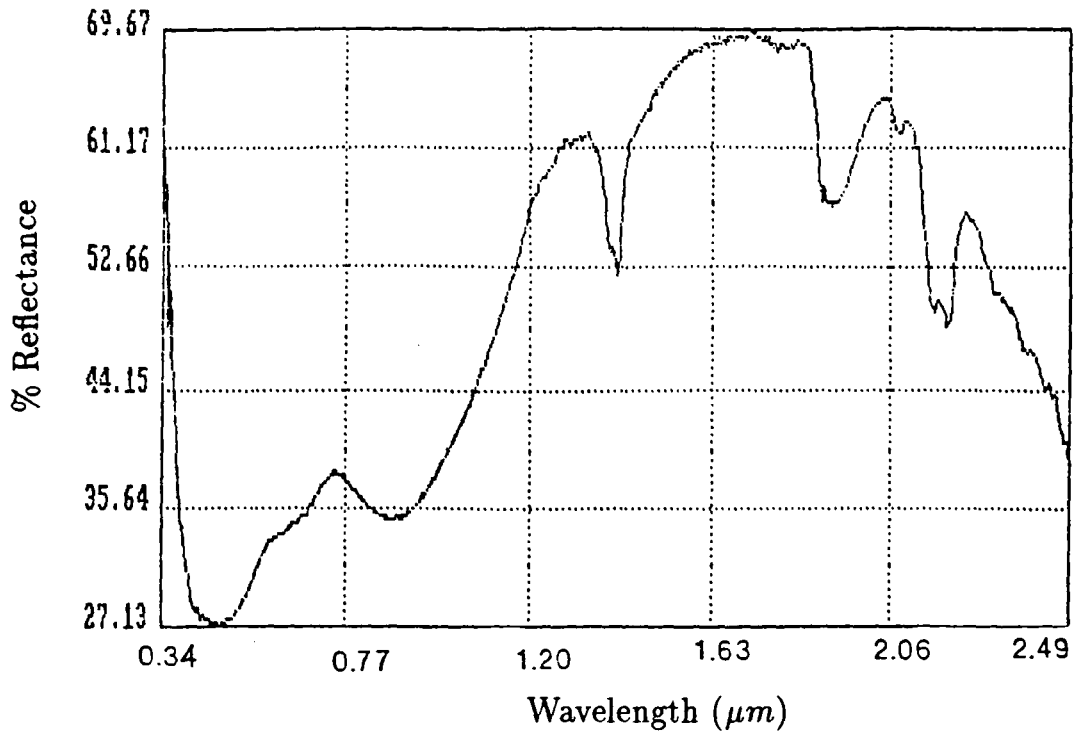
Figure 6.20   Lab spectrum from the external surface of a sample 8
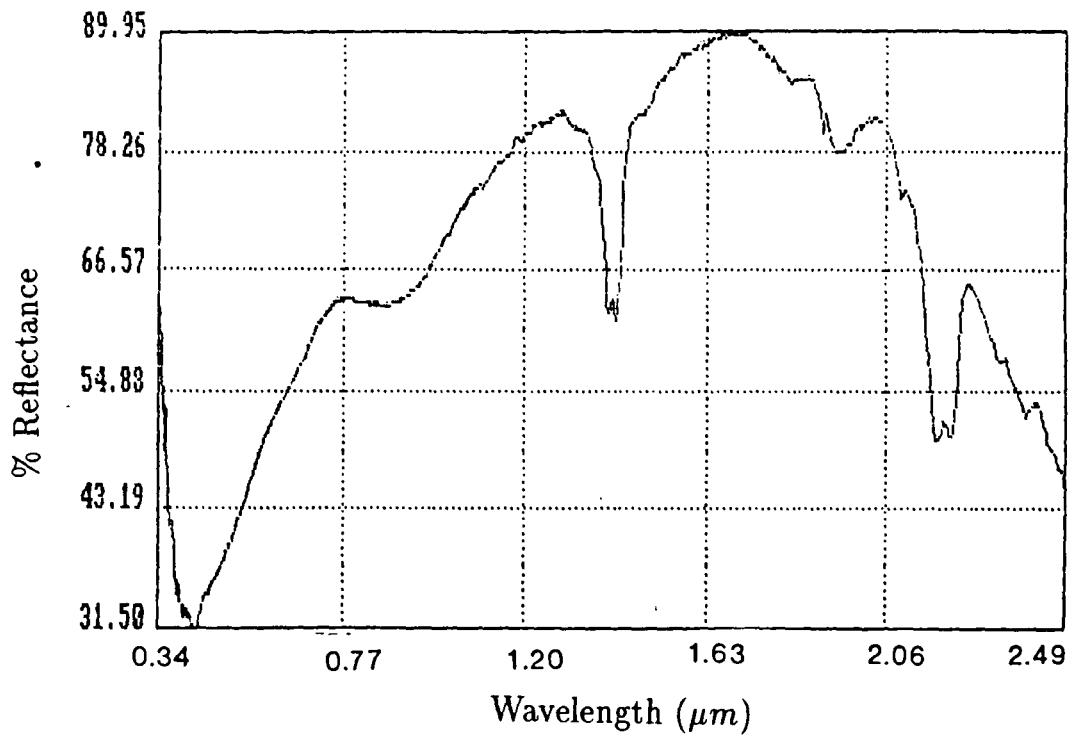
Figure 6.21   Lab spectrum from the internal surface of a sample 9
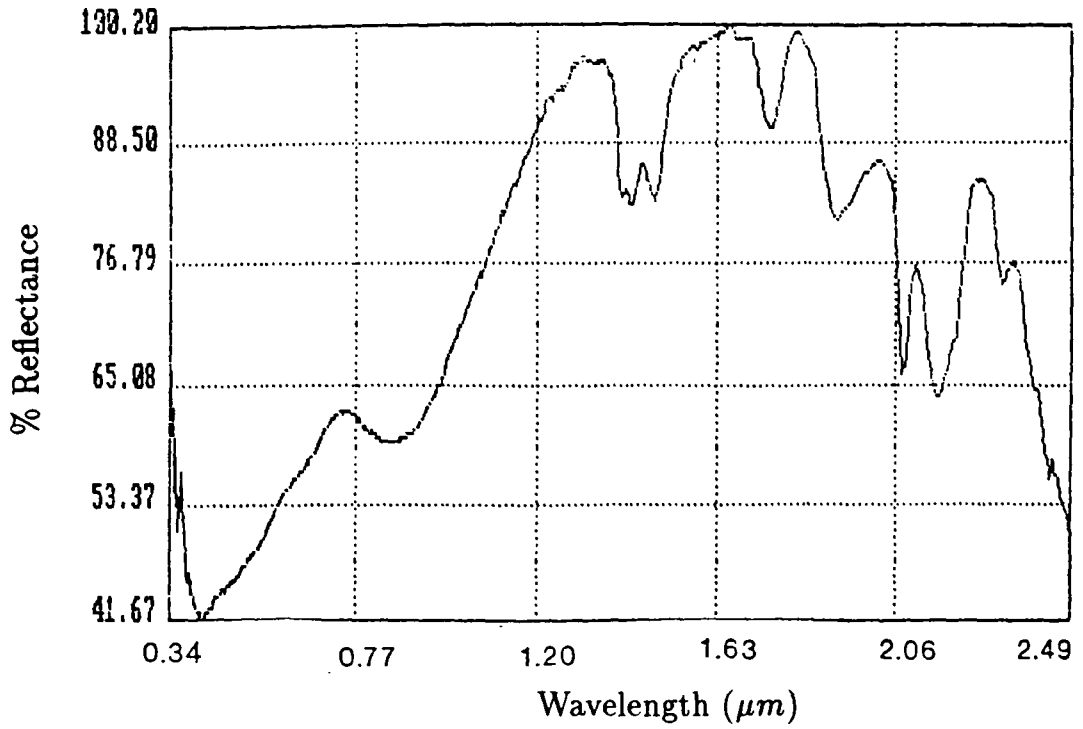
Figure 6.22   Lab spectrum from the external surface of a sample 10
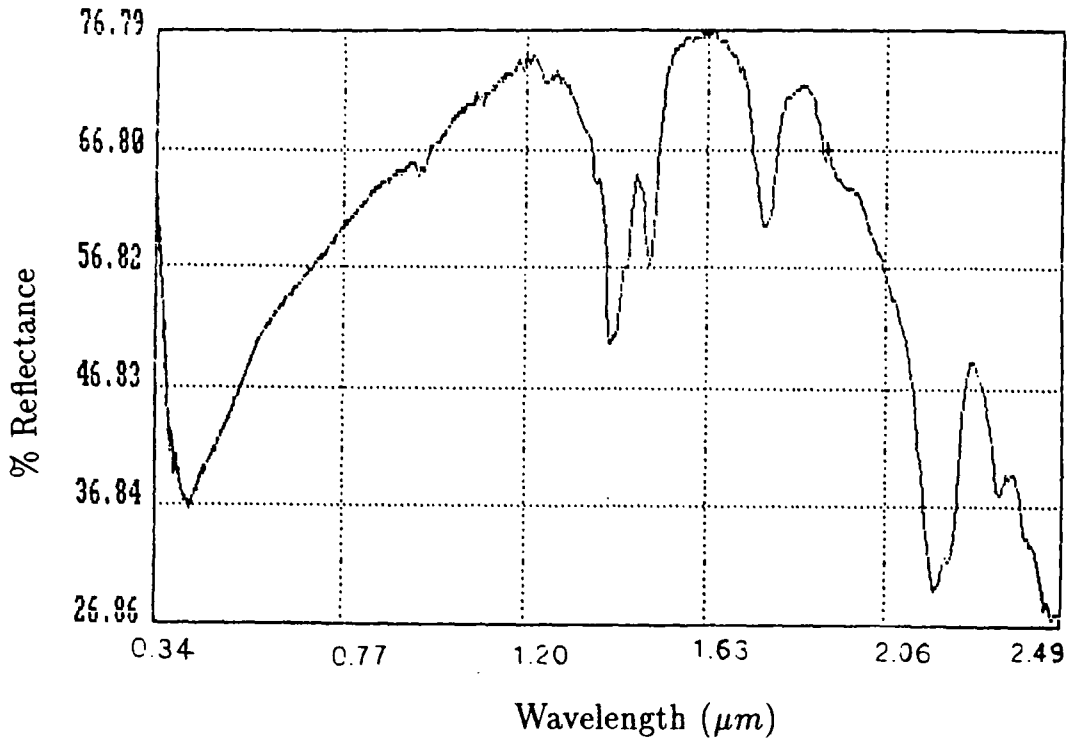
Figure 6.23   Lab spectrum from the external surface of a sample 11a
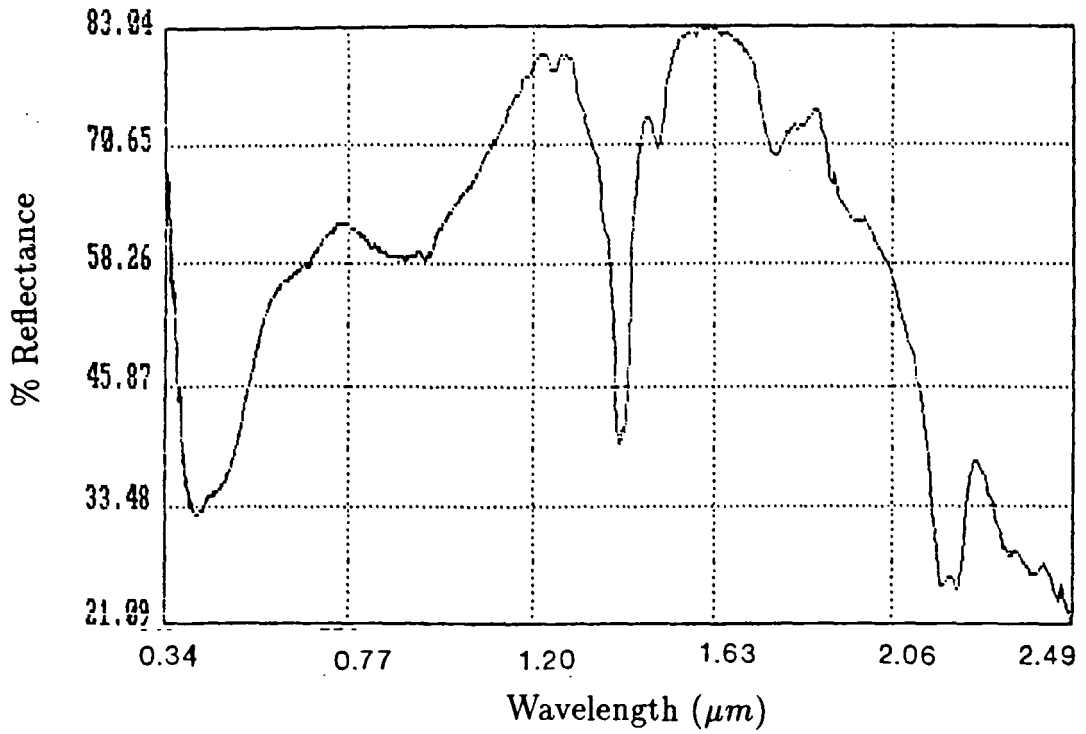
Figure 6.24   Lab spectrum from the internal surface of a sample 11a
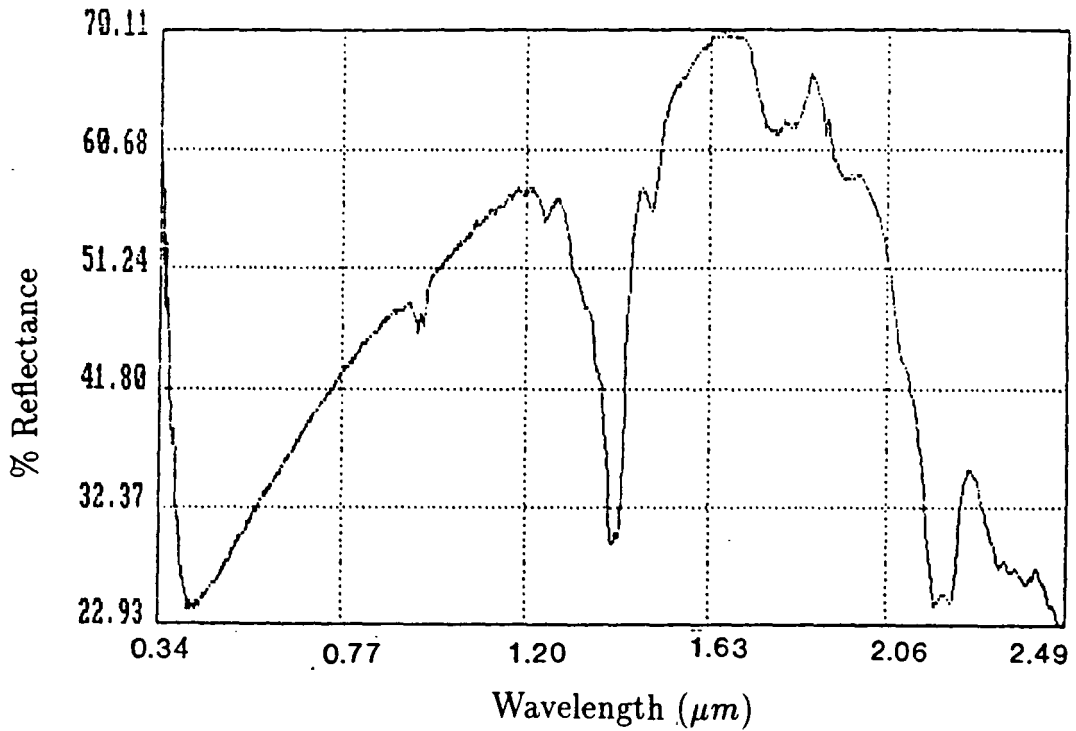
Figure 6.25   Lab spectrum from the external surface of a sample 11b
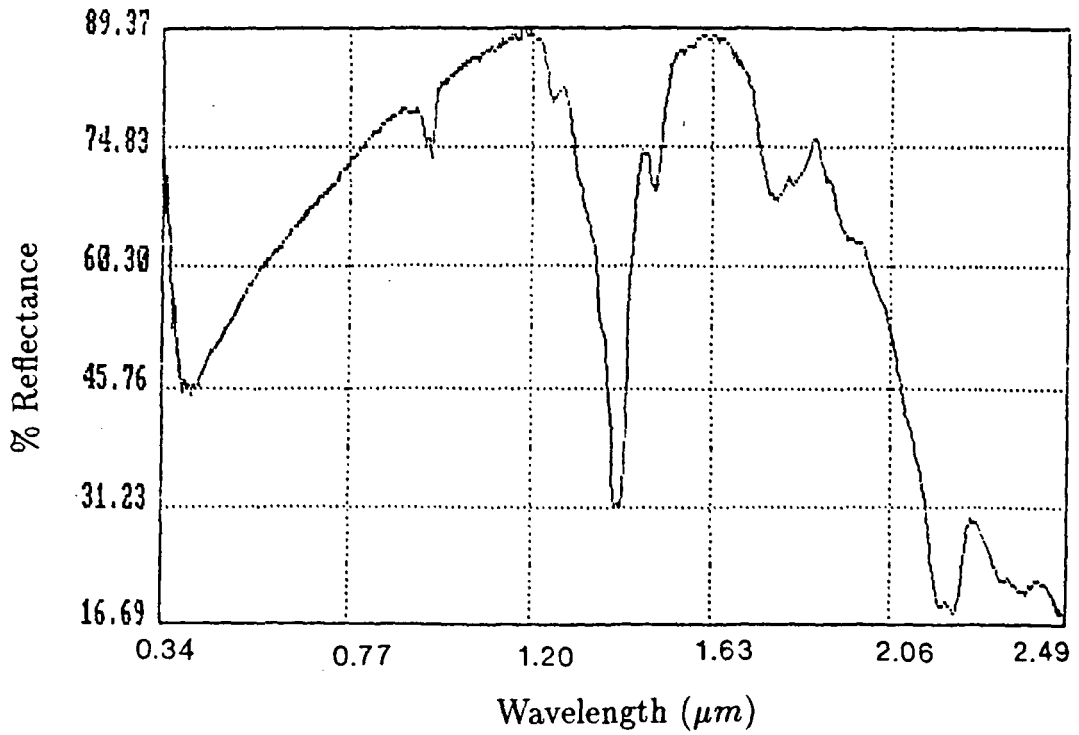
Figure 6.26   Lab spectrum from the internal surface of a sample 11b
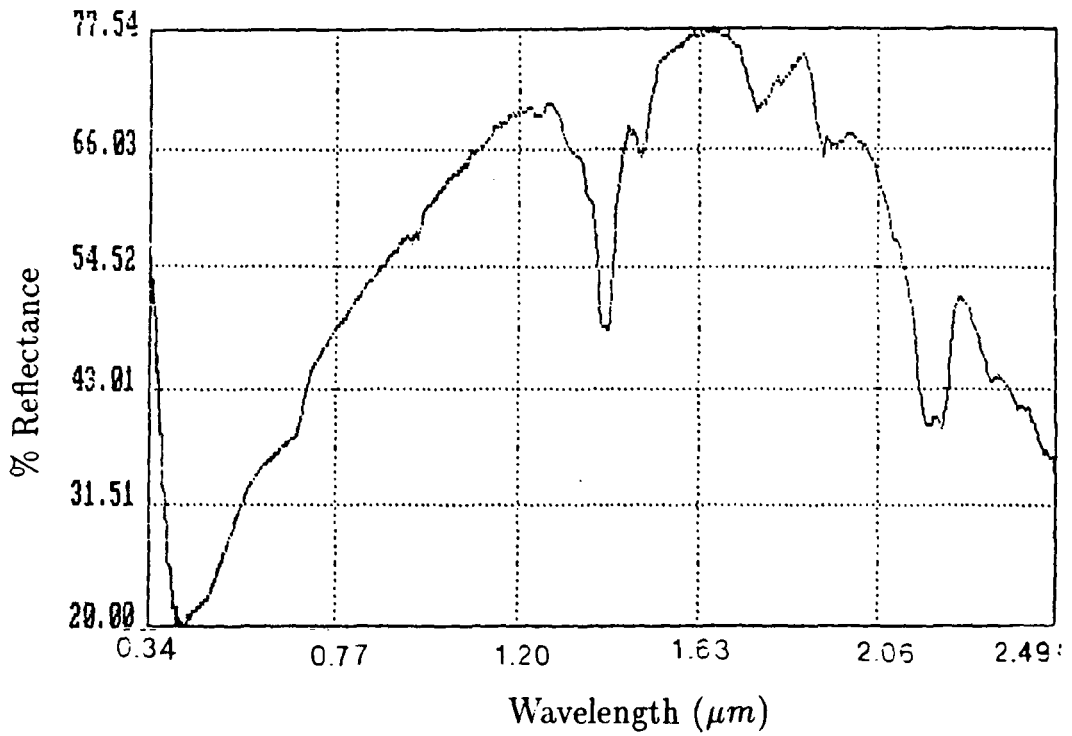
Figure 6.27   Lab spectrum from the external surface of a sample 11c

Figure 6.28 Lab spectrum from the internal surface of a sample 11c
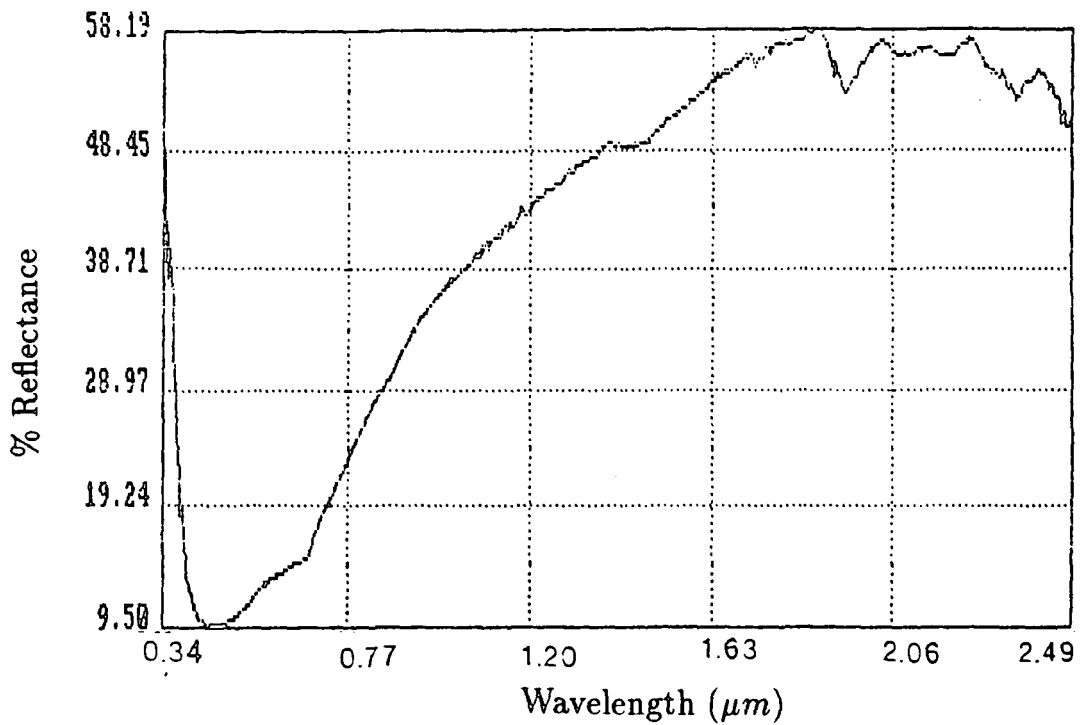
Figure 6.29 Lab spectrum from the external surface of a sample 12a
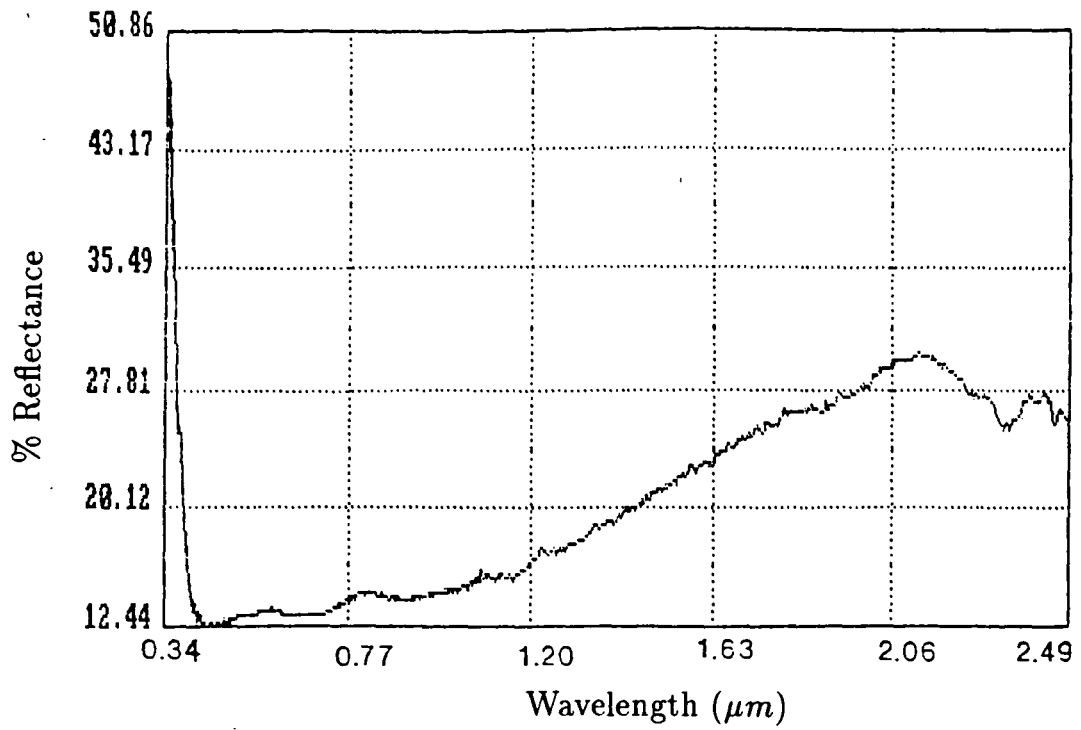
Figure 6.30   Lab spectrum from the internal surface of a sample 12a
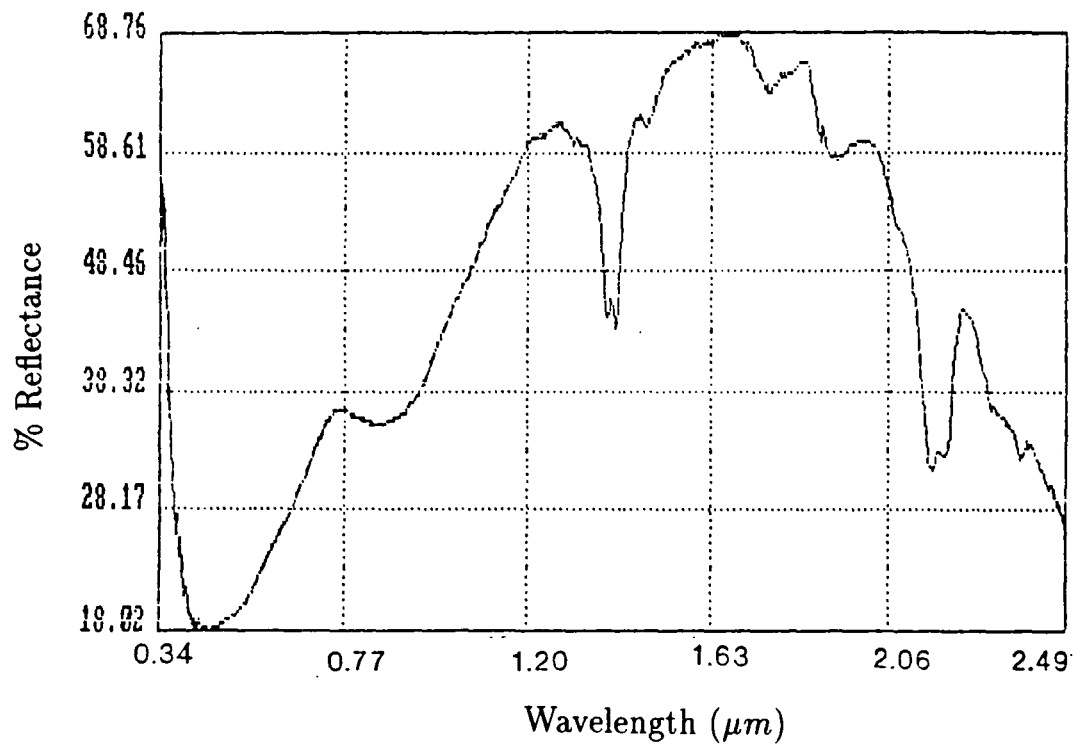
Figure 6.31   Lab spectrum from the external surface of a sample 12b
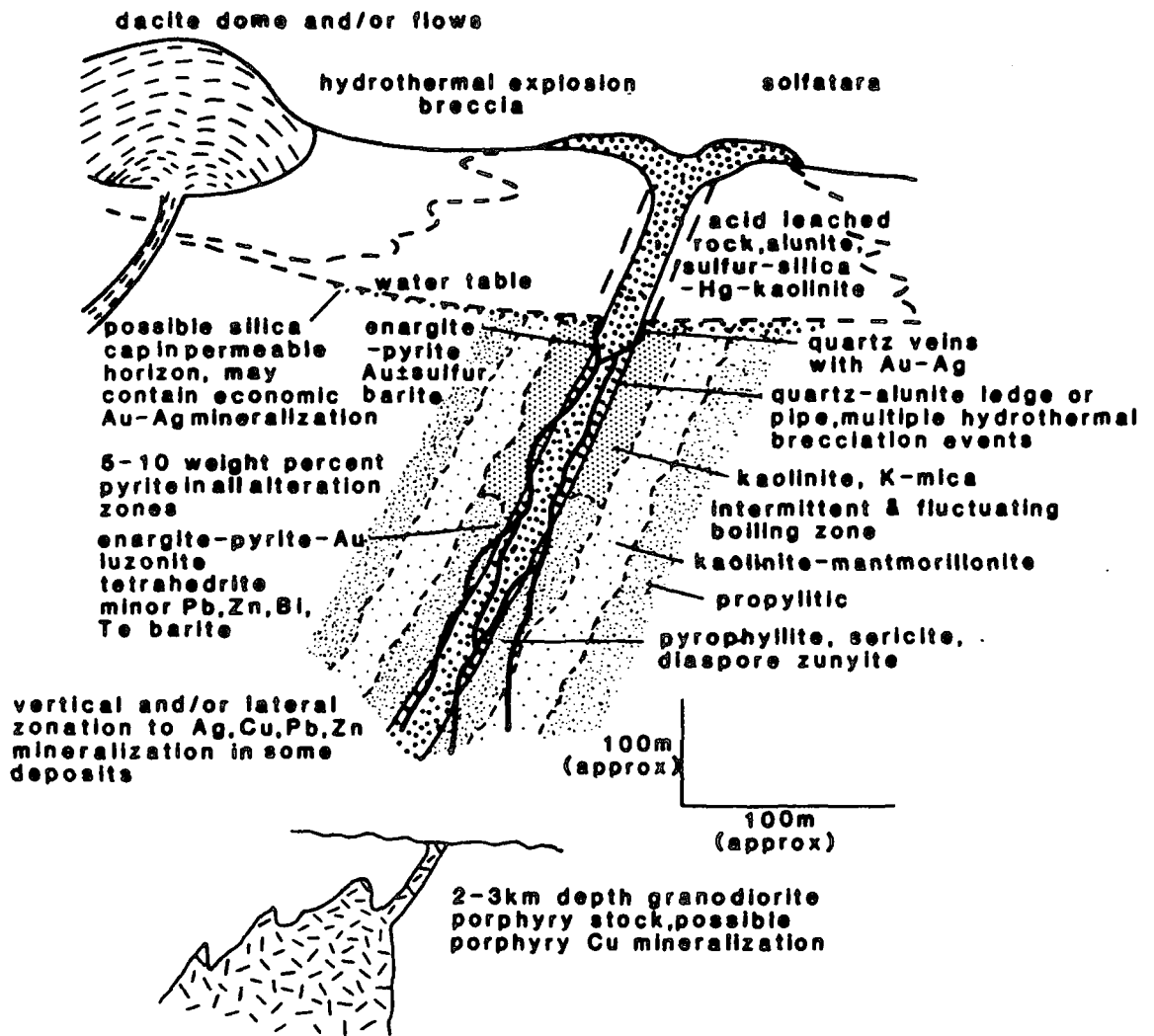
Figure 6.32 Schematic representation of a high sulphur epithermal system
- from Bonham 1986

Plate 6.1   View to Blackfellow Mountain from the West

Plate 6.2   Scree beneath the western side of Blackfellow Mountain

CHAPTER 7

SUMMARY AND RECOMMENDATIONS FOR

FURTHER RESEARCH

## 7.1 Summary and Conclusions

In October 1985 NS-001 and TIMS data were acquired over a test site near
Charters Towers, N. E. Queensland, Australia, as part of the US/Australia
Joint Scanner Project. The NS-001 sensor acquires seven channels of data
in the VNIR,SWIR (0.45-2.4μm) wavelength region. The TIMS acquires six
channels of data in the MIR (8-12μm) wavelength region. The data were ob-
tained on the 26th October 1985 in clear atmospheric conditions and had a
nominal spatial resolution of approximately $15m^2$. The test site covered an
area of largely igneous and sedimentary rocks with a variable vegetation cover
and weathering history. The availability of these data afforded an opportu-
nity to evaluate the utility of both these wavelength regions for lithological
mapping and mineral exploration over the same terrain.

Initially the data were reduced to physically meaningful parameters, re-
flectance, emittance and temperature. This permited comparison of the data
with laboratory reflectance and emittance data and also other remotely sensed
data sets obtained elsewhere which had been expressed in physical terms.

In order to reduce the data to physical terms various inherrent distortions
require correction. These are termed radiometric and geometric distortions.
Radiometric distortions alter the absolute value of the radiation received from
the ground surface whereas geometric distortions alter the spatial relation-
ships between objects.

Radiometric distortions result from both sensor-related and scene-related
effects. Sensor-related effects were removed by calibration. This involves the
accurate conversion of the sensors output (in digital counts) to the radiance
level at the entrance of the sensor. Methods were described for the calibration

of both NS-001 and TIMS data. The effect of calibration on the data was examined with reference to an algorithm for the selection of best channels. This demonstrated that unless the data were calibrated, two data sets obtained from approximately the same area with different calibration values resulted in the selection of a different best channel combination.

Scene-related distortions can be subdivided into two categories: atmospheric effects and georadiometric factors, primarily topography, illumination and view angle (Teillet, 1985). Complete removal of these effects usually requires the acquisition of auxillary information relating to the composition of the atmosphere at the time and place of sensing. Such information was not available and so techniques were devised to partially correct for these effects using scene-based parameters. This enabled the removal of view angle effects in the VNIR, SWIR. Two methods were also developed for the complete removal of atmospheric effects from the MIR data.

View angle effects were manifest as a systematic difference in brightness approximately orthogonal to the direction of flight, termed X-track shading. X-track shading inhibited the accurate quantitative comparison of data from different view angles. Four methods were presented for the removal of this effect. These were: channel ratios, nadir normalisation, scene normalisation and polynomial fitting. The latter three methods were found to be most suitable since they did not restrict the use of the data with further image processing algorithms. These three methods are all empirical profile corrections. The first method involves normalising the mean data column to the nadir column mean. The second method involves normalising each data column to the scene means. The third method involves fitting a polynomial function to the column mean. Each column mean is normalised to the nadir column mean value obtained from the polynomial function. Normalisation in each case could be undertaken in either a multiplicative or an additive manner. The manner used depends on how the data are subsequently processed. The data used in this study were corrected by nadir normalisation applied multiplicatively.

Two methods were developed during this study for the complete atmospheric correction of MIR data. These are empirical methods based upon an understanding of how the atmosphere attenuated the signal from the ground. With these methods the atmospheric effect in the MIR was attributed to two

factors. These were the transmissivity of the atmosphere and the amount of radiance that reaches the sensor through atmospheric emission and scattering. Atmospheric transmissivity has a multiplicative effect on the radiance from the ground reaching the sensor to which is added the radiance from atmospheric emission and scattering. These two factors were referred to as the multiplicative and additive effects of the atmosphere.

The first method for complete atmospheric correction was developed by Callison *et al.,* (1985), for use with MIR data obtained over the sea surface. This method was modified by the author for use with land data. The results obtained using this method suggested there was a large discrepency in the amount of radiance reaching the sensor from either side of nadir as it scans across the scene. This was attributed to the sensor receiving radiation from sun facing slopes as it scanned one half of the scene, then shadowed slopes as it scanned the other half of the scene. The sun facing slopes were hotter and therefore resulted in more radiation at the sensor. However, using this technique it was not possible to determine the magnitude of the multiplicative and additive terms to see how these varied with scan angle. Therefore, a second method for complete atmospheric correction was developed by the author in collaboration with A. A. Green. This method enabled the determination of the multiplicative and additive terms. This method confirmed the discrepency in the radiance received by the sensor either side of nadir. However, the magnitude of the discrepency differed between either side of nadir depending on the technique used. Therefore, this correction was not employed. These preliminary results indicate further work is required in this area.

The corrected VNIR,SWIR data were then analysed by a variety of techniques aimed at reducing the data to reflectance and extraction of the relevant geologic information. This included information on the presence and abundance of iron oxides and Al-OH $\pm$ Mg-OH $\pm$ CO bearing minerals. Areas particularly abundant in either often result from hydrothermal alteration. Such areas are commonly mineralised and their detection is especially valuable for mineral exploration. The techniques utilized with the VNIR,SWIR data were compositing, channel ratios, log residuals, least squares fit residuals (LRES) and directed principle components (DPC). Initially all the techniques

were evaluated over a test site 512 x 512 pixels in size centered on Camp Oven Mountain. The site was selected on the basis that it contained a variety of rock types and had a variable vegetation cover and weathering history.

Previous workers in semi-arid, sparsely vegetated terrain with little surface weathering had found channel ratios particularly useful for enhancing iron oxides and Al-OH ± Mg-OH ± CO bearing minerals (eg. Abrams *et al.*, 1984). Areas of iron oxides were enhanced in the ratio of two channels centered upon 0.66μm and 0.56μm . This was due to iron minerals absorbing radiation around 0.56μm and having a reflectance peak at around 0.66μmand hence their red appearance. Therefore areas of iron oxides had high values in this ratio compared with other materials. Areas of Al-OH ± Mg-OH ± CO bearing minerals were enhanced using the ratio of two channels centered upon 1.65μm and 2.2μm. Areas of Al-OH ± Mg-OH ± CO bearing minerals have a reflectance peak around 1.65μm and absorb radiation around 2.2μm. This resulted in these areas having high values in this ratio compared with other rocks.

Channel ratios calculated with these data were successful in enhancing areas of iron oxides. However, since the majority of the area had a strong iron oxide stain due to weathering this information was of limited value for detecting alteration. Mapping areas of Al-OH ± Mg-OH ± CO bearing minerals was even more problematic. Areas of vegetation and hydrous minerals had similar ratio values. As a result the majority of areas interpreted from the ratio values to relate to Al-OH ± Mg-OH ± CO bearing minerals were vegetation. The abundance of these false anomalies severely restricted the use of ratios as a means for detecting Al-OH ± Mg-OH ± CO bearing minerals.

The logarithmic residuals technique was developed by Green and Craig (1985). This technique removes the effects of both atmosphere and topography producing pseudo-reflectance data. These pseudo-reflectance data can be used to examine variations in the amount of iron oxide and Al-OH ± Mg-OH ± CO bearing minerals present. This information relates to the composition of the surfical material. In certain cases, this was used to infer the composition of the underlying rock type. Laboratory reflectance spectra obtained from field samples, in most cases, agreed with the pseudo-reflectance spectra

extracted over the area from which the field samples were obtained.

The log residual data were found to be biased by vegetation introduced as part of the log residual calculation. It was not possible to determine the presence of Al-OH ± Mg-OH ± CO bearing minerals in vegetated areas with this technique. Therefore, whilst these data proved useful for lithological mapping they were of limited use for the detection of areas of Al-OH ± Mg-OH ± CO bearing minerals.

In order to isolate the effects of vegetation and Al-OH ± Mg-OH ± CO bearing minerals the data were analysed using the DPC and LRES techniques. These techniques were developed to enhance areas of Al-OH ± Mg-OH ± CO bearing minerals in the vegetated terrain. Both techniques highlighted an anomalous area of Al-OH ± Mg-OH ± CO bearing minerals centered upon Blackfellow Mountain. This area had not been targeted as an area of alteration and potential mineralisation by reconnaisance exploration teams. Subsequent fieldwork confirmed this to be an area of advanced argillic alteration. Several further anomalous areas were highlighted in the area using both techniques. The majority of those highlighted were confirmed to contain Al-OH ± Mg-OH ± CO bearing minerals. However, several false anomalies remained in the DPC data relating to areas of vegetation.

The results indicated the log residual and LRES techniques were the most useful for lithological mapping and mineral exploration at the Camp Oven test site. These techniques were applied to data from a second test site, termed Plateau, to determine their wider applicability. This site was more deeply weathered and had a greater vegetation cover. The site contained a known area of gold mineralisation.

The log residual data enabled mapping of most of the known lithologic units. The pseudo reflectance spectra agreed with spectra obtained from similar rock types at the Camp Oven test site. Areas of Al-OH ± Mg-OH ± CO bearing minerals and vegetation remained confused. The LRES data enabled mapping of the distribution of the Al-OH ± Mg-OH ± CO bearing minerals. One such area coincided with the the known mineralisation. However, this was not as distinct as the alteration discovered at Blackfellow Mountain. This difference was thought to relate to the style of mineralisation present at this site. Numerous other areas of Al-OH ± Mg-OH ± CO

bearing minerals anomalies were apparent in this data. Fieldwork confirmed the increased abundance of Al-OH ± Mg-OH ± CO bearing minerals at these anomalies. However, these anomalies were the result of weathering. They occurred over the weathered Triassic kaolinitic sandstones or where the mottled zone of a laterite was exposed, usually at a breakaway. The majority of these anomalies could be separated from those relating to alteration by other photogeomorphic features.

The corrected MIR data were also evaluated for lithological mapping and mineral exploration at the Camp Oven test site. The radiance measured in the MIR is a composite of both temperature and emittance information. The temperature information is highly correlated between channels and dominates the emittance information which relates to the composition of the underlying material. Therefore, it is neccessary to enhance or extract this emittance information if it is to be of use for lithological mapping. This was achieved using three techniques: the decorrelation stretch, model emittance calculation and thermal log residuals. Decorrelation stretch data have been successfully used to discriminate various lithologies in semi-arid sparseley vegetated terrains with limited surface weathering (Kahle and Goetz 1983; Lahren *et al.*, 1988). However, using the Decorrelation Stretch data over the Camp Oven test site it was not possible to discriminate the majority of the known lithologies. Also, the alteration identified in the VNIR,SWIR data surrounding Blackfellow Mountain was not distinguished. The lack of discrimination with these data is thought to result from several factors. First, noise in the sixth channel is introduced into the other channels as part of the decorrelation stretch calculation. Secondly, any vegetation masked the response from the underlying material. In mixed pixels, it was not possible to determine the response of the underlying material only the presence of vegetation. Thirdly, the area had a thin surficial veneer of weathered sandy material which subdued any differences between the underlying lithological units. Finally, the decorrelation stretch did not separate the emittance from the temperature information it only enhanced it. This appeared to be insufficient to enable discrimination.

The second technique used to extract the emittance information from the MIR data was the Model Emittance Calculation developed by Kahle *et al.*, (1980). This method assumes a constant emittance of 0.93 (on a scale

of 0-1) in the data from the 11.7μm channel enabling the temperature at each pixel to be determined using Planck's Law. This temperature is used to extract the emittance values of a pixel in the five remaining channels of data. Since these data had not been fully atmospherically corrected the emittance data were dominated by atmospheric effects. These were removed using a flat field correction. This correction assumes a material within the image is spectrally flat. Therefore, any variations contained therein should relate to atmospheric differences. Thus by dividing each pixel by the flat field the atmospheric effects should be removed. In MIR data vegetation is commonly used for the flat field correction (Gillespie, 1986). Since the MIR data are highly correlated between channels the assumption of a constant emittance in the 11.7μm channel results in the values in 10.7μm channel also being forced to a constant. Any differences between the channels relates to noise which is enhanced and rendered the data from the 10.7μm channel useless. Therefore, it was only possible to extract emittance information from the first four TIMS channels. These data enabled the discrimination of the majority of mapped lithological units. A further unit was also discriminated which was subsequently identified as an area of siliceous breccias. This unit could not be distinguished with data from the VNIR,SWIR. The main advantage of using the Model Emittance Calculation is not visual discrimination, but that the shape of the spectral curve obtained from a given rock type can be matched with laboratory curves for rock identification. However, when the spectral curves for a variety of rock types were examined they could not be related to any known laboratory reflectance curves.

The third technique for the analyis of airborne multispectral data from the MIR was developed as part of this study by the author in collaboration with A. A. Green and A. R. Gabell of CSIRO Sydney, Australia. This technique separates the emittance information from the temperature information. The data obtained are not the absolute emittance values for a particular channel and as a result cannot be correlated between channels. However, variations in the relative emittance of a group of rocks in each channel can be used to infer the type of rock from laboratory studies. The Thermal Log Residual data permitted discrimination of the same units mapped with the model emittance data. The additional unit of siliceous breccias was also discriminated and was

visually more apparent than in the model emittance data.

Maximum discrimination with the MIR data was achieved after processing to thermal log residuals. These were calculated from the MIR data covering Plateau. These data enabled discrimination of most of the mapped lithologic units at Plateau. Furthermore, the areas of Al-OH $\pm$ Mg-OH $\pm$ CO bearing minerals resulting from exposure of the mottled zone of laterites and weathering of the kaolinitic sandstones could also be distinguished. This contrasts with the Camp Oven test site at which the Al-OH $\pm$ Mg-OH $\pm$ CO bearing minerals around Blackfellow Mountain could not be easily separated. This may relate to the types of minerals which result from weathering compared with alteration.

The vegetation and weathering characteristics of this site contrasted with the majority sites studied in the USA using TIMS data. At these sites the decorrelation stretch data had been successfully used to discriminate most of the lithologic units. Such data were found to be far inferior to the Thermal Log Residual data for discrimination at this site. Therefore, Thermal Log Residual data were calculated from TIMS data acquired over Cuprite, Nevada, W. USA to examine the wider applicability of the technique. The Thermal Log Residual data permitted discrimination of all units separated using the decorrelation stretch. Several further units were also recognised and by examining the relative changes of a group of rocks in each channel it was possible to infer the rock type from laboratory studies in the MIR.

Samples collected from the area of alteration discovered at Blackfellow Mountain were analysed by laboratory spectrometry and X-ray diffraction. These analyses were undertaken to establish which alteration minerals were present and how they were distributed to propose a hydrothermal model for the observed alteration.

Spectrometry identified the Al-OH $\pm$ Mg-OH $\pm$ CO bearing minerals alunite, kaolinite, dickite, pyrophyllite and sericite/montmorillonite/illite. The iron oxide minerals haematite, limonite, and goethite were also identified by this method. With the exception of montmorillonite/illite the remaining hydrous minerals were consistently identified in the spectra from the external and internal surfaces. This suggests these minerals were the result of hydrothermal alteration whilst the sericite/montmorillonite/illite was a weath-

ering product. The Al-OH ± Mg-OH ± CO bearing minerals identified by X-ray diffraction were alunite, a kandite, and pyrophyllite. The kandite group includes one or more of the following minerals: kaolinite, dickite, hallyosite and nacrite. In the majority of samples the minerals identified by spectrometry and X-ray diffraction were in agreement. However, there were some exceptions. Firstly, no iron oxides were identified by X. Ray Diffraction. This is attributed to a lack of crystallinity inhibiting their identification by X-ray diffraction. Secondly, pyrophyllite was not identified in samples by lab spectrometry which also contained alunite and kaolinite/dickite. This discrepency is thought to arise from the other minerals present which confuse the spectrum and mask the diagnostic absorption features of pyrophyllite. This problem does not arise with these minerals using X-ray diffraction. Thirdly, using X-ray diffraction it was not possible to determine which mineral of the kandite group was present. This was usually possible by lab spectrometry and found to be either kaolinite and/or dickite.

This study demonstrates that data from the VNIR, SWIR and MIR when reduced to physical terms are useful for lithological mapping and mineral exploration in weathered vegetated terrain. Furthermore, since the different wavelength regions are sensitive to different mineralogies this information is of a complimentary nature.

In order to reduce the data to physical terms it is necessary to correct fo radiometric and geometric distortions. These include the affects of the atmosphere which normally requires the availability of ancillary data on atmospheric composition. Two methods were developed as part of this study which whilst requiring further work indicate it should be possible to remove atmospheric effects from MIR data using scene-derived parameters.

The geologically relevant reflectance or emittance information was extracted from the corrected data using a variety of standard and advanced image processing techniques. These included compositing, channel ratios, log residuals, DPC and LRES with the VNIR,SWIR data and the decorrelation stretch, model emittance calculation and thermal log residuals with the MIR data. The log residual technique was developed by Green and Craig (1985), the LRES technique by Green (pers. comm. 1985) and DPC by Fraser and Green (1987). The log residual and LRES techniques proved most effective

for lithological mapping and mineral exploration with the VNIR,SWIR data. The success of these techniques results from their being developed specifically to enhance variations in iron oxides and Al-OH ± Mg-OH ± CO bearing minerals in vegetated, weathered terrain. The thermal log residual technique proved most effective at extracting the relevant emittance information from the MIR data. This technique was developed in 1987 by the author in collaboration with A. A. Green and A. R. Gabell of CSIRO, Sydney, Australia. The success of this technique results from it providing relative emittance information from all six TIMS channels which was not possible with the other techniques.

These algorithms can only be developed from a clear understanding of the causes of the spectral attributes of rocks and minerals at these wavelengths from laboratory studies. Such algorithms require constant modification as our understanding increases, particularly in the area of spectral mixing.

In general, the MIR data were as effective as the VNIR,SWIR data for lithological mappping and allowed the dicrimination of a further unit of siliceous breccias not apparent in the VNIR,SWIR data. The VNIR,SWIR data were far more useful for mineral exploration than the MIR and enabled the discovery of an area of alteration at Blackfellow Mountain. This area was not discriminated with the MIR data. Subsequent laboratory spectrometry coupled with X-ray diffraction identified the mineral assemblage quartz, alunite, kaolinite/dickite, pyrophyllite and sericite. These minerals together with their distribution suggest the alteration results from a high-sulphur epithermal system.

7.2   Recommendations For Further Research

Three key areas were identified in this work which require further research.

First, a full evaluation of the empirical atmospheric correction models developed for MIR data. This work should be conducted with a N-S data set for which ancillary atmospheric information has been obtained to enable comparison with established atmospheric correction models such as LOWTRAN.

Secondly, in certain samples the minerals identified by lab spectrometry did not agree with those identified by X-ray diffraction. The incorrect mineral

identification in the laboratory spectra is thought to result from overlapping of spectral features in certain combinations of minerals. Further work is required to develop models to separate these mixtures.

Thirdly, a new technique was developed for the analysis of MIR data termed thermal log residuals. This permitted greater discrimination than either the decorrelation stretch or model emittance calculation enabled using TIMS data from several test sites. Unfortunately, this technique does not allow the extraction of the absolute emittance values in all six channels for a given pixel. Further work is required to develop a technique which extracts this information. This should enable mineral identification as well as lithological discrimination.

REFERENCES

Abrams, M., Ashley, R., Rowan, L., Goetz, A., and Kahle, A., 1977. Mapping of hydrothermal alteration in the Cuprite mining district, Nevada, using aircraft scanner images from the spectral region 0.46-2.36μm : *Geology,* v. 5, p.713-718.

Abrams, M., Brown, D., Lepley, L., and Sadowski, R., 1983. Remote sensing for Porphyry Copper Deposits in Southern Arizona: *Econ. Geol.,* v. 78, p.591-604.

Abrams, M. J., Conel, J. E., and Lang, H. R., 1984. *Joint NASA/Geosat Test Case Project (final report)* Tulsa, Okalahoma: American Association of Petroleum Geologists.

Adams, J. B., 1975. Interpretation of visible and near infrared diffuse reflectance spectra of pyroxenes and other rock forming minerals: *in* Karr C., (ed.,) Infrared and Raman spectroscopy of lunar and terrestrial minerals: New York, Academic, p.91-116.

Ager, C. M., and Milton, N. M., 1987. Spectral reflectance of lichens and their effect on the reflectance of rock substrates: *Geophysics* v. 52, p.898-906.

Ashley, R. P., 1982. Occurrence model for enargite-gold deposits: *US Geological Survey Open File Report* 795p.

Barnsley, M. J., 1984. Effects of off-nadir view angles on the detected spectral response of vegetation canopies: *Internat. J. Remote Sensing,* v. 5, p.715-728.

Beams, S. D., 1986. Geology map of Plateau and the surrounding area: Unpub. Combined final report on the conditional surrender of authority to prospect 3513M Dreghorn, 3586M, Warrawee, 3998M Iguana, 4000M Rollaston and partial relinquishment report for sub-blocks dropped from the authority to prospect in 1986.

Blodget, H. W., Andre, C. G., Marcell, R. S., 1985. Composite assessment of multi-satellite thermal infrared data for rock discrimination in Basement, Volcanic and Sedimentary terrain: *Proceedings of the Fourth Thematic Conference 'Remote Sensing for Exploration Geol-*

ogy', San Francisco, California, April 1-4, p.361-362.

Bonham, Jnr., H. F., 1986. Models for vocanic-hosted epithermal precious metal deposits; A review: *Proc. Fifth Symposium on Volcanism, Hydrothermal Systems and Related Mineralisation.* University of Auckland, February, p.13-18.

Butt, C. R. M., 1983. History and characteristics of weathering in Australia: *in* Smith, R. E., (ed.) Geochemical Exlporation in Deeply Weathered Terrain: Perth, CSIRO Institute of Energy and Earth Resources, p.41-50.

Callison, R. D., Blake, P., and Anderson, J. M., 1987. The quantitative use of Airborne Thematic Mapper thermal infrared data: *Internat. J. Remote Sensing,* v. 8, p.113-126.

Chahine, M., 1983. Interaction Mechanisms within the Atmosphere: *in* Manual of Remote Sensing Second Edition, Colwell, R. N., (ed.), American Society of Photogrammetry, Falls Church, Virginia, v. 1, 1232p.

Christensen, P., Crawford, M., Prabhakara, C., Malila, M., Palluconi, F., Podwysocki, M., Salisbury, J., and Vincent, R., 1986. Geology panel report: *in* Putman, E. S., (ed.) Commerical applications and scientific requirements for thermal-infrared observations of terrestrial surfaces, a report on the joint EOSAT/NASA thermal infrared working group: Lanham, Maryland, Earth Observation Satellite Company, p.17-34.

Conel, J. E., Adams, S., Alley, R. E., Hoover, G., and Shultz, S., 1986. Analysis of AIS radiometry with emphasis on determination of atmospheric properties and surface reflectance: *Proceedings of the Second Airborne Imaging Spectrometer Data Analysis Workshop.* May 6-8, JPL Publication 86-35, p.31-51.

Deschamps, P. Y., Herman, M., and Tanre, D., 1983. Definition of Atmospheric Radiance and Transmittances in Remote Sensing: *Remote Sensing of Environment,* v. 13, p.89-92.

Drury, S. and Hunt, G. A., 1988. Remote Sensing of Laterized Archaen Greenstone Terrain: Marshall Pool Area, Northeastern Yilgarn Block, Western Australia: *Photogrammetric Engineering and Remote Sens-*

ing, v. 54, p.1717-1726.

Drury, S. and Hunt, G. A., 1989. Geological uses of remotely-sensed reflected and emitted data of lateritized Archaen terrain: *Internat. J. Remote Sensing,* v. 10, p475-498.

Elvidge, C. D., and Lyon, R. J. P., 1984. Mapping clay alteration in the Virginia Range-Comstock Lode, Nevada with airborne thematic mapper imagery: *Proceedings of the Third Thematic Conference 'Remote Sensing for Exploration Geology',* Colorado Springs, Colorado, April 16-19, p.161-170.

Elvidge, C. D., 1988. Vegetation reflectance features in AVIRIS data: *Proceedings of the Sixth Thematic Conference: 'Remote Sensing for Exploration Geology',* Houston, Texas, May 16-19, p.169-182.

Elvidge, C. D., 1988. Thermal Infrared Reflectance of Dry Plant Materials: *Remote Sensing of Environment,* v. 26, p.265-286.

Evans, D., 1988. Multisensor Classification of Sedimentary Rocks: *Remote Sensing of Environment,* v. 25, p.129-144.

Fraser, S. J., Huntington, J. F., Green, A. A., Stacey, M. R., and Roberts, G. P., 1985. Discrimination of iron oxides and vegetation anomalies with the MEIS narrow band imaging system: *Proceedings of the Fourth Thematic Conference: 'Remote Sensing for Exploration Geology',* San Francisco, California, April 1-4, p.223-253.

Fraser, S. J., Gabell, A. R., Green, A. A., and Huntington, J. F., 1986. Targeting epithermal alteration and gossans in weathered and vegetated terrains using aircraft scanners: successful Australian case histories: *Proceedings of the Fifth Thematic Conference 'Remote Sensing for Exploration Geology',* Reno, Nevada, Sept. 29-Oct. 2, p.63-84.

Fraser, S. J., and Green, A. A., 1987. A software defoliant for geological analysis of band ratios: *Internat. J. Remote Sensing,* v. 8, p.525-532.

Gabell, A. R., Huntington, J. F., Green, A. A., Cocks, T. T., and Hornibrook, M. J., 1985. Clay mineral absorption features in the 0.9-1.1μm region and their implications for proximal remote sensing: *Proceedings of the Fourth Thematic Conference 'Remote Sensing for Ex-*

ploration Geology', San Francisco, California, April 1-4, p.511-520.

Gabell, A. R., Huntington, J. F., and Green, A. A., 1985. US/Australia Joint Scanner Project: *CSIRO Institute of Energy and Earth Resources*, RIR 1616R, 209p.

Gates, D. M., Keegan, H. J., Scheter, J. C., and Weidner, V. R., 1965. Spectral properties of plants: *Applied Optics*, v. 4, p.11-20.

Gillespie, A. R., Kahle, A. B., and Palluconi, F. D., 1984. Mapping Alluvial Fans in Death California, using Multichannel Thermal Infrared Images: *Geophysical Research Letters*, v. 11, p.1153-1156.

Gillespie, A. R., 1986. Lithologic mapping of silicate rocks using TIMS: *Proceedings of the TIMS Data User's Workshop,* June 18-19, A. B. Kahle and Abbott, E., (eds.,) JPL Publication 86-38 p.29-43.

Gillespie, A. R., Kahle, A. B., Walker, R. E., 1987. Color Enhancement of Highly Correlated Images. I Decorrelation and HSI Contrast Stretches: *Remote Sensing Environment* v. 20 p.209-235.

Goetz, A. F., H., and Rowan, L. C., 1981. Geologic Remote Sensing: *Science*, v. 211, p.781-791.

Goetz, A. F., H., Rock, B. N., Lawrence, C. R., 1983. Remote Sensing for Exploration: An Overview: *Econ. Geol.* v. 78, p.573-591.

Goetz, A. F. H., and Srivastava, V., 1985. Mineralogical Mapping in the Cuprite Mining District, Nevada: *Proceedings of the Airborne Imaging Spectrometer Data Analysis Workshop,* April 8-10, JPL Publication 85-41, p.22-31.

Green, A. A., and Craig, M. D., 1985. Analysis of Aircraft Spectrometer Data with Logarithmic Residuals: *Proceedings of the Airborne Imaging Spectrometer Data Analysis Workshop*, April 8-10, JPL Publication 85-41, p.111-119.

Hardy, R., and Tucker, M., 1988. X-ray powder diffraction of sediments: *in* Techniques in Sedimentology, Tucker, M. E., (ed.,) Blackwell, London, 394p.

Henderson, R. A., and Stephenson, P. J., (eds.), 1980. *The Geology and Geophysics of Northeastern Australia*, Geological Society of Australia, Queensland Division, Brisbane, 468p.

Hunt, G. R., and Salisbury, J. W., and Lenhoff, C. J., 1971b. Visible and near infrared spectra of minerals and rocks: IV sulphides and sulphates: *Modern Geology*, v. 3, p.1-4.

Hunt, G. R., and Salisbury, J. W., and Lenhoff, C. J., 1972. Visible and near infrared spectra of minerals and rocks: V halides, phosphates, arsenates, vanadates, and borates: *Modern Geology*, v. 3, p.121-132.

Hunt, G. R., and Salisbury, J. W., and Lenhoff, C. J., 1973a. Visible and near infrared spectra of minerals and rocks: VI additional silicates: *Modern Geology*, v. 4, p.85-106.

Hunt, G. R., and Salisbury, J. W., and Lenhoff, C. J., 1973b. Visible and near infrared spectra of minerals and rocks: VII acidic igneous rocks: *Modern Geology*, v. 4, p.217-224.

Hunt, G. R., and Salisbury, J. W., and Lenhoff, C. J., 1974a. Visible and near infrared spectra of minerals and rocks: VIII intermediate igneous rocks: *Modern Geology*, v. 4, p.237-244.

Hunt, G. R., and Salisbury, J. W., and Lenhoff, C. J., 1974b. Visible and near infrared spectra of minerals and rocks: IX basic and ultrabasic rocks: *Modern Geology*, v. 5, p.15-22.

Hunt, G. R., 1977. Spectral signatures of particulate minerals in the visible and near infrared: *Geophysics*, v. 42, p.501-513.

Hunt, G. R., and Ashley R. P., 1977. Assessment of Landsat filters for rock type discrimination, based on intrinsic information: *Geophysics*, v. 43, p.738-747.

Hunt, J. R., 1980. Electromagnetic Radiation: The Communication Link in Remote Sensing: *in* Siegal, B. S., and Gillespie, A. R., (eds.) Remote Sensing in Geology, New York, Wiley, p.5-46.

Huntington, J., Green, A., and Craig, M., 1988. Mineral and lithologic mapping with the new GER 64 band scanner: U. S. and Australian examples: *in* Summaries, Sixth Thematic Conference, Houston, Texas, May 16-19, p.39.

Irons, J. R., and Labovitz, M. L., 1982. A Data Analytic Approach to Look-Angle Radiance Adjustment: *Jour. of Applied Photographic Engng.*, v. 8, p.128-137.

Irons, J. R., Ranson, K. J., and Daughtry, C. S. T., 1988. Estimating Big Bluestem Albedo from Directional Reflectance Measurements: *Remote Sensing of Environment,* v. 25, p.185-199.

JCPDS, 1974. Joint Committee for the Powder Diffraction Standards: Selected Powder Diffraction Data, JCPDS, Pennsylvania, USA.

Kahle, A. B., Madura, D. P., and Soha, J. M., 1980. Middle infrared multispectral scanner data: analysis for geological aplications: *Applied Optics,* v.19, p.2279-2290.

Kahle, A. B., 1983. The New Airborne Thermal Infrared Multispectral Scanner (TIMS): *Proceedings of the International Geoscience And Remote Sensing Symposium (IGARSS'83)* II, San Francisco, p.7.1-7.6.

Kahle, A. B., and Goetz, A. F., H., 1983. Mineralogic Information from a New Airborne Thermal Infrared Multispectral Scanner: *Science,* v. 222, p.24-27.

Kahle, A. B., 1986. Calculation of Day and Night Emittance Values for Death Valley California: *Proceedings of the TIMS Data Users Workshop,* Kahle, A. B., and Abott, E., (eds.,) JPL Publication 86-38, p.67-70.

Kahle, A. B., 1987. Surface emittance, temperature and thermal inertia derived from Thermal Infrared Multispectral Scanner (TIMS) data for Death Valley, California: *Geophysics,* v.52, p.858-874.

Kahle, A. B., Gillespie, A. R., Abbott, E. A., Abrams, M. J., Walker, R. E., Hoover, G., and Lockwood, J. P., 1988. Relative Dating of Hawaian Lava Flows Using Multispectral Thermal Images: A New Tool for Geologic Mapping of Young Volcanic Terranes: *Journal of Geophysical Research,* v.93, p.15,239-15,251.

Kastner, C. J., and Slater., P. N., 1982. In-flight radiometric calibration of advanced remote sensing systems: Proc. SPIE, 356, p.158-165.

Kimes, D. S., 1983. Dynamics of directional reflectance factor distributions for vegetation canopies: *Applied Optics,* v. 22, p.1364-1372.

Kruse, F. A., 1986. Digital Mapping of alteration zones in hydrothermal systems using Landsat Thematic Mapper Data - an example from the northern Grapevine Mountains, Nevada/California: *in* Summaries,

Fifth Thematic Conference: 'Remote Sensing for Exploration Geology', Reno, Nevada, 29 Sept.-2 Oct., p.51.

Lahren, M. M., Schweickert, R. A., and Taranik, J. V., 1986. Analysis of accreted terranes of the northern Sierra Nevada, California, with airborne thermal multispectral scanner data. *Proceedings of the Fifth Thematic Conference: 'Remote Sensing for Exploration Geology'*, Reno, Nevada, April 1-4, p.13-14.

Lahren, M. M., Schweickert, R. A., Taranik, J. V., 1988. Analysis of the northern Sierra accreted terrane, California, with airborne thermal infrared mutispectral scanner data: *Geology*, v.16, p.525-528.

Lawrence, P. M., Cargill, G., Lett, R. E., Groskopf, N., 1986. Pyrophyllite and kaolinite alteration mineral discrimination by sample reflectance measurement: *Proceedings of the Fifth Thematic Conference: 'Remote Sensing for Exploration Geology'*, Reno, Nevada, Sept. 29-Oct. 2, p.775-784.

Lillesand, T. M., and Kiefer, R. W., 1979. Remote sensing and image interpretation: John Wiley and Sons, 612p.

Lorraway, R., 1976. The petrology of the Camp-Oven mountain volcanic complex: unpubl. MSc Thesis, James Cook University of North Queensland, Australia, 150p.

Loughlin, W. P., and Taylor, M. A., 1985. Discrimination of rock types and alteration zones from airborne multipsectral data: The Samran-Shayban and Mahd Adh Dhahab areas of Saudi Arabia: *Proceedings of the Fourth Thematic Conference: 'Remote Sensing for Exploration Geology'*, San Francisco, California, April 1-4, p.207-217.

Lyon, R. J., P., 1965. Analysis of Rocks by Spectral Infrared Emission (8 to 25 microns): *Econ. Geol.*, v. 60, p.715-736.

Marsh, S. E., and Mckeon, J. B., 1983. Integrated Analysis of High Resolution Field and Airborne Spectrometer Data for Alteration Mapping: *Econ. Geol.* v.78, p.618-632.

Macias, L. F., Simpson, C. J., Moore, R. F., and Needham, R. S., 1987. Differentiation of sedimentary and mafic volcanic rock types using NS-001 and TIMS data, Eastern Creek Volcanics, Mount Isa: *Proceedings*

of the Fourth Australasian Remote Sensing Conference, v. 1, p.352-363.

McFarlane, M. J., 1976. Laterite and Landscape: Academic Press, London, 151p.

Milton, E. J., and Rollin, E. M., 1987. The GER IRIS Mk IV Spectroradiometer: A Guide for UK Users: Dept. of Geography, Univ. of Southampton, 138p.

Norwood, V. T., and Lansing, Jr. J. C., 1983. Electro-Optical Imaging Sensors: *in* Manual of Remote Sensing Second Edition, Colwell. R. N., (ed.,) American Society of Photogrammetry, v. 1, 1232p.

Palluconi, F. D., and Meeks, G. R., 1985. Thermal Infrared Multispectral Scanner (TIMS): An Investigators Guide to TIMS Data: JPL Publication, 85-32, 14p.

Petzold, D. E., and Goward, S. N., 1988. Reflectance Spectra of Subartic Lichens: *Remote Sensing Environment*, v.24, p.481-492.

Podwysocki, M. H., Segal, D. B., and Abrams, M. J., 1983. Use of Multispectral Scanner Images for Assessment of Hydrothermal Alteration in the Marysvale, Utah, Mining Area: *Econ. Geol.*, v.78, p.675-687.

Raines, G. L., and Canney, F. C., 1980. Vegetation and Geology: *in* Siegal, B. S., and Gillespie, A. R., (eds.), Remote sensing in geology, New York, John Wiley and Sons, p365-380.

Rickman, D., and Grant, S. K., 1985. Nightime TIMS, and chemical data for the Pyramid Mountains, South of Lordsburgh, New Mexico: *Proceedings of the Fourth Thematic Conference: 'Remote Sensing for Exploration Geology'*, San Francisco, California, April 1-4, p.361-362.

Roberts, D. A., Yamaguchi, Y. and Lyon, R. J., P., 1985. Comparison of various techniques for calibration of AIS data: Proc. of the Second Airborne Imaging Spectrometer Data Analysis Workshop, May 6-8, JPL Publication 86-35 p21-30

Robinson, B. F., and DeWITT, D. P., 1983. Electro-Optical Non-Imaging Sensors: *in* Manual of Remote Sensing, Colwell, R. N ., (ed.), Second Edition, American Society of Photogrammetry, Falls Church, Virginia, p.363.

Rowan, L. C., Wetlaufer, P. H., Goetz, A. F. H., Billingsley, F. C., and Stewart, J. H., 1974. Discrimination of rock types and the detection of hydrothermally altered areas in south-central Nevada by use of computer-enhanced ERTS images: United States Geological Survey Prof. Paper 883, 35p.

Rowan, L. C., Goetz, A. F. H., and Ashley, R. J. P., 1977. Discrimination of hydrothermally altered and unaltered rocks in visible near-infrared mutispectral images: *Geophysics*, v. 42, p.522-535.

Royer, A., Vincent, P., Bonn, F., 1985. Evaluation of Correction of Viewing angle Effects on Satellite Measurements of Bidirectional Reflectance: *Photogrammetric Engineering and Remote Sensing, v. 51* p.1899-1914.

Sabins, Jr. F. F., 1978. Remote Sensing Principles and Intperetation: W. H. Freeman and Company, San Francisco, 426p.

Salisbury, J. W., and Milton, N. M., 1987. Preliminary measurements of spectral signatures of tropical and temperate plants in the thermal infrared: *Proceedings of the Fifth Thematic Conference on Remote Sensing for Exploration Geology*, Environmental Research Institute of Michigan, Ann Arbor, Michigan, v. 1, p.131-143.

Salisbury, J. W., Hapke, B., and Eastes, J. W., 1987a. Usefulness of weak bands in mid-infrared remote sensing of particulate planetary surfaces: *Journal of Geophysical Research*, v.92, p702-710.

Salisbury, J. W., Hapke, B., and Eastes, J. W., 1987b. *Mid Infrared (2.1 to 25μm) Spectra of Minerals: First Edition* U. S. Geological Surveu Open-File Report 87-263, 356p.

Salisbury, J. W., and Milton, N. M., 1988. Thermal Infrared (2.5μm - 13.5μm) Directional Hemispherical Reflectance of Leaves: *Photogrammetric Engineering and Remote Sensing* v.54, p.1301-1304.

Salisbury, J. W., Walter, L. S., D'Aria, D., 1988. *Mid Infrared (2.5 to 13.5μm) Spectra of Igneous Rocks* U. S. Geological Survey Open-File Report 88-686, 114p.

Scatterwhite, M. B., Henley, J. P., and Carney, J. M., 1985. Effects of lichens on the reflectance of granitic rock surfaces: *Remote Sensing of*

Environment, v. 18, p.105-112.

Segal, D. B., 1983. Use of Landsat Multispectral Scanner Data for the Definition of Limonitic Exposures in Heavily Vegetated Areas: *Econ. Geol.*, v. 78 p.711-722

Selby, J. E. A., Kneizys, F. X., Chetwynd, Jr., J. H., and McClatchey, R. A., 1978. Atmospheric Transmittance/Radiance : Computer Code LOWTRAN 4, AFGL-TR-78-0053, Hanscom, AFB, 100p.

Settle, M., Abrams, M. J., Conel, J. E., Goetz, A. F. H., and Lang, H. R., 1984. Section Assessment Report: Paley, H. N., (ed.), *Joint NASA/Geosat Test Case Project (final resport)*, American Association of Petroleum Geologists, Tulsa, Oklahoma, p.2-1-2-4.

Sheffield, C., 1985. Selecting Band Combinations from Multispectral Data. *Photogrammetric Engineering and Remote Sensing*, v.51, p.681-687.

Simpson, C. J., Macias, L. F., and Moore, R. F., 1987. Differentiation of mafic and ultramafic rock types using NS-001 and TIMS data: *Proceedings of the Fourth Australasian Remote Sensing Conference*, v. 1 p.352-363.

Sjoberg, R. W., and Horn, B. P. k., 1982. Atmospheric effects in satellite imaging of mountainous terrain: *Applied Optics*, v. 22, p.1702-1716.

Soha, J. M., Schwartz, A. A., 1978. Multispectral Histogram Normalisation Contrast Enhancement: *Proceedings Fifth Canadian Symposium on Remote Sensing*, Victoria, B. C., Canada, p.86-93.

Suits, G. H., 1983. The Nature of Electromagetic Radiation: *in* Manual of Remote Sensing, Second Edition, American Society of Photogrammetry, v. 1, 1232p.

Teillet, P. M., Guindon, B., and Goodenough, D. G., 1982. On the slope-aspect correction of multispectral scanner data: *Canadian Journal of Remote Sensing*, v. 8., p.84-106.

Teillet, P. M., 1986. Image correction for radiometric effects in remote sensing: *Internat. J. Remote Sensing*, v.7, p.1637-1651.

Vincent, R. K., Pleitner, P. K., and Wilson, M. L., 1984. Integration of airborne thematic mapper and thermal infrared multispectral scanner

data for lithological and hydrothermal alteration mapping: *Proceedings of the Third Thematic Conference, 'Remote Sensing for Exploration Geology'*, Colorado Springs, April 16-19, p.219-226.

Wyatt, D. H., Paine, A. G. L., Clarke, D. E., Gregory, C. M., and Harding, R. R., 1971. Geology of the Charters Towers 1:250,000 Sheet Area, Queensland. *Bureau of Mineral Resources Report 137*, 84p.

Watson, K., Hummer-Miller, S., and Kruse, F. A., 1988. Co-Registered TIMS, Geology and Topography Data Sets for Evaluating Lithologic Discrimination, Carlin District, Nevada: *Summaries of the Sixth Thematic Conference 'Remote Sensing for Exploration Geology'*, Houston, Texas, May 16-19, p.34

APPENDIX I : SENSOR CHARACTERISTICS AND DATA FORMATS

The NS-001 Multispectral Scanner

The NS-001 airborne multispectral scanner has 8 bands, 7 of which are located in the visible/near infrared and 1 in the mid infrared. The data are contained on 9 track computer compatible tapes (CCT'S). The CCT'S have a density of 1600 bpi. The logical record length is fixed at 750 8-bit bytes. The first 50 bytes of all records are house-keeping information; the next 699 are digitized pixel data. A single "filler" byte is added at the end of each logical record to maintain even numbered byte lengths. The tapes are blocked to contain all channels of a single scanline sequentially in one block. Therefore, the physical record length equals the number of channels multiplied by the logical record length (6000 bytes). The contents of a logical record are given in Figure 1. The house-keeping information consists of 16-bit integers, unless otherwise noted (Figure 1). Video pixel data consists of two 8-bit samples packed in a 16-bit word. Digitized video pixels are reversed to compensate for the fact that the NS-001 scans right to left; pixel number 1 is the leftmost and pixel number 2 is the rightmost.

The Thermal Infrared Multispectral Scanner (TIMS)

The TIMS is a six channel airborne system aquiring digital data between 8-12μm . The data are contained on CCT at 1600 bpi. The logical record length is fixed at 698 8-bit bytes. The first 60 bytes for all records are house keeping information, the next 638 are digitized video pixel data. The tapes are blocked to contain all channels of a single scanline sequentially in one record (block). Therefore, the physical record length equals the number of channels multiplied by the logical record length (4188 bytes). The house-keeping information is stored as 16-bit integers unless otherwise noted (Figure 2). Video pixel data consist of two 8-bit samples packed two per 16-bit word. TIMS data is also available in a reformatted structure (see Palluconi and Meeks, 1985). All software developed in this project can handle either unformatted or formatted data.

Figure 1.1   Logical Format of the NS-001 User Tape

16-BIT WORD
   NUMBER   CONTENTS OF WORD

1-25   Channel Scanline Housekeeping Information

1   Data Frame Status
                0   Good frame
                10 Interpolated data
                20 Repeated data
                30 Zero-fill for data
2   Radiance Per Count Calibration Values
                Visible channel (1-7) flight calibration values modified for
                gain as follows: integer, tens of nanowatts per square
                centimeter per micron per steradian per count.
                Thermal channel is not used.
3-4   Scanline Count (32-bit integer)
5   Black Body 1 Thermistor Count
6   Black Body 2 Thermistor Count
7   Black Body 1 Thermal Reference Temperature (degrees C X 100)
8   Black Body 2 Thermal Reference Temperature (degrees C X 100)
9   Scan Speed (X 100)
10   GMT Hours
11   GMT Minutes
12   GMT Seconds (X 10)
13   Demagnification Value (X 100)
14   Total Air Temperature (TAT)
15   Gain Value (X 1000)
                Visible channel (1-7) gain value is defined as 1000 times (word
                24 minus word 19) divided by (the laboratory value of reference
                lamp less tare).
                Thermal channel (8) is not used.
16   Channel Number
17-18   Time (GMT)
                Expressed as a 7-digit number HHMMSST (32-bit integer)
19   Black Body 1 Radiance Count
20   Black Body 2 Radiance Count
21   Reference Lamp Voltage
22   Reference Lamp Current
23   Reference Lamp State (16 bits 000000000ab00000)
                a=1 means reference lamp selected as visible high-value
                    calibration source

                b=0 means lamp has not degraded below predetermined level
24   Reference Lamp Radiance Count
25   Precision Radiation Thermometer (PRT-5)
                Degrees Celcius X 10

304

Figure 1.2   Logical Format of the TIMS User Tape

| 16-BIT WORD	DESCRIPTION
1-30	Housekeeping Information:
1	Status: 0 implies the data are good; non-zero bad
	10 Interpolated data
	20 Repeated data
	30 Zero fill data
2	Filler
3-4	Scanline count (32-bit integer)
5-6	Thumbwheel switches (32-bit integer)
	Consists of 8 digits of the form DDMMYSSS
7	Blackbody 1 Thermal Reference Temperature
	(degrees C times 100)
8	Blackbody 2 Thermal Reference Temperature
	(degrees C times 100)
9	Scan Speed (scans/seconds times 10)
10	GMT hours
11	Minutes of the hour
12	Seconds (times 10) of the minute
13	Filler (set to 100; Reserve for Demagnification)
14	Filler
15	Gain value (times 1000)
16	Channel Number
17-18	Time, 7 digits, hhmmsst (32-bit integer)
19	Blackbody 1 response (count)
	(What the sensor sees when it looks at Blackbody 1)
20	Blackbody 2 response (count)
	(What the sensor sees when it looks at Blackbody 2)
21	Aircraft roll angle (degrees times 10):
	Signed integer, positive is left roll
22	Aircraft pitch angle, degrees times 10:
	Signed integer, positve is nose up.
23	True Heading (degrees times 10, 0 to 360.0 degrees)
24	Latitude degrees (Plus = North, Minus = South)
25	Latitude minutes times 10 (0 to 59.9 minutes)
26	Longitude degrees (Plus = East, Minus = West)
27	Longitude minutes times 10 (0 to 59.9 minutes)
28	Ground Speed (knots)
29	Drift Angle (degrees times 10), Plus = Left.
30	Navigation data status bits:
	1-bit -- Latitude
	2-bit -- Longitude
	4-bit -- Ground Speed
	8-bit -- Drift Angle
	(Bit on implies Valid data; off implies not valid)
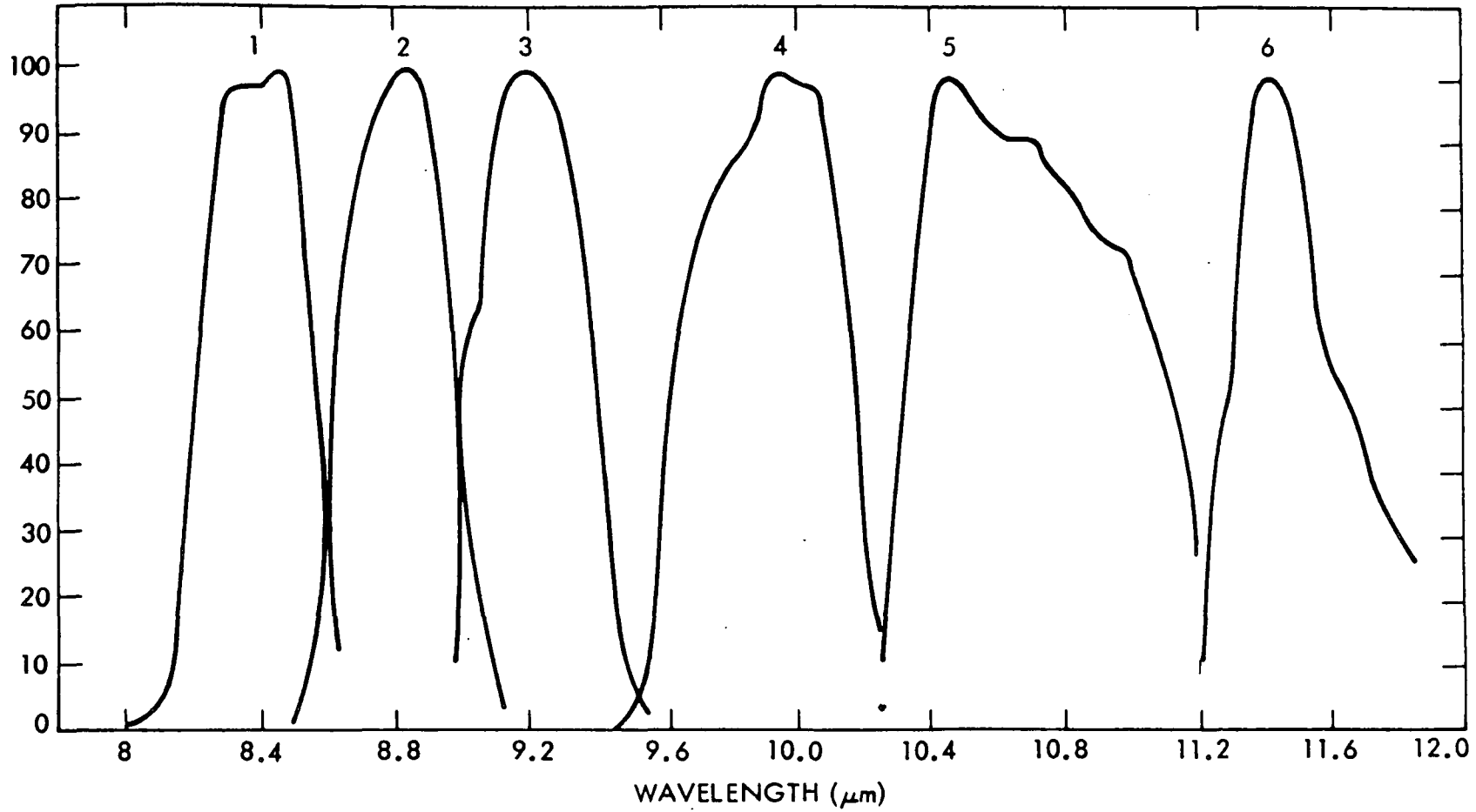
Figure 1.3 Response Function of the TIMS Sensor (from Palluconi and Meeks, 1985)